Porous coordination polymers for the capture of simple gases and environmentally harmful emissions

Aloysius David Dharma

ORCID 0000-0002-3784-3795

Submitted in total fulfilment of the requirements

of the degree of Doctor of Philosophy

School of Chemistry

University of Melbourne

October 2019

Abstract

The thesis describes a synthetic and structural investigation of coordination polymers in addition to an analysis of their adsorption properties.

In chapter 2 the synthesis and structure of Li^+ based network materials are described. An open-type network of composition Li(paa)·DMF (Hpaa = (2E)-3-(pyridine-4-yl)prop-2-enoic acid) was successfully synthesised. Exposure to the atmosphere, however, resulted in the material redissolving into mother liquor. Crystals of a dense Li(paa) network subsequently separated from the solution.

Open-type frameworks have yet to be generated using the longer peb^- (Hpeb = 4-[(E)-2-(pyridin-4-yl)ethenyl]benzoic acid) ligand. The coordination environment of Li^+ ions in $[Li_2(peb)(H_2O)_7](peb)\cdot H_2O$ is dominated by water molecules whilst the presence of a coordinated DMSO molecule in Li(peb)DMSO prevents the formation of channels.

In chapter 3 the synthesis and structures of five framework materials analogous to Zn(hba) (H_2hba = 4-hydroxybenzoic acid) are reported. The single crystal X-ray diffraction data of the structures are of poor quality, with broad streaky diffraction spots and low resolution, however X-ray powder diffraction unambiguously confirms that all frameworks adopt the same topology to that of Zn(hba).

The tetrafluoro hba^{2-} ligand did not form Zn(hba)-type frameworks. Instead two dense frameworks, Zn_2(tetrafluoro hba)$(OAc)_2$ and Zn(tetrafluoro hba)(MeOH)·MeOH, were formed. Zn_2(tetrafluoro hba)$(OAc)_2$ is formed when $Zn(OAc)_2$ is combined with tetrafluoro hba^{2-} while Zn(tetrafluoro hba)(MeOH)·MeOH is formed when $Zn(SiF_6)$ is used instead of $Zn(OAc)_2$.

Attempts to synthesise Zn(hba) family like frameworks with ligands related to cma^{2-} (H_2cma = (2*E*)-3-(4-Hydroxyphenyl)prop-2-enoate) have proven unsuccessful to date with the ligands $HhpOa^-$ and $HhpHNa^-$ (H_2hpOa = 4-hydroxyphenoxyacetic acid and H_2hpHNa = *N*-(4-Hydroxyphenyl)glycine) chelating to metal centres. The $HhpOa^-$ ligand formed a relatively simple mononuclear complex with Cu^{2+}. The complexes participate in extensive hydrogen bonding resulting in a 3D hydrogen bonded network. The combination of $HhpHNa^-$ ligands with Zn^{2+}, results in binuclear Zn^{2+} clusters, bridged by $HhpHNa^-$ ligands to form chains. These chains are linked through phenol-phenol and phenol-carboxylate hydrogen bonds to give a 3D hydrogen bonded network.

In chapter 4 and 5 the sorption properties of the Zn(hba) family of networks are reported. The networks are robust and exhibit the capability of adsorbing a variety of small molecules including the gases N_2, CH_4, CO_2, H_2 and the anaesthetics, isoflurane, sevoflurane, xenon and nitrous oxide. The smaller non-intersecting channels in the Zn(hba) family of networks lead to lower overall gas uptake capacity, although the adsorption of gases at 100 kPa is comparable to MOF materials that do not possess open metal sites.

Collaboration with Prof Cameron Kepert and Dr Peter Southon from the University of Sydney showed that Zn(hba) is capable of capturing significant quantities of sevoflurane and isoflurane well below the concentration of the anaesthetics exhaled by patients. Thermogravimetric analysis revealed that Zn(hba) is capable of retaining ~83% of captured isoflurane below 60 °C.

A prototype anaesthetic capture device was shown to capture 74% of the anaesthetic passed through an anaesthesia machine. The sevoflurane that was captured by the host in theatre was then transported to the candidate's laboratory and separated from the host network by application of gentle heating under vacuum. The sevoflurane vapour was then condensed by cooling. The isolated sevoflurane was then characterised by NMR.

Declaration

This is to declare that:

i. This thesis comprises my original work towards the PhD except where indicated in the preface.

ii. Due acknowledgement has been made in the text to all other material used.

iii. The thesis is less than 100,000 words in length.

_____

Aloysius David Dharma

Preface

Initial work on the coordination polymers with 2-methyl hba^{2-} were performed as part of the candidate's Master of Science (chemistry) degree, with A/Prof. Brendan Abrahams and Prof. Richard Robson at the University of Melbourne. Preliminary investigations included an unsuccessful structure determination, and gas adsorption studies involving H_2, CH_4 and CO_2. These results have been improved upon during the candidature of the candidate. The structure and gas sorbing properties of Zn(2-methyl hba) have since been published during the PhD candidature of the candidate.

The compounds Zn(hba), Zn(cma) and Zn(hbpc) were initially synthesised by Prof. Richard Robson and Dr Keith White.

Initial gas sorption measurements were conducted with Dr Keith White during his tenure in the Abrahams-Robson research group.

The initial idea of capturing anaesthetic vapour with the Zn(hba) family of networks was conceived by Prof. Paul Donnelly, chair of the candidate's review committee.

Computer simulations of the structure of Zn(2-methyl hba) and Zn(2-6,dimethyl hba) were conducted by Dr Ravi Babarao from the Royal Melbourne Institute of Technology.

IGA measurements on the sevoflurane and isoflurane uptake of Zn(hba) were conducted by Dr Peter Southon and Prof. Cameron Kepert from the University of Sydney.

The work presented was supported by the University of Melbourne through a Melbourne Research Scholarship. Additional support was provided by the Australian Research Council (ARC), the Science and Industry Endowment Fund, the Australian Synchrotron and The Australian Nuclear and Scientific Research Organisation (ANSTO).

Publications resulting from this thesis

"A New Structural Family of Gas-Sorbing Coordination Polymers Derived from Phenolic Carboxylic Acids"

White, Keith F.; Abrahams, Brendan F.; Babarao, Ravichandar; Dharma, A. David; et al.

CHEMISTRY-A EUROPEAN JOURNAL Volume: 21 Issue: 50 Pages: 18057-18061
Published: DEC 7 2015 **DOI: 10.1002/chem.201503252**

"Tunable Porous Coordination Polymers for the Capture, Recovery and Storage of Inhalation Anesthetics"

Abrahams, Brendan F.; Dharma, A. David; Donnelly, Paul S.; et al.

CHEMISTRY-A EUROPEAN JOURNAL Volume: 23 Issue: 33 Pages: 7871-7875

Published: JUN 12 2017 **DOI: 10.1002/chem.201700389**

"Lattice response of the porous coordination framework Zn(hba) to guest adsorption"

Auckett, Josie E.; Dharma, A. David; Cagnes, Marina P.; et al.

POWDER DIFFRACTION Volume: 32 Pages: S49-S53 Supplement: 2

Published: DEC 2017 **DOI: 10.1017/S0885715617000720**

"Methods of capturing and storing anaesthetics using metal organic frameworks"

Abrahams, Brendan F.; Dharma, A. David; Donnelly, Paul S; White, Keith; Robson, Richard.

Published: JAN 17 2019 **Patent ID: WO2019010517A1**

Other publications by the candidate, not directly related to the thesis

"Isomeric Ionic Lithium Isonicotinate Three-Dimensional Networks and Single-Crystal-to-Single-Crystal Rearrangements Generating Microporous Materials"

Abrahams, Brendan F. ; Dharma, A. David ; Grannas, Martin J.; Hudson, Timothy A.; et al.

INORGANIC CHEMISTRY Volume 53 Issue 10 Page 4956-4969

Published 2014 **DOI: 10.1021/ic403134c**

"An indirect generation of 1D M-II-2,5-dihydroxybenzoquinone coordination polymers, their structural rearrangements and generation of materials with a high affinity for H-2, CO2 and CH4"

Abrahams, Brendan F.; Dharma, A. David; Dyett, Brendan; Hudson, Timothy A.; et al.

DALTON TRANSACTIONS Volume 45 Issue 4 Page 1339-1344

Published 2016 **DOI: 10.1039/c5dt04095g**

"Square Grid Metal-Chloranilate Networks as Robust Host Systems for Guest Sorption"

Kingsbury, Christopher J.; Abrahams, Brendan F.; Auckett, Josie E.; Chevreau, Hubert; Dharma, A. David.; et al.

CHEMISTRY-A EUROPEAN JOURNAL Volume 25 Issue 20 Page 5222-5234

Published 2019 **DOI: 10.1002/chem.201805600**

Acknowledgements

I would like to thank the following people for their support throughout my candidature:

A/Prof. Brendan Abrahams for going above and beyond his duty as a supervisor; his fantastic spirit, friendly nature and patient guidance helped me through many a rough spot in my PhD.

Prof. Richard Robson for being a constant source of chemical insights, words of wisdom and inspiration.

Dr Timothy Hudson, for teaching me everything he knows, and more, about crystallography.

Dr Keith White, for his constant friendship, advice and sense of humour.

Dr Forbes McGain for his kind advice relating to anaesthetics and for providing generous access to facilities at the Sunshine and Footscray Hospitals of Western Health.

The members of my review panel, Prof. Paul Donnelly and A/Prof. Colette Boskovic, whose direction and critique were invaluable.

The members of the Abrahams-Robson group, past and present: Hui Min, Martin, Simon, Rob, Chris C, Chris K, Oliver, Katelyn, Ash, Jess, Anna, Tara, Robin, tall Owen and short Owen. I could not have asked for a better bunch of weirdos to hang out with during my candidature.

The Boskovic and Hua Groups: Carol, Tina, Maja, Gemma, Jett, Moya, Vincent, Katya, Aiden, Will, Elodie and Hui Min. I could not have asked for a better bunch of people to hang out with during my candidature.

Our collaborators: Prof. Cameron Kepert and Dr Peter Southon for the IGA measurements and Dr Ravi Babarao for his structure simulations.

The University of Melbourne for a Melbourne Research Scholarship.

The Australian Research Council and the Science and Industry Endowment Fund for financial support.

The Australian and New Zealand Society of Anaesthetists and Western Health for funding relating to the capture of anaesthetics.

The Balwyn Rotary Club and the School of Chemistry at the University of Melbourne for two generous travel scholarships, the Global Environmental Sustainability Award and the Masson Postgraduate Travel Award respectively.

The Australian Synchrotron and the Australian Nuclear and Scientific Research Organisation for providing key research infrastructure.

My siblings, Megan and Hans, and my parents Budhi and Lina, their love and support that carried me through.

And finally, Fred Basset – I can never quite guess what he is thinking.

Abbreviations

CP	=	Coordination polymer
PCP	=	Porous coordination polymer
MOF	=	Metal organic framework
DMF	=	*N*,*N*-dimethyl formamide
DMSO	=	Dimethyl sulfoxide
MeOH	=	Methanol
PentOH	=	Pentanol
OAc	=	Acetate
1-D	=	one-dimensional
2-D	=	two-dimensional
3-D	=	three-dimensional
TGA	=	Thermogravimetric Analysis
NMR	=	Nuclear magnetic resonance
hba	=	4-hydroxybenzoate
3-fluoro hba	=	3-fluoro-4-hydroxybenzoate
2-fluoro hba	=	2-fluoro-4-hydroxybenzoate
2-chloro hba	=	2-chloro-4-hydroxybenzoate
2-methyl hba	=	2-methyl-4-hydroxybenzoate
2,6-dimethyl hba	=	2,6-dimethyl-4-hydroxybenzoate
cma	=	*p*-coumarate; (2*E*)-3-(4-Hydroxyphenyl)prop-2-enoate
hbpc	=	4'-hydroxy-4-biphenylcarboxylate
paa	=	(2E)-3-(pyridin-4-yl)prop-2-enoate
peb	=	4-[(E)-2-(pyridin-4-yl)ethenyl]benzoate
H_2hpOa	=	4-hydroxyphenoxyacetic acid
H_2hpHNa	=	*N*-(4-Hydroxyphenyl)glycine

Table of contents

Table of figures

Table of tables

Chapter 1 Table of Contents

Chapter 1 – Introduction

The field of supramolecular chemistry gained general recognition as an important and emerging area of modern science when the 1987 Nobel prize in chemistry was awarded to Cram, Lehn and Pederson for "the development and use of molecules with structure specific interactions of high selectivity".[1] Key themes to emerge from their work relate to the concepts of complementarity and recognition as applied to the field of host-guest chemistry. In the late 1980s, interest in the related field of crystal engineering was growing. Gautum Desiraju, as a significant contributor in this area, was interested in the secondary bonding interactions present between organic molecules in crystalline materials. He was able to demonstrate that the relatively weak interactions between molecules, such as hydrogen-bonding and van der Waals forces can play a powerful structure directing role in the extended crystal structure. Desiraju identified a variety of secondary bonding motifs that could be relied upon to form certain types of associations involving discrete molecules. The link between supramolecular chemistry and crystal engineering was emphasised by Desiraju in his 1996 book entitled "The Crystal as a Supramolecular Entity".[2]

Around the same time that Desiraju was outlining principles in the area of crystal engineering, Richard Robson was employing what he described as a net-based approach for the generation of infinite metal - ligand network materials he referred to as coordination polymers. Although Desiraju and Robson employed different strategies, both had an interest in exploiting non-covalent interactions to generate novel crystalline materials and in this sense both approaches may be described as crystal engineering.

Coordination polymers may be formed by linking metal centres with bridging ligands. As represented by examples depicted in **Figure 1.1**, they may be described as 1-D, 2-D and 3-D structures.

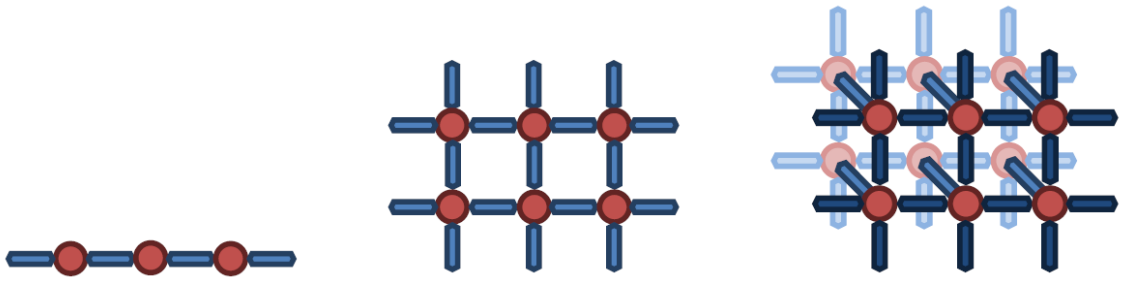

a) **b)** **c)**

Figure 1.1: Schematic representations of **a)** a 1-D chain, **b)** a 2-D sheet and **c)** a 3-D framework; red spheres represent nodes, blue rods represent connections.

The Robson approach involves taking a simple net, either corresponding to an archetypal inorganic material or a hypothetical mathematical net and use it as a topological model for generating new coordination polymers. The process involves the selection of metal ions and ligands that possess geometries that are appropriate for a targeted network. Although this approach often succeeds in generating the desired product, the targeted network is far from guaranteed. In addition to providing a basis for generating a specific product, the net description is also useful in describing the underlying connectivity of a coordination polymer.

Given the wide variety of metal ions with preferences for certain types of geometries and the near infinite number of bridging ligands, there is great scope for creating a wide variety of coordination polymers. Through the introduction of various groups onto the

bridging ligands there exists great opportunities to tailor networks for specific purposes.

An illustration of the use of the net based approach is provided by the generation of metal-ligand networks that possess the PtS topology. PtS consists of planar 4-connecting Pt^{2+} centres and 4-connecting tetrahedral sulfide centres in a 1:1 ratio, where each platinum centre is co-ordinated to four sulfur atoms and each sulfur atom coordinates to four platinum atoms. A feature of the PtS network is parallel hexagonal and square "channels" that run parallel to the *a*-axis directions, **Figure 1.2a**. Identical channels run parallel to the b-axis within this tetragonal structure. Square channels are observed along the unique *c*-axis in PtS, shown in **Figure 1.2b**. Of course given the van der Waals radii of the atoms these channels are much too small to incorporate any guest molecules.

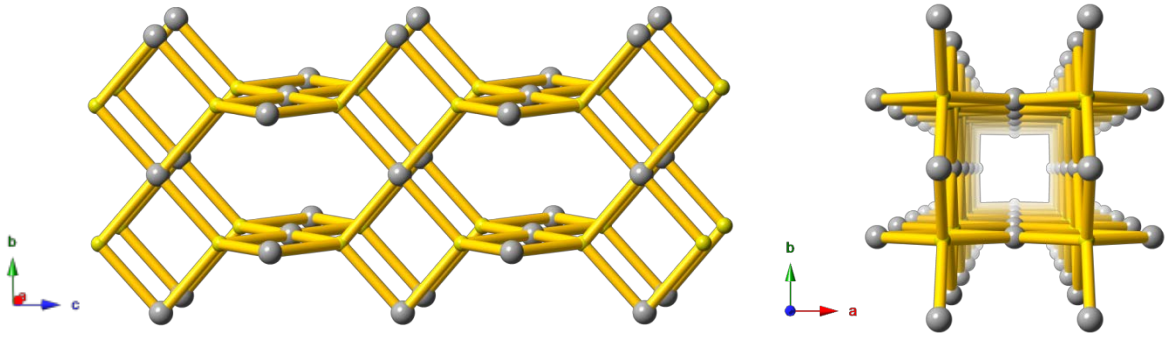

a) **b)**

Figure 1.2: The structure of PtS showing **a)** the hexagonal and square "channels" of PtS down the *a*-axis **b)** the square channels of PtS viewed down the *c*-axis. Pt atoms are represented by grey sphere and S atoms are represented by yellow spheres.

Robson considered that a PtS-type network could be generated if 4-connected planar centres were combined with tetrahedral centres in a 1:1 ratio. This led to the deliberate

synthesis of a PtS like network reported by Robson in 1990,[3] $[NMe_4][CuPt(CN)_4]$ in which the $Pt(CN)_4^{2-}$ anion served as a square planar unit and Cu^I acted as a tetrahedral centre, as shown in **Figure 1.3**. The relationship between PtS and the anionic $[CuPt(CN)_4]^-$ network is clearly apparent upon comparison of **Figure 1.2** and **Figure 1.3**. Importantly, the larger separation between tetrahedral and square planar centres in the $[CuPt(CN)_4]^-$ network leads to the generation of channels which are large enough to accommodate tetramethylammonium counter cations, as shown in **Figure 1.4**.

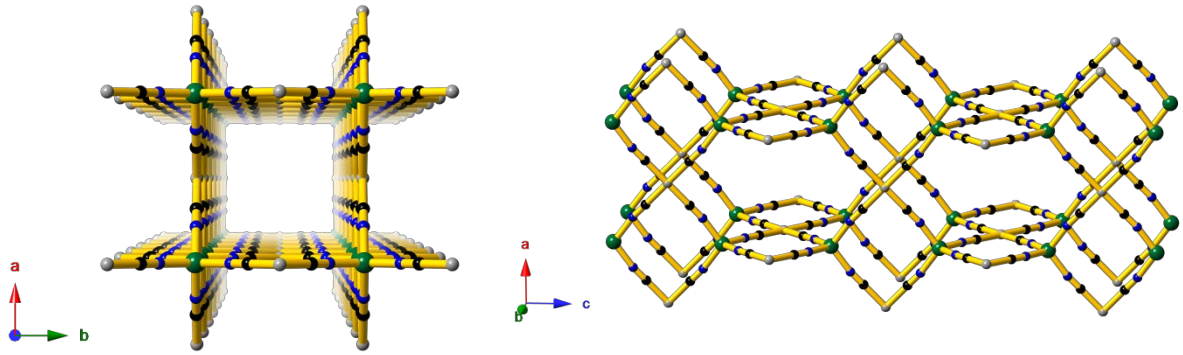

a) **b)**

Figure 1.3: A view down the **a)** square channel and **b)** hexagonal channel of $[NMe_4][CuPt(CN)_4]$. Tetramethylammonium cations have been omitted for clarity. Tetrahedral Cu^+ centres are represented by green spheres while planar Pt^{2+} centres are represented by grey spheres. Carbon and nitrogen atoms are represented by black and blue spheres respectively.

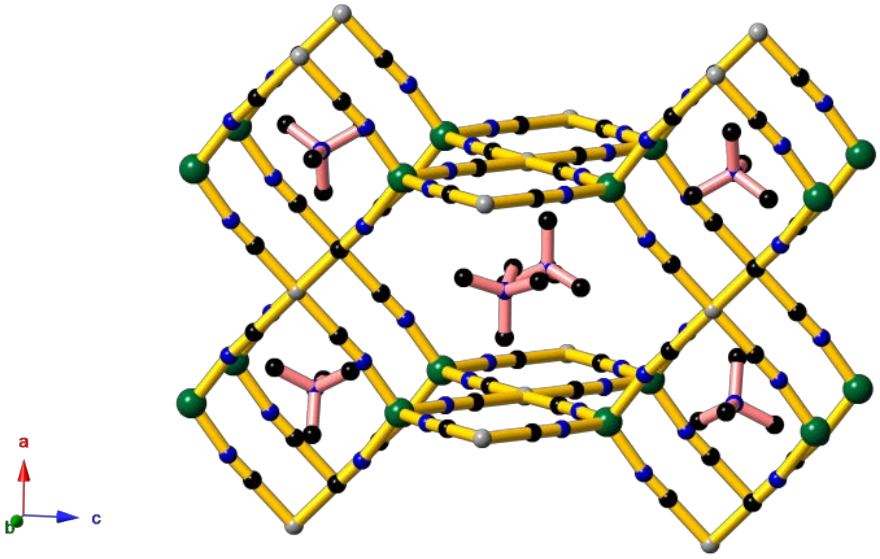

Figure 1.4: A view slightly off the *b* axis of $[NMe_4][CuPt(CN)_4]$. The NMe_4^+ counter cations, which occupy the intra-framework channels, are highlighted with pink bonds.

The deliberate synthesis of $[NMe_4][CuPt(CN)_4]$ provided encouragement that PtS type networks could be synthesised with larger 4-connecting planar building blocks leading to even wider channels. Cu^{2+} tetrapyridylporphyrin (Cutpp, **I**) is potentially a 4-connecting unit with the pyridyl groups directed towards the vertices of a square and as such, it was anticipated that it could play the role of the square planar unit in a PtS-type network. The tetrahedral centre would require a metal centre that was capable of binding four pyridyl groups which would belong to four distinct tpp^{2-} units. It was anticipated that Cu^+ would be well suited to this role. The combination of Cutpp and Cu^+ did in fact yield the anticipated PtS-type network (**Figure 1.5**).[4] The cationic network had the composition $[(Cutpp)Cu]^+$ and indeed possessed much wider channels than had been generated with $[CuPt(CN)_4]^-$.

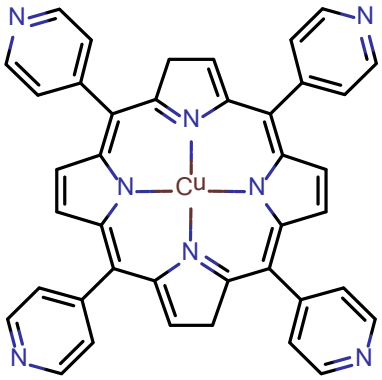

(I)

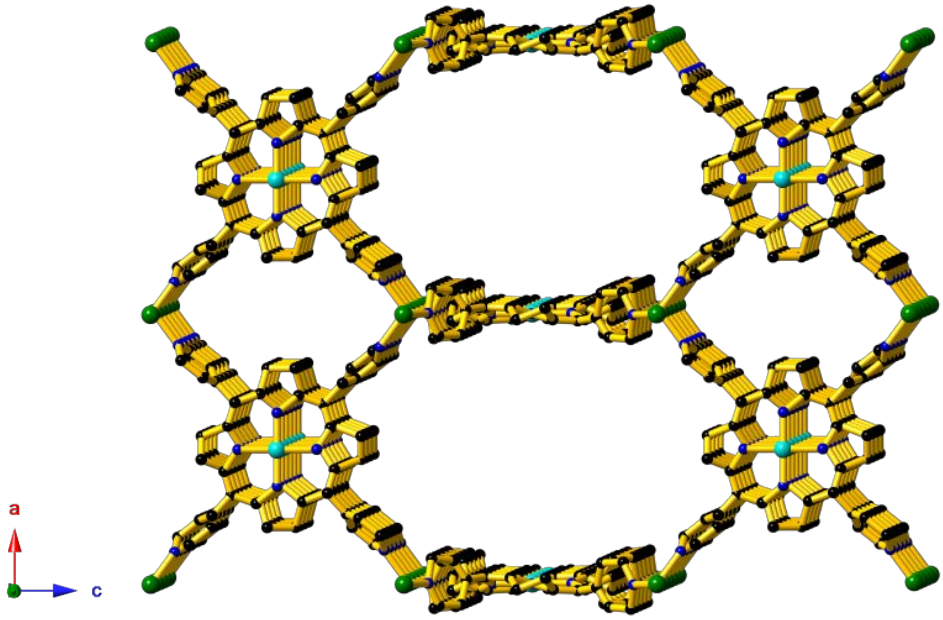

Figure 1.5: A view slightly off the *b*-axis of the [(Cu^{II}tpp)Cu]$^{+}$framework. Hydrogen atoms have been omitted for clarity, planar Cu^{2+} in is represented as light blue spheres.

The large voids of the [(Cutpp)Cu]$^{+}$ cationic framework are occupied by disordered BF_4^- anions and nitrobenzene. The distance between parallel porphyrin faces is 14.2 Å in contrast with the separation of Pt centres of 3.5 Å in the PtS itself. Unfortunately the compound loses single crystal character upon exposure to the atmosphere.

In 1997 S. Kitagawa *et al* successfully demonstrated the adsorption of O_2, CH_4 and N_2, into coordination polymers with the general formula $\{[M_2(4,4'\text{-bpy})_3(NO_3)_4]\cdot n H_2O\}$ (where M = Co, Ni and Zn; 4,4'-bpy = 4,4'-bipyridine), shown below in **Figure 1.6**.[5] Although only able to adsorb small amounts of these gases (2.5 mmol/g CH_4, 0.8 mmol/g N_2 and 0.8 mmol/g of O_2 each at 30 atm) this early work from the Kitagawa group marked the advent of rapidly growing interest in the use of coordination networks for the uptake of volatile guest molecules.

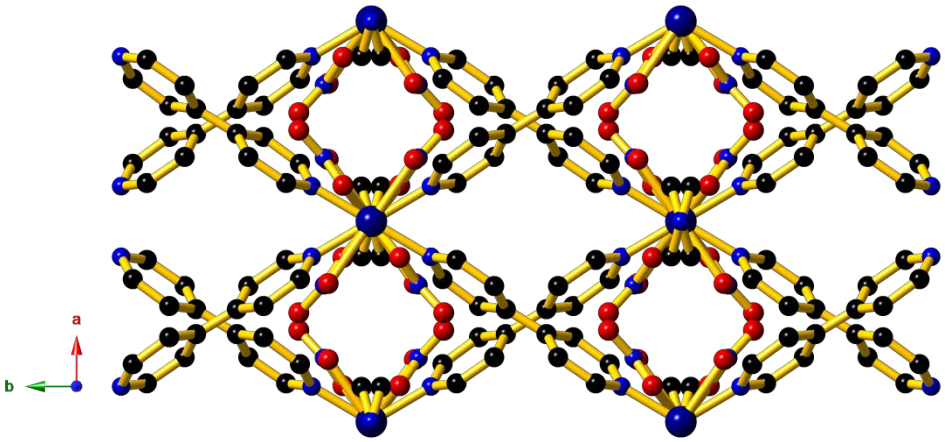

Figure 1.6: A view down the *c* axis of the 3-D network $[Co_2(4,4'\text{-bpy})_3(NO_3)_4]\cdot 4H_2O$ The hydrogen atoms and solvent water molecules have been omitted for clarity. Co^{2+} is shown as navy spheres and oxygen atoms are represented as red spheres.

1.1 Gas adsorption

The adsorption properties of porous coordination polymer (PCP) materials are most commonly investigated using isothermal adsorption/desorption measurements. This involves placing a weighed sample of the adsorbent polymer in a cell of known volume and exposing it to a gas at a selected pressure and temperature. Upon equilibrium, the pressure is remeasured, with the difference indicating the amount of gas adsorbed into

the material. The sample is then exposed to a higher pressure and the amount adsorbed is remeasured. A gas adsorption isotherm is obtained once a sequence of measurements is completed.

The International Union of Pure and Applied Chemistry (IUPAC) have proposed conventions for the classification of gas sorption isotherms, shown in **Figure 1.7**.[6] PCP materials are typically microporous and adsorb gas with type I behaviour evident in the isotherm.

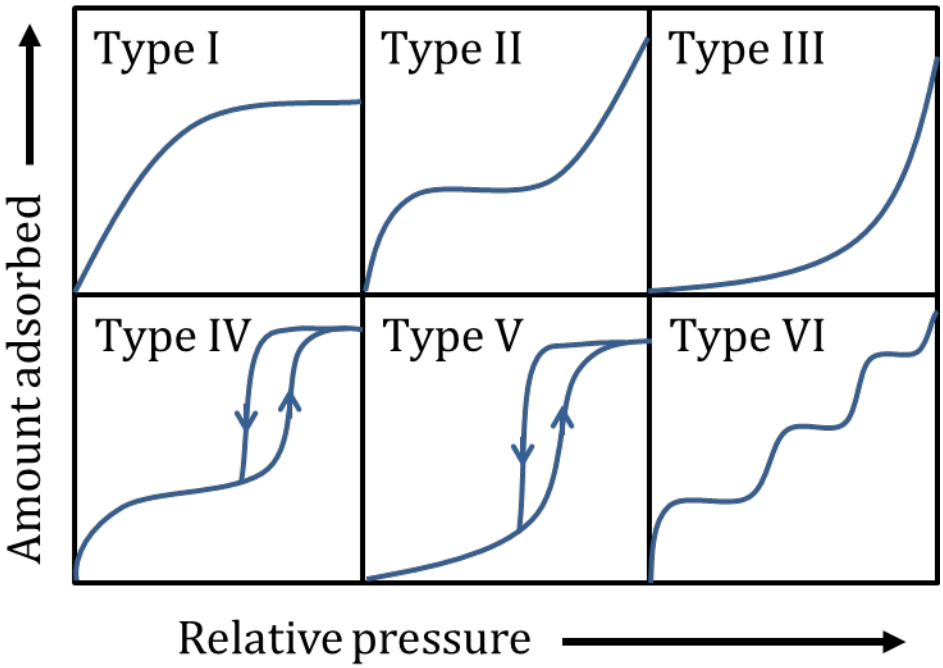

Figure 1.7: A representation of the six different types of isotherms classified by IUPAC.[6]

In a typical gas adsorption isotherm it is not the absolute adsorption, that is measured but rather the surface excess. Surface excess is the amount of adsorbate adsorbed that exceeds the amount of gas that would be present in the volume taken up by the

adsorbent.[7] As the pressure is increased the amount sorbed reaches a maximum, however, the density of the adsorbate in the bulk phase continues to increase. As a result, at high pressures the true amount of gas adsorbed on the surface is underestimated. Commonly this results in a slight downward curve in the isotherm after the material has reached a 'maximum' adsorption, **Figure 1.8**.

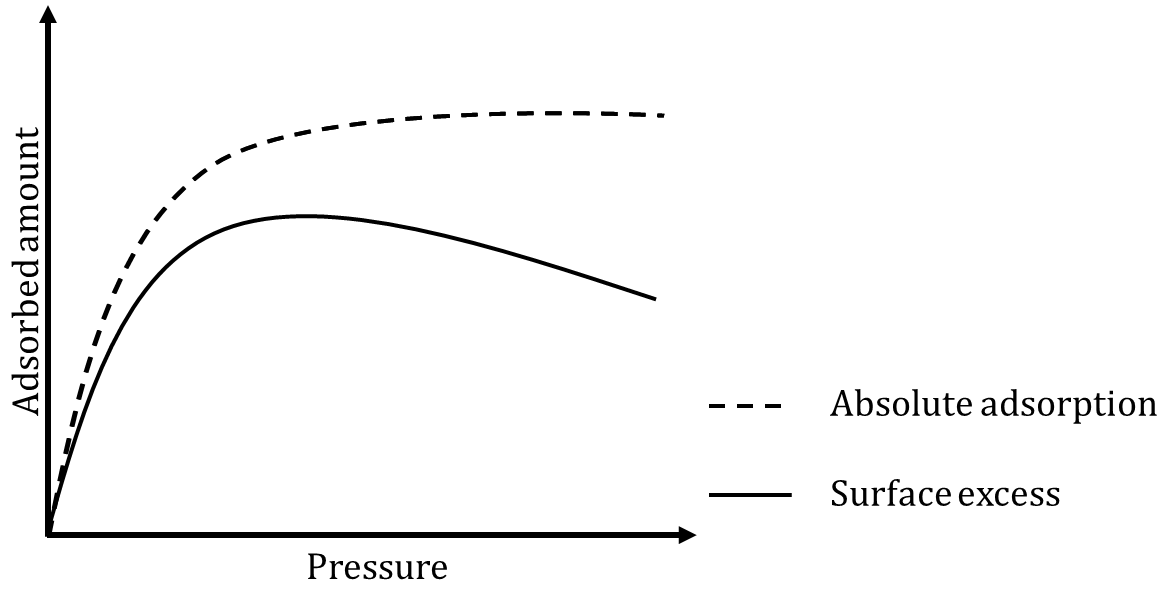

Figure 1.8: A representation highlighting the difference in isotherms between 'absolute adsorption' and 'surface excess'.

The surface areas of PCP materials are generally obtained using N_2 adsorption isotherms at 77 K and applying the Langmuir and/or BET(Brunauer–Emmett–Teller) calculations. Although both calculations are widely employed[8] they need to be used with caution when applied to 3-D PCP type materials due to the inherent assumptions associated with the calculation of the surface area. These assumptions include:

1) the surface is perfectly flat and homogeneous
2) all adsorption sites are equivalent and

3) the adsorbate is in an immobile state and does not interact with molecules on adjacent sites.[9]

In PCP materials, these assumptions may cause a significant deviation from the actual surface area. Furthermore, the Langmuir method tends to overestimate the surface area as it assumes mono-layer coverage only. BET improves on this limitation, allowing for multilayer adsorption with the additional assumptions:

1) adsorbates physically sorb in layers,
2) adsorbates interact only with adjacent layers and
3) Langmuir theory can be subsequently applied to each individual layer.[9,10]

It has been experimentally observed that the difference between the Langmuir and BET surface area is lower in PCPs with a higher crystal density, suggesting that as the void volume increase so does the difference in the Langmuir and BET surface area.[11] Both methods are only an approximation of the true internal surface area of MOF/PCP materials.

Physisorption occurs when a gas molecule adheres to a solid surface, including the internal pore surfaces of PCPs. This is opposed to gas chemisorption where the gas molecule forms a chemical bond with the solid phase. The vast majority of PCP compounds bind guest molecules through physisorption, as guest gas molecules only adhere to the surface of the pores through secondary bonding interactions. Physisorption uptake at low pressures tends to be much less than chemisorption and the energy required to release the gas molecules is significantly less.[12] Chemisorption results in the formation of stronger interactions with the surface, allowing for higher

uptake under lower pressures. Not surprisingly, considerable energy is commonly required to release the gas. The strength of the interaction of a guest molecule and a host material is usually quantified as the isosteric heat of adsorption (Q_{st}).

Once gas uptake isotherms at multiple temperature are measured, the heat of adsorption (Q_{st}) can be calculated using the Clausius-Clapeyron equation.[13] To determine Q_{st} the isotherms are fitted to a high-order polynomial equation to obtain an expression of pressure (P) in terms of number of mol of adsorbed guest (N). The Q_{st} at each adsorption point can be obtained from the slope of $\ln(P)$ as a function of $(1/T)$:

$$\ln(P) = -\frac{Q_{st}}{R}\frac{1}{T} + C$$

where P is pressure, R is the universal gas constant, T is the temperature and C is a constant. In this thesis Q_{st} is evaluated by first fitting the isotherm data to a virial-type expression:

$$\ln(P) = \ln(N) + \frac{1}{T}\sum_{i=0}^{m} a_i N^i + \sum_{i=0}^{n} b_i N^i$$

Where a_i and b_i are virial coefficients, m and n are the number of virial coefficients that allow adequate fitting of the isotherm (for the purpose of this thesis m=5 and n=0) and N is number of mol of adsorbed guest. Then, Q_{st} can be calculated as:

$$Q_{st} = \sum_{i=0}^{m} a_i N^i$$

This approach to calculating Q_{st} is commonly referred to as the 'virial method'. This virial method allows the calculation of Q_{st} at any point of adsorption, including zero

coverage, whereas other methods, such as the Langmuir-Freundlich[14][15] and 'two single site Langmuir'[13][16] methods can only give Q_{st} at low coverage.

In 1999 Yaghi *et al* reported a breakthrough in N_2 uptake in porous materials and published details of a metal ligand network, referred to as metal organic framework-5 (MOF-5).[17] The cubic network resulted from the combination of Zn^{2+} metal centres and benzene dicarboxylate (bdc^{2-}). The network can be described as having an α-polonium type network topology (**Figure 1.9a**) with basic zinc carboxylate-type units, $Zn_4O(CO_2)_6$, linked by benzene rings (**Figure 1.9b**). However, despite the large voids in the framework (**Figure 1.9c**), the material proved quite stable and did not collapse upon removal of the solvent molecules. Gas adsorption experiments indicated very large gas uptake, an unprecedented 800 mg of N_2 per gram of activated material, almost 29 mmol/g.

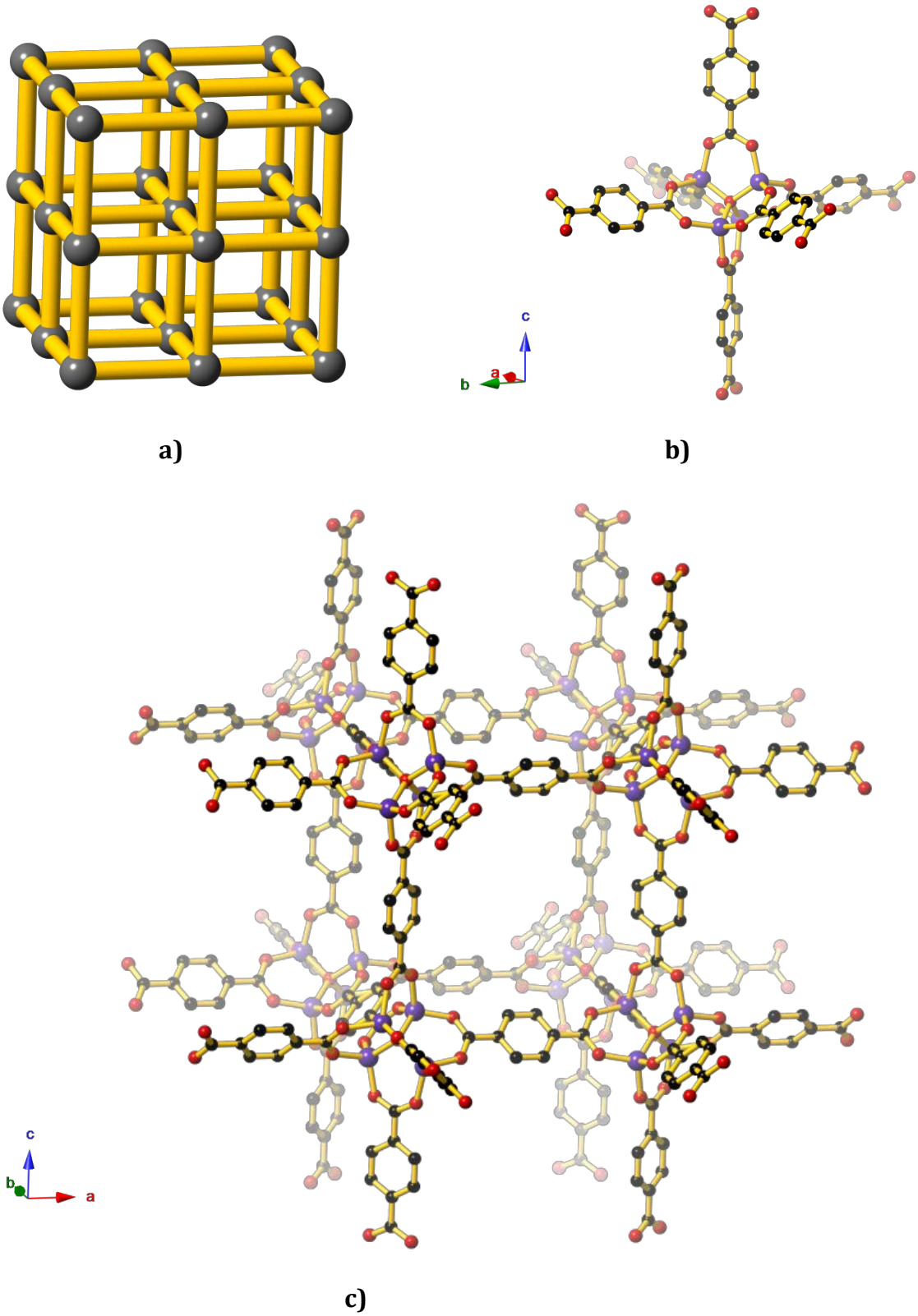

a) **b)**

c)

Figure 1.9: a) A representation of the α-polonium network, in which each octahedral centre is connected to six other octahedral centres. **b)** A single $Zn_4O(bdc)_6$ octahedral unit within MOF-5 and, **c)** the extended cubic structure of MOF-5. Zn^{2+} is represented by purple spheres

The robust behaviour of MOF-5 with respect to solvent loss and gas uptake has been attributed to the basic zinc carboxylate clusters that make up the 6-connecting octahedral nodes of the framework. Many other dicarboxylate frameworks have been generated employing the approach used to generate MOFs. When the dicarboxylate used is longer than bdc^{2-}, larger intra-network cavities are formed leading to the uptake of even greater quantities of gas. Materials capable of adsorbing large quantities of gas have potential applications in areas such as energy storage and carbon dioxide sequestration.

Yaghi referred to a structurally similar set of compounds with linkers of different length or with substituents of the linker, as an isoreticular MOF series (IRMOF).[18] For example MOF-5 has been redesignated as IRMOF-1. Below is a diagram of IRMOF-10, **Figure 1.10**, where the pore size of the framework has been increased by the using the 4-(4-carboxyphenyl)benzoate ligand instead of the bdc^{2-} ligand present in IRMOF-1. The increased distance between the Zn_4O clusters results in a decrease of crystal density from 0.61 g/cm^3 in IRMOF-1 to 0.33 g/cm^3 in IRMOF-10, for the evacuated crystals.[18]

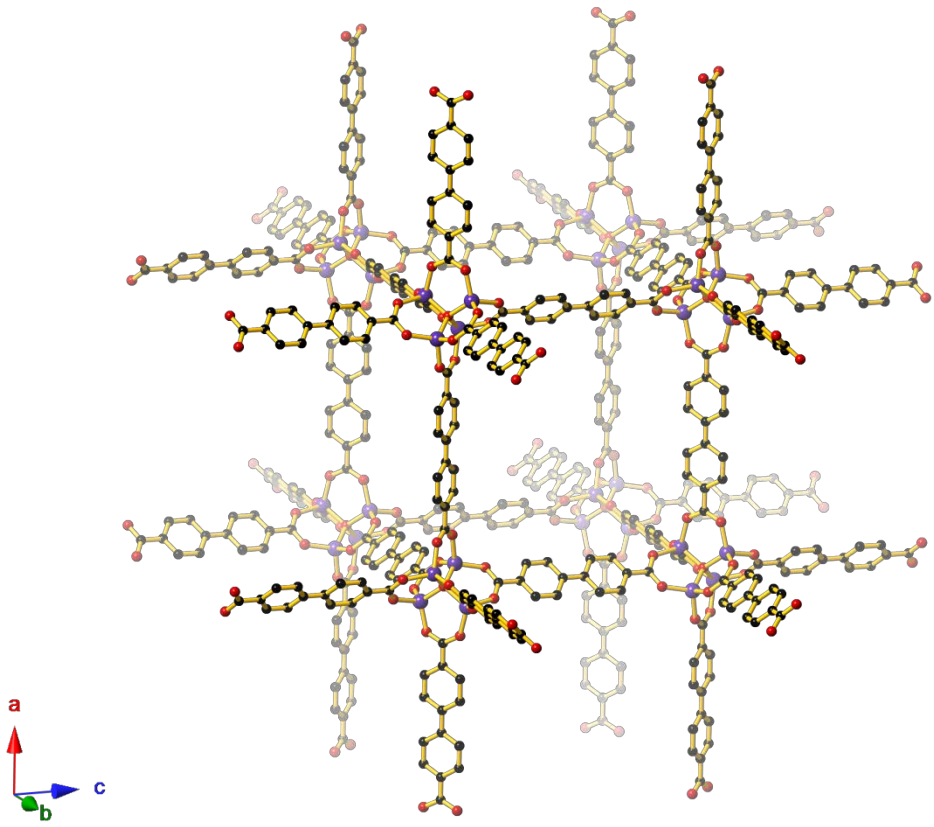

Figure 1.10: The cubic structure of IRMOF-10

Many more MOF type materials have been designed and synthesised with the intent of capturing large quantities of gas. Many of these frameworks contain metal-carboxylate clusters which serve as nodes within an infinite network. These clusters are commonly referred to in the MOF community as secondary building units or SBUs. It can be imagined that, by theoretically taking any of these pre-existing SBUs and linking them together by an appropriate organic carboxylate linker, frameworks with voids of controllable size could be synthesised. Indeed, in the past two decades a large number of MOF/PCP compounds have been generated with pore sizes that have allowed very high uptake of guest molecules. In the discussion below some of the most important PCP/MOF materials are described.

Mg-MOF-74, CPO-27-Mg or Mg/DOBDC (DOBDC = dihydroxy benzenedicarboxylate, **II**), which possesses a very different topology to preceding IRMOFs discussed, is reported to have a BET estimated surface area of 1495 m^2/g and is comprised of Mg^{2+} centres bridged by $DOBDC^{4-}$ anions within a 3-D network with parallel hexagonal channels, reminiscent of honeycomb (**Figure 1.11**).[19,20] After the removal of coordinated solvent molecules which protrude into the channels, the diameter of the channels is approximately 10.8 Å, van der Waals surface to van der Waals surface.

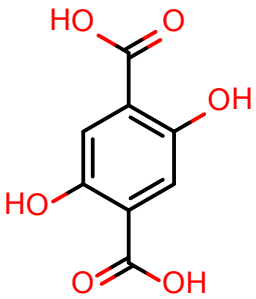

(II) H_4DODBC

In 1999 Williams *et al* reported the network material HKUST-1 (Hong Kong University of Science and Technology framework 1) or "Cu-BTC".[21] The framework combines the planar four connecting "Chinese lantern" Cu^{2+} dimers, as shown **Figure 1.12a**, with 1,3,5-benzene tricarboxylate (BTC^{3-}) in 3:2 proportions to generate a compound of composition $Cu_3(BTC)_2(H_2O)_3$, as shown in **Figure 1.12b**. The 3-D network possesses sizable cavities which may be filled with various guest molecules. Within the framework, the Cu^{2+}–dimers serve as planar 4-connecting nodes and the ligand acts as a 3-connecting node to give a network that possesses the twisted boracite topology.

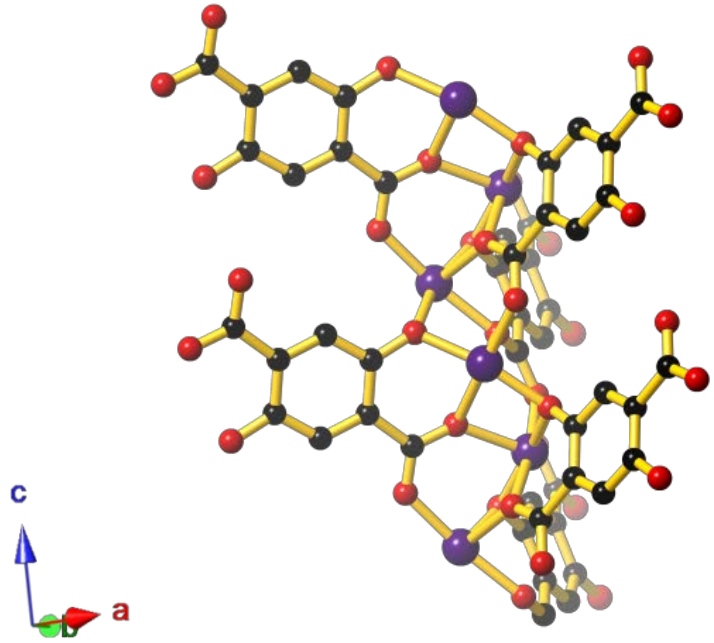

a)

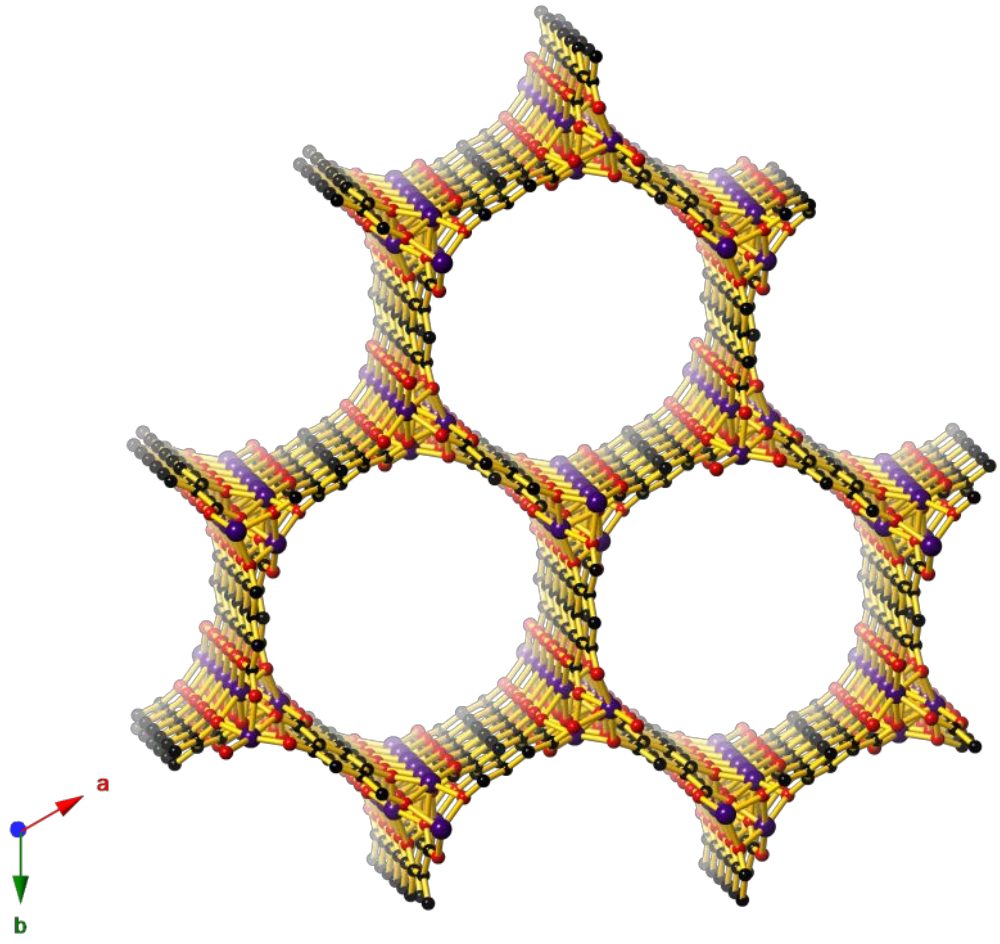

b)

Figure 1.11: The structure of Mg-MOF-74 showing **a)** Zn centres linked along the *c*-direction by $DOBDC^{2-}$ anions and **b)** the extended network showing the hexagonal channels

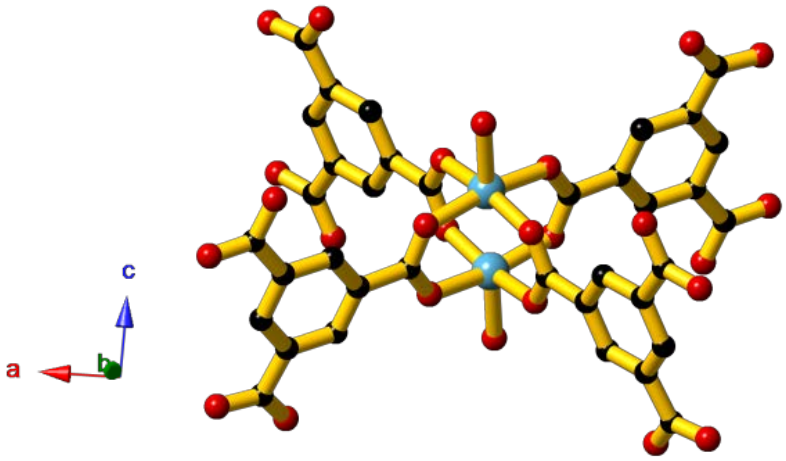

a)

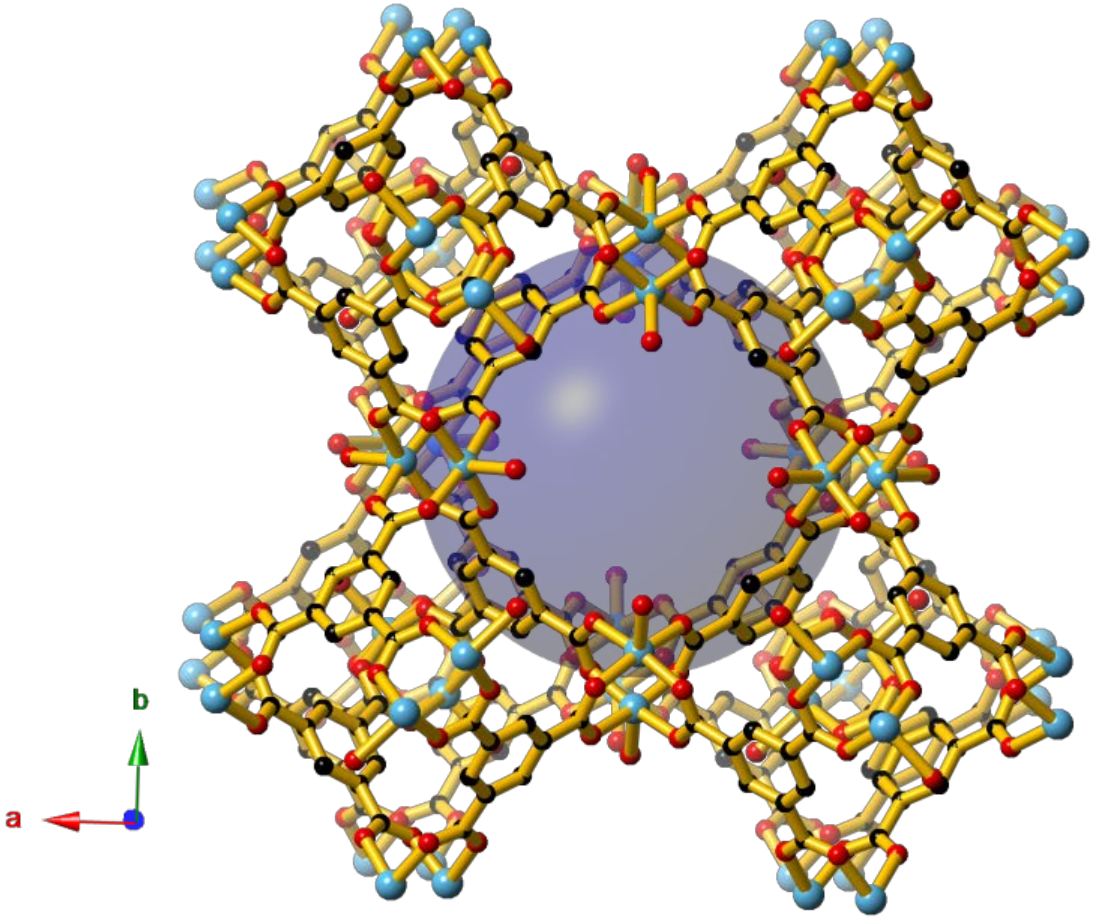

b)

Figure 1.12: The structure of HKUST-1 showing **a)** the coordination of four BTC^{3-} trianions to a $Cu_2(H_2O)_2$ unit and **b)** the extended structure with a translucent blue sphere indicating the large intra-framework space.

MOF-177 is formed by the combination of the trigonal 1,3,5-tris(4-carboxyphenyl)benzene with Zn_4O units of the type that played the role of the 6-connecting node in MOF-5 (**Figure 1.13**). The trigonal network contains intersecting channels of diameter 11.8 and 10.8 Å. The framework has a reported BET surface area of 4750 m^2/g.[22] Not surprisingly, given the intra-framework space, it can adsorb significant amounts of gas. MOF-177 can adsorb 1550 mg/g of CO_2, which is approximately 50% more than MOF-5 (1030 mg/g). [23]

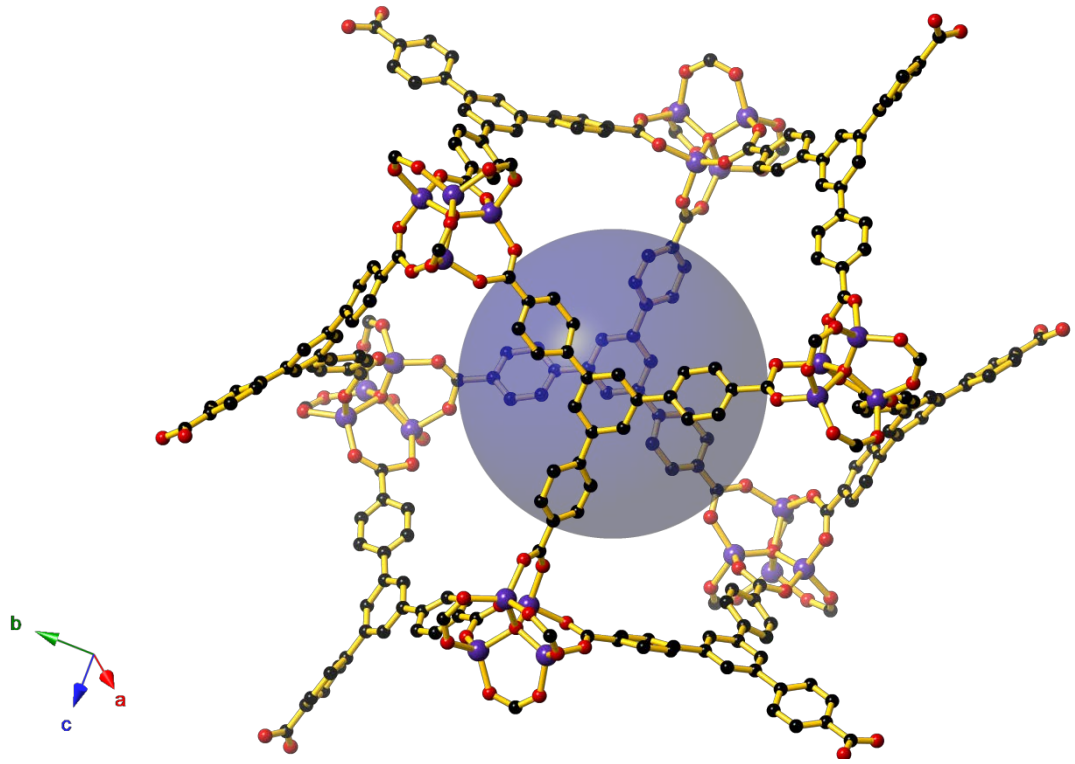

Figure 1.13: The extended structure of MOF-177 with a transparent blue sphere indicating the large intra-framework space.

UiO-66 is widely recognised as a particularly stable material, showing surprising resistance to moisture; a weakness that plagues many MOF/PCP materials.[24] The framework is made up of clusters where the Zr(IV) metal centres are at the vertices of an octahedron, the faces of which are capped by μ_3-O or μ_3-OH and the edges spanned

by μ_2 carboxylate groups. These twelve-connected nodes are identical to that of the hexanuclear Zr(IV) acetate species, $Zr_6(O)_4(OH)_4(CH_3COO)_{12}$, (**Figure 1.14**).[25] The extended framework is formed by linking the Zr(IV) clusters by bdc^{2-} ligands, as shown in **Figure 1.15**.

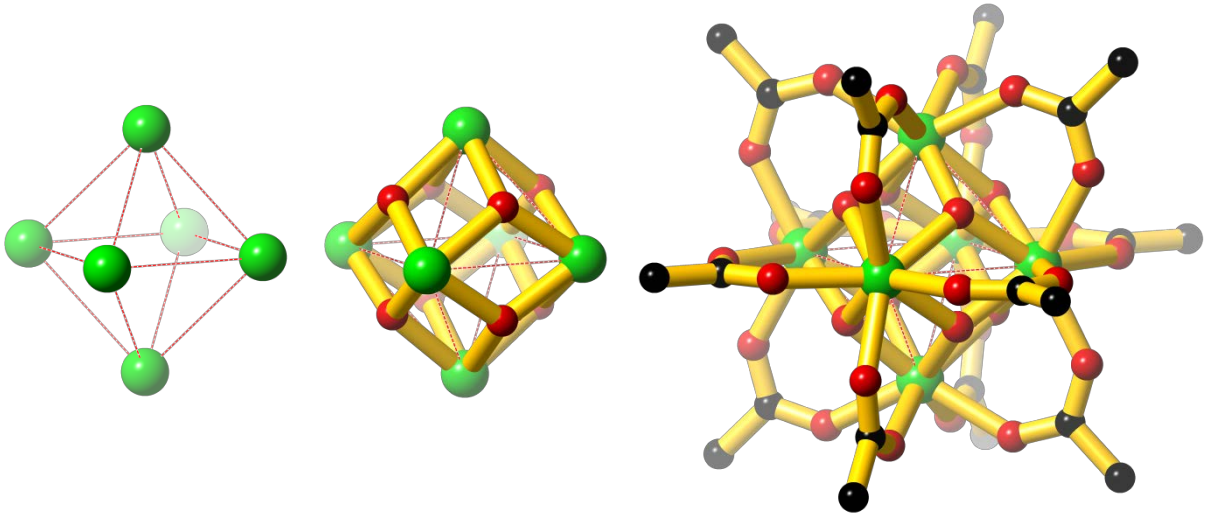

a) **b)** **c)**

Figure 1.14: The Zr(IV)acetate unit showing **a)** the octahedral arrangement of Zr(IV) metal centres, **b)** μ_3-O or μ_3-OH (hydrogen atoms omitted) capping the octahedral faces and **c)** the complete hexanuclear Zr(IV) acetate species. (An octahedron of Zr_6 centres is indicated by a dotted red line). Zr(IV) centers are represented by green spheres

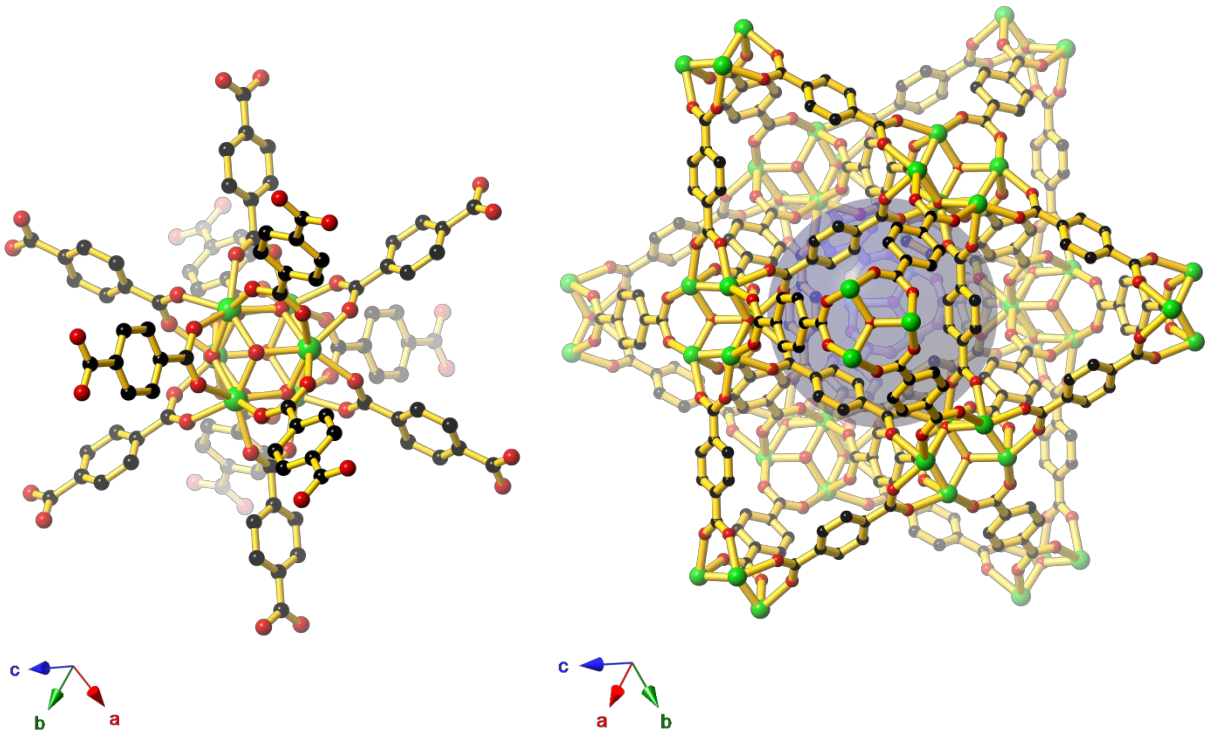

a) **b)**

Figure 1.15: The structure of UiO-66 showing **a)** the 12-connecting Zr and terephthalate ligands extending outwards and **b)** the extended structure with a translucent blue sphere indicating the large intra-framework space.

The compound MIL-101 (MIL = Matérial Institut Lavoisier)($Cr_3F(H_2O)_2O[bdc]_3.nH_2O$ (n ~25)) is formed from the hydrothermal reaction of H_2bdc and Cr^{3+}. The metal centres form Cr^{3+} trimers with a central μ_3 oxide ion. Each $[Cr_3O]^{7+}$ cluster is linked to six equivalent clusters through bridging bdc^{2-} ligands, as shown in **Figure 1. 16**. The overall framework forms a face centred cubic arrangement with a large unit cell (a ~ 89 Å). The structure possesses large voids with an BET estimated surface area of over 4100 m^2/g. A single large cavity in MIL-101 is shown in **Figure 1.17**.[26]

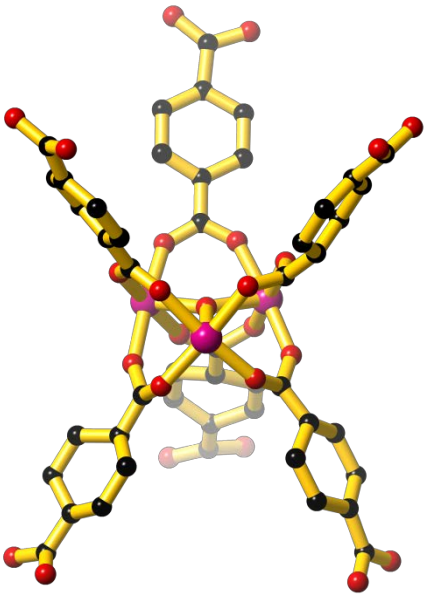

Figure 1. 16: The Cr^{3+} trimer with a centre μ_3 O^{2-} and six bridging bdc^{2-} ligands. Cr atoms are represented by pink spheres.

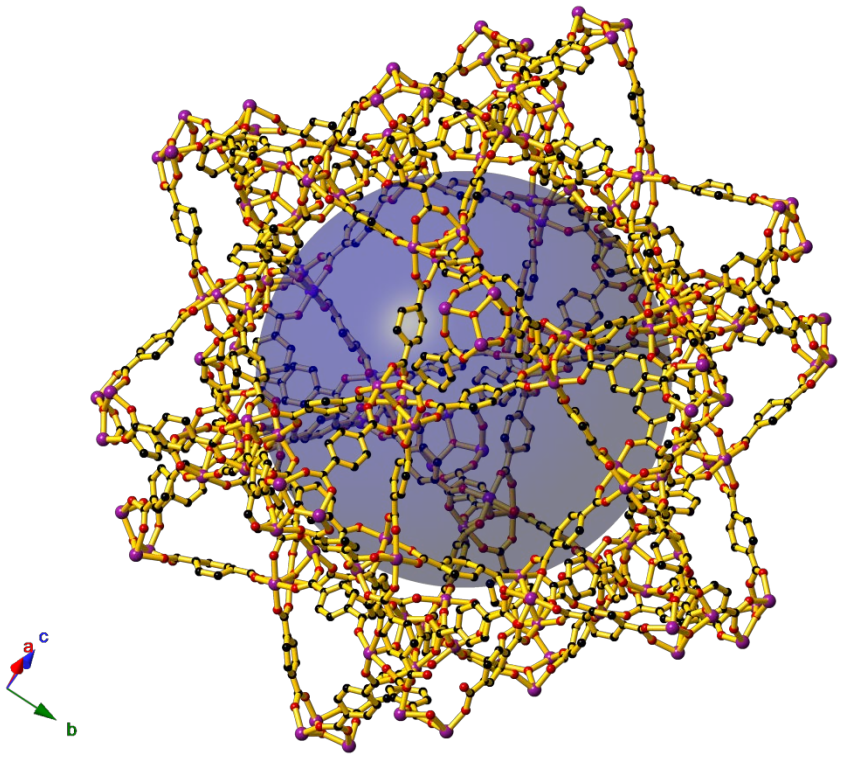

Figure 1.17: The extended structure of MIL-101 with a transparent blue sphere indicating the large intra-framework space.

The NOTT-116 framework consists of 4-connecting planar "chinese lantern" Cu^{2+} dimers similar to those found in HKUST-1. In NOTT-116 the Cu^{2+} dimers are linked by 6-connecting 5-(2-{4-[3,5-bis({4-[2-(3,5-dicarboxyphenyl)ethynyl]phenyl})phenyl]phenyl}ethynyl)benzene-1,3-dicarboxylic acid (**III**, H_6L1) molecules. Each Cu^{2+} dimer is connected to four different $L1^{6-}$ ligands, as shown in **Figure 1.18**. Cavities in NOTT-116 are shown in **Figure 1.19**.

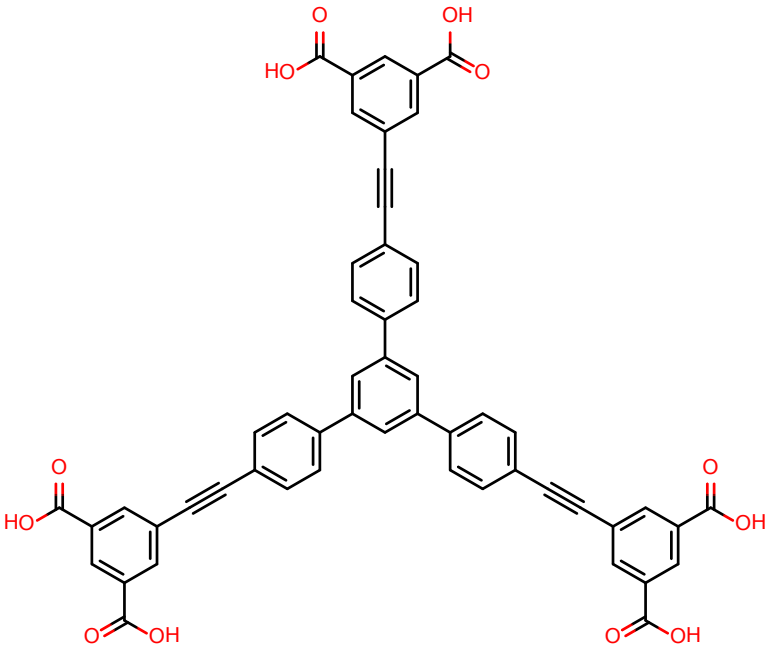

(III)

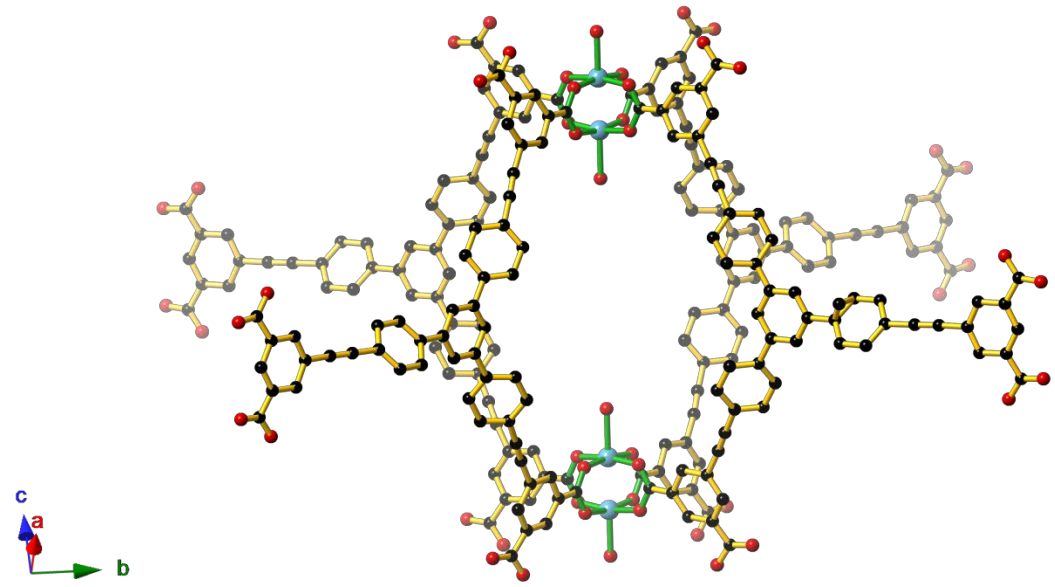

Figure 1.18: Four **III** ligands bridged by two 'Chinese lantern' Cu^{2+} dimers, highlighted with green bonds.

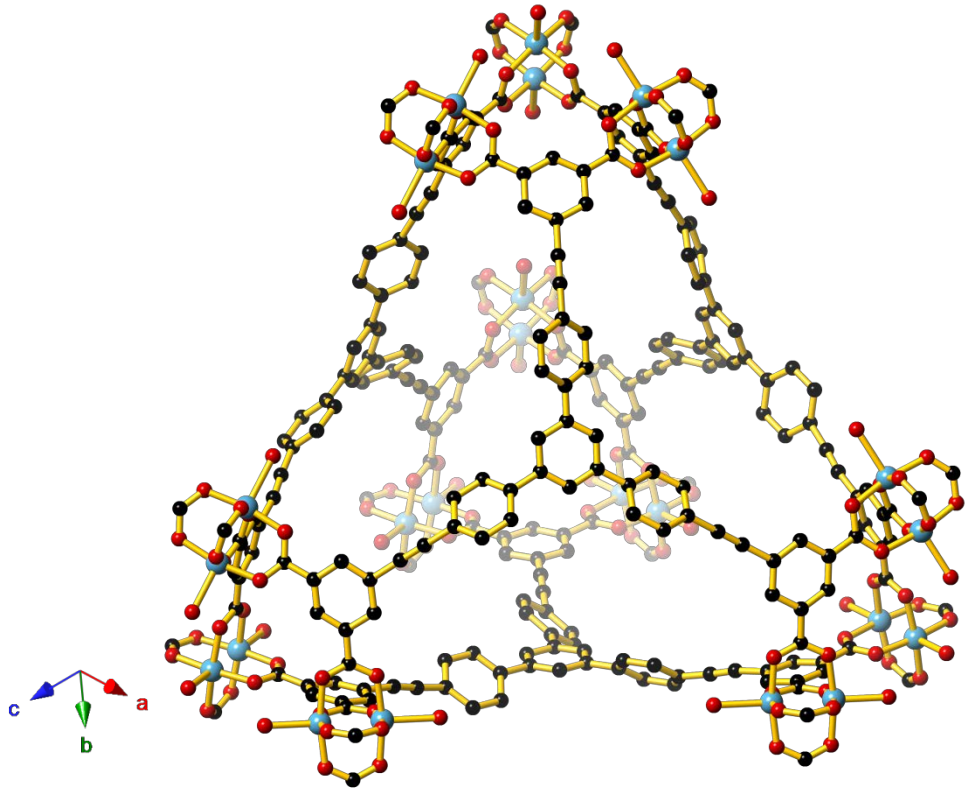

Figure 1.19: A cavity of the extended network of NOTT-116.

Topologically identical to NOTT-116, NU-110E is formed by the same Cu^{2+} dimers present in HKUST-1 and NOTT-116. The bridging ligand in this case is 5-(2-{4-[2-(4-{3,5-bis[4-(2-{4-[2-(3,5-dicarboxyphenyl)ethynyl]phenyl}ethynyl)phenyl] phenyl}phenyl)ethynyl]phenyl}ethynyl)benzene-1,3-dicarboxylic acid **(IV)** which, as can be seen below is much larger, results in much larger voids (**Figure 1.20**).

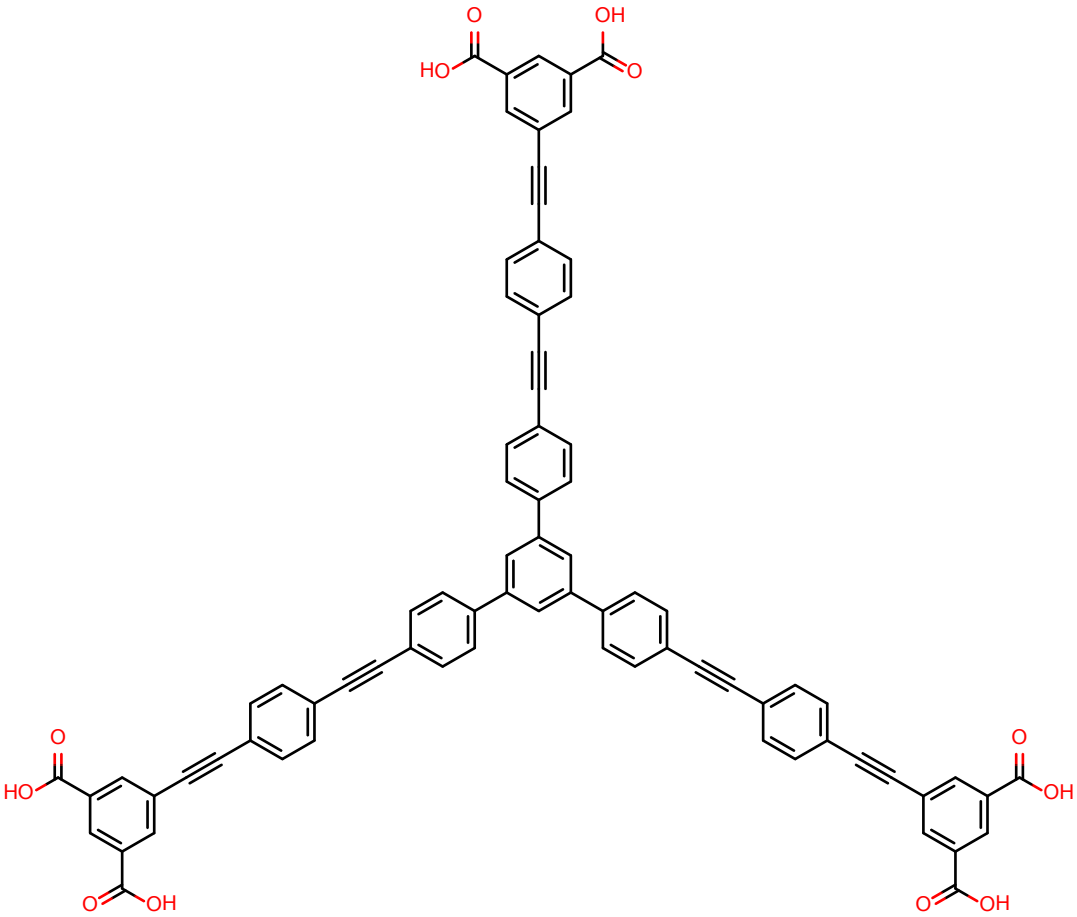

(IV)

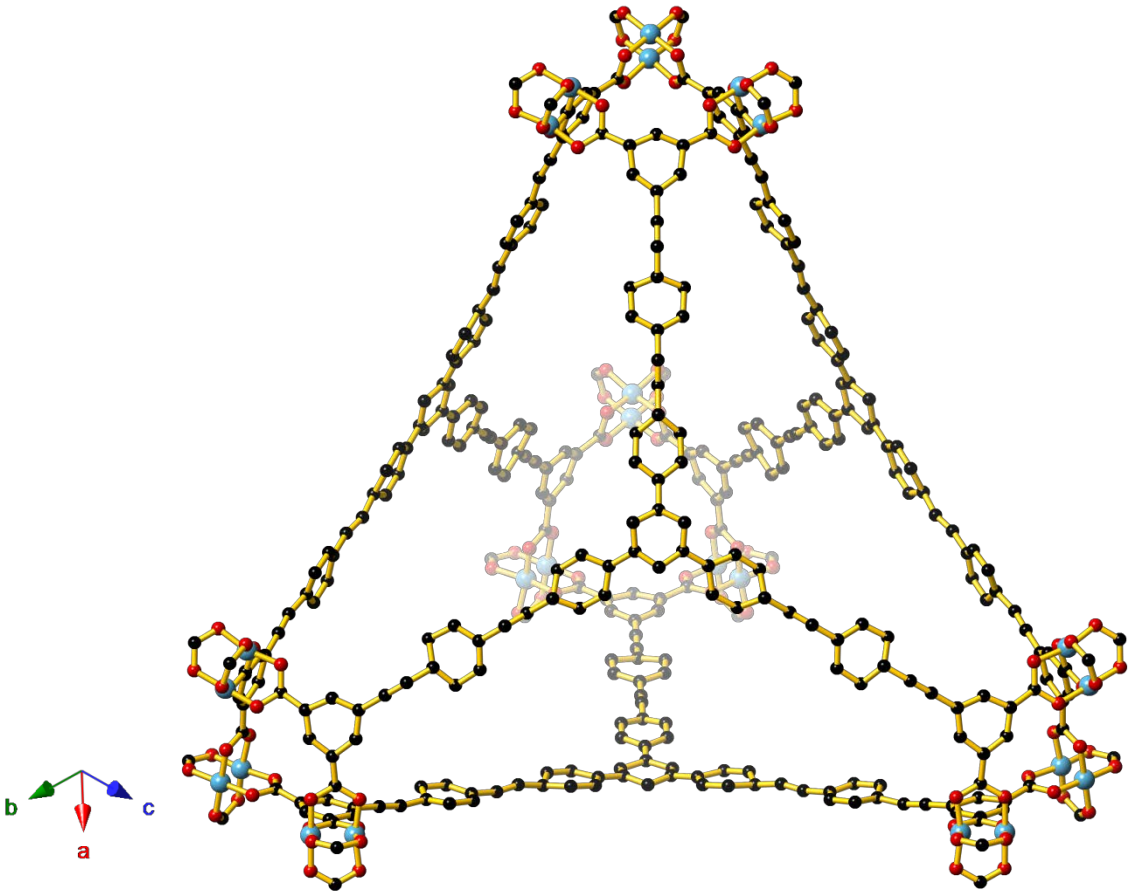

Figure 1.20: A cavity of the extended network of NU-110E.

A comparison of surface areas of the aforementioned PCP/MOF material is present in **Table1-1.**

Table 1-1: Surface areas of notable MOF/PCP compounds

Compound	**Surface area (m^2/g)**
MOF-5[27]	3800†
MOF-177[22]	4750†
MgDOBDC\IRMOF-74\Mg-MOF-74[28]	1350†
UIO-66[24]	1187‡
HKUST-1[29]	1615†
MILL-101[26]	4100†
NOTT-116/PCN-68[30]	5110†
NU-110E[31]	7140†

†Brunauer-Emmett-Teller surface area, ‡Langmuir surface area

1.2 The use of substituted and functionalised ligands in MOF/PCPs

In many of the previously described structures, the use of longer linkers has been shown to lead to larger intra-framework spaces and therefore greater adsorption capacities. The introduction of linkers with substituents, which can extend into the framework channels and voids, has the potential to increase the affinity for a specific gas, thus offering the prospect of selectivity and gas separation. The following examples illustrate how the use of substituents on MOF/PCPs impacts upon their gas adsorption behaviour.

Within the isoreticular IRMOF series, the bdc^{2-} bridges of IRMOF-1 have been replaced with bicyclo[4.2.0]octa-1,3,5-triene-2,5-dicarboxylate (**V**), to form IRMOF-6, which is shown in **Figure 1.21**. IRMOF-1 was reported to be capable of adsorbing 135 $cm^3(stp)/cm^3$ of methane, at 298 K and 36 atm, while IRMOF-6 was able to adsorb 155

$cm^3(stp)/cm^3$ under the same conditions.[18] This improvement in gas adsorption capability has been attributed to the hydrophobic nature of the appended C_2H_4 units in IRMOF-6.

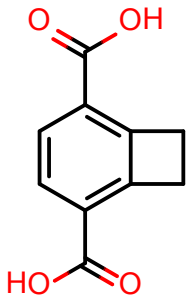

(V)

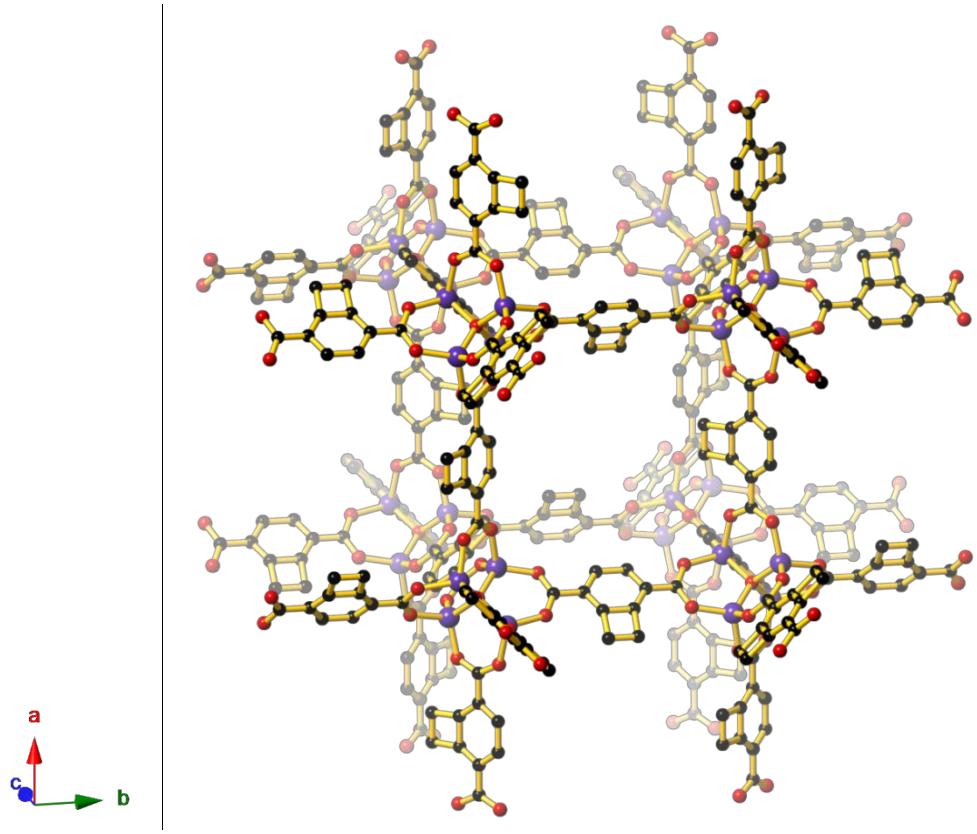

Figure 1.21: The structure of IRMOF-6 showing the topological similarity to IRMOF-1/MOF-5 (**Figure 1.10**).

Another notable example, of the effect of substituents on the uptake of guests includes the use of 2-amino-terephthalic acid (**VI**) to form UiO-66-NH_2. The BET surface area is reported to be very similar to UiO-66, at 1123 m^2/g but it displays significantly greater uptake of CO_2, CH_4 and N_2, as shown in **Table 1-2**.[32] Unfortunately this marked increase in uptake is accompanied by an increased affinity for water.

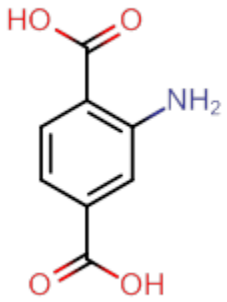

(VI)

Table 1-2: Uptake at 298 K and 1 bar by UiO-66 and UiO-66-NH_2

	Amount of gas adsorbed 298 K and 1 bar (mmol/g)		
	CO_2	**CH_4**	**N_2**
UiO-66	1.786	0.493	0.155
UiO-66-NH_2	2.973	0.665	0.223

Data from G. E. Cmarik, *Langmuir* 2012, 28, 44, 15606-15613[32]

Fluorine atoms have also been incorporated into a number of MOF/PCPs and this has led to a high enthalpy of H_2 adsorption,[33,34] higher levels of H_2 and CO_2 adsorption,[35] selective adsorption of heptane,[36] oil/water separation,[37] high tolerance to water, [37–40] better ionic conductivity,[41] higher enthalpy of CO_2 adsorption,[42] and better fluorophilicity.[43]

1.3 Post synthetic modification

Post synthetic modification may refer to any process that changes the physical or chemical properties of the framework material after it has been assembled. In its broadest definition this may include procedures as simple as desolvating the framework, to form the active material and ion or solvent exchange, however, in general post synthetic modification (PSM) normally refers to modifications of the framework, such as functionalisation of the organic linkers. The PSM approach can offer significant advantages over the use of a pre-functionalised ligand in framework assembly. The employment of a pre-functionalised ligand can be problematic because the functional group may interfere with the self-assembly of the intended network, especially when solvothermal synthetic approaches are employed. To circumvent these issues, many researchers have turned to PSM, to chemically modify the synthesised framework, rather than the molecular precursors. In such cases the reaction to introduce these functional groups need only be compatible with the assembled network. Since these framework materials are highly porous, functionalisation can be achieved throughout the framework, as proposed by Robson in 1990.

"Relatively unimpeded migration of species throughout the lattice may allow chemical functionalisation of the rods subsequent to construction of the framework"

-Richard Robson, 1990

Over the past decade PSM has become a commonly employed technique in the systematic functionalisation of PCP/MOFs. PSM can be broadly categorised into covalent PSM, dative PSM and post synthetic deprotection.[44] More recently the

processes of post synthetic metal exchange, post synthetic ligand exchange as well as post synthetic elimination and installation have been demonstrated.[45]

1.4 Capture of CO_2 and other environmentally harmful species by PCP/MOFs

In the last two decades, coordination polymers have proven to have a variety of applications, including the areas of sensors,[46] catalysis,[47,48] luminescence,[49] drug delivery,[50–52] separation[53] and storage.[54,55] In particular, there has been considerable interest is the use of coordination polymers for the use of the sequestration of environmentally harmful gases, such as CO_2.[56]

The National Oceanic and Atmospheric Administration (NOAA) of the United States of America has reported a gradually increasing concentration of CO_2 in the atmosphere, as indicated in **Figure 1.22**.[57] There is a clear correlation between the increase in the average global temperature and the steadily increasing concentration of CO_2 in the atmosphere. Since the industrial revolution in the 18th century humanity has become more and more dependent on the production of energy through the burning of fossil fuels. Although many nations have taken significant steps to generate power from renewable resources, such as wind, solar and hydro-electricity, the world's growing population and demand for electricity means that reliance on coal power plants is likely to continue. Carbon Capture and Sequestration (CCS) is a technology that aims to reduce the emissions of CO_2 into the atmosphere from stationary sources. The CCS process involves the extraction of CO_2 from an exhaust gas stream followed by transportation to an underground geological formation for permanent storage.[58,59] A major hurdle for

CCS to overcome is the selective capture of CO_2 from post-combustion flue gas. Typically, the composition of coal-fired flue gas is 12.5-12.8% CO_2, 6.2% H_2O, 4.4% O_2, 76-77% N_2 and trace amounts of CO, NO_x, and SO_2.[60] Current technologies employed to remove CO_2 include wet amine scrubbing, involving the chemical adsorption of CO_2 by an aqueous amine solution, such as 20-30% monoethanolamine.[61] There are, however, several major drawbacks with the use of wet amine scrubbing, including a high regenerative energy cost and degradation of the amine solution as well as its evaporation. In addition to solvent loss and degradation, the corrosive nature of the solvent causes damage to equipment.[61,62] Given the porosity and tuneable nature of PCP/MOFs, framework materials have been the subject of wide ranging investigations directed towards the capture of CO_2.

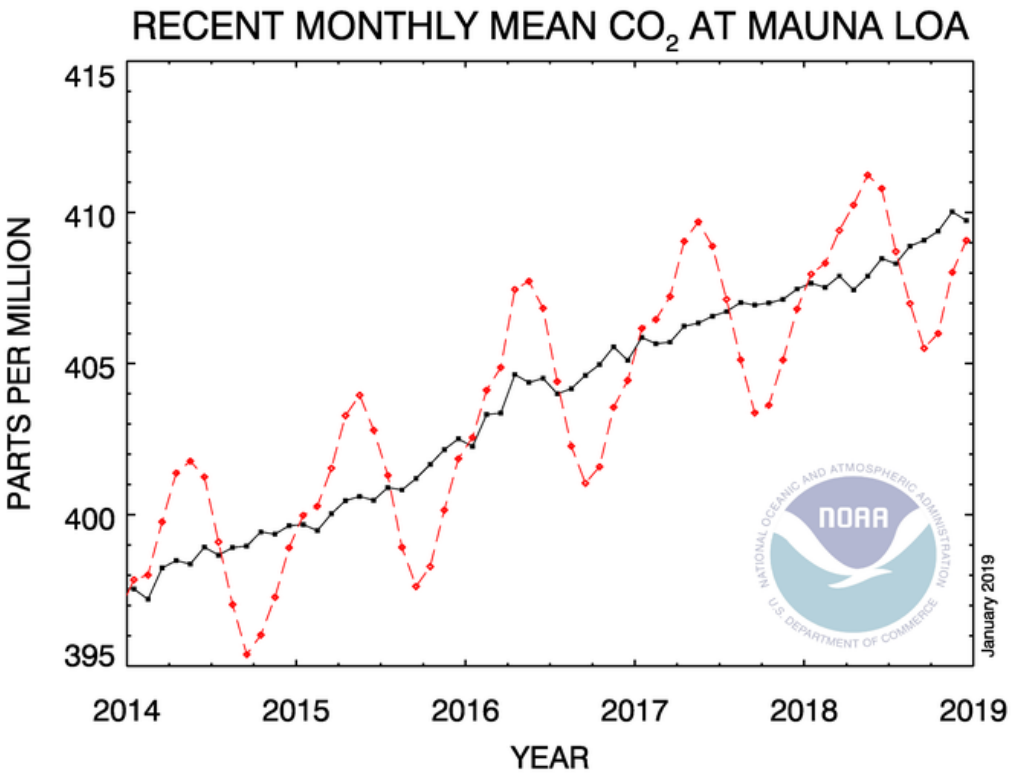

Figure 1.22: Monthly mean atmospheric CO_2 measured at the Mauna Loa Observatory. The dashed redline represents the monthly mean value while the dashed black line includes a correction for the average seasonal cycle.[57]

The CO_2 uptake of various MOF/PCPs are summarised in **Table 1-3**.

Table 1-3: Uptake of CO_2 in MOF/PCPs

	Uptake of CO_2 @ 1 bar		
Compound	**(ml(STP)/g)**	**(mmol/g)**	**Temp (K)**
Mg-MOF-74[20]	195	8.0	296
HKUST-1[63]	130	5.3	298
UiO-66[32]	41	1.7	298
UiO-66-NH_2[32]	64	2.6	298
MIL-101[64]	215	9.0	303
NOTT-116/PCN-68[65]	34	1.4	298
MOF-177[66]	20	0.8	298
MOF-5[66]	40	1.6	298

Although MOF/PCPs with larger channels, such as MOF-177 and NOTT-116, can hold large quantities of CO_2, the uptake at low pressures (at a level found in flue gas) are lower than is practically useful. To achieve increased loading at appropriate pressures for CO_2 capture it is clear that the framework must possess sites that can provide a relatively strong interaction with CO_2, as in the case of Mg-MOF-74 and MIL-101 which have open metal sites for the CO_2 to bind.

In regards to the capture of environmentally harmful species, the capture and recycling of inhalation anaesthetic vapours is an emerging area.[67–70] The mechanism of action for inhalation anaesthetics is not well understood, but the vast majority of the inhaled

anaesthetic molecules are not metabolised by the body and are instead exhaled in their unchanged form. In the case of an anaesthetic such as sevoflurane, approximately 95% of the inhaled gas is eventually exhaled.[71]

It was estimated that in 2004, 226.4 million surgical operations where conducted throughout the world. Eight years later, in 2012 the number of major surgical operations increased to 312.9 million.[72] Coupled with the discovery that anaesthetic vapours can have a Global Warming Potential (GWP) a hundred to a thousand of times greater than that of CO_2,[73] there is undoubtedly both an environmental and economic incentive to develop a material that can capture and recycle waste anaesthetic vapour. In this regard, PCP/MOF materials may serve as useful adsorbents.

1.5 Li^+ based networks

Although large pore size is clearly linked to increased storage capacity of an adsorbent material the binding enthalpy is commonly lower than that found in smaller pore materials. This is because there is less chance for a guest molecule to interact with multiple surfaces. Smaller pores offer the prospect of higher binding enthalpies and are therefore desirable when gases are present in only very low concentrations or alternatively, as in the case of H_2, associate only very weakly with a host material. Despite generally superior binding enthalpies of small pore materials, their limited capacity is a significant drawback to their use.

One strategy to address the issue of low capacity in small pore materials, in terms of mass/mass uptake, is to employ molecular building blocks, both linkers and nodes, which are relatively light. For example, the use of a single light metal cation such as Li^+ instead of aggregates, such as Zn_4O, in a small pore material may be expected to result in an improved mass per mass uptake.

Within the Abrahams-Robson group the generation of a lightweight small pore network was attempted by using the isonicotinate ion (inic$^-$, **VII**), with both pyridyl and carboxylate functional groups it has the potential to bridge metal centres. Preliminary investigations with isonicotinate focused on reactions involving water which resulted in hydrated Li(inic) salts that converted to a dense structure upon dehydration. These materials contained no voids.

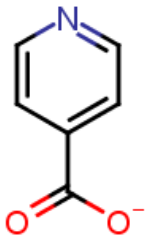

(VII)

When synthesised in the absence of water and in the presence of a suitable templating solvent, porous Li(inic)·S frameworks (S = morpholine, 1,4-dioxane, *n*-hexanol, dmf, N-methyl pyrrolidinone, *n*-propanol, cyclohexanol, diethyl digol, *n*-pentanol, pyridine and *t*-butanol) are formed.[74] In the Li(inic)·S frameworks each lithium centre is co-ordinated by three carboxylate oxygen atoms and a pyridyl nitrogen atom belonging to four different isonicotinate anions (**Figure 1.23a**). Li^+ $inic^-$ chains as depicted in **Figure**

1.23b, are formed with the ligands extending out from a chain to four parallel neighbouring chains. The chains consist of alternating 4-membered Li-O-Li-O rings and 8-membered Li-O-C-O-Li-O-C-O rings. This leads to the generation of a Li(inic)·S network containing infinite parallel channels, with an approximately rhombohedral cross-section (**Figure 1.23c**).

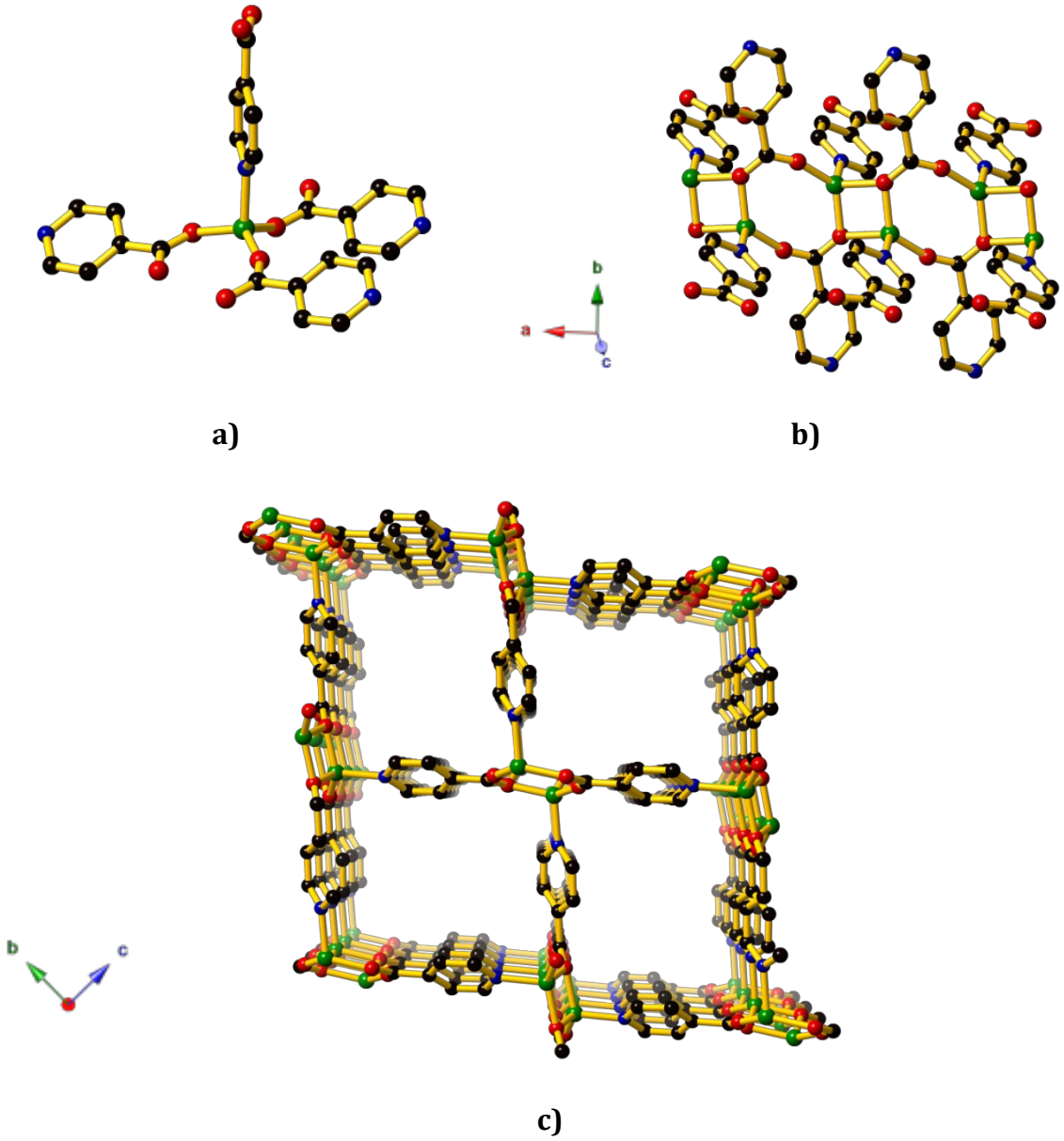

a) **b)**

c)

Figure 1.23: The structure of Li(inic)·S showing **a)** the environment of a lithium centre **b)** the lithium isonicotinate chains and **c)** the 3-D structure showing the parallel channels extending into the page; the chains depicted in part **(b)** are now running directly into the page. Li^+ atoms are shown as green spheres.

With its infinite channels of appropriately square cross-section, Li(inic)·S was able, upon desolvation, to adsorb a variety of guest molecules. The channels have approximate dimensions of ~3.3 x 4.2 Å which is relatively small for a MOF/PCP network and thus the uptake of gas molecules such as H_2, CH_4 and CO_2 is modest compared to some of the large pore MOFs described earlier in the chapter. Nevertheless, as anticipated the binding enthalpy is relatively high (9.9, 17.7 and 34.9 kJ/mol respectively). [75]

The use of a larger ligand has the potential to generate wider channels that may allow greater uptake of guest molecules, whilst still offering good binding enthalpy. The larger anion isonicotinic acid *N*-oxide, Hinox **(IX)** was used in place of Hinic **(VIII)** in an effort to form a similar network. It was anticipated that the ligand, $inox^-$, may yield metal network materials with larger uptake capacity, than Li(inic)

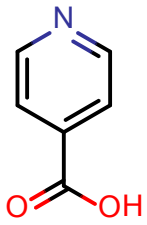

(VIII)

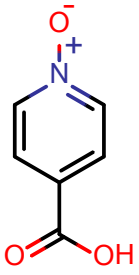

(IX)

Li^+ and $inox^-$ anions in DMF yield crystals of composition Li(inox)·⅔DMF. Single crystal X-ray diffraction revealed the presence of a 3-D Li(inox) framework. This material consists of tetrahedral Li^+ centres linked by bridging $inox^-$ anions to crystallographically

equivalent lithium centres within a helical chain, as shown in **Figure 1.24a**. From a topological perspective, the network has the same connectivity as PtS, in which the $inox^-$ ions act as the 4-connecting square planar nodes and the Li^+ cations fulfil the role of the 4-connecting tetrahedral nodes, (**Figure 1.24b**). The bridging ligands extend out in four directions, normal to the tetragonal axis, to lithium centres in four equivalent chains to form a 3D network that possesses large, parallel, square channels, as shown in **Figure 1.24c**.

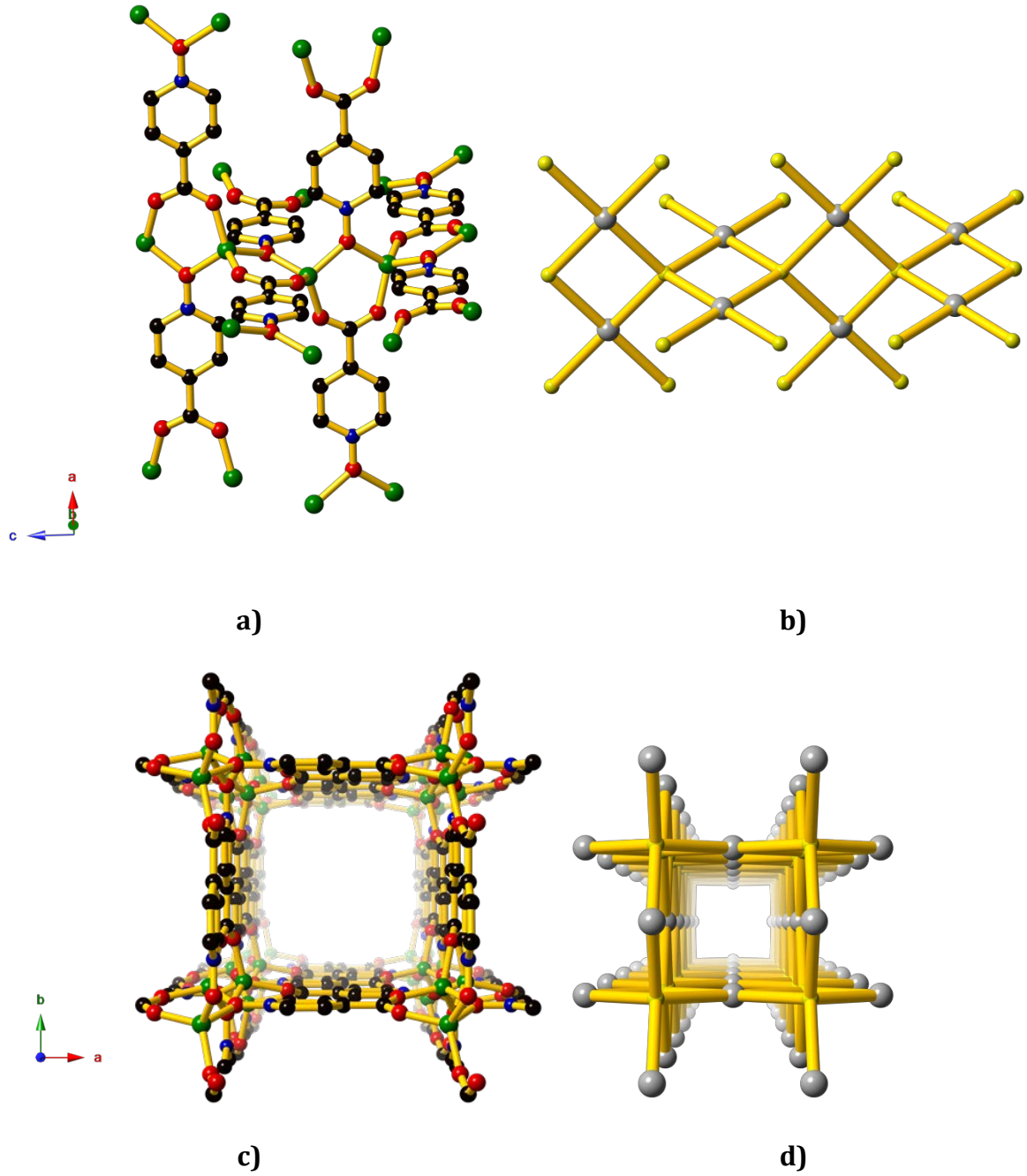

Figure 1.24: The structure of Li(inox) showing **a)** the chain in the Li(inox) structure with the planar $inox^-$ ligand and the tetrahedral Li^+ atoms, **b)** the corresponding chain in the PtS structure showing the planar four connecting Pt(II) atoms and tetrahedral S^{2-} atoms **c)** a view down a channel in Li(inox) and **d)** a view down the equivalent "channels" of PtS

Unfortunately, the material did not exhibit gas absorbing properties. This has been attributed to framework collapse upon the loss of the templating DMF molecules when the crystals are exposed to the atmosphere.

Despite the fact that the Li(inox) framework failed to act as an adsorbent material the open–type structure with PtS connectivity represented an example of an appealing metal-ligand network from a topological perspective. It occurred to the research group that a more robust version of the network could be formed if the singly charged anion and metal centre could be substituted for geometrically similar anions and cations that possessed -2 and +2 charges respectively.

The diagram of 4-hydroxybenzoic acid (H_2hba) displays how it is geometrically similar to Hinox, **Figure 1.25**. It was anticipated that hba^{2-} could play a similar structural role in a new network when combined with a divalent metal ion that was capable of adopting tetrahedral coordination geometry such as Co^{2+} and Zn^{2+}.

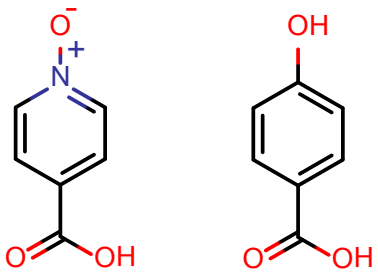

a) **b)**

Figure 1.25: The structurally similar compounds **a)** Hinox and **b)** H_2hba

1.6 The Zn(hba) family of networks

The combination of $Zn^{2+}$and hydroxybenzoate did in fact yield a robust 3-D coordination polymer, topologically similar to Li(inox), **Figure 1. 26**. Unlike Li(inox), the network shows good adsorption behaviour towards a wide variety of guest molecules, in particular H_2, N_2, CH_4 and CO_2.[76]

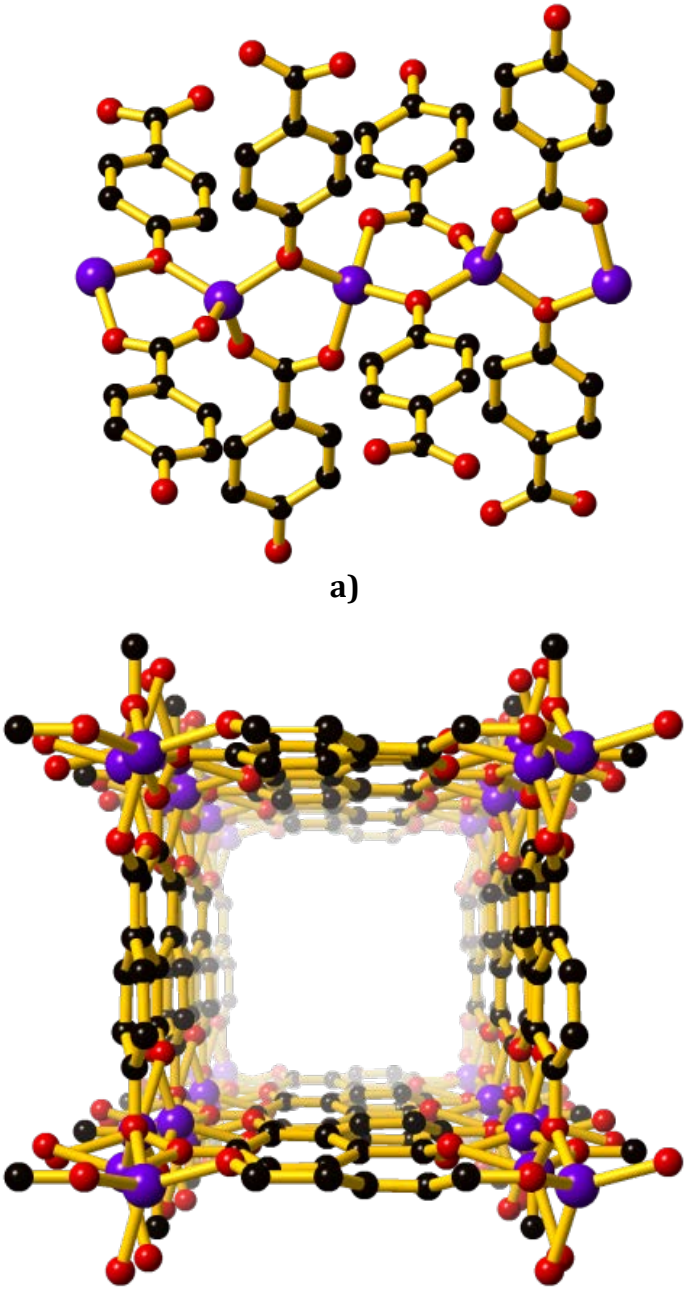

a)

b)

Figure 1. 26: A view of **a)** a chain in Zn(hba) showing the planar hba^{2-} ligand and the tetrahedral Zn^{2+} atoms and **b)** the view down a square channel in the Zn(hba) network.

The compound Zn(hba) may be considered as the archetype for a family of Zn (or Co) coordination networks involving the phenolate-carboxylate ligands, coumarate (cma^{2-}) and 4,4'-hydroxy biphenyl carboxylate ($hbpc^{2-}$). The compounds Zn(hba), Zn(cma), Zn(hbpc), Co(hba), Co(hbpc) , **Figure 1.27**, have been previously synthesised by members of the Abrahams-Robson group. Unsurprisingly, materials with longer ligands provide structures with larger channel cross-sectional areas leading to high levels of guest uptake.

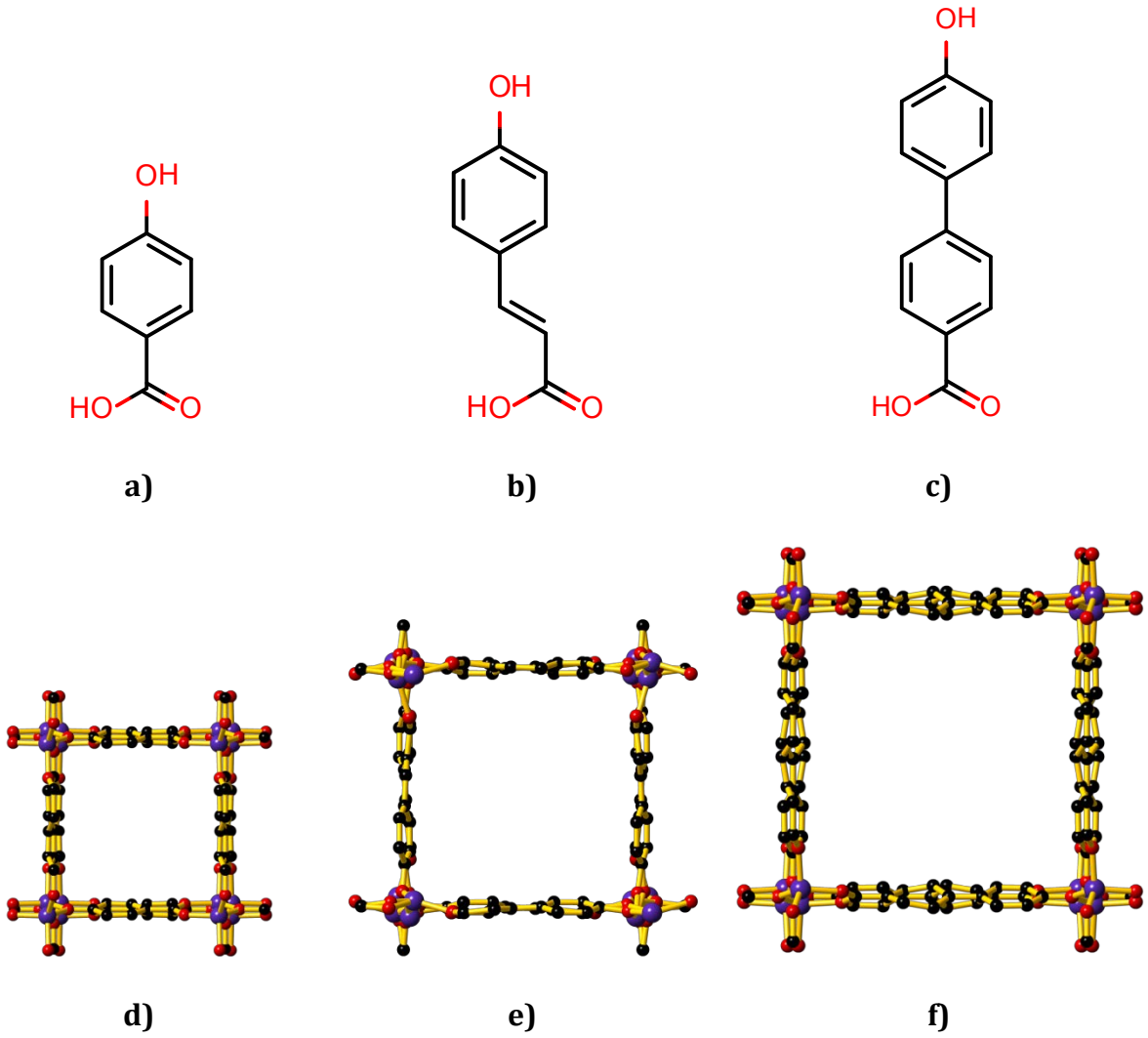

Figure 1.27: The linkers **a)** H_2hba, **b)** H_2cma and **c)** H_2hbpc. Ball and stick representations of the square channels in **d)** Zn(hba), **e)** Zn(cma) and **f)** Zn(hbpc)

1.7 Work reported in this thesis

The work presented in this thesis has been divided into four results chapters, chapters 2 through to 5.

In chapter 2 the synthesis and structures of Li^+ based ionic networks generated by the compounds (2E)-3-(pyridin-4-yl)prop-2-enoic acid (Hpaa, **X**) and 4-[(E)-2-(pyridin-4-yl)ethenyl]benzoic acid, (Hpeb, **XI**) is reported. This research was inspired by the work with Hinic **(VIII)** described above. The investigation was largely directed toward producing new types of lightweight networks with small non-intersecting pores.

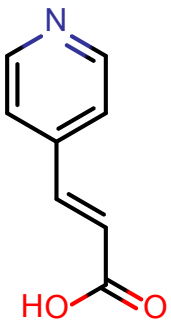

(X)

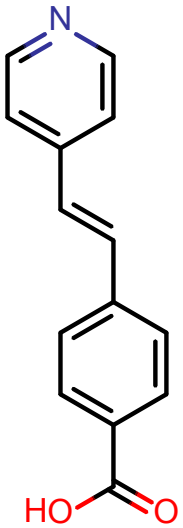

(XI)

In chapter 3 the use of substituted hba^{2-} ligands in generating frameworks that share a similar structure to Zn(hba) are described. Network materials isostructural to Zn(hba)

were formed with the ligands 2-chloro H_2hba **(XII)**, 2-fluoro H_2hba **(XIII)**, 3-fluoro H_2hba **(XIV)**, 2-methyl H_2hba **(XV)** and 2,6-dimethyl H_2hba **(XVI)**. The chapter also describes the synthesis and structure of compounds that have a different topology to Zn(hba), generated from ligands that are topologically related to hba^{2-}.

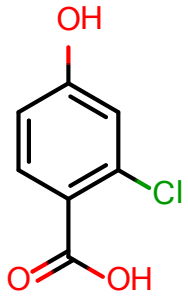

(XII)

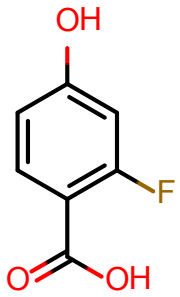

(XIII)

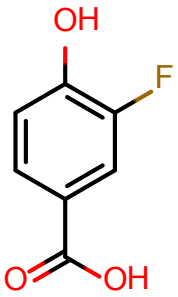

(XIV)

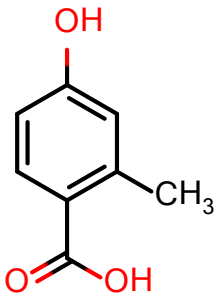

(XV)

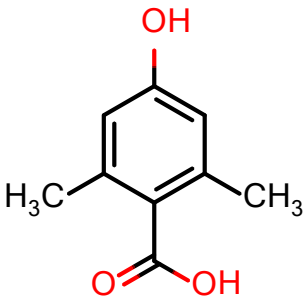

(XVI)

In chapter 4 the gas sorption properties of the 'Zn(hba) family of networks' is reported. The gases investigated are CO_2, CH_4, N_2, and H_2. There is a particular focus on the effects that substitution of the hba^{2-} ligand has on gas uptake and binding enthalpy. The effectiveness of the Zn(hba) family of networks as capture and storage agents are also compared to prominent MOFs present in the literature.

In chapter 5 the ability of the Zn(hba)family of frameworks to capture common anaesthetics, N_2O, isoflurane **(XVII)** and sevoflurane **(XVIII)**, and the effectiveness of Zn(hba) for practical anaesthetic capture and recovery is discussed. The xenon adsorption isotherms of select members of the Zn(hba) family are also presented.

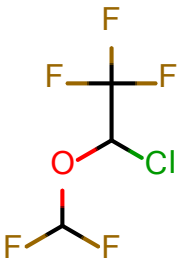

(XVII)

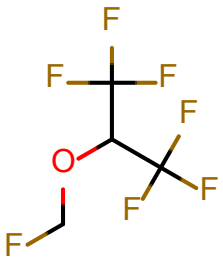

(XVIII)

1.8 References

[1] "The Nobel Prize in Chemistry 1987," can be found under https://www.nobelprize.org/prizes/chemistry/1987/summary/, **n.d.**

[2] G. R. Desiraju, *The Crystal as a Supramolecular Entity*, Wiley, Chichester, **1996**.

[3] R. W. Gable, B. F. Hoskins, R. Robson, *J. Chem. Soc. Chem. Commun.* **1990**, *96*, 762.

[4] B. F. Abrahams, B. F. Hoskins, D. M. Michail, R. Robson, *Nature* **1994**, *369*, 727–729.

[5] M. Kondo, T. Yoshitomi, K. Seki, H. Matsuzaka, S. Kitagawa, *Angew. Chemie* **1997**, *109*, 1844–1846.

[6] M. Thommes, K. Kaneko, A. V. Neimark, J. P. Olivier, F. Rodriguez-Reinoso, J. Rouquerol, K. S. W. Sing, *Pure Appl. Chem.* **2015**, *87*, 1051–1069.

[7] P. G. Menon, *Chem. Rev.* **1968**, *68*, 277–294.

[8] F. Ambroz, T. J. Macdonald, V. Martis, I. P. Parkin, *Small Methods* **2018**, *2*, 1800173.

[9] R. I. Masel, *Principles of Adsorption and Reaction on Solid Surfaces*, Wiley, New York, **1996**.

[10] S. Brunauer, P. H. Emmett, E. Teller, *J. Am. Chem. Soc.* **1938**, *60*, 309–319.

[11] M. P. Suh, H. J. Park, T. K. Prasad, D.-W. Lim, *Chem. Rev.* **2012**, *112*, 782–835.

[12] S. R. Batten, *Coordination Polymers*, Royal Society Of Chemistry, Cambridge, UK, **2009**.

[13] P. M. Mathias, R. Kumar, J. D. Moyer, J. M. Schork, S. R. Srinivasan, S. R. Auvil, O. Talu, *Ind. Eng. Chem. Res.* **1996**, *35*, 2477–2483.

[14] R. Sips, *J. Chem. Phys.* **1948**, *16*, 490–495.

[15] R. Sips, *J. Chem. Phys.* **1950**, *18*, 1024–1026.

[16] J. A. Mason, K. Sumida, Z. R. Herm, R. Krishna, J. R. Long, *Energy Environ. Sci.* **2011**, *4*, 3030–3040.

[17] H. Li, M. Eddaoudi, M. O'Keeffe, O. Yaghi, *Nature* **1999**, *402*, 276–279.

[18] M. Eddaoudi, J. Kim, N. Rosi, D. Vodak, J. Wachter, M. O'Keeffe, O. M. Yaghi, *Science* **2002**, *295*, 469–472.

[19] P. D. C. Dietzel, R. Blom, H. Fjellvåg, *Eur. J. Inorg. Chem.* **2008**, 3624–3632.

[20] A. J. Matzger, S. R. Caskey, A. G. Wong-Foy, A. J. Matzger, S. R. Caskey, A. G. Wong-Foy, *J. Am. Chem. Soc.* **2008**, *130*, 10870–10871.

[21] S. S. Chui, S. M. Lo, J. P. H. Chartman, A. G. Orpen, I. D. Williams, *Science* **1999**, *283*, 1148–1150.

[22] H. Furukawa, M. A. Miller, O. M. Yaghi, *J. Mater. Chem.* **2007**, *17*, 3197.

[23] H. Furukawa, N. Ko, Y. B. Go, N. Aratani, S. B. Choi, E. Choi, A. O. Yazaydin, R. Q. Snurr, M. O'Keeffe, J. Kim, et al., *Science* **2010**, *329*, 424–428.

[24] J. H. Cavka, S. Jakobsen, U. Olsbye, N. Guillou, C. Lamberti, S. Bordiga, K. P. Lillerud, *J. Am. Chem. Soc.* **2008**, *130*, 13850–13851.

[25] C. Hennig, S. Weiss, W. Kraus, J. Kretzschmar, A. C. Scheinost, *Inorg. Chem.* **2017**, *56*, 2473–2480.

[26] G. Férey, C. Mellot-Draznieks, C. Serre, F. Millange, J. Dutour, S. Surblé, I. Margiolaki, *Science* **2005**, *309*, 2040–2.

[27] S. S. Kaye, A. Dailly, O. M. Yaghi, J. R. Long, *J. Am. Chem. Soc.* **2007**, *129*, 14176–14177.

[28] S. Kim, E. Brostromer, D. Xing, J. Jin, S. Chong, H. Ge, S. Wang, C. Gu, L. Yang, Y. Q. Gao, et al., *Science* **2013**, *339*, 816–819.

[29] Y. Chen, X. Mu, E. Lester, T. Wu, *Prog. Nat. Sci. Mater. Int.* **2018**, *28*, 584–589.

[30] Y. Yan, I. Telepeni, S. Yang, X. Lin, W. Kockelmann, A. Dailly, A. J. Blake, W. Lewis, G. S. Walker, D. R. Allan, et al., *J. Am. Chem. Soc.* **2010**, *132*, 4092–4094.

[31] O. K. Farha, I. Eryazici, N. C. Jeong, B. G. Hauser, C. E. Wilmer, A. A. Sarjeant, R. Q. Snurr, S. T. Nguyen, A. Ö. Yazaydin, J. T. Hupp, *J. Am. Chem. Soc.* **2012**, *134*, 15016–15021.

[32] G. E. Cmarik, M. Kim, S. M. Cohen, K. S. Walton, *Langmuir* **2012**, *28*, 15606–15613.

[33] Z. Hulvey, E. H. L. Falcao, J. Eckert, A. K. Cheetham, *J. Mater. Chem.* **2009**, *19*, 4307–4309.

[34] K. A. Forrest, T. Pham, P. A. Georgiev, F. Pinzan, C. R. Cioce, T. Unruh, J. Eckert, B. Space, *Langmuir* **2015**, *31*, 7328–7336.

[35] D. S. Zhang, Z. Chang, Y. F. Li, Z. Y. Jiang, Z. H. Xuan, Y. H. Zhang, J. R. Li, Q. Chen, T. L. Hu, X. H. Bu, *Sci. Rep.* **2013**, *3*, 1–7.

[36] Y. S. Bae, O. K. Farha, J. T. Hupp, R. Q. Snurr, *J. Mater. Chem.* **2009**, *19*, 2131–2134.

[37] S. Mukherjee, A. M. Kansara, D. Saha, R. Gonnade, D. Mullangi, B. Manna, A. V.

Desai, S. H. Thorat, P. S. Singh, A. Mukherjee, et al., *Chem. - A Eur. J.* **2016**, *22*, 10937–10943.

[38] N. Nijem, P. Canepa, U. Kaipa, K. Tan, K. Roodenko, S. Tekarli, J. Halbert, I. W. H. Oswald, R. K. Arvapally, C. Yang, et al., *J. Am. Chem. Soc.* **2013**, *135*, 12615–12626.

[39] C. Yang, U. Kaipa, Q. Z. Mather, X. Wang, V. Nesterov, A. F. Venero, M. A. Omary, *J. Am. Chem. Soc.* **2011**, *133*, 18094–18097.

[40] F. Drache, V. Bon, I. Senkovska, C. Marschelke, A. Synytska, S. Kaskel, *Inorg. Chem.* **2016**, *55*, 7206–7213.

[41] K. Fujie, K. Otsubo, R. Ikeda, T. Yamada, H. Kitagawa, *Chem. Sci.* **2015**, *6*, 4306–4310.

[42] P. Deria, J. E. Mondloch, E. Tylianakis, P. Ghosh, W. Bury, R. Q. Snurr, J. T. Hupp, O. K. Farha, *J. Am. Chem. Soc.* **2013**, *135*, 16801–16804.

[43] M. Jang, T. Yamaguchi, K. Ohara, M. Kawano, M. Fujita, *Chem. - An Asian J.* **2009**, *4*, 1524–1526.

[44] S. M. Cohen, *Chem. Rev.* **2012**, *112*, 970–1000.

[45] Z. Yin, S. Wan, J. Yang, M. Kurmoo, M. H. Zeng, *Coord. Chem. Rev.* **2019**, *378*, 500–512.

[46] I. Stassen, N. Burtch, A. Talin, P. Falcaro, M. Allendorf, R. Ameloot, *Chem. Soc. Rev.* **2017**, *46*, 3185–3241.

[47] A. Dhakshinamoorthy, Z. Li, H. Garcia, *Chem. Soc. Rev.* **2018**, *47*, 8134–8172.

[48] C. J. Doonan, C. J. Sumby, *CrystEngComm* **2017**, *19*, 4044–4048.

[49] W. P. Lustig, S. Mukherjee, N. D. Rudd, A. V. Desai, J. Li, S. K. Ghosh, *Chem. Soc. Rev.* **2017**, *46*, 3242–3285.

[50] M. Al Haydar, H. R. Abid, B. Sunderland, S. Wang, **2017**, 11–2685.

[51] C.-Y. Sun, C. Qin, X.-L. Wang, Z.-M. Su, *Expert Opin. Drug Deliv.* **2012**, *10*, 89–101.

[52] L. Wang, M. Zheng, Z. Xie, *J. Mater. Chem. B* **2018**, *6*, 707–717.

[53] Z. Kang, L. Fan, D. Sun, *J. Mater. Chem. A* **2017**, *5*, 10073–10091.

[54] L.-H. Xie, X. Wang, J. Li, B. Wang, X.-M. Liu, J.-R. Li, *Green Energy Environ.* **2018**, *3*, 191–228.

[55] Y. He, W. Zhou, G. Qian, B. Chen, *Chem. Soc. Rev.* **2014**, *43*, 5657–78.

[56] C. A. Trickett, A. Helal, B. A. Al-Maythalony, Z. H. Yamani, K. E. Cordova, O. M. Yaghi, *Nat. Rev. Mater.* **2017**, *2*, 1–16.

[57] National Oceanic & Atmospheric Administration of the United States, "No Title," can be found under https://www.esrl.noaa.gov/gmd/ccgg/trends/, **n.d.**

[58] Z. M. Harris, S. Milner, G. Taylor, *Greenh. Gas Balanc. Bioenergy Syst.* **2017**, *325*, 55–76.

[59] E. S. Rubin, *Framework* **2009**, *325*, 1–26.

[60] X. Xu, C. Song, R. Wincek, J. M. Andresen, B. G. Miller, A. W. Scaroni, *ACS Div. Fuel Chem. Prepr.* **2003**, *48*, 162–163.

[61] W. B. Jacobs, *SSRN Electron. J.* **2014**, *325*, 1652–1655.

[62] X. Wang, X. Wang, C. Song, C. Song, *Transform* **2009**, 5777–5783.

[63] L. Grajciar, A. D. Wiersum, P. L. Llewellyn, J. S. Chang, P. Nachtigall, *J. Phys. Chem. C* **2011**, *115*, 17925–17933.

[64] P. L. Llewellyn, S. Bourrelly, C. Serre, A. Vimont, M. Daturi, L. Hamon, G. De Weireld, J.-S. Chang, D.-Y. Hong, Y. Kyu Hwang, et al., *Langmuir* **2008**, *24*, 7245–7250.

[65] D. Yuan, D. Zhao, D. Sun, H. C. Zhou, *Angew. Chemie - Int. Ed.* **2010**, *49*, 5357–5361.

[66] D. Saha, Z. Bao, *Environ. Sci. Technol.* **2010**, *44*, 1820–1826.

[67] T. Chen, W. Kaveevivitchai, J. Jacobson, O. Š. Miljanić, **2015**, 1–5.

[68] N. Gargiulo, a. Peluso, P. Aprea, Y. Hua, D. Filipović, D. Caputo, M. Eić, *RSC Adv.* **2014**, *4*, 49478–49484.

[69] Y. Hua, N. Gargiulo, A. Peluso, P. Aprea, M. Eić, D. Caputo, *Chemie-Ingenieur-Technik* **2016**, *88*, 1730–1738.

[70] T.-H. Chen, W. Kaveevivitchai, A. J. Jacobson, O. Š. Miljanić, *Chem. Commun.* **2015**, *51*, 14096–14098.

[71] E. D. Kharasch, M. D. Karol, C. Lanni, R. Sawchuk, *Anesthesiology* **1995**, *82*, 1369–78.

[72] T. G. Weiser, A. B. Haynes, G. Molina, S. R. Lipsitz, M. M. Esquivel, T. Uribe-Leitz, R. Fu, T. Azad, T. E. Chao, W. R. Berry, et al., *Bull. World Health Organ.* **2016**, *94*, 201-209F.

[73] T. Stocker, *Climate Change 2013 Ipcc*, WMO, IPCC Secretariat, Geneva, **2013**.

[74] B. F. Abrahams, A. D. Dharma, M. J. Grannas, T. A. Hudson, H. E. Maynard-Casely, G.

R. Oliver, R. Robson, K. F. White, *Inorg. Chem.* **2014**, *53*, 4956–4969.

[75] B. F. Abrahams, M. J. Grannas, T. A. Hudson, R. Robson, *Angew. Chemie - Int. Ed.* **2010**, *49*, 1087–1089.

[76] K. F. White, B. F. Abrahams, R. Babarao, A. D. Dharma, T. A. Hudson, H. E. Maynard-Casely, R. Robson, *Chem. - A Eur. J.* **2015**, *21*, 18057–18061.

Chapter 2 Table of Contents

Chapter 2 – Lithium network materials

2.1 Introduction

As discussed in chapter 1, one of the aims of the Abrahams-Robson group is to synthesise porous network materials for gas sorption that contain parallel channels. The channels in these networks offer the prospect of strong host guest interactions, leading to higher enthalpy of adsorption values. The isonicotinate ion ($inic^-$, **VII**) represents a relatively simple anion that has the potential to combine with Li^+ metal centres to form networks with parallel channels.

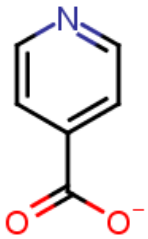

(VII)

The combination of $inic^-$ and Li^+ generates a Li(inic)·S network material containing infinite parallel channels each with an approximately square cross-section (**Figure 2.1**),[1] described in further detail in chapter 1.

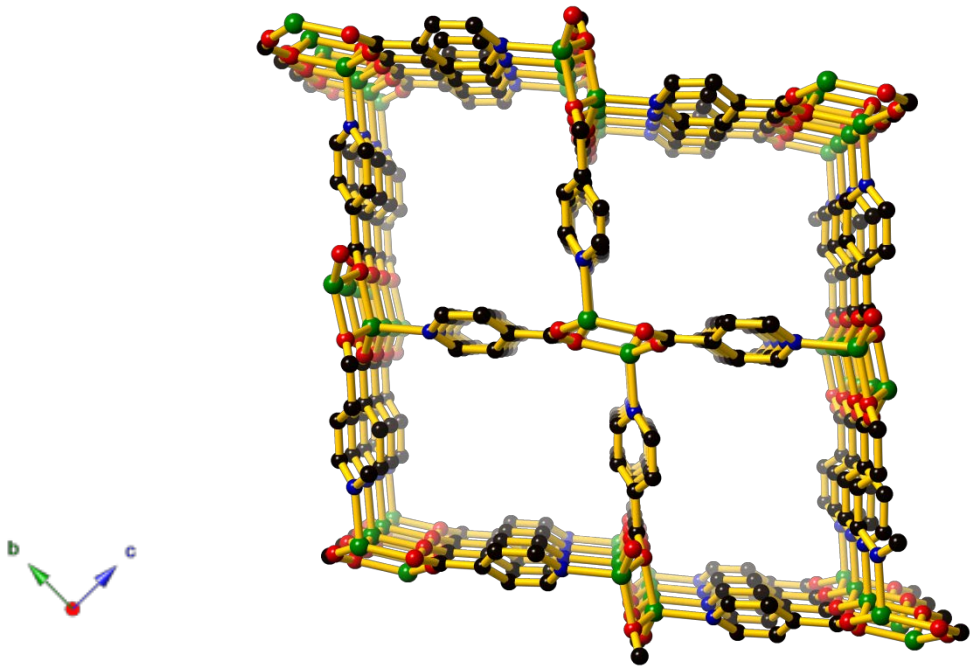

Figure 2.1: The 3-D framework of Li(inic)·S showing the parallel channels extending along the *a*-axis.

When the solvent molecules are removed from the channels of Li(inic)·S, the network undergoes a single-crystal-to-single-crystal rearrangement.[2] The chains within the network, which consist of alternating 4-membered Li-O-Li-O rings and 8-membered Li-O-C-O-Li-O-C-O rings, rearrange into chains consisting of 6-membered edge sharing Li-O-Li-O-C-O rings, as shown in **Figure 2.2**. This results in the inic$^-$ ligands no longer remaining parallel but rather adopting a "herringbone" arrangement as depicted in **Figure 2.2b**.

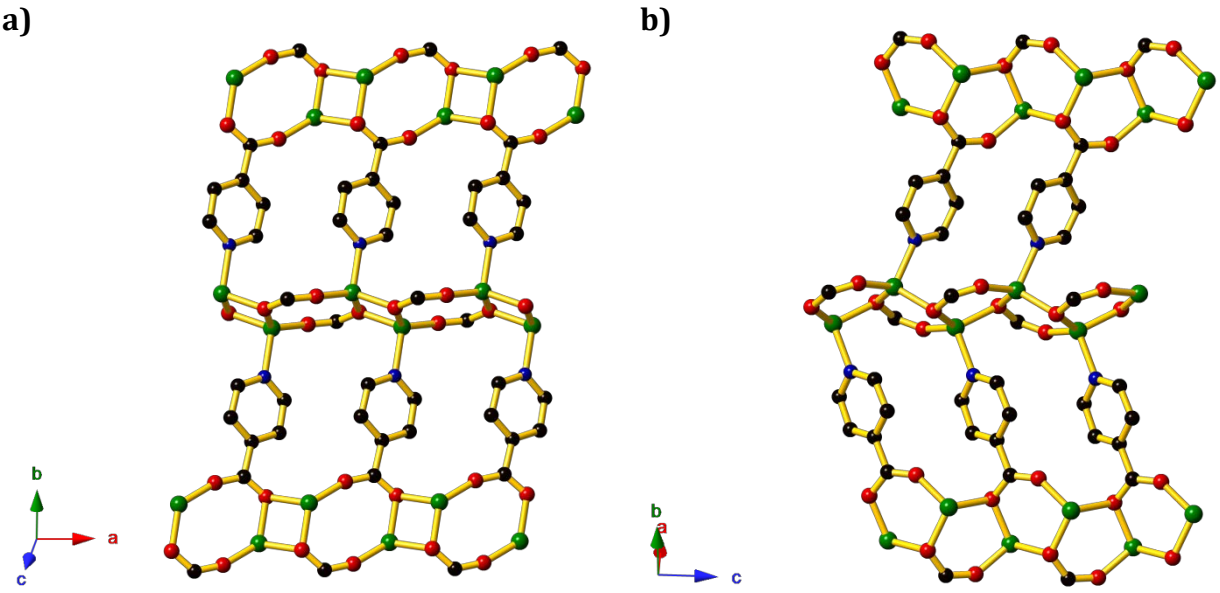

Figure 2.2: The channel walls **a)** of Li(inic)·S and **b)** Li(inic) showing the "herringbone" arrangement of inic$^-$ ligands.

When Li^+ is combined with inic$^-$ in a "non-templating" solvent, such as 2-methylbutan-2-ol, a non-porous, solvent-free framework of composition Li(inic) is formed.[2] The dense Li(inic) structure contains chains similar to those in Li(inic), as shown in **Figure 2.3a**. In this case however, a chain bonds directly with its nearest neighbour, as shown in **Figure 2.3b,** to form a linked double chain. Half the Li^+ atoms on the linked double chain bond to pyridyl groups extending from adjacent double chains, as shown in **Figure 2.4**. Only half the pyridyl groups on the chain coordinate to adjacent chains, as shown in the extended network, **Figure 2.4b**.

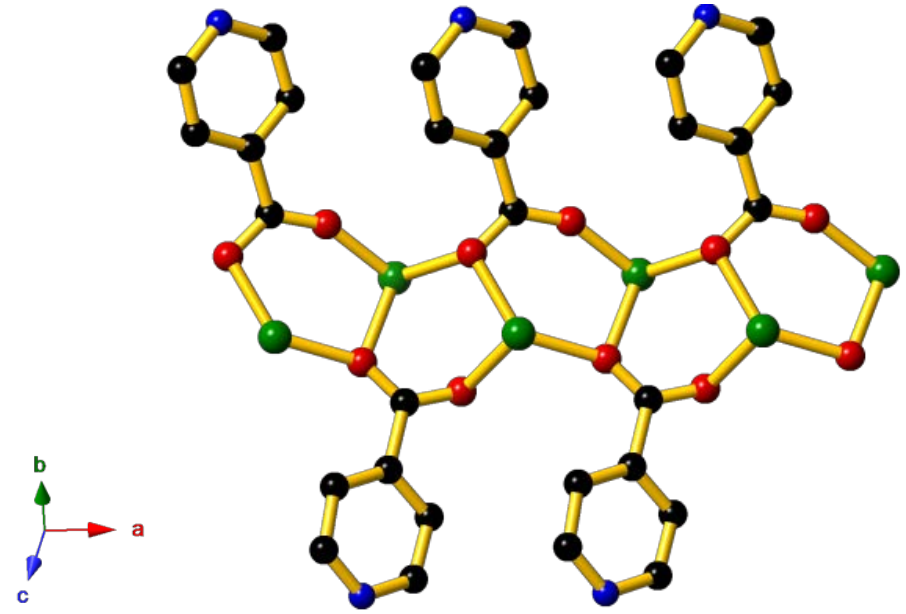

a)

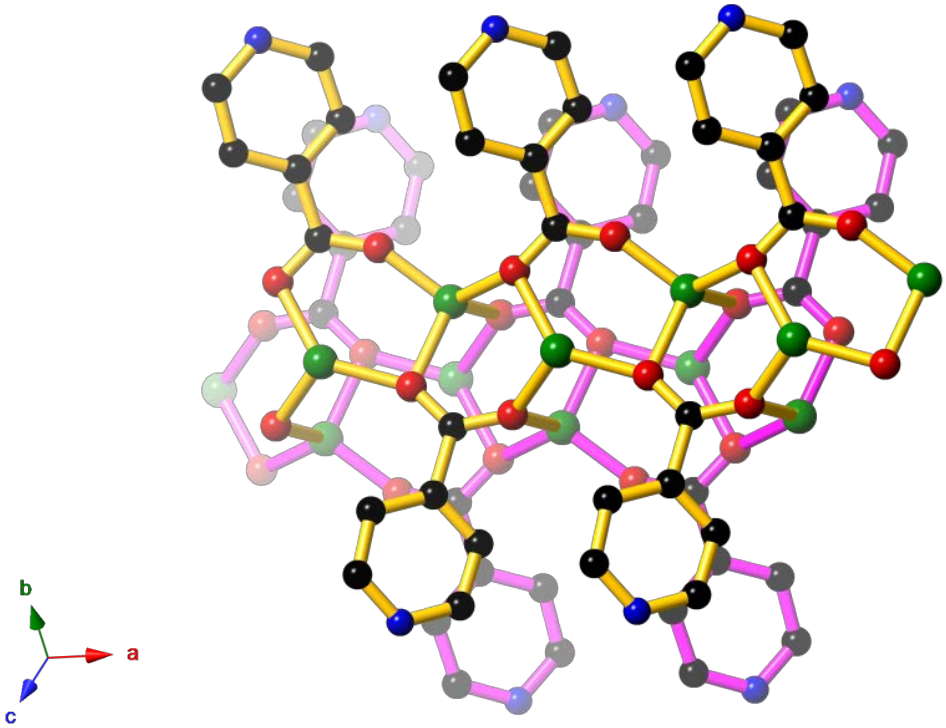

b)

Figure 2.3: The structure of Li(inic) showing **a)** the presence of lithium carboxylate chains similar to that in the Li(inic) structure and **b)** the double linked chains in Li(inic)

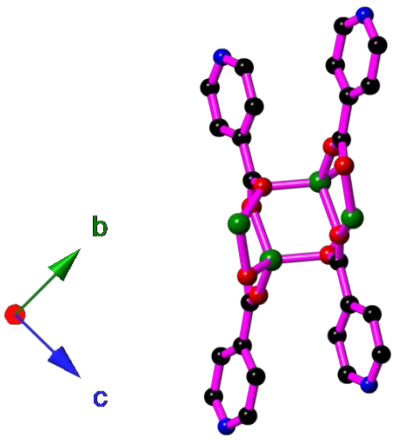

a)

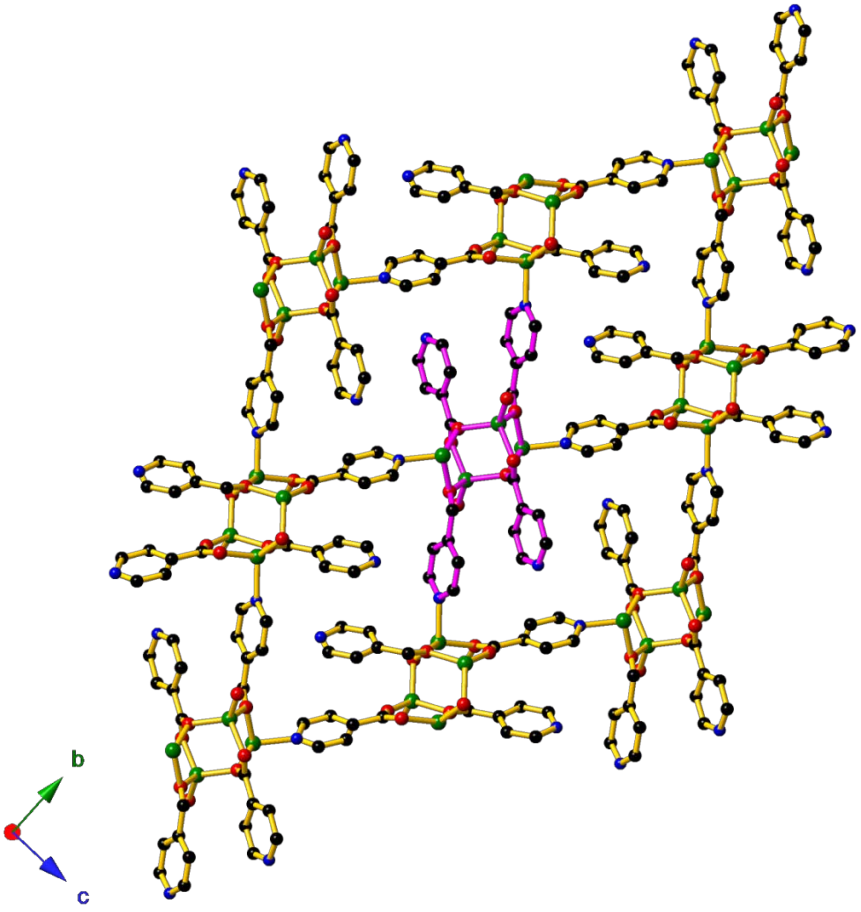

b)

Figure 2.4: The structure of Li(inic) showing **a)** the linked double chain viewed down the *a*-axis and **b)** the extended Li(inic) network with the double chains now extending into and out of the page. A double chain is highlighted in the centre with magenta bonds.

There have been numerous reported Li^+ based coordination polymers to date. One such network is ULMOF-5, which was reported by Banerjee *et al* in 2010. The ULMOF-5 network contains Li^+ centres coordinated by pyridine-2,5-dicarboxylate ligands **(XIX)**.[3] Coordinated DMF molecules complete the coordination geometry of half the Li^+ centres and protrude into the channels of the extended network, as shown in **Figure 2.5**.

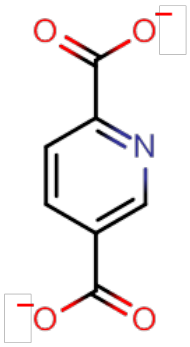

(XIX)

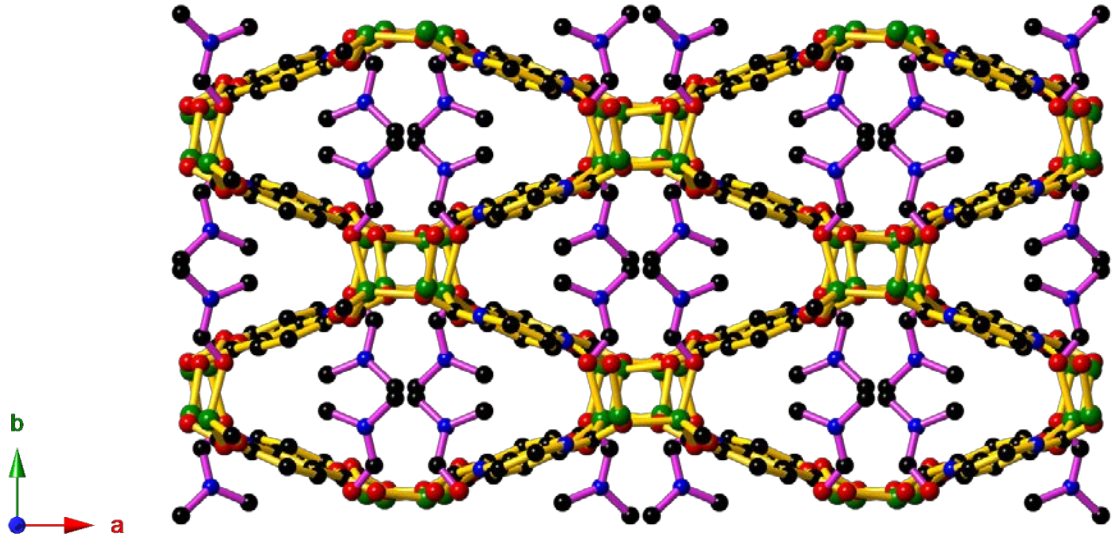

Figure 2.5: The extended network of ULMOF-5 viewed down the *c*-axis. DMF molecules have been highlighted with purple bonds. Hydrogen atoms have been omitted for clarity.

When the DMF molecules are removed from the channels, the framework undergoes structural change into a framework with a low BET estimated surface area and low H_2 uptake. As observed with Li(inox), the removal of the DMF results in a material that is non-porous.

The compound $Li_4(OPy)_4$ (OPy^- = 4-pyridinolate$^-$, **XX**) is a microporous 3D framework comprising interconnected $Li_4(OPy)_4$ cubane units, **Figure 2.6**.[4] All lithium atoms are bound to three oxygen atoms and one nitrogen atom, each from a different linker. $Li_4(OPy)_4$ cubane units are connected to eight of its nearest neighbours to form the extended network, as seen in **Figure 2.7**. $Li_4(OPy)_4$ has high thermal stability and, once activated, is capable of adsorbing N_2, H_2 and CO_2.

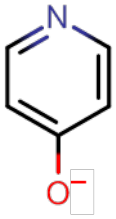

(XX)

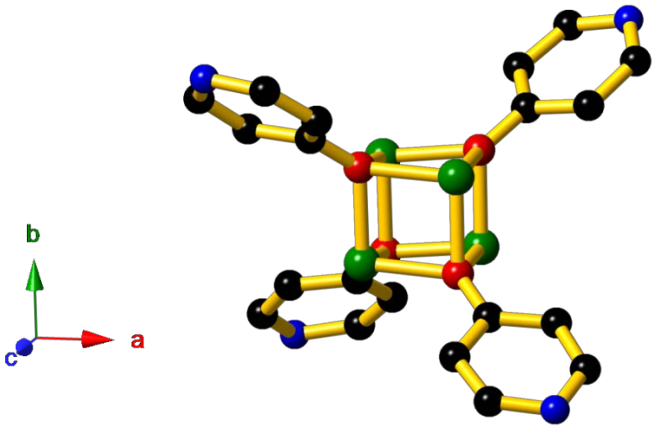

Figure 2.6: The $Li_4(OPy)_4$ cubane unit

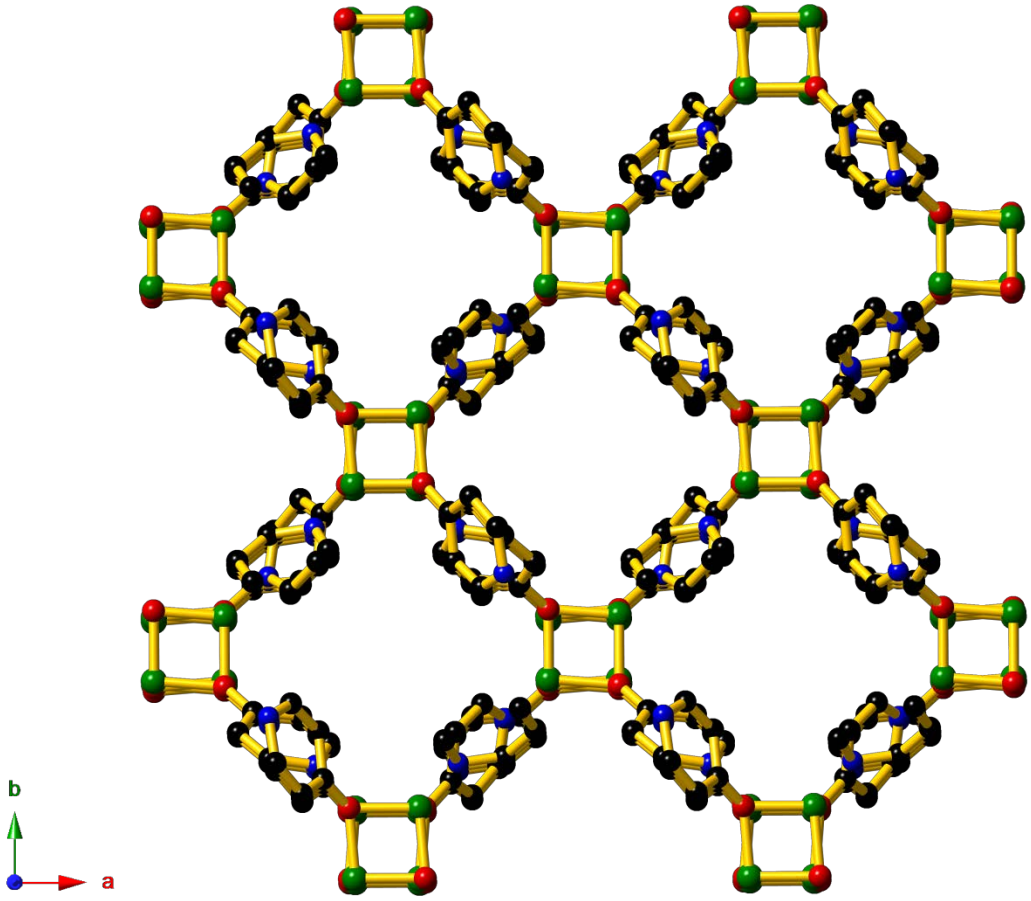

Figure 2.7: The extended network of $Li_4(OPy)_4$ viewed down the *c*-axis.

Another Li^+ based coordination polymer in the literature is MIL-145, formed by the combination of Li^+ centres and 3,3′,5,5′-azobenzenetetracarboxylate^{4-} ligands **(XXI)**,[5] shown in **Figure 2.8**.

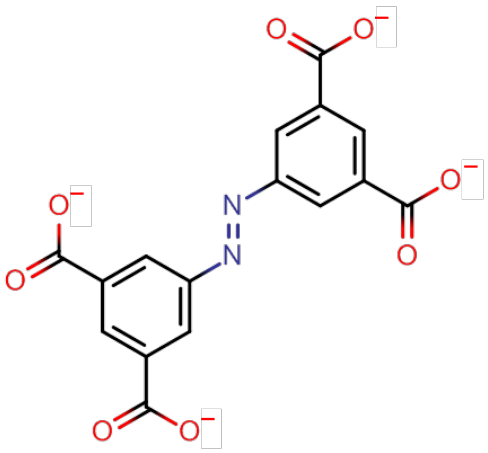

(XXI)

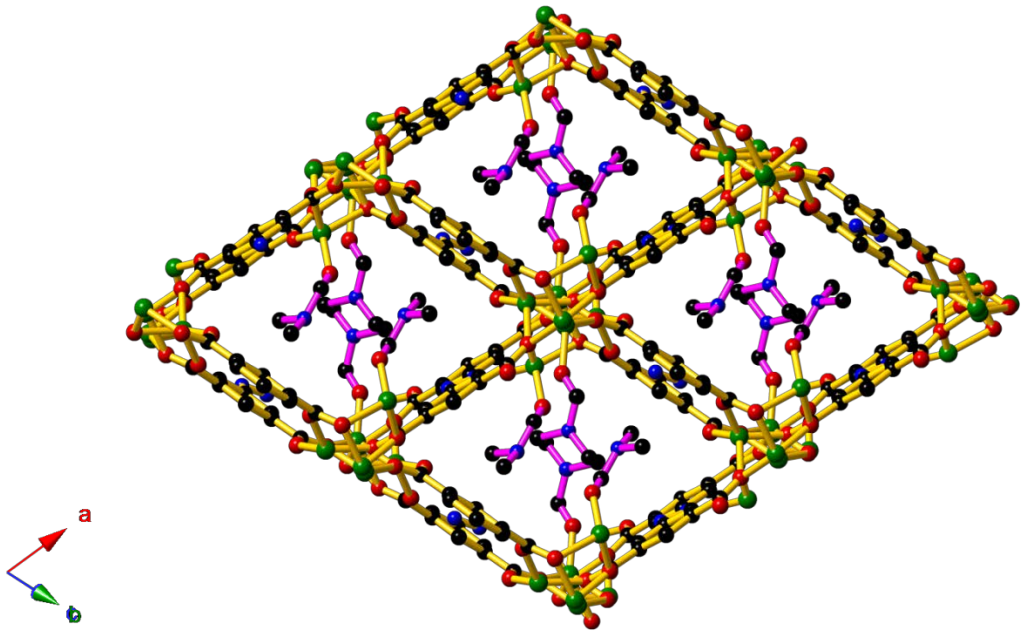

Figure 2.8: The extended structure of MIL-145 viewed perpendicular to the *a*-axis. DMF molecules are highlighted in purple.

Similar to Li(inic)·S, MIL-145 undergoes a structural rearrangement when the DMF molecules are removed from the channels, however, the structural rearrangement in MIL-145 is much more pronounced. MIL-145 transforms to MIL-146 (**Figure 2.9**) when thermally activated above 443 K, which has been shown to adsorb gas molecules, with selective adsorption of CO_2 over N_2.

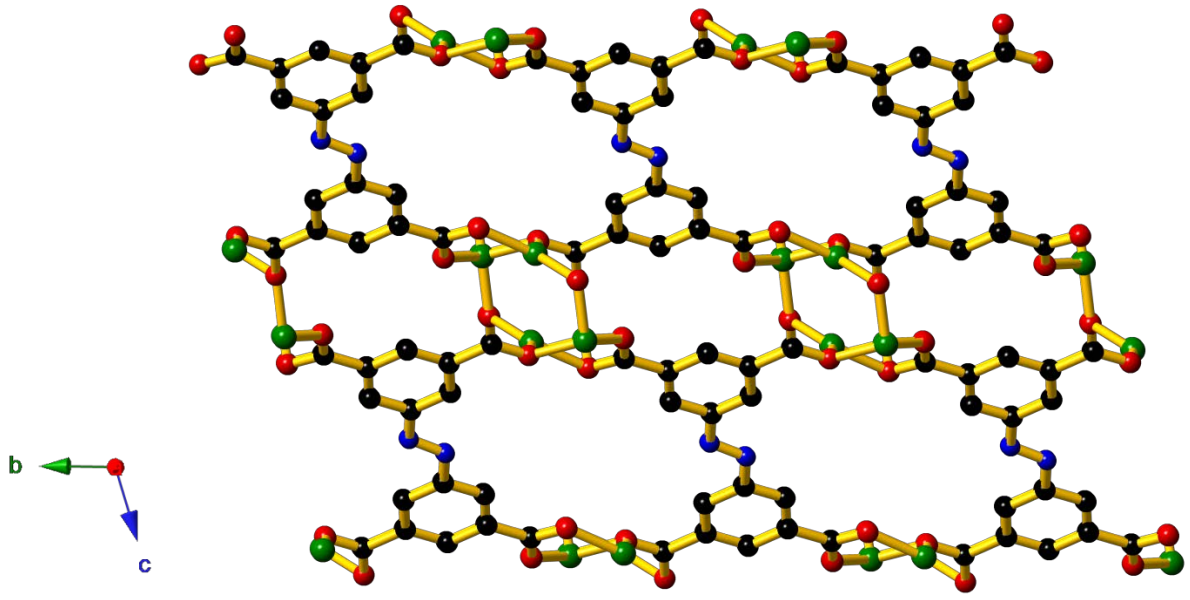

Figure 2.9: The extended structure of MIL-146 viewed down the *a*-axis

2.2 Work reported in this chapter

Given the successful generation of the porous ionic network Li(inic), the synthesis and characterisation of other porous lithium-based networks were investigated. In particular the focus is on 'longer' ligands which have potential to produce larger channels capable of accommodating greater quantities of guest molecules.

2.3 Li^+ based structures with paa^-

The compound (2E)-3-(pyridin-4-yl)prop-2-enoic acid, **(X)**, referred herein as pyridyl acrylic acid (Hpaa), possesses a structure related to that of isonicotinic acid and it was anticipated that it may yield a similar ionic network but with larger channels.

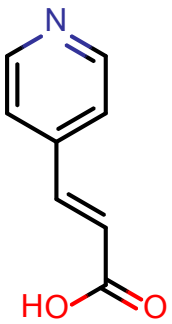

(X)

When a hot solution of Hpaa and LiOH in methanol and DMF is allowed to cool, colourless needle-like crystals of Li(paa)·DMF separate from solution. Li(paa)·DMF crystals possess orthorhombic symmetry and adopt the space group $Pna2_1$. As with the Li(inic)·S structure, each lithium centre in Li(paa)·DMF is coordinated by three carboxylate oxygen atoms and a pyridyl nitrogen atom belonging to four different isonicotinate anions, as shown in **Figure 2.10a**. Lithium pyridylacrylate chains, as depicted in **Figure 2.10b**, are linked to four parallel neighbouring chains. In contrast to Li(inic)·S, the chains in Li(paa)·DMF consist of 6-membered edge sharing Li-O-Li-O-C-O rings, much like in the desolvated porous Li(inic) framework. Crosslinking of the

parallel chains leads to the generation of infinite channels, as depicted in **Figure 2.10c**. The channels resemble those present in Li(inic) but are significantly larger.

The channel dimensions within Li(paa)·DMF are larger than those of Li(inic) and Li(inic)·S (S = DMF), as can be seen in **Figure 2.11**:.The Li(inic)·S framework has channel dimensions of approximately 3.8 x 5.4 Å, van der Waals surface to van der Waals surface. When Li(inic)·S is desolvated it undergoes single crystal to single transformation in which the Li(inic) network is formed. This causes the channel dimensions to constrict to 3.3 x 4.2 Å. The longer paa^- ligand allows Li(paa)·DMF to have larger channel dimensions of 5.4 x 6.1 Å.

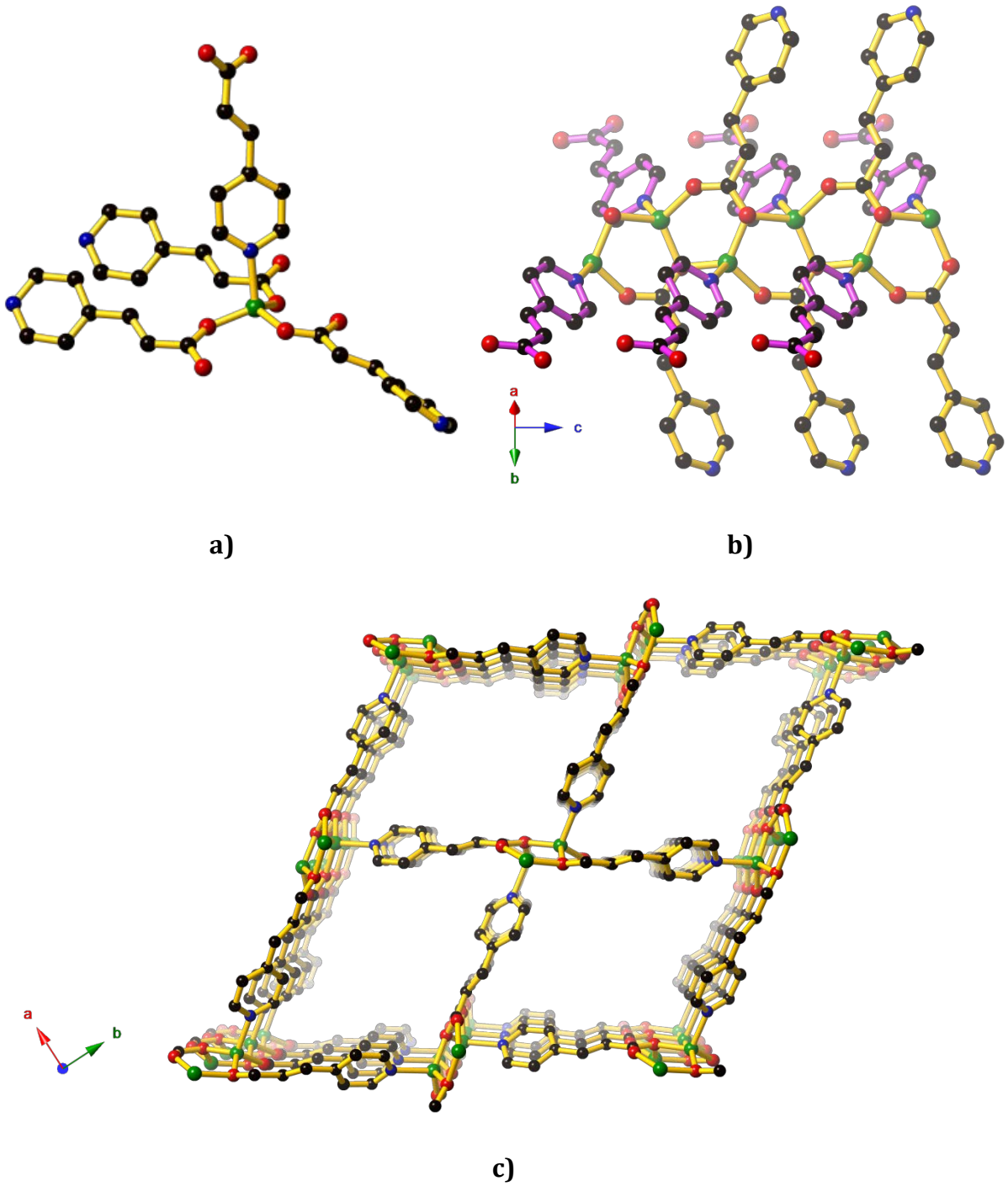

Figure 2.10: The structure of Li(paa)·S showing **a)** the environment of a lithium centre **b)** a single Li^+ paa^- chain and **c)** the 3-D structure showing the parallel channels extending along the *c*-axis.

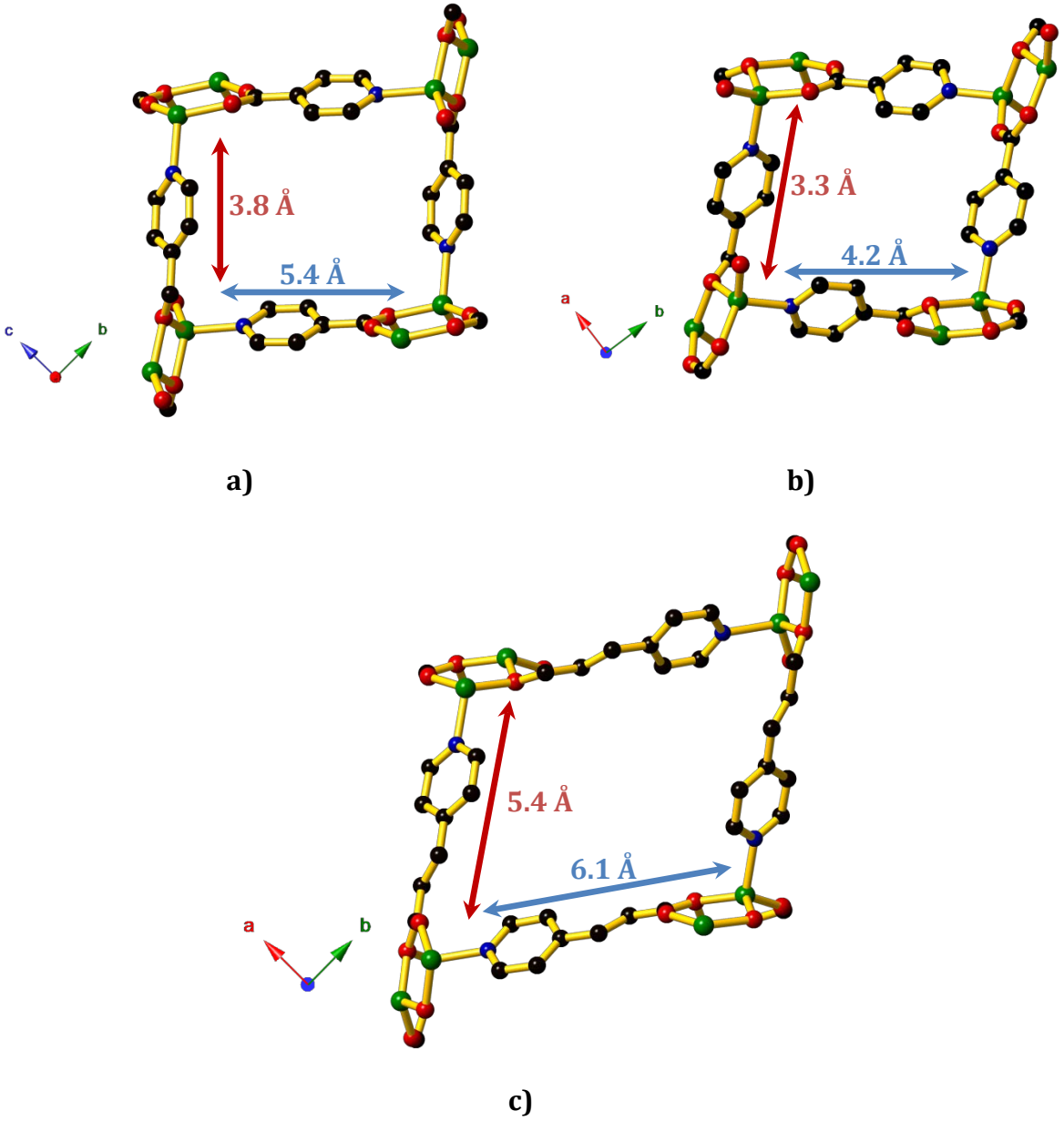

Figure 2.11: A single channel of **a)** Li(inic)·S showing the internal channel dimensions, van der Waals surface to van der Waals, of approximately 3.8 x 5.4 Å, **b)** Li(inic) showing the internal channel dimensions of approximately 3.3 x 4.2 Å and **c)** Li(paa)·S showing the internal channel dimensions of approximately 5.4 x 61 Å.

Crystals of Li(paa)·S in mother liquor dissolve when exposed to the atmosphere for more than five minutes (< 30 seconds if crystals are placed on a glass slide in mother liquor). Presumably this dissolution results from exposure to moisture in the

atmosphere. The structural work provides encouragement that Li(paa)·S would be able to serve as a host network for a variety of guest molecules, however the stability of the crystals is less than desirable. Following dissolution new crystals of composition Li(paa) separate almost immediately. The crystals do not contain any solvent and closely resemble the dense Li(inic) network previously reported by the group (**Figure 2.4**). Li(paa) crystallises in the monoclinic space group $P2_1/n$ and contains similar chains to those within the 'open-type' network (**Figure 2.10c**) described above, as shown in **Figure 2.12a**. Much like the dense Li(inic) network, the chains in dense Li(paa), containing the 6-membered edge sharing Li-O-Li-O-C-O rings, as shown in **Figure 2.12b**, are linked to form a linked double chain.

There are two crystallographically unique Li^+ centres, one bound to four carboxylate oxygen atoms, Li(1), and the other coordinated to three carboxylate oxygen atoms and a nitrogen atom, Li(2). The Li(1) centre is bound to three oxygen atoms within the same chain and one oxygen atom from its neighbouring chain, to form the linked double chain. The nitrogen centre coordinated to Li(2) extends from an adjacent linked double chain, as shown in **Figure 2.12c**.

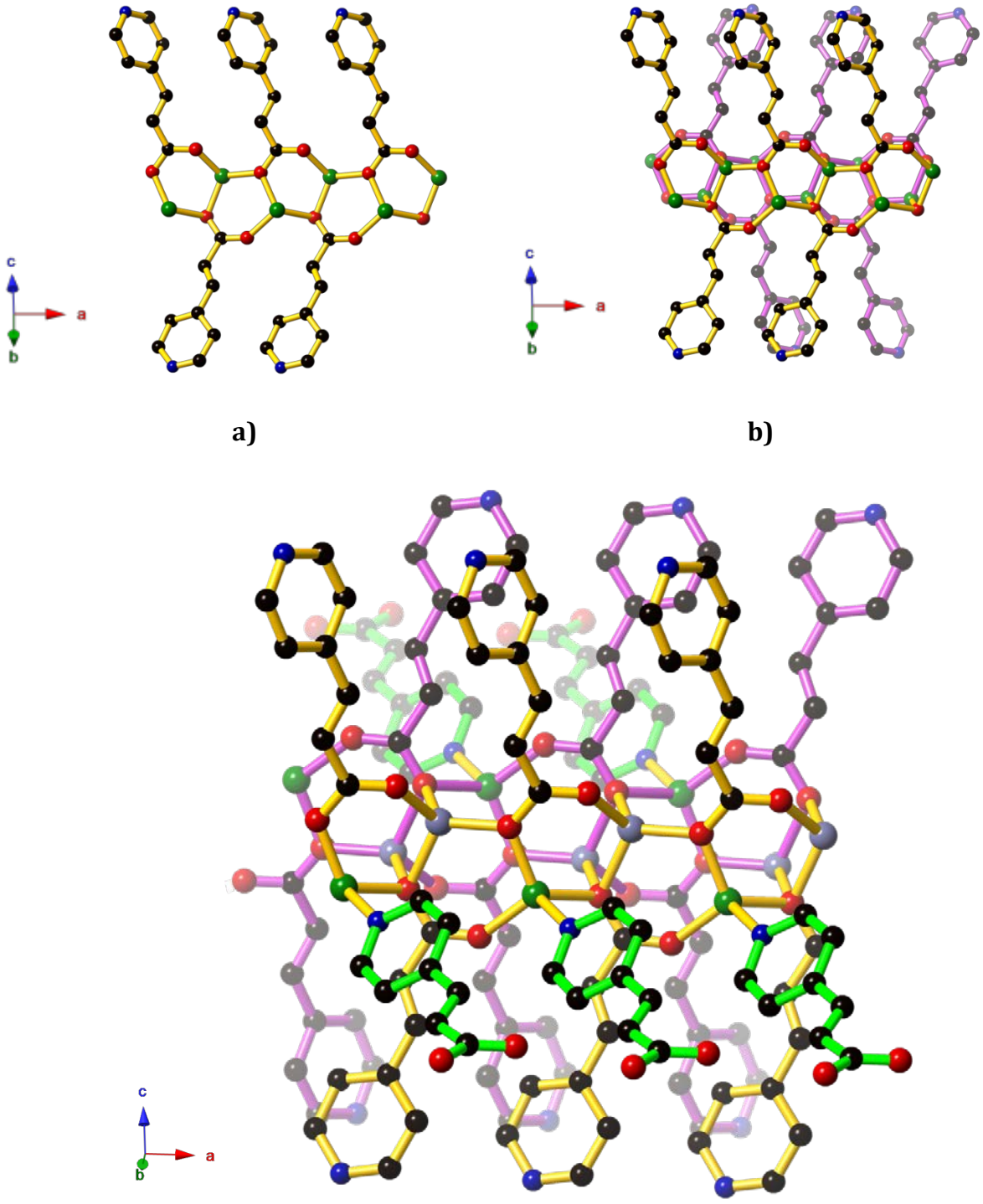

Figure 2.12: the structure of Li(paa) showing **a)** the chains containing the 6-membered edge sharing Li-O-Li-O-C-O rings, similar to those of Li(paa)·S, 'open' Li(inic) and dense Li(inic), **b)** the linked double chains and **c)** the extended dense Li(paa) network with Li(1) atoms shown in lilac, Li(2) atoms shown in green and paa^- ligands from adjacent double chains highlighted with green bonds.

All the linked double chains in the crystal structure are parallel to the *a* axis. Half the pyridyl groups on the linked double chain coordinate to adjacent chains, as shown in **Figure 2.13**.

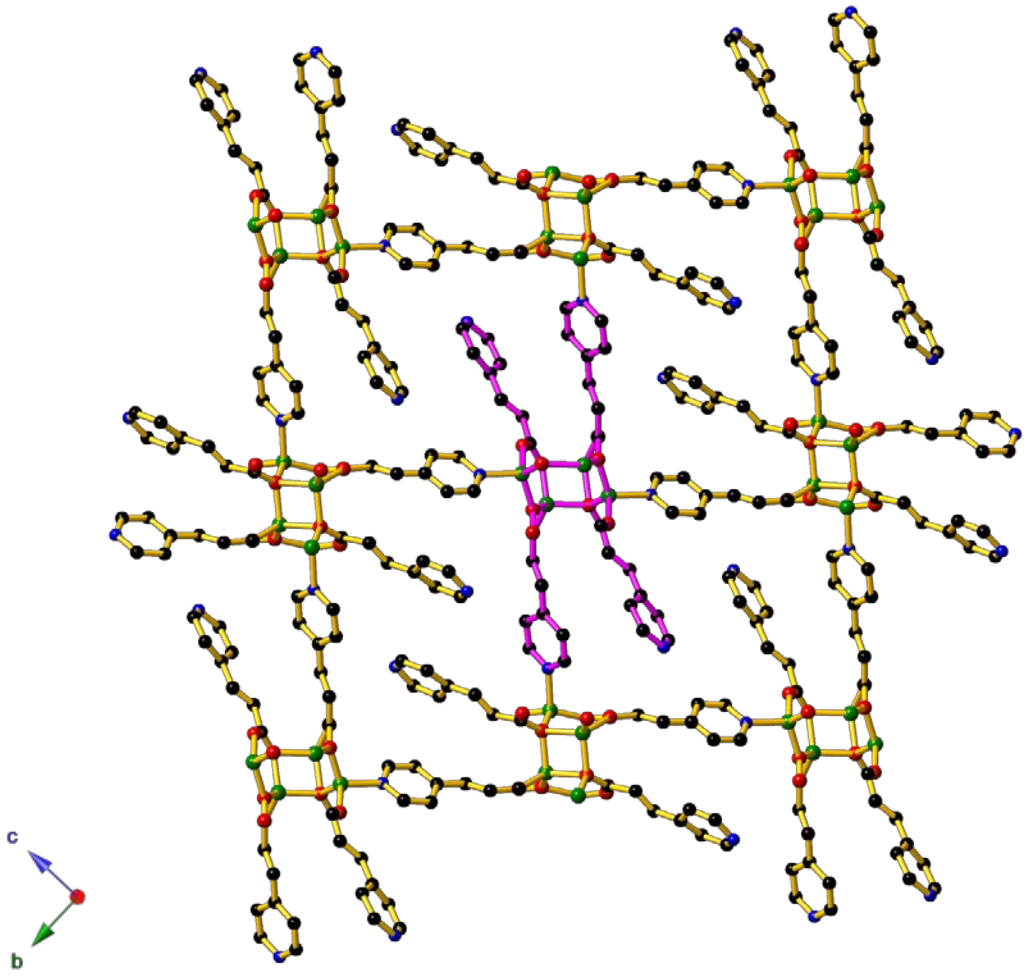

Figure 2.13: The extended dense Li(paa) network viewed down a central double chain is highlighted with purple bonds.

2.4 Lithium based structures with peb⁻

Attempts were also made to form the square channel network with a longer ligand. 4-[(E)-2-(pyridin-4-yl)ethenyl]benzoic acid, hereon pyridylethenyl benzoic acid (Hpeb, **XI**), was chosen because of the molecule's similar functionality to Hinic, however the inclusion of an extra phenyl group in the ligand has the potential to create channels with an even larger cross-section than those present in Li(paa).

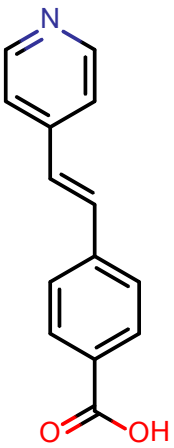

(XI)

Perhaps not surprisingly, when pyridylethenyl benzoic acid was reacted with lithium in the presence of water, $[Li_2(peb)(H_2O)_7](peb)\cdot H_2O$ crystallised as a dense network. Elucidation of the crystal data reveals that $[Li_2(peb)(H_2O)_7](peb)\cdot H_2O$ crystals form in the monoclinic space group *Pc*. Crystal structure analysis revealed two distinct types of Li^+ centre, one being a tetraaqua centre hydrogen bonded to a peb^- (**Figure 2.14a**) and the other bonded directly to a carboxylate oxygen atom on the peb^- ligand and three

water molecules (**Figure 2.14b**). The oxygen atoms of these two distinct lithium coordination environments participate in extensive hydrogen bonding leading to the formation of a dense network, as indicated in **Figure 2.14c**.

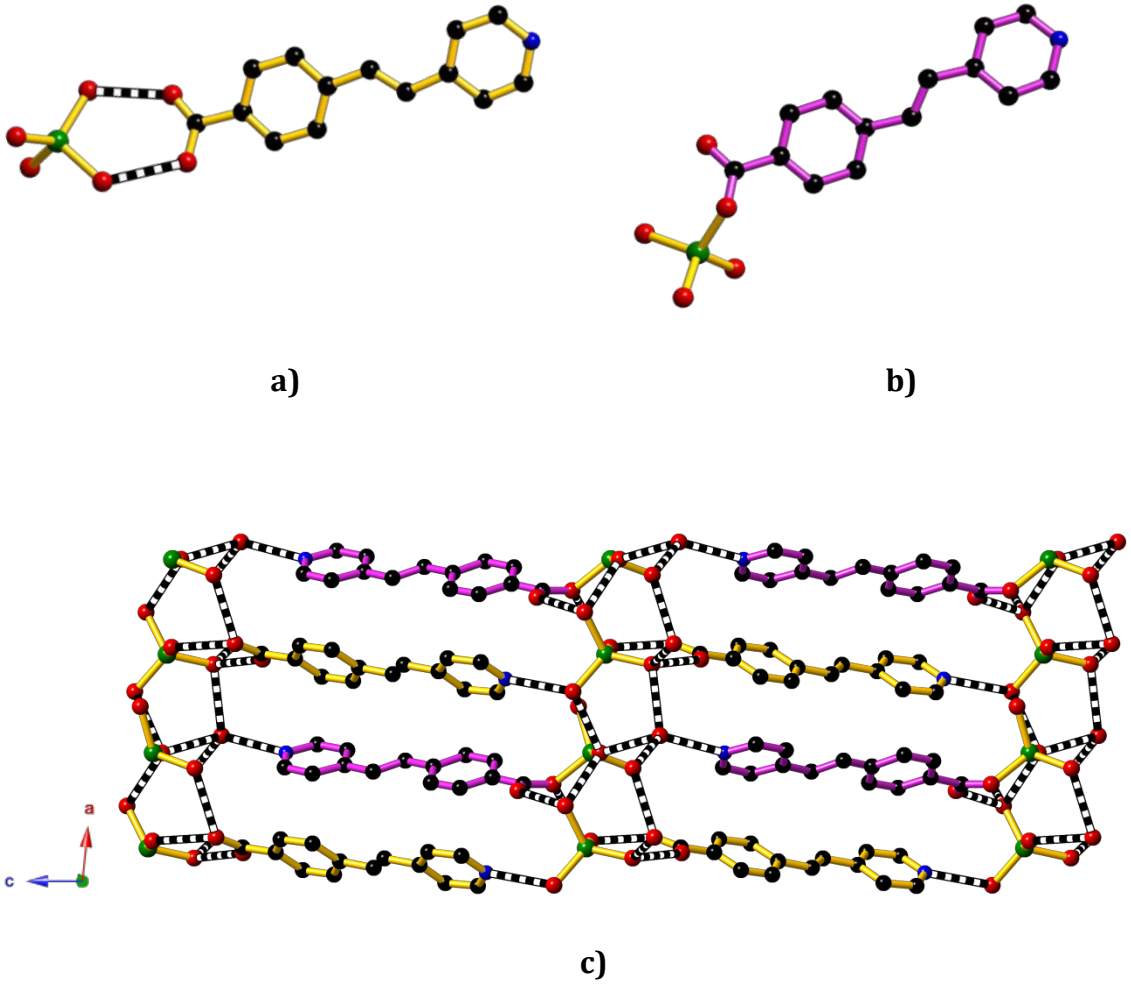

a) **b)**

c)

Figure 2.14: The hydrated $[Li_2(peb)(H_2O)_7](peb)\cdot H_2O$ network showing **a)** the peb^- ligand hydrogen bonding to a tetraaqua lithium centre, **b)** the peb^- ligand co-ordinating directly to a Li^+ centre and **c)** the close packed hydrogen bonded network. Hydrogen bonds depicted as black and white striped connections.

When Hpeb is combined with Li^+ in DMSO, in the absence of water, brownish-yellow crystals of Li(peb)DMSO form in the monoclinic space group $P2_1/n$ along with amorphous material. Li^+ peb^- chains are formed which consist of alternating

4-membered Li-O-Li-O rings and 8-membered Li-O-C-O-Li-O-C-O rings, much like in the case of Li(inic), (**Figure 2.2**), but with coordinated DMSO molecules instead of pyridyl groups occupying the fourth site on the Li^+ centre (**Figure 2.15a**). Infinite chains extend in the *a* direction. A view along the direction of the chain is presented in **Figure 2.15b**. Parallel chains are arranged in a manner in which the peb^- ligands interweave as indicated in **Figure 2.15c**. The pyridyl nitrogen atoms appear to make close contact (~3.4 Å) with the S atoms of the coordinated DMSO molecules.

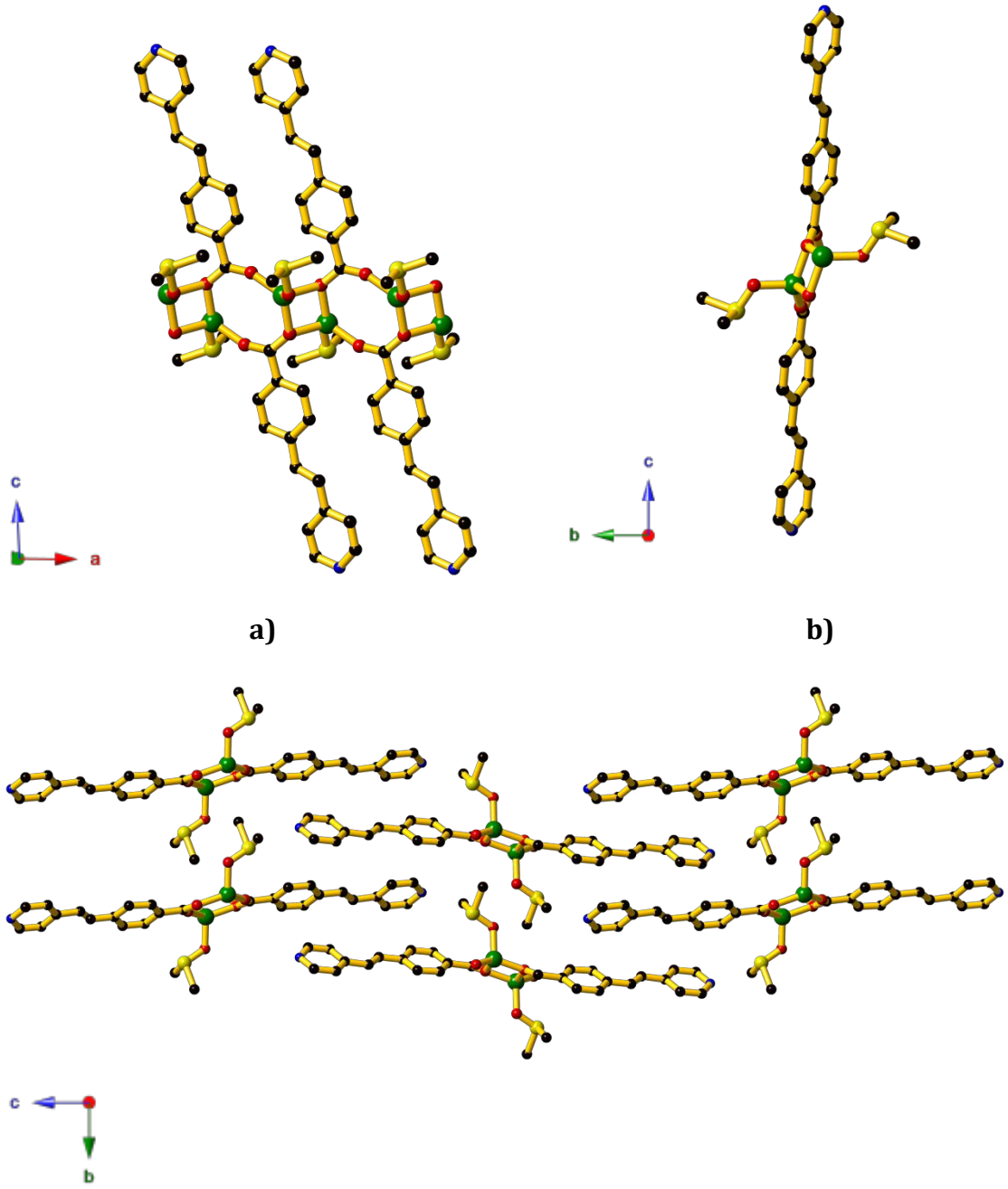

Figure 2.15: The Li(peb)DMSO structure showing **a)** the chains consisting of alternating 4-membered Li-O-Li-O rings and 8-membered Li-O-C-O-Li-O-C-O rings and coordinated DMSO **b)** a view of the chain extending into and out of the page **c)** the packing of the chains resulting in a dense structure with close contact (N-S ~3.4 Å)

Given that the compounds Li(paa), Li(paa)·DMF, $[Li_2(peb)(H_2O)_7](peb)\cdot H_2O$ and Li(peb)DMSO crystals either have dense structures or exhibit instability, no adsorption measurements were performed on these compounds.

2.5 Concluding remarks

The Li(inic) framework has been previously shown to be reasonably robust and able to crystallise from a variety of solvents. Li(paa)·DMF on the other hand is more delicate. Shortly after crystallisation the crystals begin to adopt a 'moth eaten' appearance as they redissolve into solution. The dense non-solvated, Li(paa) structure subsequently separates from the solution. The acceleration of this process observed on glass slides suggests that crystals of Li(paa)·DMF are strongly hygroscopic and re-dissolve as the concentration of water in the mother liquor increases. The fragility of the crystals may be a result of the larger channels of the Li(paa)·DMF framework, compared to that of the Li(inic)·S series of framework, allowing water to more easily permeate through the crystal.

Frameworks similar to Li(inic)·S have yet to be generated with the longer ligand peb^-. The larger channels in Li(paa)·DMF are presumed to cause an increased susceptibility of the framework to water. The synthesis of robust frameworks with even larger channels may be a somewhat futile endeavour. Although such frameworks with larger channels

would have significantly lower densities, their fragility diminishes the possibility of any practical applications.

The coordination environment of Li^+ ions in $Li_2(peb)_2(H_2O)_7{\cdot}H_2O$ is dominated by water molecules. Of the two crystallographically unique Li^+ ions, the first forms a tetraaqua complex that interacts via hydrogen bonds with a peb^- ligand. The second lithium centre bonds to three water molecules and one peb^- ligand through a single carboxylate oxygen atom. Perhaps not surprisingly, the pyridyl nitrogen atom appears to prefer forming hydrogen bonds with coordinated water molecules rather than coordinating directly with the Li^+ centre.

As previously indicated, pyridyl N-atoms coordinate to Li^+ ions in frameworks where the solvent molecules play a templating role, e.g. Li(inic)·DMF, Li(inic)·cyclohexanol and Li(paa)·DMF. However, when short chain alcohols are used, the pyridyl N-atom has a tendency to form a hydrogen bond with the coordinated alcohol ligands.[2] Similarly, when water is present, the pyridyl N-atom again forms hydrogen bonding interactions with coordinated water molecules.[2]

Crystals of Li(peb)DMSO contain 1-D Li^+ peb^- chains, shown in **Figure 2.15a**. The chains consist of alternating 4-membered Li_2O_2 rings and 8-membered $Li_2(OCO)_2$ rings similar to that found in the Li(inic)·S family of frameworks discussed in chapter 1 (**Figure1.22**). The presence of a coordinated DMSO molecule prevents the formation of channels

within the crystal. The use of a larger 'templating' solvent less inclined to compete with the ligand in coordinating to the Li^+ may allow the formation of channels.

In all of the structures considered in this chapter the anion has a single negative charge, whilst the metal serves as a singly charged cation. It would seem reasonable to expect that networks formed from related dianions and dications may be considerably more robust.

2.6 Experimental

2.6.1 Synthesis of Hpaa

Hpaa was synthesised according to literature procedure of Marvel *et al*.[6]

2.6.2 Synthesis of Hpeb

Hpeb was synthesised as per the reported literature procedure of Kashida *et al*.[7]

2.6.3 Synthesis of Li(paa)·DMF and Li(paa)

Hpaa (150 mg, 0.100 mmol) and $LiOH{\cdot}H_2O$ (42 mg, 0.100 mmol) were dissolved in hot methanol (5ml). DMF (10ml) was added to the hot solution. The temperature was monitored to ensure that the solution was heated without boiling. When the temperature of the solution reached ~150 °C the mixture was removed from heat. The reaction vessel was then sealed with parafilm. Slow cooling of the mixture, naturally at ambient temperature overnight, allowed the separation of colourless needle-like crystals of Li(paa)·DMF. Upon exposure to the atmosphere the crystals would redissolve and crystallise into colourless needles of composition Li(paa). Li(paa) Yield 40 mg.

Infrared Spectrum (KBr): 3429(b), 3029(w), 1650(s), 1600(s), 1405(s), 1294(w), 1006(m) cm^{-1}, (as shown in **Figure A.73** in the Appendix).

Powder diffraction data were collected to confirm purity of the bulk product (**Figure 2.16**).

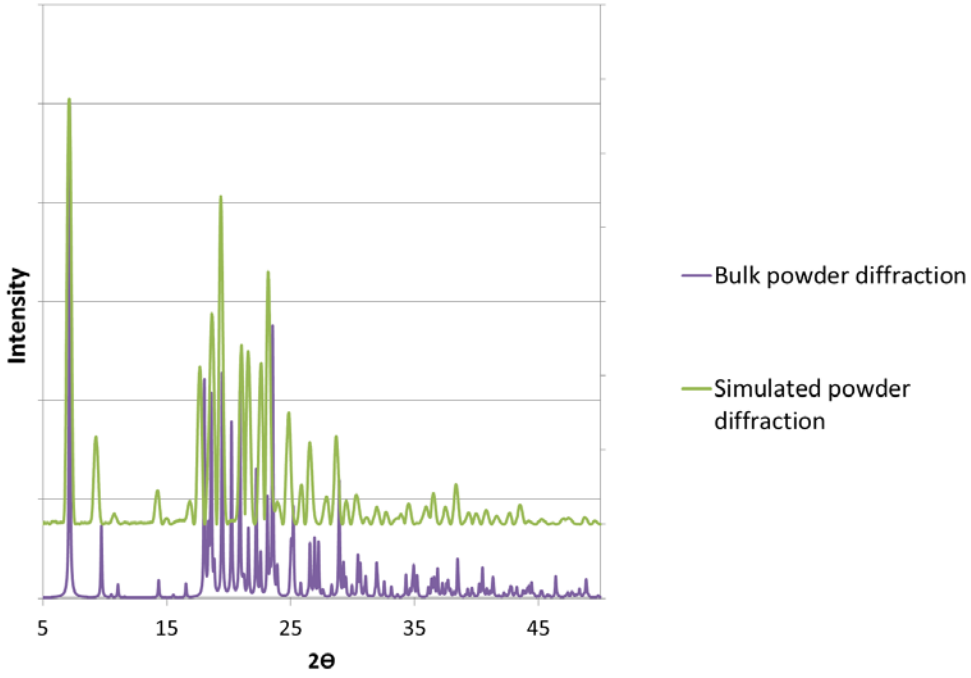

Figure 2.16: The X-ray powder diffraction pattern of the bulk sample of Li(paa) compared to a X-ray powder diffraction pattern simulated from the crystal structure of Li(paa).

2.6.4 Synthesis of $[Li_2(peb)(H_2O)_7](peb)\cdot H_2O$

An aqueous solution (10 ml) of Hpeb (225 mg, 0.100 mmol) and $LiOH\cdot H_2O$ (42 mg, 0.100 mmol) was allowed to sit at room temperature. Slow evaporation over several days resulted in the separation of colourless needle-like crystals of $[Li_2(peb)(H_2O)_7](peb)\cdot H_2O$. Yield 10 mg. Infrared Spectrum (KBr): 3422(b), 1649(s), 1602(s), 1546(s), 1396(s), 1004 (m) cm^{-1}, (as shown in **Figure A.74** in the Appendix)

Powder diffraction data were collected to confirm purity of the bulk product (**Figure 2.17**).

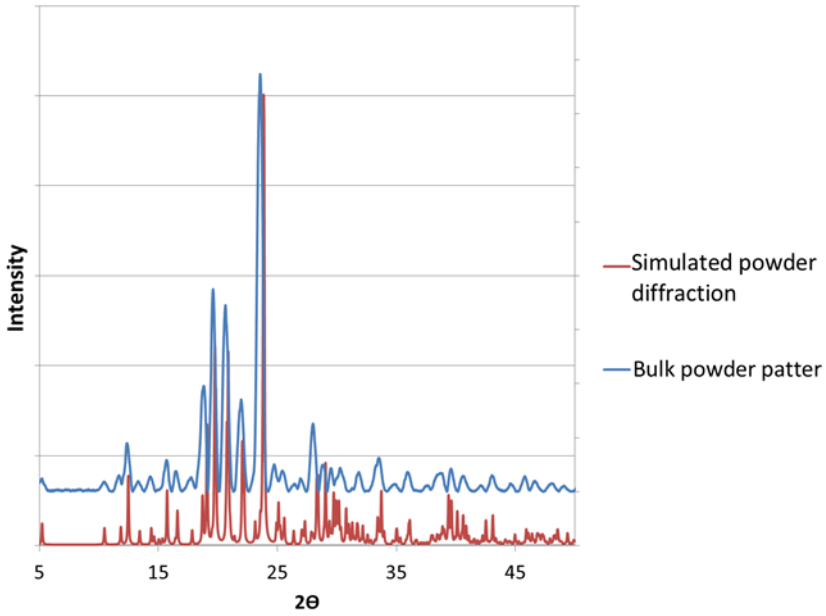

Figure 2.17: The X-ray powder diffraction pattern of the bulk sample of $[Li_2(peb)(H_2O)_7](peb)\cdot H_2O$ compared to a X-ray powder diffraction pattern simulated from the crystal structure of $[Li_2(peb)(H_2O)_7](peb)\cdot H_2O$.

2.6.5 Synthesis of Li(peb)DMSO

DMSO (10ml) was added to a methanolic solution (5 ml) of Hpeb (112 mg, 0.050 mmol) and $LiOH\cdot H_2O$ (21 mg, 0.050 mmol). The solution was heated to evaporate the more volatile methanol without boiling. A mixture of an amorphous brown yellow precipitate and brown-yellow crystals of Li(peb)DMSO separated from solution. Despite numerous attempts a homogenous product was unable to be obtained.

2.7 Details of structure determination

Single crystal X-ray diffraction techniques were performed on Li(paa)·DMF and Li(peb)DMSO on an Oxford Diffraction SuperNova equipped with CuKα X-ray radiation, using the general techniques described in Chapter 7.

Single crystal X-ray diffraction techniques were performed on Li(paa) and $[Li_2(peb)(H_2O)_7](peb)\cdot H_2O$ and were collected on the MX1 beamline at the Australian Synchrotron, the details of which are described in Chapter 7.

X-ray powder diffraction data for $[Li_2(peb)(H_2O)_7](peb)\cdot H_2O$ and Li(paa)were collected on a Rigaku Oxford Diffraction Synergy-S diffractometer equipped with CuKα monochromated X-ray radiation, the details of which are described in Chapter 7.

2.7.1 Li(paa)·0.4DMF

Single crystal X-ray data were collected on a colourless needle-like crystal of Li(paa)·DMF. Elucidation of the data revealed the crystal possessed orthorhombic symmetry and a satisfactory solution was obtained in the space group $Pna2_1$. All non-hydrogen framework atoms were clearly defined and refined with anisotropic displacement parameters. All hydrogen framework atoms were placed in geometrically estimated positions. Solvent mask (SQUEEZE) was used to treat disordered DMF molecules within the channels. The SQUEEZE results indicated 0.4 DMF molecules per formula unit. Despite numerous attempts crystals were weakly diffracting, resulting in poor data completeness. The connectivity of the framework, however, is unambiguous. The crystallographic data table is presented in **Table 2-1**.

2.7.2 Li(paa)

Single crystal x -ray data were collected on a colourless needle-like crystal of Li(paa). In order to limit the extent of crystal deterioration the crystal was transferred directly from the mother liquor to a protective oil before being placing it in a stream of cold nitrogen on the diffractometer. Whilst this process was performed as quickly as possible some deterioration of the crystal was apparent and this impacted upon the quality of the diffraction data. As a consequence, high angle data proved to be quite weak and elevated agreement values (R_1 = 0.1468 wR_2 = 0.3242) were obtained. Nonetheless, the connectivity of the material is unambiguous.

Elucidation of the data revealed the crystal possessed monoclinic symmetry in the space and a satisfactory solution was obtained in the space group $P2_1/n$. All non-hydrogen framework atoms were clearly defined and refined with anisotropic displacement parameters. All hydrogen framework atoms were placed in geometrically estimated positions. Four carbon atoms (C13-C16) of an aromatic ring are modelled over two orientations, each site with 50% occupancy. Two carbon atoms of the ring were common to both orientations. The crystallographic data table is shown in **Table 2-2**.

2.7.3 $[Li_2(peb)(H_2O)_7](peb)\cdot H_2O$

Single crystal X-ray data were collected on a colourless needle-like crystal of $[Li_2(peb)(H_2O)_7](peb)\cdot H_2O$. Elucidation of the structure revealed the crystal possessed monoclinic symmetry and a satisfactory solution was obtained in the space group *Pc*. All non-hydrogen framework atoms were clearly defined and refined with anisotropic displacement parameters. All hydrogen framework atoms were placed in geometrically estimated positions. The crystallographic data table is shown in **Table 2-3**.

2.7.4 Li(peb)DMSO

Single crystal X-ray data were collected on a colourless needle-like crystal of Li(peb)DMSO. Elucidation of the structure revealed the crystal possessed monoclinic symmetry and a satisfactory solution was obtained in the space group $P2_1/n$. All non-hydrogen atoms within the framework were clearly defined and refined with anisotropic displacement parameters. All hydrogen framework atoms were placed in geometrically estimated positions. The crystals were inherently twinned and weakly diffracting resulting in a poor agreement index (R_1=21.13%), however the connectivity of the framework is unambiguous. Attempts to treat the crystal twinning were unsuccessful. The crystallographic data table is shown in **Table 2-4**.

2.8 Crystallographic data tables

2.8.1 Li(paa)·DMF

Table 2-1: Crystallographic data table of Li(paa)·DMF

Empirical formula	$C_8H_6LiNO_2$
Formula weight	155.08
Temperature/K	130(1)
Crystal system	orthorhombic
Space group	$Pna2_1$
a/Å	11.751(4)
b/Å	18.685(2)
c/Å	4.9656(4)
Volume/Å^3	1090.3(4)
Z	4
ρ_{calc}g /cm^3	0.945
μ / mm^{-1}	0.554
F(000)	320.0
Crystal size/mm^3	0.75 × 0.04 × 0.03
λ (CuKα)	1.54184
2Θ range for data collection/°	8.89 to 147.908
Index ranges	-13 ≤ h ≤ 14, -23 ≤ k ≤ 23, -3 ≤ l ≤ 6
Reflections collected	8252
Independent reflections	1797 [R_{int} = 0.1130, R_{sigma} = 0.0698]
Data/restraints/parameters	1797/1/109
Goodness-of-fit on F^2	0.965
Final R indexes [I>=2σ (I)]	R_1 = 0.0980, wR_2 = 0.2710
Final R indexes [all data]	R_1 = 0.1468, wR_2 = 0.3242
Largest diff. peak/hole / e Å^{-3}	0.14/-0.29
Flack parameter	0.3(9)

2.8.2 Li(paa)

Table 2-2: Crystallographic data table of Li(paa)

Empirical formula	$C_8H_6LiNO_2$
Formula weight	155.08
Temperature/K	100(1)
Crystal system	monoclinic
Space group	$P2_1/n$
a/Å	4.9760(10)
b/Å	18.182(4)
c/Å	16.822(3)
β/°	92.62(3)
Volume/Å^3	1520.4(5)
Z	8
ρ_{calc}g /cm^3	1.355
μ /mm^{-1}	0.096
F(000)	640.0
Crystal size/mm^3	0.29 × 0.02 × 0.01
λ (Synchrotron Radiation)	0.7109
2Θ range for data collection/°	3.3 to 55.78
Index ranges	-6 ≤ h ≤ 6, -23 ≤ k ≤ 23, -21 ≤ l ≤ 21
Reflections collected	24964
Independent reflections	3460 [R_{int} = 0.0735, R_{sigma} = 0.0345]
Data/restraints/parameters	3460/0/253
Goodness-of-fit on F^2	1.041
Final R indexes [I>=2σ (I)]	R_1 = 0.0547, wR_2 = 0.1272
Final R indexes [all data]	R_1 = 0.0752, wR_2 = 0.1394
Largest diff. peak/hole / e Å^{-3}	0.21/-0.32

2.8.3 $[Li_2(peb)(H_2O)_7](peb)\cdot H_2O$

Table 2-3: Crystallographic data table of $[Li_2(peb)(H_2O)_7](peb)\cdot H_2O$

Empirical formula	$C_{14}H_{17}LiNO_6$
Formula weight	302.22
Temperature/K	100 (1)
Crystal system	monoclinic
Space group	*Pc*
a/Å	7.4990(15)
b/Å	6.1440(12)
c/Å	33.934(7)
β/°	95.70(3)
Volume/Å^3	1555.7(5)
Z	4
ρ_{calc}g /cm^3	1.290
μ /mm^{-1}	0.100
F(000)	636.0
Crystal size/mm^3	0.12 × 0.08 × 0.07
λ (Synchrotron Radiation)	0.7109
2*Θ* range for data collection/°	2.41 to 55.78
Index ranges	-9 ≤ h ≤ 9, -8 ≤ k ≤ 8, -43 ≤ l ≤ 43
Reflections collected	23854
Independent reflections	7077 [R_{int} = 0.0334, R_{sigma} = 0.0276]
Data/restraints/parameters	7077/18/447
Goodness-of-fit on F^2	1.078
Final R indexes [I>=2σ (I)]	R_1 = 0.0657, wR_2 = 0.1581
Final R indexes [all data]	R_1 = 0.0699, wR_2 = 0.1612
Largest diff. peak/hole / e Å^{-3}	0.96/-0.38
Flack parameter	0.0(3)

2.8.4 Li(peb)DMSO

Table 2-4: Crystallographic data table of Li(peb)DMSO

Empirical formula	$C_{16}H_{16}LiNO_3S$
Formula weight	309.30
Temperature/K	130 (1)
Crystal system	monoclinic
Space group	$P2_1/n$
a/Å	5.5122(7)
b/Å	7.7929(15)
c/Å	34.802(5)
β/°	93.204(14)
Volume/Å^3	1492.6(4)
Z	4
ρ_{calc}g /cm^3	1.376
μ /mm^{-1}	2.012
F(000)	648.0
Crystal size/mm^3	0.16 × 0.08 × 0.04
λ (CuKα)	1.54184
2Θ range for data collection/°	10.182 to 150.6
Index ranges	-5 ≤ h ≤ 6, -6 ≤ k ≤ 9, -43 ≤ l ≤ 41
Reflections collected	6485
Independent reflections	2921 [R_{int} = 0.0739, R_{sigma} = 0.0725]
Data/restraints/parameters	2921/0/201
Goodness-of-fit on F^2	2.127
Final R indexes [I>=2σ (I)]	R_1 = 0.2113, wR_2 = 0.5629
Final R indexes [all data]	R_1 = 0.2367, wR_2 = 0.5803
Largest diff. peak/hole / e Å^{-3}	1.86/-0.59

2.9 References

[1] B. F. Abrahams, M. J. Grannas, T. A. Hudson, R. Robson, *Angew. Chemie - Int. Ed.* **2010**, *49*, 1087–1089.

[2] B. F. Abrahams, A. D. Dharma, M. J. Grannas, T. A. Hudson, H. E. Maynard-Casely, G. R. Oliver, R. Robson, K. F. White, *Inorg. Chem.* **2014**, *53*, 4956–4969.

[3] D. Banerjee, S. J. Kim, W. Li, H. Wu, J. Li, L. A. Borkowski, B. L. Philips, J. B. Parise, *Cryst. Growth Des.* **2010**, *10*, 2801–2805.

[4] X. Zhao, T. Wu, S. T. Zheng, L. Wang, X. Bu, P. Feng, *Chem. Commun.* **2011**, *47*, 5536–5538.

[5] R. El Osta, M. Frigoli, J. Marrot, N. Guillou, H. Chevreau, R. I. Walton, F. Millange, *Chem. Commun.* **2012**, *48*, 10639.

[6] C. S. Marvel, L. E. Coleman, G. P. Scott, *J. Org. Chem.* **1955**, *20*, 1785–1792.

[7] H. Kashida, H. Ito, T. Fujii, T. Hayashi, H. Asanuma, *J. Am. Chem. Soc.* **2009**, *131*, 9928–9930.

Chapter 3 Table of Contents

Chapter 3 – Investigations of coordination polymers formed from hydroxybenzoic acid

3.1 Introduction

As discussed in chapter 1, the Zn(hba) framework (**Figure 3.1a**) was formed from the combination of 4-hydroxybenzoic acid and zinc acetate in a hot solution of pentanol and methanol. The aim of this synthesis was to produce a PtS type framework similar to that found from the combination of lithium hydroxide and the N-oxide of isonicotinic acid, shown in figure **Figure 3.1b.** The similarity in the structures of the hba^{2-} and $inox^{-}$ is apparent upon inspection of **Figure 3.1c** and **Figure 3.1d**. It was anticipated that the use of the +2 metal ion and a -2 ligand in Zn(hba) would lead to a more robust framework than Li(inox) where the metal ion and ligand have charges of +1 and -1 respectively.

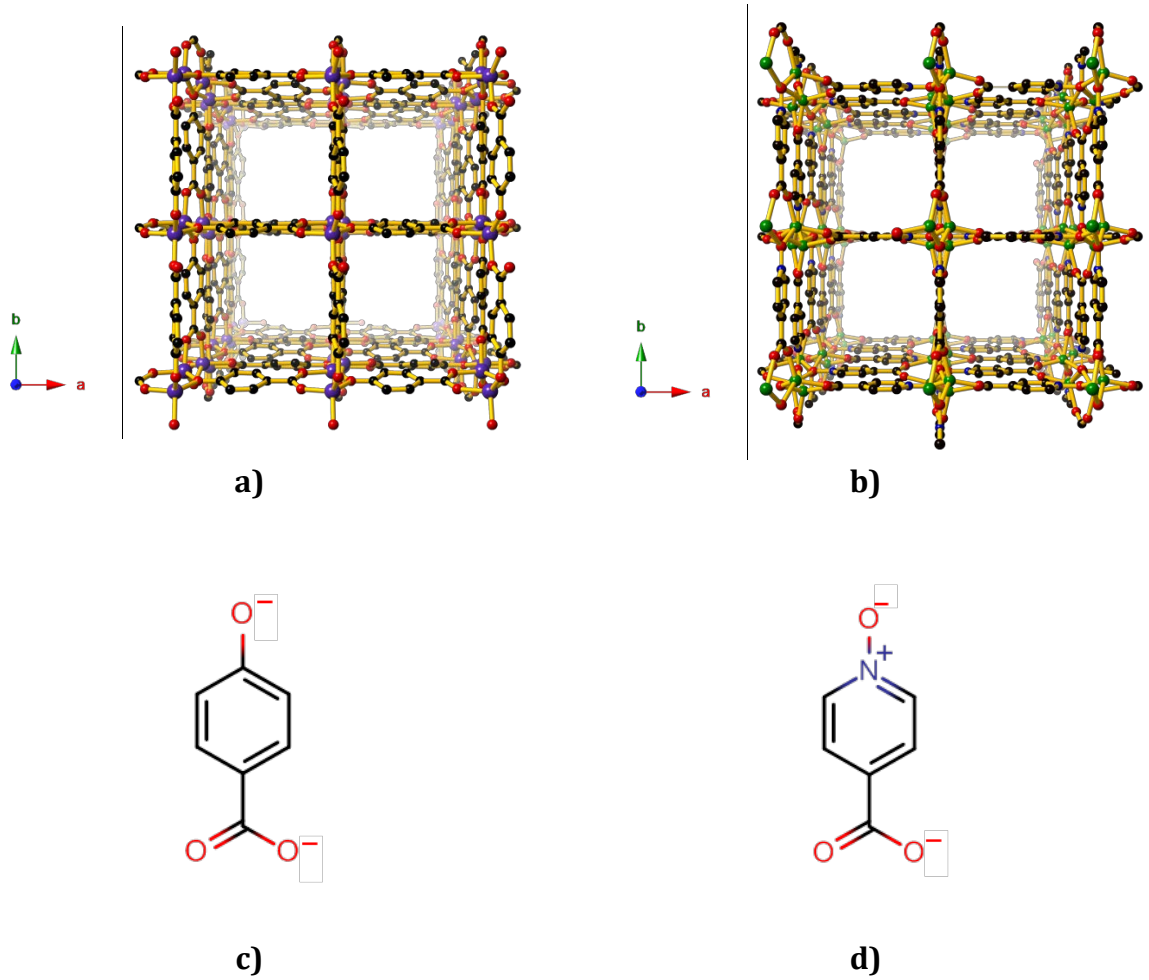

Figure 3.1: A view **a)** down the *c* axis in the Zn(hba) crystal structure **b)** down the *c* axis in the Li(inox) crystal structure and the **c)** hba^{2-} and **d)** $inox^{-}$ ligands. Purple spheres represent Zn atoms, green spheres represent Li atoms, black spheres represent C atoms, red spheres represent O atoms and N atoms are represented with blue spheres. Hydrogen atoms have been omitted for clarity.

The Zn(hba) network displays good adsorption behaviour with a wide variety of guest molecules, in particular H_2, N_2, CH_4 and CO_2, which is discussed in detail in chapter 4. The Zn(hba) compound is considered as the progenitor for a family of Zn (or Co) coordination networks involving the phenolate-carboxylate ligands, coumarate (cma^{2-}) and 4,4'-hydroxy biphenyl carboxlyate ($hbpc^{2-}$). The structures and gas sorption properties of the compounds Zn(hba), Zn(cma), Zn(hbpc), Co(hba), Co(hbpc), shown in **Figure 3.2** , have been previously reported in 2015. [1]

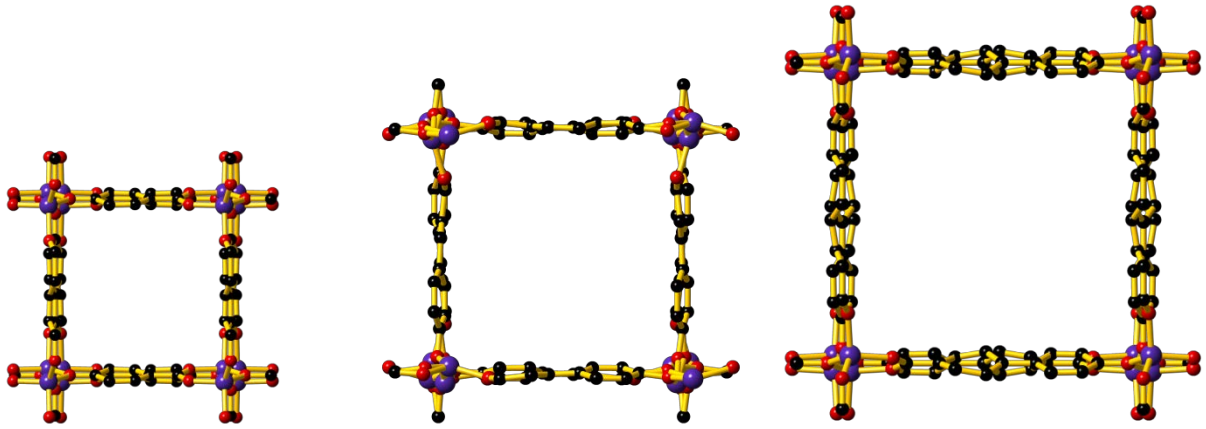

a) **b)** **c)**

Figure 3.2: A view showing the square channels and the relative sizes therein of **a)** Zn(hba), **b)** Zn(cma) and **c)** Zn(hbpc).

Whilst the compounds are crystalline, single crystal x-ray diffraction data are typically of poor quality with broad streaky diffraction spots and low resolution (>1.2 Å). Despite this, the data unambiguously shows that all frameworks are similar in topology to the well-ordered Li(inox) (**Figure 1.23**). The poor quality of the diffraction data is attributed to extensive twinning in addition to disorder associated with the orientation of the phenolate-carboxylate ligand.

3.2 Work reported in this chapter

In this chapter the synthesis and characterisation of a series of metal compounds in which variations on the hba^{2-} ligand have been investigated. The aim of the work is to investigate the structural impact of appending groups to the hba^{2-} ligand in addition to determining the extent of ligand variation that can be tolerated with preservation of the Zn(hba)-type structure.

3.3 Substituted Zn(hba) networks

Networks containing square channels that are isostructural with Zn(hba) were obtained from the starting materials 4-hydroxy-2-chlorobenzoic acid, (2-chloro H_2hba, **XII**), 4-hydroxy-2-fluorobenzoic acid, (2-fuoro H_2hba, **XIII**), 4-hydroxy-3-fluorobenzoic acid, (3-fuoro H_2hba, **XIV**), 4-hydroxy-2-methylbenzoic acid (2-methyl H_2hba, **XV**) and 4-hydroxy-2,6-dimethylbenzoic acid (2,6-dimethyl H_2hba, **XVI**).

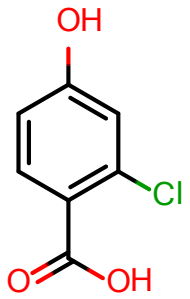

(XII)

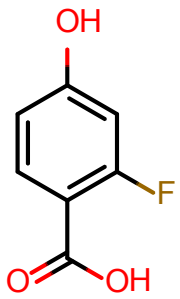

(XIII)

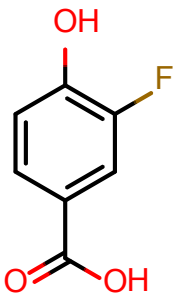

(XIV)

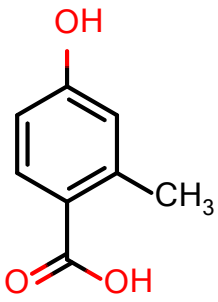

(XV)

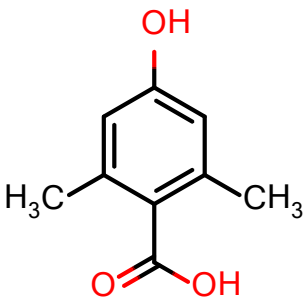

(XVI)

Although each network was unambiguously determined to possess the targeted PtS topology, in each case the substituent could not be successfully resolved in the structure refinement. This is due to the same diffuse scattering observed in the parent compound and the disorder of the substituent over numerous sites. Powder diffraction studies

performed at the PD beamline at the Australian Synchrotron, however, strongly indicate that the frameworks generated from the compounds **I** - **V**, possess the targeted networks, as is apparent from inspection of, **Figure 3.3**.

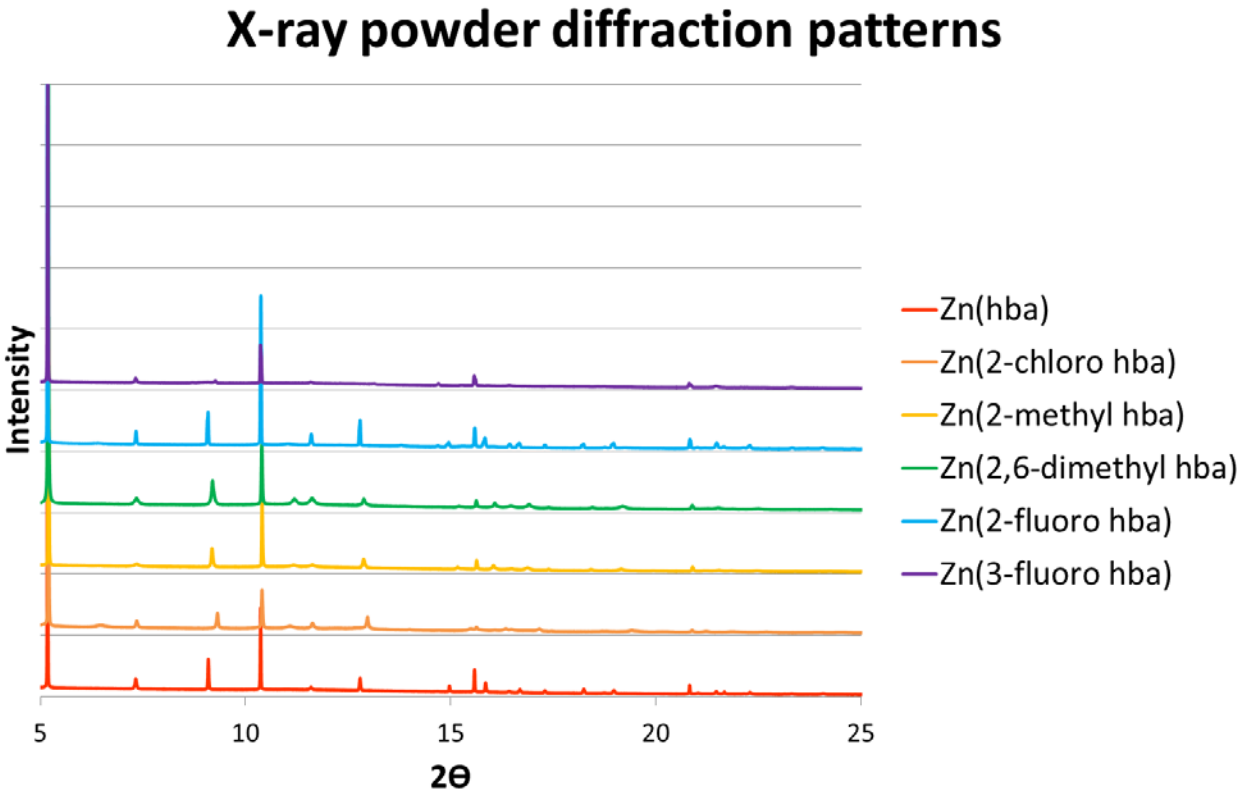

Figure 3.3: X-ray powder diffraction patterns of Zn(hba), Zn(2-chloro hba), Zn(2-methyl hba), Zn(2,6-dimethyl hba), Zn(2-fluoro hba) and Zn(3-fluoro hba).

As can be seen in **Figure 3.3**, the positions in the peaks in the powder diffraction pattern of Zn(hba) closely match the peak positions of the powder patterns of Zn(2-chloro hba), Zn(2-methyl hba), Zn(2,6-dimethyl hba), Zn(2-fluoro hba) and Zn(3-fluoro hba). Small discrepancies in the peak position are consistent with minor differences in cell dimensions. There are also minor differences in the relative intensity

of peaks which are attributed to the ligand substituents. The corresponding X_{20} and M_{20} values of the indexed powder patterns are listed in **Table 3-1**. An M_{20} larger than 10 with less than 2 superfluous peaks (X_{20}) indicates a reliable agreement with the indexed cell.[2]

Table 3-1: A table of the substituted networks Zn(hba) and their corresponding indexed unit cells.

Compound	M_{20}	X_{20}	Laue Class	*a*	*c*	Cell volume
Zn 2-chloro hba	60.51	0	*4/mmm*	9.119 Å	12.263 Å	1019.7 Å^3
Zn 2-methyl hba	27.37	0	*4/mmm*	9.108 Å	12.525 Å	1039.1 Å^3
Zn 2,6-dimethyl hba	34.77	0	*4/mmm*	9.118 Å	12.496 Å	1038.8 Å^3
Zn 2-fluoro hba	93.10	0	*4/mmm*	9.148 Å	12.707 Å	1063.4 Å^3
Zn 3-fluoro hba	36.03	0	*4/mmm*	9.140 Å	12.226 Å	1021.4 Å^3

Table 3-1 provides strong evidence that all of the above mentioned derivatives of hba^{2-} when combined with Zn^{2+} are isostructural to Zn(hba). However, it is anticipated that the introduction of functional groups into the system will result in slight changes in the dimensions and physical surface of the channel. **Figure 3.4** provides a representation of the channel wall in the Zn(hba) framework. The ligands are arranged in a manner that allows them to be co-planar with no spaces between the ligands large enough for a small molecule to pass through. The introduction of substituents on the phenyl ring

makes it impossible for adjacent ligands to remain co-planar and thus rotation of the phenyl group needs to occur in order for the PtS type structure to form.

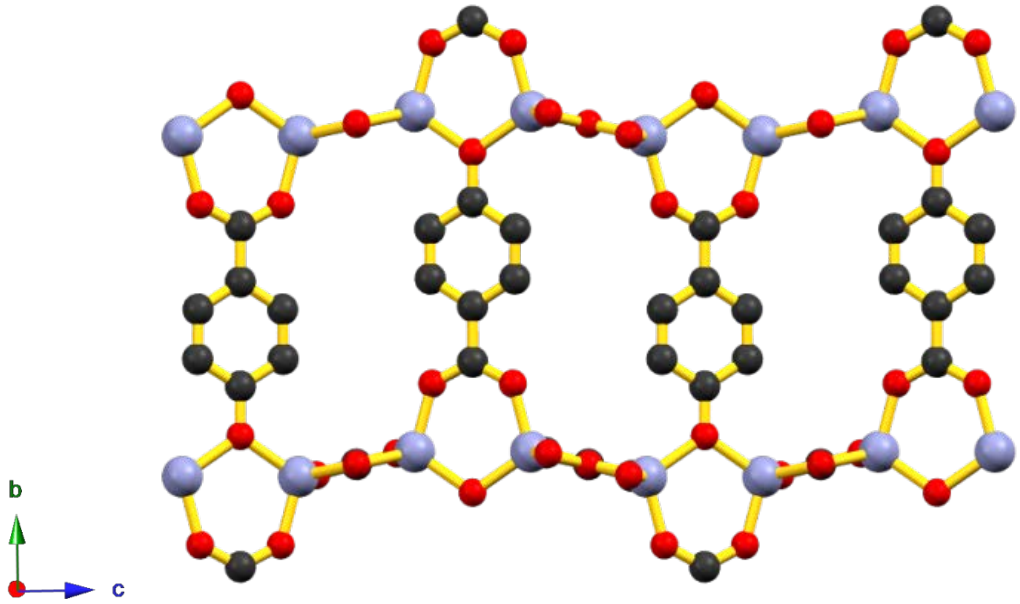

Figure 3.4: A view of the channel wall within the Zn(hba) parent compound. Zn atoms are in lilac.

The inability to resolve the exact position of the substituents in the substituted Zn(hba) family of frameworks, led to a collaboration with Dr Ravi Babarao, from the Royal Melbourne Institute of Technology (RMIT), who has considerable experience with molecular modelling. Dr Babarao completed computational simulations to predict the lowest energy conformations of both the Zn(2-methyl hba) and Zn(2,6-dimethyl hba), shown in **Figure 3.5** and **Figure 3.6** respectively. (The details of which can be found in chapter 7)

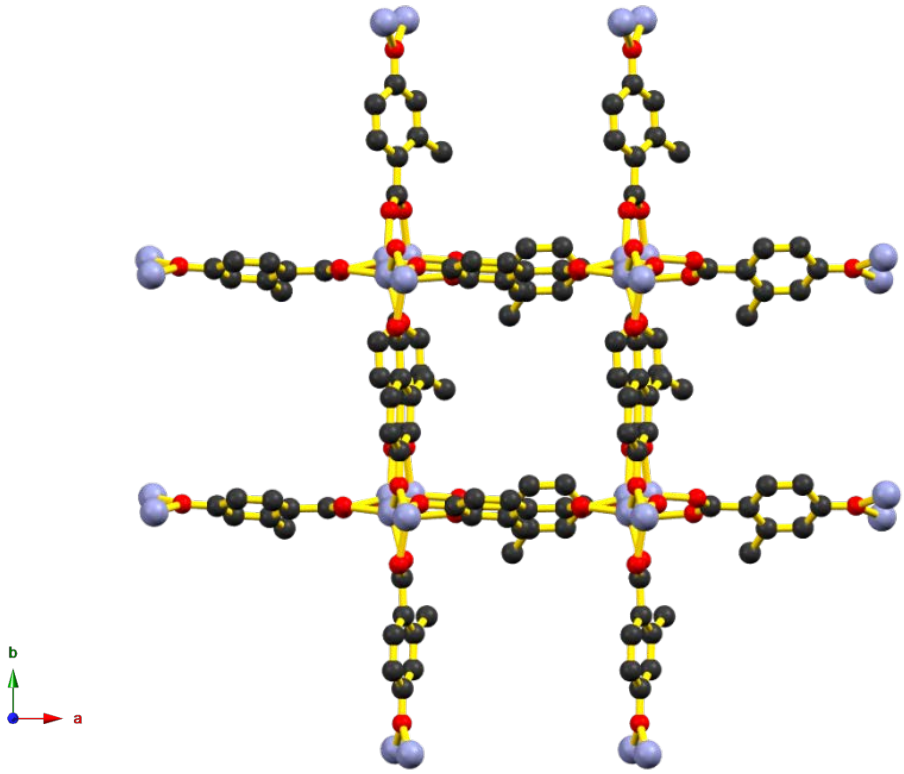

a)

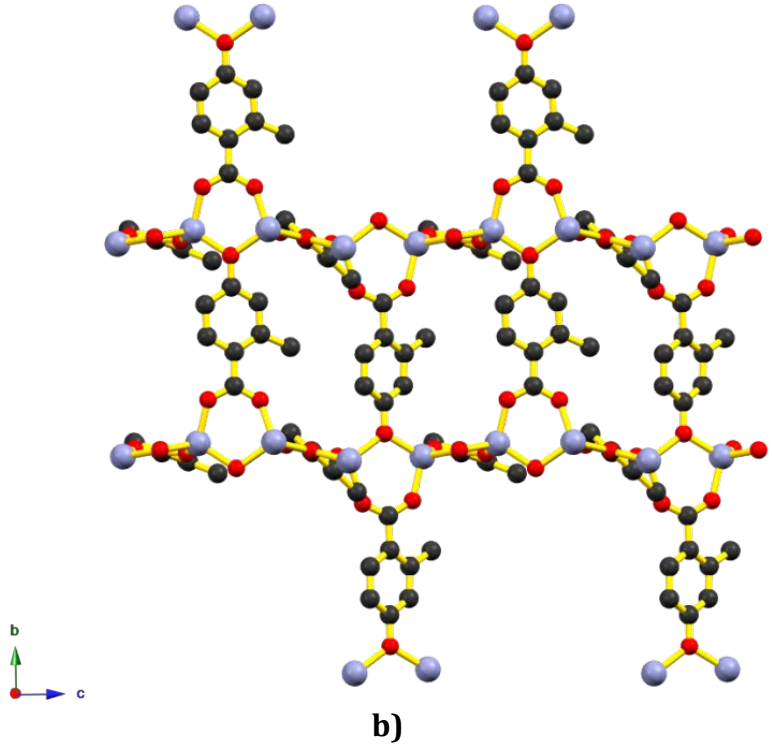

b)

Figure 3.5: Computational simulations predicting the lowest energy conformation of **a)** the channels of Zn(2-methyl hba) and **b)** the channel walls of Zn(2-methyl hba).

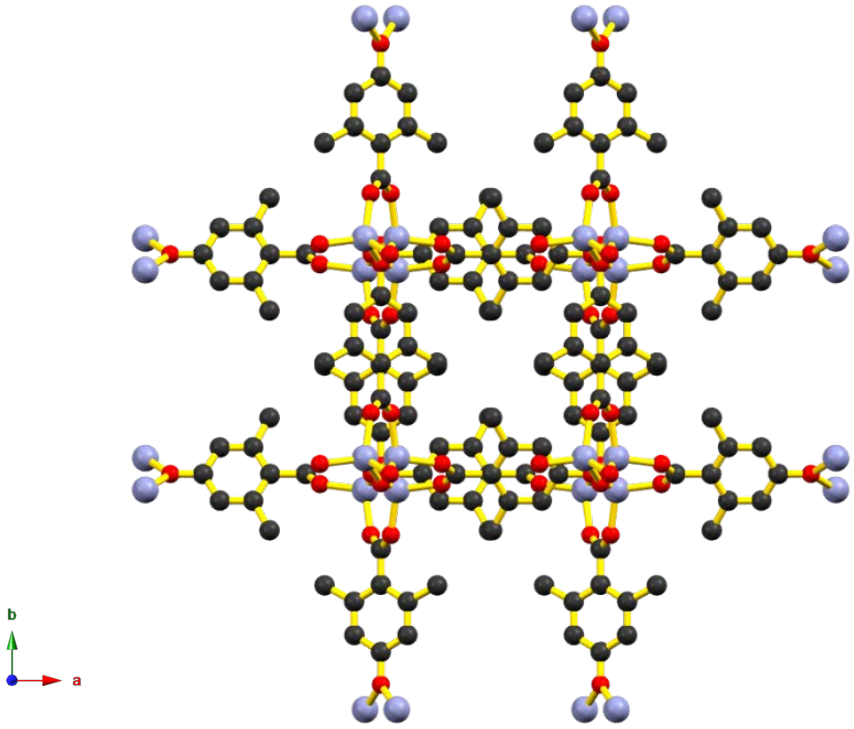

a)

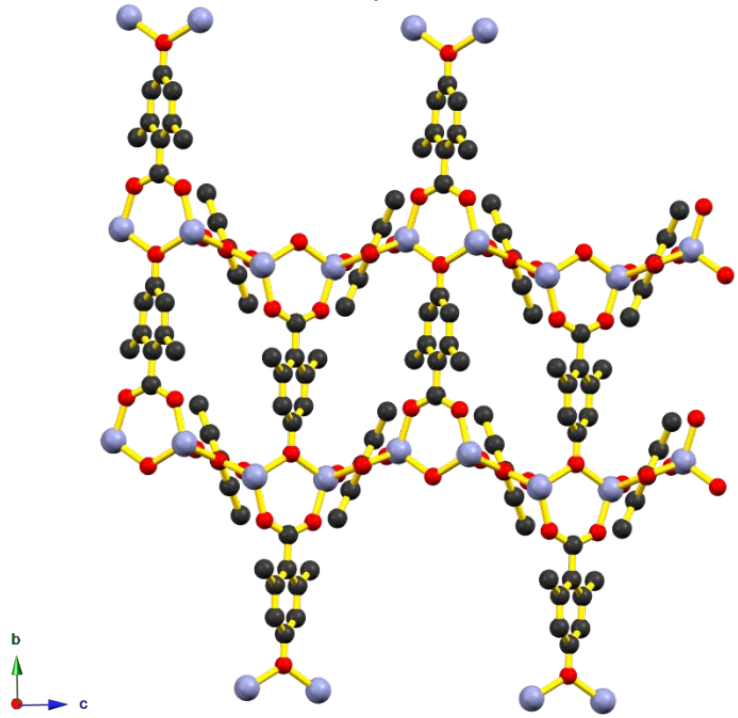

b)

Figure 3.6: Computational simulations predicting the lowest energy conformation of **a)** the channels of Zn(2,6-dimethyl hba) and **b)** the channel walls of Zn(2,6-dimethyl hba).

It is clear from inspection of **Figure 3.5a**, and **Figure 3.6a** that the intra-framework channels within Zn(2,6-dimethyl hba) are far smaller than those available in Zn(2-methyl hba). This is a direct result of the degree of rotation of the aromatic rings in the ligands. With respect to the orientation of the ligand, there are two types of 2-methyl hba^{2-} ligands in Zn(2-methyl hba), as can be seen in **Figure 3.5b**. The aromatic rings of the two types of 2-methyl hba^{2-} ligands in the Zn(2-methyl hba) network tilt out of the plane by 15° and 43°, resulting in half the methyl groups in Zn(2-methyl hba) occupying significant space in the channel. In contrast all the 2,6-dimethyl hba^{2-} ligands in the Zn(2,6-dimethyl hba) network tilt out of the plane by 67°, **Figure 3.6b**. The two methyl groups on 2,6-dimethyl hba^{2-} prevent the aromatic faces on 2,6-dimethyl hba^{2-} aligning parallel with the channel wall, resulting in the methyl groups occupying more space in the channels of Zn(2,6-dimethyl hba) than Zn(2-methyl hba). The void volume in Zn(2-methyl hba) and Zn(2,6-dimethyl hba) were estimated to be 17% and 34% respectively of the unit cell volume. On this basis, and barring significant structural rearrangement, the adsorption capacity of Zn(2,6-dimethyl hba) should be far less than that of Zn(2-methyl hba).

3.4 Materials that do not possess square channels

Attempts to generate derivatives of Zn(hba) with various ligands structurally related to hba^{2-} were not all successful and resulted in either dense networks or discrete complexes. These are discussed in the following sections.

3.4.1 Zn_2(tetrafluoro hba)$(OAc)_2$

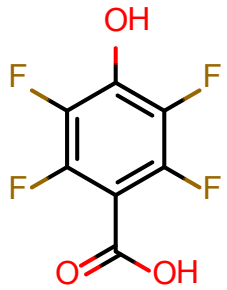

(XXII)

When $Zn(OAc)_2$ is combined with tetrafluoro-4-hydroxybenzoic acid, tetrafluoro H_2hba **(XXII)**, in a hot solution of methanol and pentanol, crystals of composition Zn_2(tetrafluoro hba)$(OAc)_2$ separate upon the removal of methanol. Although acetate was present to act as a base, as was the case in the synthesis of Zn(hba), single crystal x-ray diffraction studies revealed that the acetate was incorporated into the resultant network.

Within Zn_2(tetrafluoro hba)$(OAc)_2$ the Zn^{2+} centres are crystallographically equivalent and adopt a distorted tetrahedral geometry. Zn^{2+} centres are bridged by a carboxylate group from one tetrafluoro ligand and a phenoxy oxygen centre from another, to form a dinuclear unit, as can be seen in **Figure 3.7**. Pairs of acetate ligands complete the coordination environment. The 6-membered ring formed from the phenolate oxygen atom, the tetrafluoro hba^{2-} carboxylate group and two Zn^{2+} centres is a motif that is commonly observed in the M(hba) structures.[1]

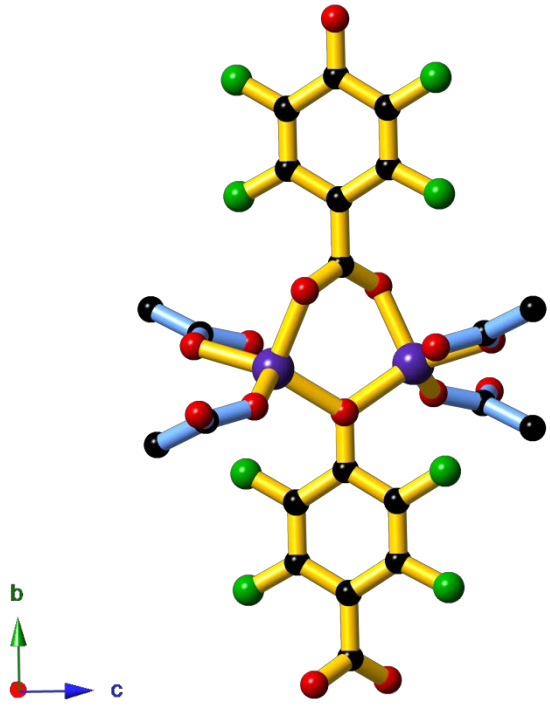

Figure 3.7: A view of the dinuclear unit of Zn(tetrafluoro hba)(OAc). Acetate anions are highlighted with blue bonds. Fluorine atoms are represented in green.

The dinuclear units are linked through the tetrafluoro hba ligands to form $[Zn_2(\text{tetrafluoro hba})]^{2+}$ chains that run parallel to the *b* axis, as indicated in **Figure 3.8**. The chains are linked to parallel chains by bridging acetate ligands to form the two dimensional sheets of $Zn_2(\text{tetrafluoro hba})(OAc)_2$, as can be seen in **Figure 3.9**.

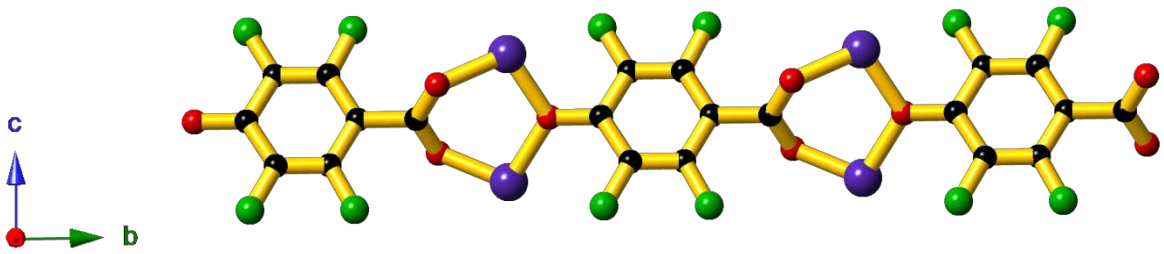

Figure 3.8: A $[Zn_2(\text{tetrafluoro hba})]^{2+}$ chain viewed down the *a*-axis.

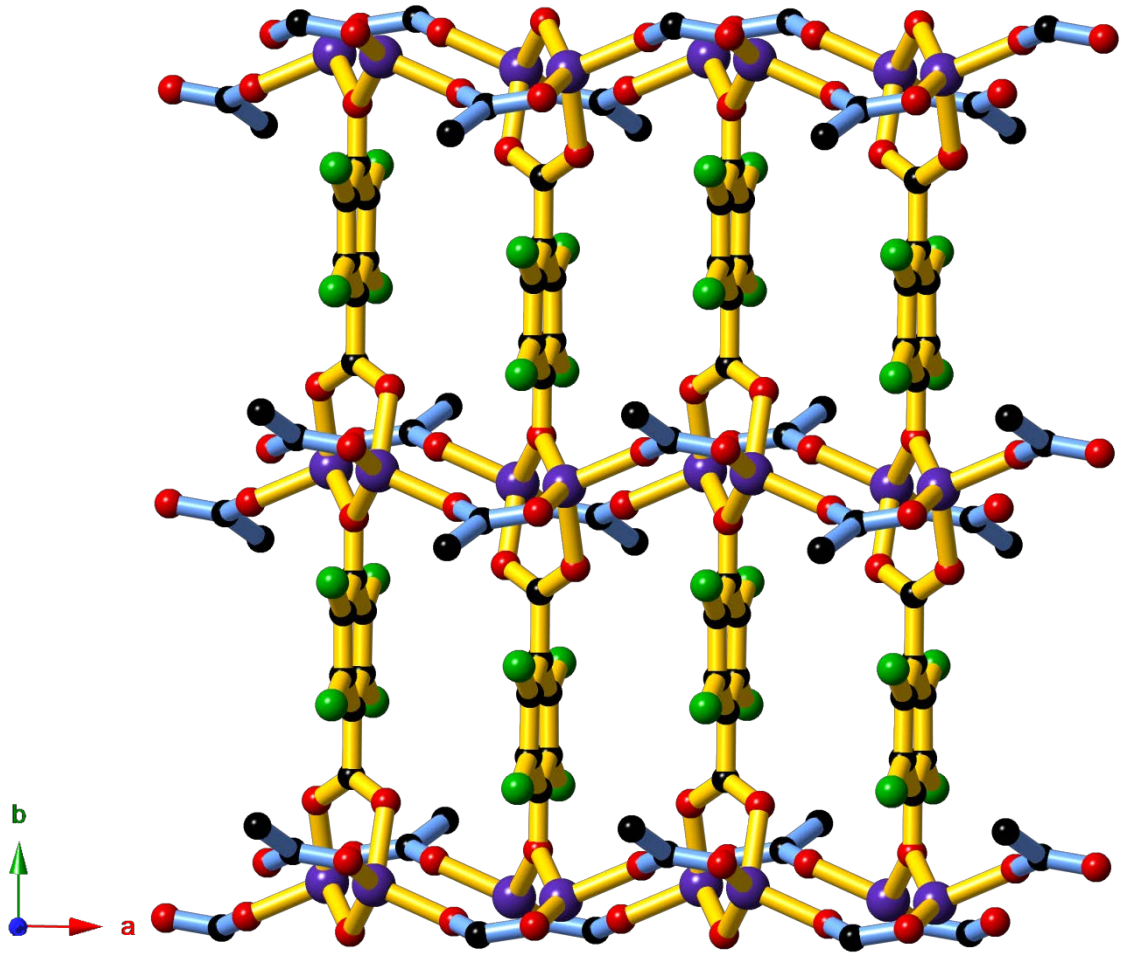

Figure 3.9: A single sheet in Zn_2(tetrafluoro hba)$(OAc)_2$ viewed down the *c*-axis.

The sheets in Zn_2(tetrafluoro hba)$(OAc)_2$ pack in a ABAB fashion parallel to the *c* axis to form a dense structure, as shown in **Figure 3.10**.

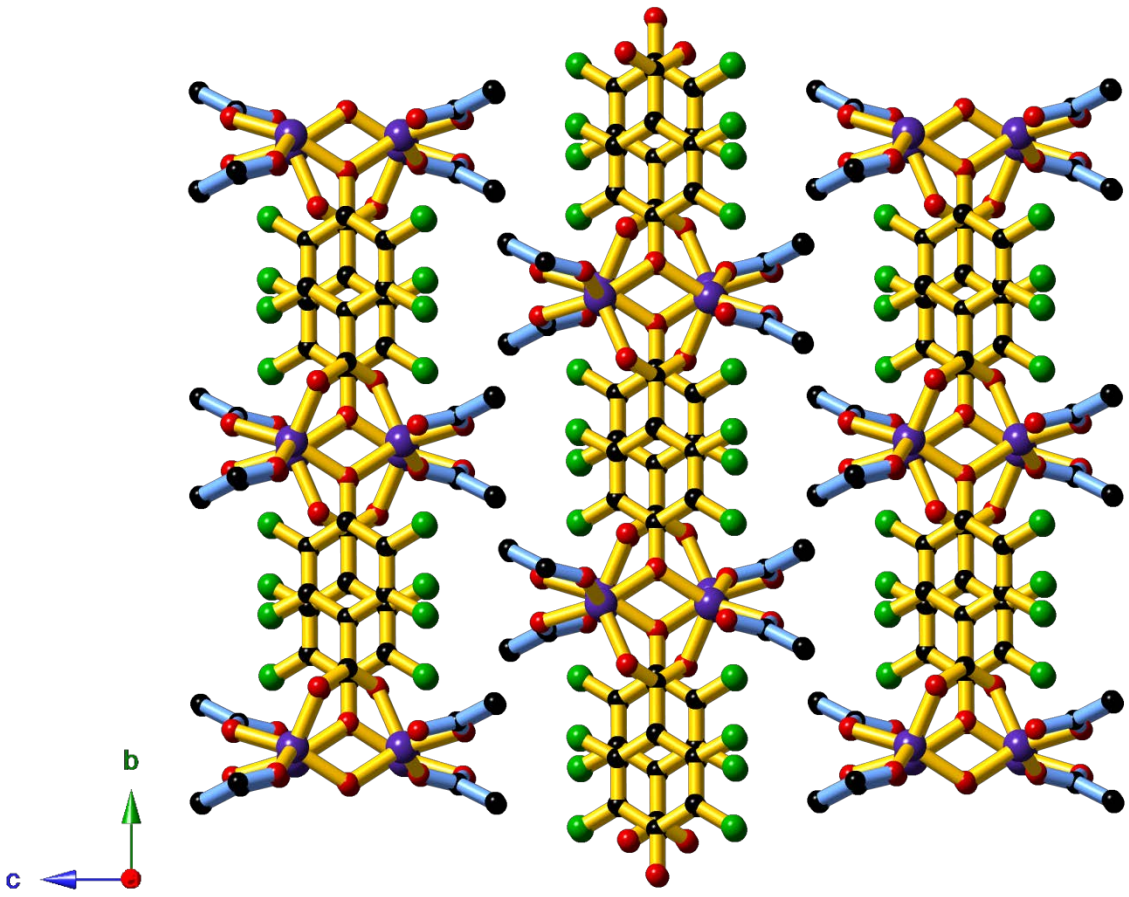

Figure 3.10: An edge on view of the sheets in Zn_2(tetrafluoro hba)$(OAc)_2$ which pack in an ABAB fashion.

Under similar reaction conditions, when $Zn(SiF_6)$ is used, with KOH present as base, a different network is obtained. Single crystal x-ray studies revealed a compound of formula Zn(tetrafluoro hba)(MeOH)·MeOH. The Zn^{2+} centres are all crystallographically equivalent and are coordinated by two ligands through carboxylate oxygen donors and two ligands through phenoxy oxygen atoms (**Figure 3.11**). Completing the coordination environment is a methanol ligand. As can be seen upon inspection of **Figure 3.11**, the

coordination geometry is very close to trigonal bipyramidal (τ_5=0.7525, α=130.42°, β=175.57°).[3]

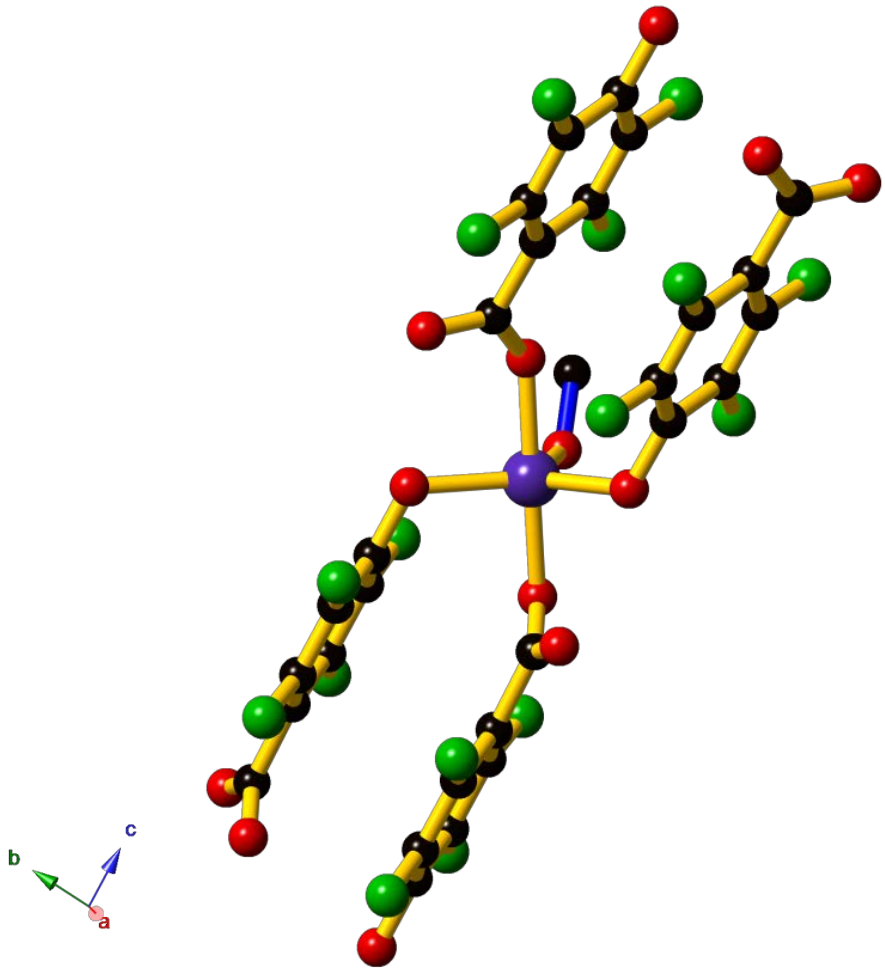

Figure 3.11: A view of the trigonal bipyramid coordination geometry of the Zn^{2+} centres found in Zn(tetrafluoro hba)(MeOH)·MeOH. For clarity hydrogen atoms have been omitted.

The carboxylate groups on the tetrafluoro hba^{2-} ligands are rotated with respect to the plane of the phenyl ring by approximately 25°. The 5-coordinate geometry of the Zn atoms allows adjacent tetrafluoro hba^{2-} ligands in a chain to align in a face-to-face manner with a separation of rings of ~3.2 Å. Zn^{2+} atoms are bridged by a phenoxy oxygen atom of one ligand and a carboxylate group of another tetrafluoro hba^{2-} ligand to

produce Zn-O-C-O-Zn-O chains (**Figure 3.12a**) similar to those observed in Zn(hba) (**Figure 3.12b**). However, in contrast to Zn(hba), these chains are linked by the tetrafluoro hba^{2-} ligands to parallel chains to give a two dimensional sheet, as shown in **Figure 3.13**. It is worth noting that although the chains in Zn(tetrafluoro hba)(MeOH)·MeOH are similar to those found in Zn(hba), the parallel orientation of the tetrafluoro hba ligands results in a 2-D sheet, whereas in Zn(hba) neighbouring ligands are perpendicular to each other yielding a 3-D net.

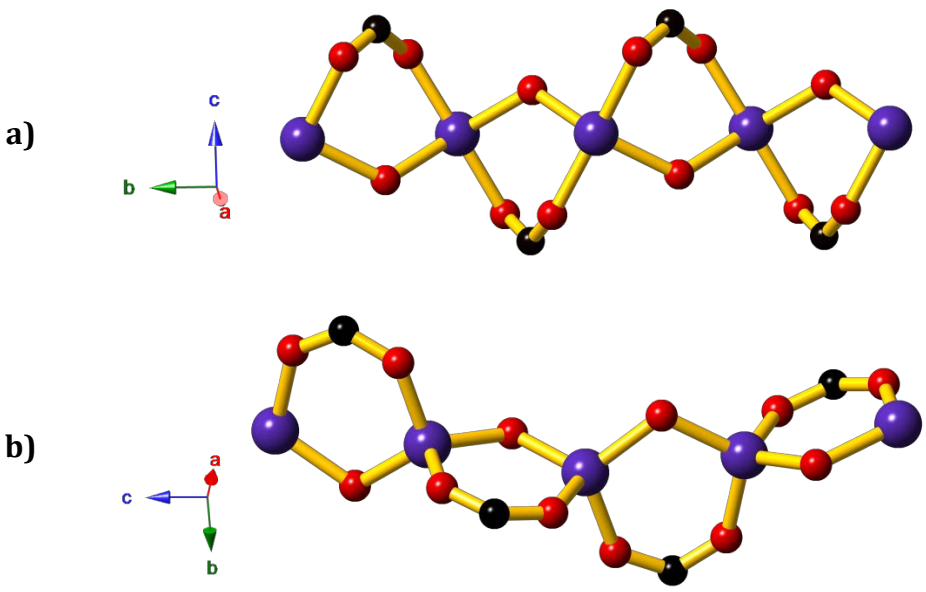

Figure 3.12: A view of the Zn-O-C-O-Zn-O chains in **a)** Zn(tetrafluoro hba)(MeOH) and **b)** Zn(hba)

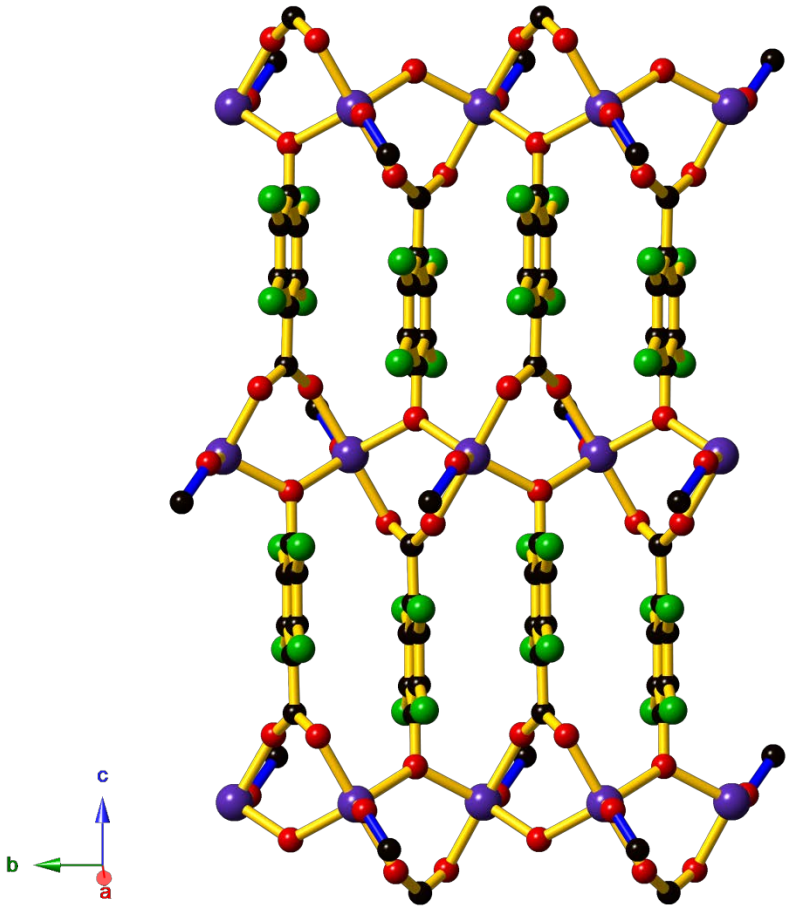

Figure 3.13: A single sheet of Zn(tetrafluoro hba)(MeOH) viewed from a direction slightly off the *a*-axis.

Sheets of Zn(tetrafluoro hba)(MeOH) are linked by hydrogen bonds between coordinated methanol ligands and uncoordinated solvent methanol molecules, (2.67 Å O-H···O distance) that are situated in between the 2-D sheets,(**Figure 3.14**). However, despite numerous attempts a homogenous bulk product of Zn(tetrafluoro hba)(MeOH)·MeOH was unable to be obtained.

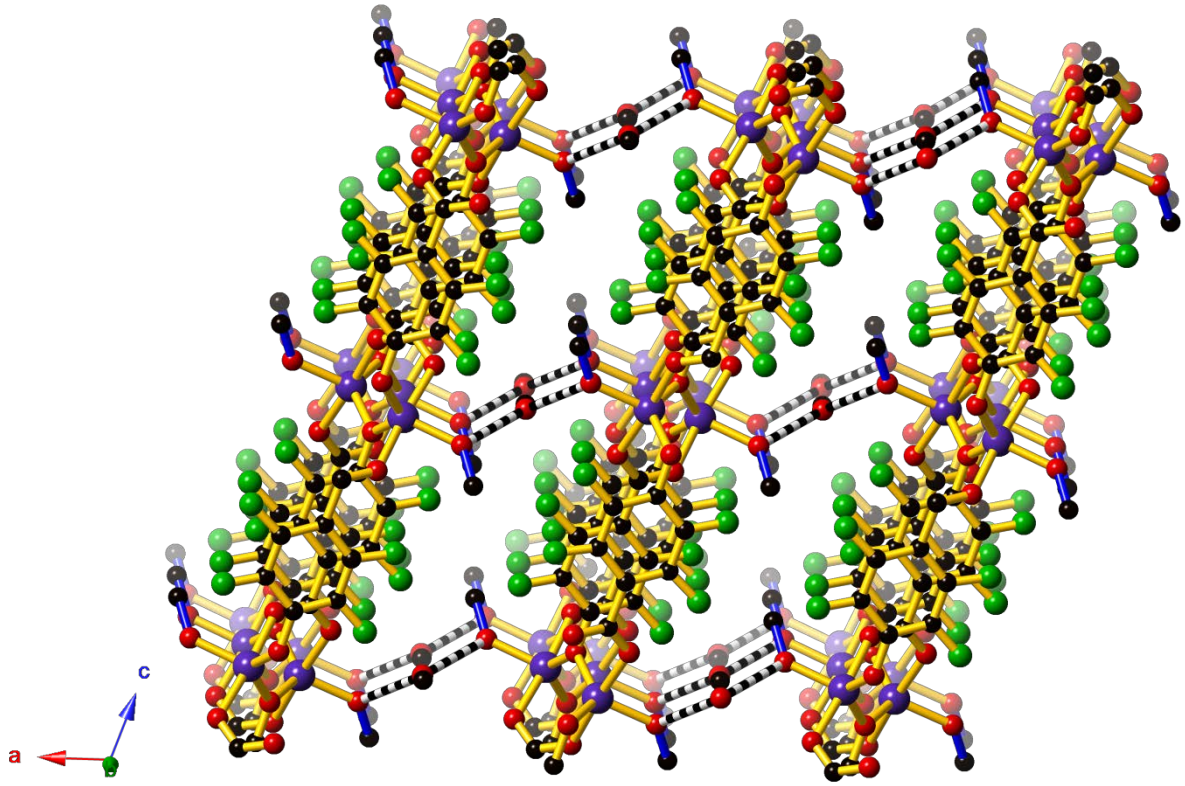

Figure 3.14: The crystal packing in Zn(tetrafluoro hba)(MeOH)·MeOH viewed down the *b*-axis. Solvent methanol molecules between the sheets participate in hydrogen bonding with the coordinated methanol molecules, hydrogen atoms have been omitted for clarity.

The sheets observed in Zn(tetrafluoro hba)(MeOH)·MeOH are similar to those observed in [Zn(tetrafluoro hba)4,4'-bipyridine](4,4'-bipyridine) which was reported by Hulvey *et al.* in 2010. Within [Zn(tetrafluoro hba)4,4'-bipyridine](4,4'-bipyridine), however, instead of terminal methanol molecules, the sheets are linked by bridging 4,4'-bipyridine ligands to give a beautiful 3-D network (**Figure 3.15**).[4]

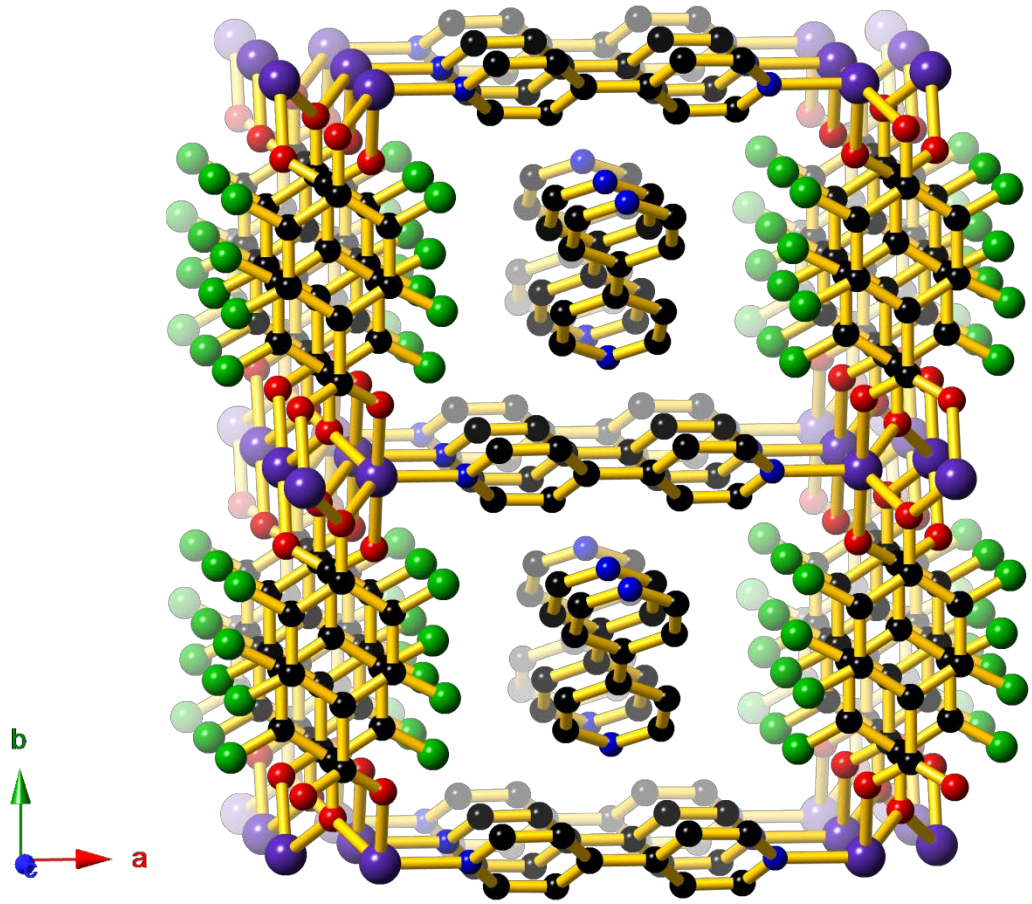

Figure 3.15: Hulvey's [Zn(tetrafluoro hba)4,4'-bipyridine](4,4'-bipyridine) structure depicting the bridging 4,4'-bipyridine molecules and non-coordinating 4,4'-bipyridine molecules within rectangular channels.

3.4.2 Structures with $HhpOa^-$ and $HhpNa^{2-}$

The compounds 4-hydroxyphenoxyacetic acid (H_2hpOa, **VII**) and N-(4-Hydroxyphenyl)glycine (H_2hpHNa, **VIII**) are structurally related to coumaric acid **(XXV)**. Attempts to synthesise PtS-type networks involving the deprotonated forms of these ligands have to-date been unsuccessful. Two crystalline compounds, however, were generated and these are described below.

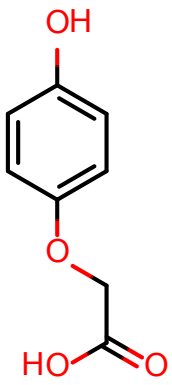

(XXIII)

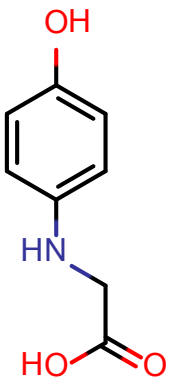

(XXIV)

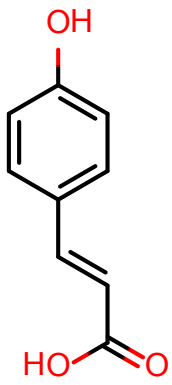

(XXV)

When a methanolic solution of H_2hpOa is diffused into an aqueous solution of $Cu(OAc)_2$ pale blue crystals separate overnight. Single crystal diffraction reveals a discrete mononuclear complex of composition $Cu(HhpOa)_2(H_2O)_2$. Each Cu^{2+} centre lies on a centre of symmetry and is chelated by monoprotonated ligands through the ether and carboxylate oxygen atoms, as can be seen in **Figure 3.16**. Completing the coordination environment are two water molecules occupying the *trans* positions of the Cu^{2+} centre. The aromatic ring of the HhpOa ligand is inclined to the equatorial plane of the metal centre by 17.30°. Non-coordinated water molecules form hydrogen bonds with the discrete complexes.

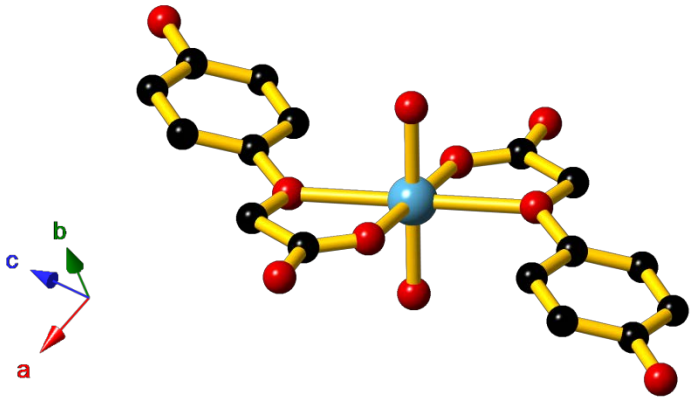

Figure 3.16: A view of $Cu(HhpOa)_2(H_2O)_2$ showing the octahedral coordination environment of the Cu^{2+} centre.

The crystal packing of the complexes is shown in, **Figure 3.17**. Each complex is hydrogen bonded to uncoordinated water molecules leading to a 3-D hydrogen bonded network.

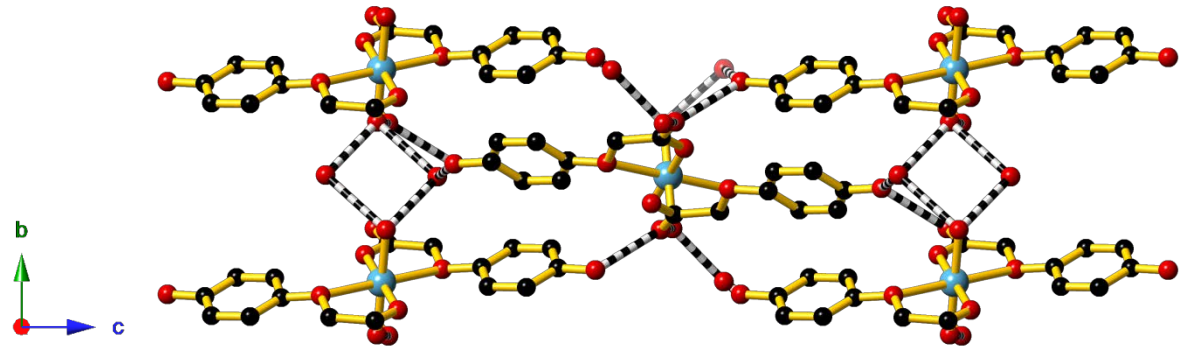

Figure 3.17: A view of $Cu(HhpOa)_2(H_2O)_2$ hydrogen bonding to adjacent $Cu(HhpOa)_2(H_2O)_2$ units to form an extended hydrogen bonded net.

When pentanol is added to a hot methanolic solution of H_2hpHNa and $Zn(OAc)_2$ brown crystals subsequently separate. Crystallographic analysis reveal 1-D chains of composition Zn(HhpHNa), in which only the carboxylate group is deprotonated.

Chains of $Zn(HhpHNa)_2$ comprise binuclear units with two crystallographically unique Zn^{2+} metal centres (A and B) and four unique anionic HhpHNa ligands (C-F), as shown in **Figure 3.18**. Although C and D are crystallographically distinct, they do play a similar structural role. Ligands E and F also play a structural role similar to each other, but different to C and D. The Zn(A) centre adopts an almost trigonal prismatic geometry, chelated by two ligands (C and D) each binding through the carboxylate oxygen atom

and the amine group. The 6-coordinate geometry is completed by two *cis* carboxylate oxygen atoms from two other ligands (E and F) in a *cis* arrangement. The Zn(B) centre which is also 6-coordinate has a distinctly different coordination environment. Zn(B) is an octahedral environment produced by two chelating $HhpHNa^{-}$ ligands which form a square plane with *cis* N donors. The remaining *trans* sites are occupied by carboxylate O atoms from C and D type ligands. The bridging carboxylate groups of ligands C, D, E and F leads to the generation of a double chain that is represented in **Figure 3.19**.

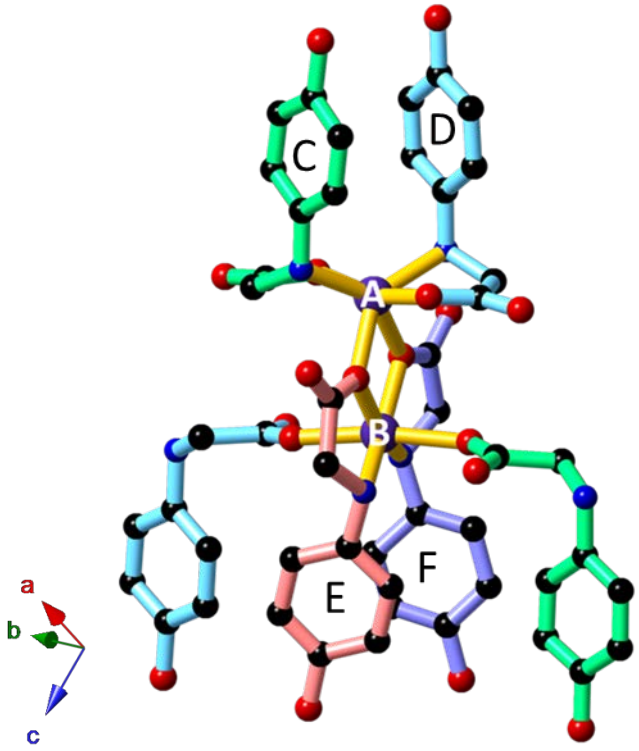

Figure 3.18: Zn^{2+} binuclear unit comprises of two unique Zn^{2+} centres (A and B) and four unique ligands (C green, D blue, E pink and F purple).

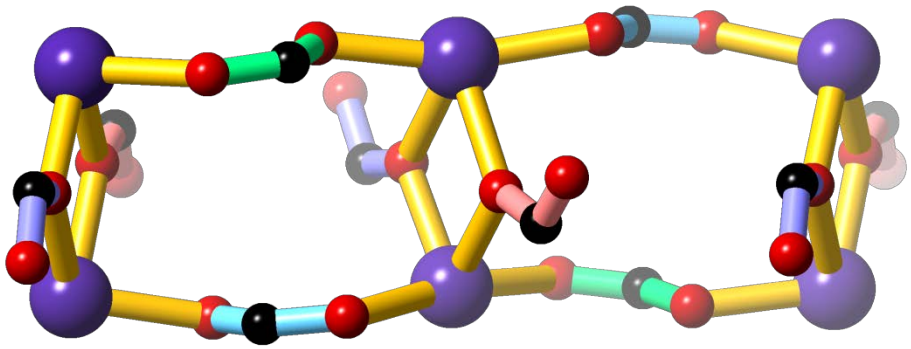

a)

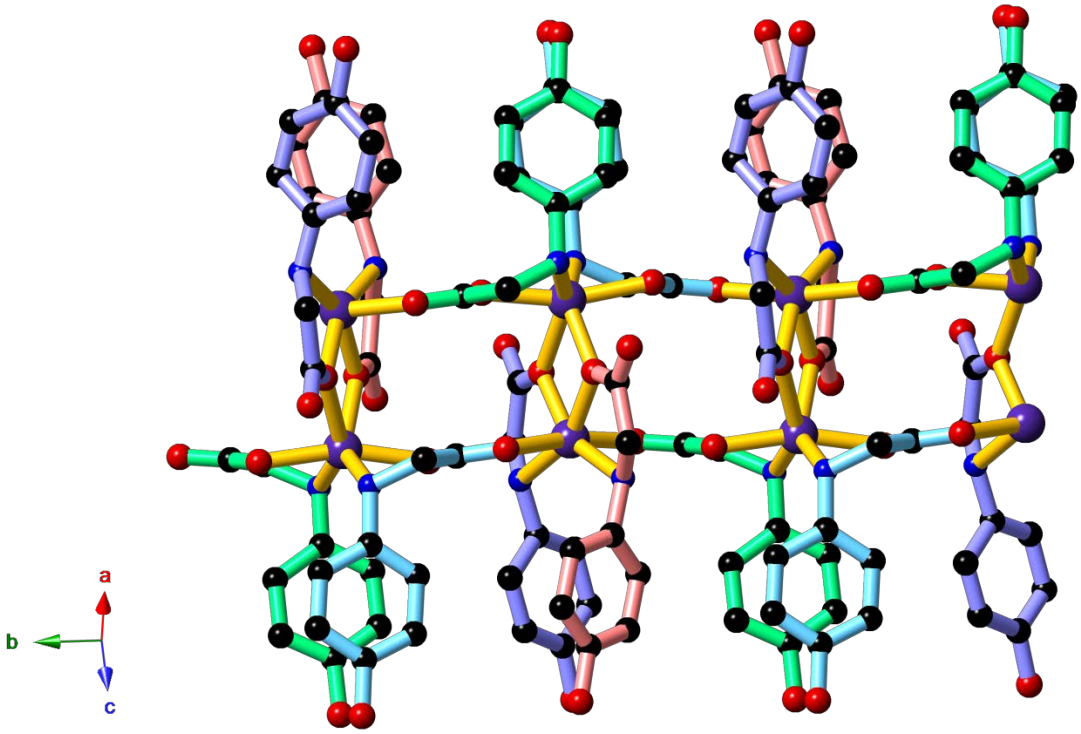

b)

Figure 3.19: a) A view showing binuclear Zn^{2+} units linked by bridging carboxylate groups of ligands C and D. For clarity only the Zn^{2+} and carboxylate groups are shown. **b)** A single Zn(HhpHNa) chain viewed perpendicular to the *b*-axis. Hydrogen atoms omitted for clarity.

Each chain interacts with neighbouring chains through hydrogen bonding between the phenol groups and carboxylate groups to give a 3-D hyrogen bonded network as shown in **Figure 3.20**.

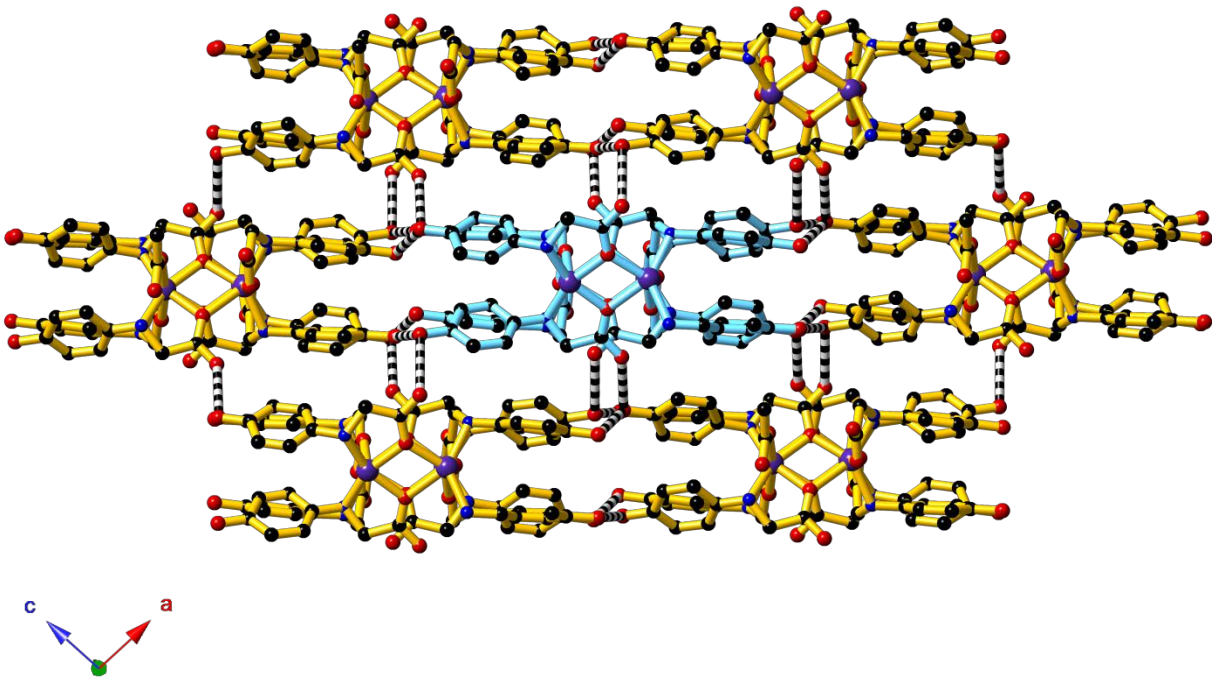

Figure 3.20: The crystal packing of Zn(HhpHNa) viewed down the *b*-axis. The chains run parallel to the *b* axis. For clarity the central chain is indicted with blue bonds. Hydrogen bonds are shown as black and white banded bonds.

3.5 Concluding remarks

PtS-like frameworks have been successfully generated employing a number of new ligands. Although single crystal diffraction data quality was inherently poor due to extensive twinning and disorder, the frameworks were unambiguously confirmed through powder diffraction studies. The compounds Zn(2-chloro hba), Zn(2-methyl hba), Zn(2,6-dimethyl hba), Zn(2-fluoro hba) and Zn(3-fluoro hba) were confirmed to be isostructural with Zn(hba).

Computational simulations were undertaken to predict the lowest energy conformation of both the Zn(2-methyl hba) and Zn(2,6-dimethyl hba) which provided useful insights into the potential locations of the substituents in the Zn(hba) family of compounds.

Attempts to generate the PtS-like framework with the ligand tetrafluoro hba^{2-} resulted in two distinctly different frameworks, Zn(tetrafluoro hba)(MeOH)·MeOH and Zn_2(tetrafluoro hba)($OAc)_2$. The use of $Zn(OAc)_2$ results in the incorporation of acetate into the resultant framework. When the anion SiF_6^{2-} is used in place of acetate, an entirely different network is formed in which coordinated MeOH ligands are present.

It is noted that both structures involving tetrafluoro hba^{2-} involve face-to-face arrangements of the ligand suggesting that a preference for this π – π association contributes to the failure to form a Zn(hba)-type network. The face-to-face arrangement is also apparent in Hulvey's [Zn(tetrafluoro hba)4,4'-bipyridine](4,4'-bipyridine) structure.

Attempts to synthesise PtS-type framework s with ligands related to cma^{2-}, i.e. $HhpOa^-$ and $HhpHNa^-$, proved unsuccessful. It is perhaps unsurprising that the targeted networks were not formed, as the ligands employed were able to chelate to metal centres, which is thermodynamically favoured due to the stabilising chelate effect. The $HhpOa^-$ ligand formed a relatively simple mononuclear complex with Cu^{2+}. The complexes were involved in extensive hydrogen bonding resulting in a 3D hydrogen

bonded network. The combination of $HhpHNa^-$ ligands with Zn^{2+} results in binuclear Zn units which are bridged to form 1D chains. These chains are linked through phenol-phenol and phenol-carboxylate hydrogen bonds to give a 3-D hydrogen bonded network. There were no channels or significant voids in each case, hence no investigations of the host properties were performed. Future work involving the protection of the amine group before the subsequent reaction with Zn^{2+} may result in the desired network. Subsequent de-protection of the amine may lead to the generation of Zn(hba)-type networks that possess uncoordinated amine sites.

3.6 Experimental

3.6.1 Synthesis of Zn(2-fluoro hba)

2-fluoro H_2hba (62.2 mg, 0.398 mmol) and $Zn(OAc)_2{\cdot}2H_2O$ (87.8 mg, 0.400 mmol) were dissolved in hot methanol (20ml) and *n*-pentanol (20ml). The temperature was monitored to ensure that the solution was heated without boiling. With continued heating the more volatile methanol was lost from the reaction mixture. The removal of nearly all of the MeOH (monitored by a significant reduction in the volume of the solution) allowed the separation of colourless needle-like crystals. Yield 59.2 mg. Infrared Spectrum (KBr disc): 3425(b), 1619(s), 1403(s), 1319(m), 1274(m), 1161(m), 1104(m) cm^{-1}, (as shown in **Figure A.75** in the Appendix). Elemental analysis calc'd (%) Zn(2-fluoro hba)·0.4H_2O·0.4PentOH: C 41.26, H 3.32, N 0.0; found (%): C 41.3, H 3.36, N 0.0

3.6.2 Synthesis of Zn(3-fluoro hba)

3-fluoro H_2hba (65.3 mg, 0.418 mmol) and $Zn(OAc)_2 \cdot 2H_2O$ (92.2 mg, 0.420 mmol) were dissolved in hot MeOH (20ml). PentOH (20ml) was added to the hot solution. As with Zn(2-fluoro hba), the temperature was monitored to ensure that the solution was heated without boiling. With continued heating the more volatile methanol was lost from the reaction mixture. Upon removal of nearly all of the MeOH colourless needle-like crystals separated from the solution. Yield 64.2 mg. Infrared Spectrum (KBr disc): 3610(m), 3525(m), 1696(m), 1576(s), 1538(m), 1406(s), 1290(s), 1199(s), 1131(w) cm^{-1}, (as shown in **Figure A.76** in the Appendix). Elemental analysis calc'd (%) for Zn(3-fluoro hba): C 38.30, H 1.38, N 0.0; found (%): C 38.37, H 1.75, N 0.0

3.6.3 Synthesis of Zn(2-chloro hba)

A hot methanol solution (20 ml) of 2-chloro H_2hba (100 mg, 0.580 mmol) and $Zn(OAc)_2 \cdot 2H_2O$ (128 mg, 0.583 mmol) was prepared and *n*-pentanol (20ml) was added to the hot solution. The solution was heated without boiling, to slowly remove methanol. A red-brown precipitate formed in solution as the mixture was heated. Periodic swirling of the reaction vessel was required to keep the material dissolved. The removal of nearly all of the methanol allowed the separation of an orange micro crystalline material was formed at the bottom of the reaction vessel. Yield 50.5 mg. Infrared Spectrum (KBr disc): 3424(b), 1591(s), 1406(s), 1289(s), 1230(m), 1162(m), (w)1040 cm^{-1}, (as shown in **Figure A.77** in the Appendix). Elemental analysis calc'd (%) for Zn(2-chloro hba)$\cdot 1.4H_2O \cdot$0.8PentOH: C 38.3, H 2.7, N 0.0; found (%): C 37.9, H 2.7, N 0.0

3.6.4 Synthesis of Zn(2-methyl hba)

N-pentanol (10 ml) was added to a hot methanol solution (5 ml) of 2-methyl H_2hba (160 mg, 1.05 mmol) and $Zn(OAc)_2 \cdot 2H_2O$ (230 mg, 1.05 mmol). Heating of the solution was continued until the more volatile methanol was lost from the reaction mixture. Upon removal of nearly all of the methanol colourless needle-like crystals separated from the solution. Yield 124 mg. Infrared Spectrum (KBr disc): 3439(b), 1604(s), 1574(s), 1520(s), 1424(s), 1387(s), 1278(w), 1246(s), 1174(m), 1099(w), 1015(w) cm^{-1}, (as shown in **Figure A.78** in the Appendix). Elemental analysis calc'd (%) for Zn(2-methyl hba)$\cdot 3H_2O$: C 43.45, H 2.72, N 0.0; found (%): C 43.42, H 2.77, N 0.0

3.6.5 Synthesis of Zn(2,6-dimethyl hba)

2,6-dimethyl H_2hba (70 mg, 0.421 mmol) and $Zn(OAc)_2 \cdot 2H_2O$ (92.4 mg, 0.421 mmol) were dissolved in hot methanol (20ml). *N*-pentanol (20ml) was added to the hot solution. The temperature was monitored to ensure that the solution was heated without boiling. With continued heating the more volatile methanol was lost from the reaction mixture. The removal of nearly all of the MeOH resulted in colourless needle-like crystals separating from the solution. Yield 77 mg. Infrared Spectrum (KBr disc): 3440(b), 1598(m), 1527(m), 1445(m), 1385(m), 1304(w), 1169(w), 1125(w), 1035(w) cm^{-1}, (as shown in **Figure A.79** in the Appendix). Elemental analysis calc'd (%) for Zn(2,6-dimethyl hba): C 47.08, H 3.52, N 0.0; found (%): C 47.15, H 3.67, N 0.0

3.6.6 Synthesis of Zn_2(tetrafluoro hba)$(OAc)_2$

Tetrafluoro H_2hba (100 mg, 0.476 mmol) and $Zn(OAc)_2 \cdot 2H_2O$ (104 mg, 0.476 mmol) were dissolved in hot methanol (20ml) and *n*-pentanol (20ml). The temperature was monitored to ensure that the solution was heated without boiling. With continued heating the more volatile methanol was lost from the reaction mixture. Upon removal of nearly all of the methanol colourless needle-like crystals separated from the solution. Yield 107 mg. Powder diffraction was used to confirm the purity of the bulk product (below). Infrared Spectrum (KBr disc):3440(b), 2927(w), 1620(s), 1543(m), 1512(m), 1403(s), 1281(w), 1134(m) cm^{-1}, (as shown in **Figure A.80** in the Appendix).

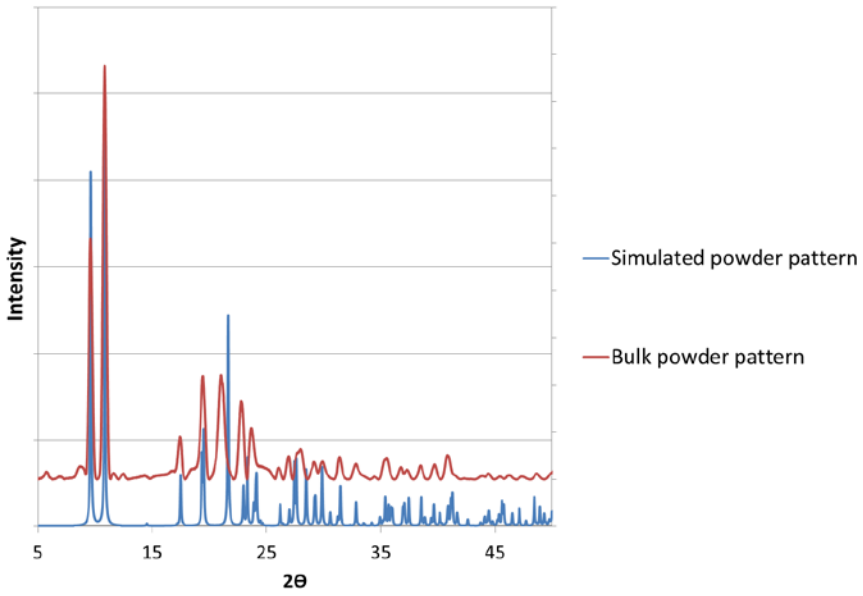

Figure 3.21: The x-ray powder diffraction pattern of the bulk sample of Zn_2(tetrafluoro hba)$(OAc)_2$ compared to a x-ray powder diffraction pattern simulated from the crystal structure of Zn_2(tetrafluoro hba)$(OAc)_2$.

3.6.7 Synthesis of Zn(tetrafluoro hba)(MeOH)·MeOH

2,6-Dimethyl H_2hba (100 mg, 0.476 mmol) and $Zn(SiF_6) \cdot 2H_2O$ (150 mg, 0.476 mmol) were dissolved in hot MeOH (20ml). PentOH (20ml) was added to the hot solution,

followed by KOH (54 mg, 0.952 mmol). Colourless crystals instantly precipitated from the solution. Despite numerous attempts a homogenous bulk product was unable to be obtained.

3.6.8 Synthesis of $Cu(HhpOa)_2(H_2O)_2$

A methanolic solution (1ml) of H_2hpOa (11.5 mg, 0.0684 mmol) was slowly diffused into a aqueous solution (1ml) of $Cu(OAc)_2{\cdot}H_2O$ (13.6 mg, 0.0684 mmol). Light blue rod-like crystals separated from the solution overnight. Yield 2 mg. Powder diffraction data was collected to confirm the purity of the bulk product (below). Infrared Spectrum (KBr disc): 3488(w), 3412(w), 3198(b), 1589()s, 1512(s), 1454(m), 1422(s), 1342(m), 1221(s), 1112(w), 1058(m) cm^{-1}, (as shown in **Figure A.81** in the Appendix).

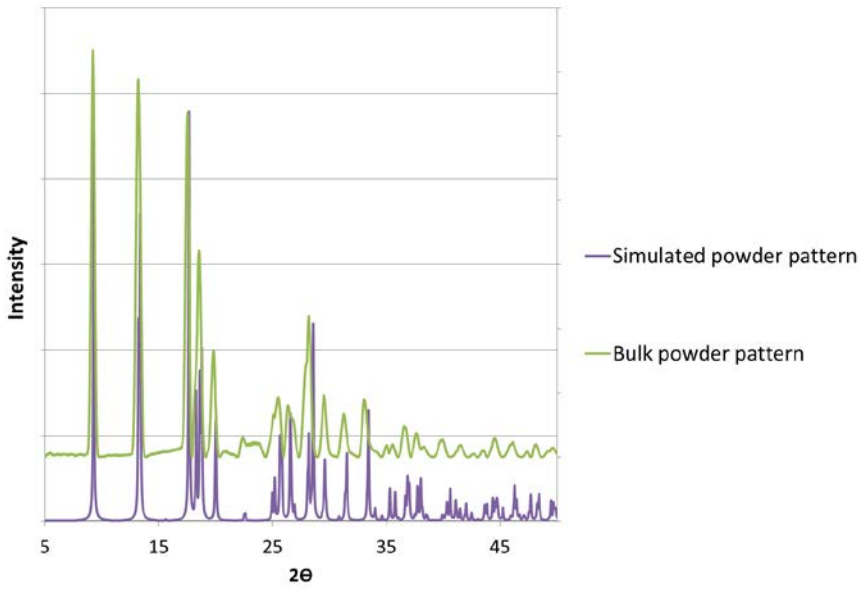

Figure 3.22: The x-ray powder diffraction pattern of the bulk sample of $Cu(HhpOa)_2(H_2O)_2$ compared to a x-ray powder diffraction pattern simulated from the crystal structure of $Cu(HhpOa)_2(H_2O)_2$.

3.6.9 Synthesis of Zn(HhpHNa)

H_2hpHNa (100 mg, 0.598 mmol) and $Cu(OAc)_2 \cdot H_2O$ (120mg, 0.600 mmol) were dissolved in hot methanol (20ml). *N*-pentanol (20ml) was added to the hot solution. The temperature was monitored to ensure that the solution was heated without boiling. With continued heating the more volatile methanol was lost from the reaction mixture. The removal of nearly all of the MeOH resulted in the separation of brown needle-like crystals. Yield 90 mg. Powder diffraction data was collected to confirm the purity of the bulk product (below). Infrared Spectrum (KBr disc): 3422(b), 2925(w), 1599(s), 1516(s), 1398(m), 1290(m), 1122(w) cm^{-1}, (as shown in **Figure A.82** in the Appendix).

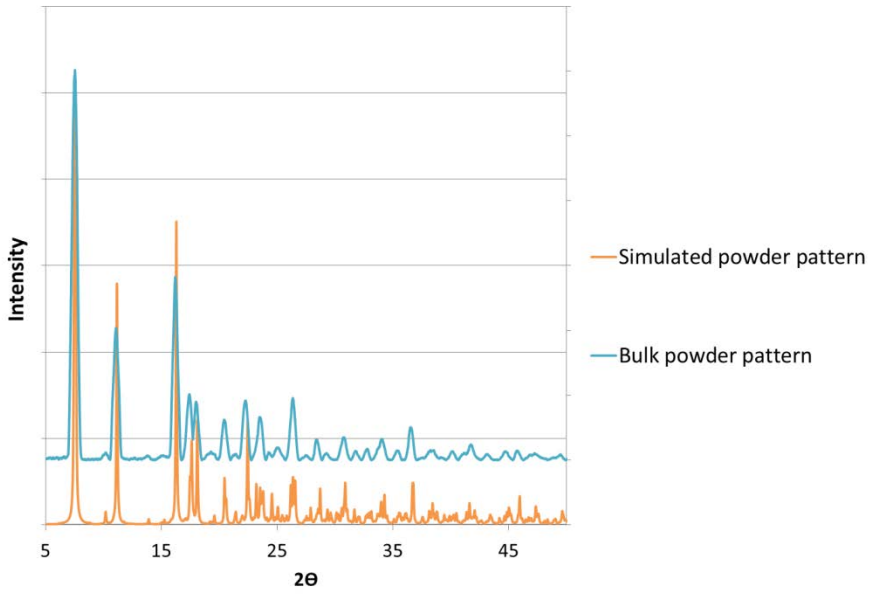

Figure 3.23: The x-ray powder diffraction pattern of the bulk sample of Zn(HhpHNa)compared to a x-ray powder diffraction pattern simulated from the crystal structure of Zn(HhpHNa).

3.7 Details of structure determination

X-ray powder diffraction data for Zn(2-chloro hba), Zn(2-methyl hba), Zn(2,6-dimethyl hba), Zn(2-fluoro hba) and Zn(3-fluoro hba) were collected on the PD beamline at the Australian Synchrotron, the details of which are described in chapter 7.

X-ray powder diffraction data for Zn_2(tetrafluoro hba)$(OAc)_2$, $Cu(HhpOa)_2(H_2O)_2$ and Zn(HhpHNa) were collected on a Rigaku Oxford Diffraction Synergy-S diffractometer equipped with CuKα monochromated X-ray radiation, the details of which are described in chapter 7.

Single crystal X-ray diffraction techniques were performed on Zn_2(tetrafluoro hba)$(OAc)_2$, Zn(tetrafluoro hba)(MeOH)·MeOH, $Cu(HhpOa)_2(H_2O)_2$ and Zn(HhpHNa) on an Oxford diffraction SuperNova equipped with CuKα X-ray radiation, using the general techniques described in chapter 7.

3.7.1 Zn_2(tetrafluoro hba)$(OAc)_2$

X-ray data was collected on a colourless needle like crystal of Zn_2(tetrafluoro hba)$(OAc)_2$. Elucidation of the data revealed the crystal possessed monoclinic symmetry in the space group $I2/a$ (a non-standard setting of $C2/c$). All non-hydrogen framework atoms were clearly defined and refined with anisotropic displacement parameters. All hydrogen framework atoms were placed in geometrically estimated positions. The crystallographic data table is shown in **Table 3-2**.

3.7.2 Zn(tetrafluoro hba)(MeOH)·MeOH

X-ray data were collected on a colourless needle-like crystal of Zn(tetrafluoro hba)(MeOH)·MeOH. Elucidation of the data revealed the crystal possessed monoclinic symmetry and a satisfactory solution was obtained in the space group $C2/c$. All non-hydrogen framework atoms were clearly defined and refined with anisotropic displacement parameters. All hydrogen framework atoms were placed in geometrically estimated positions. The crystallographic data table is shown in **Table 3-3**.

3.7.3 $Cu(HhpOa)_2(H_2O)_2$

X-ray data was collected on a light blue transparent rod like crystal of $Cu(HhpOa)_2(H_2O)_2$. Elucidation of the data revealed the crystal possessed monoclinic symmetry in the space group $P2_1/n$. All non-hydrogen framework atoms were clearly defined and refined with anisotropic displacement parameters. All hydrogen framework atoms were placed in geometrically estimated positions. The crystallographic data table is shown in **Table 3-4**.

3.7.4 Zn(HhpHNa)

X-ray data was collected on a light blue transparent rod like crystal of Zn(HhpHNa). Elucidation of the data revealed the crystal possessed monoclinic symmetry in the space group $P2_1/n$. All non-hydrogen framework atoms were clearly defined and refined with anisotropic displacement parameters. SIMU and RIGU cards were used for C15 and C16. All hydrogen framework atoms were placed in geometrically estimated positions. The crystallographic data table is shown in **Table 3-5**.

3.8 Crystallographic data tables

3.8.1 Zn_2(tetrafluoro hba)$(OAc)_2$

Table 3-2: Crystallographic data table of Zn_2(tetrafluoro hba)$(OAc)_2$.

Empirical formula	$C_{11}H_6F_4O_7Zn_2$
Formula weight	456.90
Temperature/K	130.0(1)
Crystal system	monoclinic
Space group	$I2/a$
a/Å	8.2166(3)
b/Å	9.0885(2)
c/Å	18.3399(7)
β/°	92.565(3)
Volume/Å^3	1368.19(8)
Z	4
ρ_{calc}g /cm^3	2.218
μ /mm^{-1}	5.173
F(000)	896.0
Crystal size/mm^3	0.182 × 0.041 × 0.037
λ (CuKα)	1.54184
2Θ range for data collection/°	9.65 to 149.02
Index ranges	-4 ≤ h ≤ 9, -10 ≤ k ≤ 11, -22 ≤ l ≤ 22
Reflections collected	2431
Independent reflections	1343 [R_{int} = 0.0285, R_{sigma} = 0.0286]
Data/restraints/parameters	1343/0/112
Goodness-of-fit on F^2	1.073
Final R indexes [I>=2σ (I)]	R_1 = 0.0402, wR_2 = 0.1077
Final R indexes [all data]	R_1 = 0.0432, wR_2 = 0.1131
Largest diff. peak/hole / e Å^{-3}	1.37/-0.99

3.8.2 Zn(tetrafluoro hba)(MeOH)·MeOH

Table 3-3: Crystallographic data table of Zn(tetrafluoro hba)(MeOH)·MeOH

Empirical formula	$C_{17}H_{12}F_8O_9Zn_2$
Formula weight	643.01
Temperature/K	130.0(1)
Crystal system	monoclinic
Space group	$C2/c$
a/Å	18.4395(13)
b/Å	6.4258(4)
c/Å	17.9899(10)
β/°	108.398(7)
Volume/Å^3	2022.6(2)
Z	4
ρ_{calc}g /cm^3	2.112
μ /mm^{-1}	4.121
F(000)	1272.0
Crystal size/mm^3	0.103 × 0.04 × 0.016
λ (CuKα)	CuKα (λ = 1.54184)
2Θ range for data collection/°	10.11 to 149.00
Index ranges	-21 ≤ h ≤ 22, -7 ≤ k ≤ 7, -21 ≤ l ≤ 22
Reflections collected	6531
Independent reflections	2019 [R_{int} = 0.0645, R_{sigma} = 0.0595]
Data/restraints/parameters	2019/0/169
Goodness-of-fit on F^2	1.041
Final R indexes [I>=2σ (I)]	R_1 = 0.0550, wR_2 = 0.1478
Final R indexes [all data]	R_1 = 0.0659, wR_2 = 0.1638
Largest diff. peak/hole / e Å^{-3}	0.95/-0.94

3.8.3 $Cu(HhpOa)_2(H_2O)_2$

Table 3-4: Crystallographic data table of $Cu(HhpOa)_2(H_2O)_2$

Empirical formula	$C_{16}H_{22}CuO_{12}$
Formula weight	469.87
Temperature/K	130.0(1)
Crystal system	monoclinic
Space group	$P2_1/n$
a/Å	7.1067(3)
b/Å	7.0650(3)
c/Å	19.0913(7)
β/°	90.077(3)
Volume/Å^3	958.55(7)
Z	2
ρ_{calc}g /cm^3	1.628
μ /mm^{-1}	2.206
F(000)	486.0
Crystal size/mm^3	0.289 × 0.096 × 0.073
λ (CuKα)	CuKα (λ = 1.54184)
2Θ range for data collection/°	9.26 to 149.1
Index ranges	$-8 \leq h \leq 8$, $-8 \leq k \leq 8$, $-23 \leq l \leq 10$
Reflections collected	5779
Independent reflections	1905 [R_{int} = 0.0582, R_{sigma} = 0.0460]
Data/restraints/parameters	1905/0/149
Goodness-of-fit on F^2	1.073
Final R indexes [I>=2σ (I)]	R_1 = 0.0451, wR_2 = 0.1274
Final R indexes [all data]	R_1 = 0.0491, wR_2 = 0.1337
Largest diff. peak/hole / e Å^{-3}	0.82/-0.82

3.8.4 Zn(HhpHNa)

Table 3-5: Crystallographic data table of Zn(HhpHNa)

Empirical formula	$C_{32}H_{32}N_4O_{12}Zn_2$
Formula weight	795.35
Temperature/K	130.0(1)
Crystal system	monoclinic
Space group	$P2_1/c$
a/Å	11.8453(8)
b/Å	11.1826(9)
c/Å	23.2918(16)
β/°	95.198(7)
Volume/Å^3	3072.6(4)
Z	4
ρ_{calc}g /cm^3	1.719
μ /mm^{-1}	2.580
F(000)	1632.0
Crystal size/mm^3	0.145 × 0.035 × 0.033
λ (CuKα)	1.54184
2Θ range for data collection/°	7.49 to 135.00
Index ranges	-11 ≤ h ≤ 14, -13 ≤ k ≤ 11, -27 ≤ l ≤ 24
Reflections collected	11793
Independent reflections	5539 [R_{int} = 0.0554, R_{sigma} = 0.0671]
Data/restraints/parameters	5539/9/451
Goodness-of-fit on F^2	0.970
Final R indexes [I>=2σ (I)]	R_1 = 0.0468, wR_2 = 0.1104
Final R indexes [all data]	R_1 = 0.0773, wR_2 = 0.1228
Largest diff. peak/hole / e Å^{-3}	0.94/-0.51

3.9 References

[1] K. F. White, B. F. Abrahams, R. Babarao, A. D. Dharma, T. A. Hudson, H. E. Maynard-Casely, R. Robson, *Chem. - A Eur. J.* **2015**, *21*, 18057–18061.

[2] P. M. de Wolff, *J. Appl. Crystallogr.* **1968**, *1*, 108–113.

[3] A. W. Addison, T. N. Rao, J. Reedijk, J. van Rijn, G. C. Verschoor, *J. Chem. Soc., Dalt. Trans.* **1984**, *876*, 1349–1356.

[4] Z. Hulvey, B. C. Melot, A. K. Cheetham, *Inorg. Chem.* **2010**, *49*, 4594–4598.

Chapter 4 Table of Contents

Chapter 4 – Gas Sorption

4.1 Introduction

Considerable effort has been devoted to the investigation of the uptake of gases by porous coordination polymers (including MOFs). In many of these systems the void spaces are accessed from intersecting channels running in two or more directions, such as HKUST, MOF-5, MOF-177 and UiO-66.[1–3] The structure determinations of Zn(hba) and its analogues presented in Chapter 3 indicate the presence of framework voids that form parallel and non-intersecting channels. The dimensions and properties of the isolated channels are determined by the dianion employed in its synthesis. Materials containing parallel, non-intersecting channels may be expected to possess different adsorption properties owing to the fact that guest molecules are constrained in two out of three dimensions. Furthermore, the presence of isolated channels provides increased opportunities for guest molecules to simultaneously interact with multiple channel surfaces, which may lead to increased affinity with the network surfaces. Whilst coordination polymers that possess isolated parallel channels such as IRMOF-74 and the Li(inic) structures described in the introduction are known, there are fewer examples of this type of adsorbent metal-ligand framework. Investigation of the Zn(hba) family of compounds provides a further opportunity to examine the uptake of guests within isolated channels that have a square, or an approximate square, cross-section. Given the variety of structures that exist within the Zn(hba) family of frameworks, there is the opportunity to thoroughly investigate how the choice of ligand impacts upon the adsorption properties of the resulting framework material.

In this chapter the gas adsorption properties of Zn(hba), Zn(cma), Zn(hbpc), Zn(2-chloro hba), Zn(2-methyl hba), Zn(2,6-dimethyl hba), Zn(2-fluoro hba) and Zn(3-fluoro hba) are described. It is anticipated that network materials with channels of large cross-sectional area, such as Zn(cma) and Zn(hbpc), will allow for greater quantities of guest uptake and therefore such materials are of interest where the capture or storage of large quantities of gases is required. In contrast, Zn(hba)-type networks that contain bridging ligands with sterically active ring substituents, such as 2-chloro hba^{2-}, 2-methyl hba^{2-}, 2,6-dimethyl hba^{2-}, 2-fluoro hba^{2-} and 3-fluoro hba^{2-} may have narrowed pore apertures which would be expected to lead to lower quantities of guest uptake. The inclusion of electron withdrawing substituents could also enhance the uptake of certain guests, due to favourable electrostatic interactions. Network materials with channel dimensions similar to that of the guest molecule of interest offer the prospect of enhancing interactions between guest molecule and network surfaces as this offers the opportunity for the guest to interact with multiple host surfaces at once. Adsorbent materials with narrow pore dimensions may exclude the uptake of some gaseous molecules based on their size.[4]

The carbon dioxide (CO_2), hydrogen (H_2) and methane (CH_4) uptake properties of the 'square channel materials' will be presented and discussed. Interest in the adsorption of CO_2 extends to the capture of anthropogenic emissions as well as its separation from other gas mixtures. The development of materials for the storage of H_2 and CH_4 is also of interest. H_2 and CH_4 have advantages as energy sources for mobile applications. However, technologies that allow for both safe and convenient on-board storage of H_2 and CH_4 are yet to be realised. The development of vessels containing porous materials

may permit the storage of these fuels under moderate temperatures and pressures. The limiting factor for the use of methane in on-board applications is the lower energy density of the gas compared to traditional fossil fuels. As such, significant efforts have been put into increasing the storage density of the gas for mobile application. In 2012 the United States Department of Energy (DOE) released a volumetric storage capacity target of 263 cm^3(STP)/cm^3 at room temperature and 65 bar, which is the equivalent storage to that of a compressed natural gas tank at 250 bar. The DOE has set an additional CH_4 gravimetric storage target of 500 mg/g.[2]

In addition to the adsorption behaviour of CO_2, H_2 and CH_4, the uptake behaviour of N_2, which is commonly used to determine porosity, will also be described. A particular focus of the work is to investigate the differences in adsorption properties in networks with related connectivity but with different pore structure. As the uptake behaviour of guest molecules depends upon the size and shape of the pores for the host network, comparisons within a family of network materials may shed light on tuning the pore environment to maximise guest affinity. When considering size, it is common to consider the kinetic diameters of the guest molecule. The kinetic diameters for N_2, H_2, CH_4 and CO_2 are presented in **Table 4-1**.[5]

Table 4-1: The kinetic diameters of N_2, H_2, CH_4 and CO_2[5]

	H_2	**CO_2**	**N_2**	**CH_4**
Kinetic Diameter	2.89 Å	3.30 Å	3.64 Å	3.80 Å

The solvent filled open spaces of the network are evacuated by heating the materials under vacuum. Thermogravimetric analysis (TGA) was used to determine the temperature at which each compound may be heated in order to remove solvent molecules without decomposing the host network. The TGA trace of Zn(hba) is representative of the Zn(hba) family of networks. Inspection of the TGA trace of Zn(hba), **Figure 4.1**, shows that mass attributed to guest molecules in the channels begins to be lost when the temperature reaches 50 °C. Further heating shows that the mass of the sample plateaus at 250 °C, indicating that the channels have been completely evacuated at this temperature. The material is stable until decomposition begins at 400 °C. For gas sorption analysis, Zn(hba) was activated at 250°C under vacuum overnight. Further to this, the pressure of the evacuated sample chamber is monitored until no change in pressure is observed, indicating the absence of vapour emanating from the network. The new compounds in the family of networks show similar thermogravimetric traces, but decompose at slightly lower temperatures than Zn(hba). Given these materials are less thermally stable than Zn(hba), for gas sorption measurements the new materials are activated between 200 °C and 250 °C at a pressure <15 Pa overnight and for one hour between each isotherm measurement. (The TGA data of the remaining compounds are presented in Appendix A.2.)

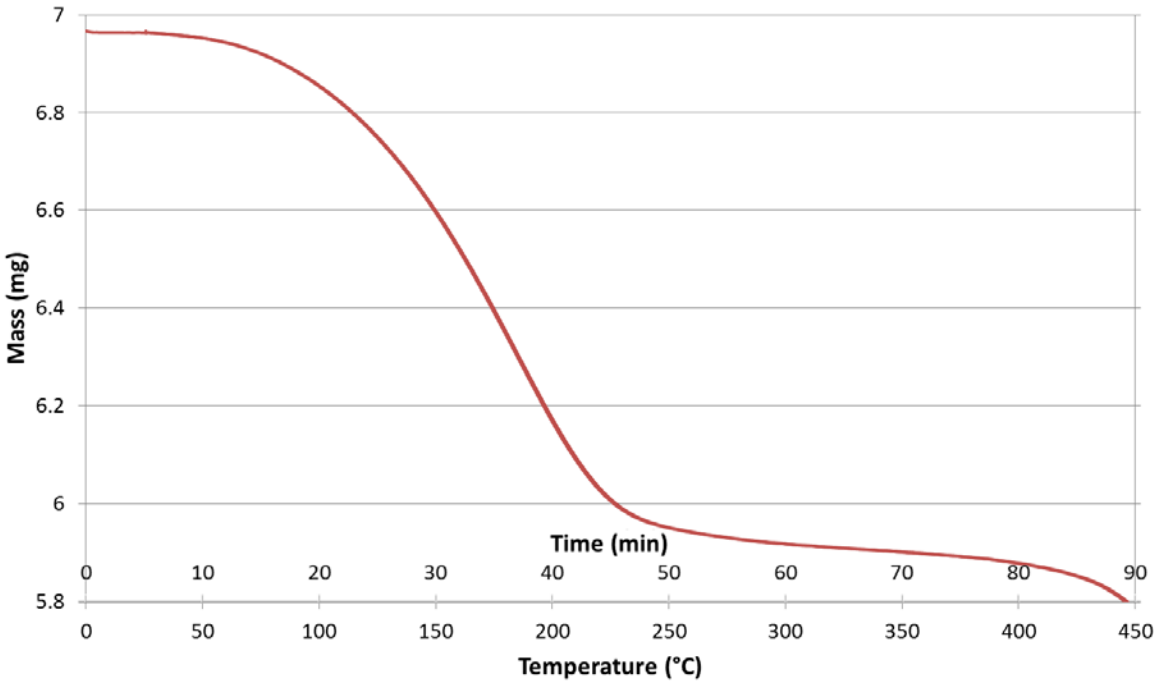

Figure 4.1: TGA trace of Zn(hba). Time (min) and temperature (°C) are indicated on the horizontal axis while mass (mg) is indicated on the vertical axis.

4.2 Work reported in this chapter

Herein the gas sorption isotherms are reported for the compounds Zn(hba), Zn(cma), Zn(hbpc), Zn(2-chloro hba), Zn(2-methyl hba), Zn(2,6-dimethyl hba), Zn(2-fluoro hba) and Zn(3-fluoro hba) for the gases N_2, H_2, CH_4 and CO_2.

4.3 Nitrogen adsorption

The surface areas of PCP/MOF materials are generally calculated using N_2 adsorption isotherms measured at 77 K and applying the Langmuir and/or BET (Brunauer-Emmett–Teller) approaches.[6] The 77 K N_2 isotherms for Zn(hba), Zn(cma),

Zn(hbpc), Zn(2-chloro hba), Zn(2-methyl hba), Zn(2,6-dimethyl hba), Zn(2-fluoro hba) and Zn(3-fluoro hba) are shown in **Figure 4.2.**

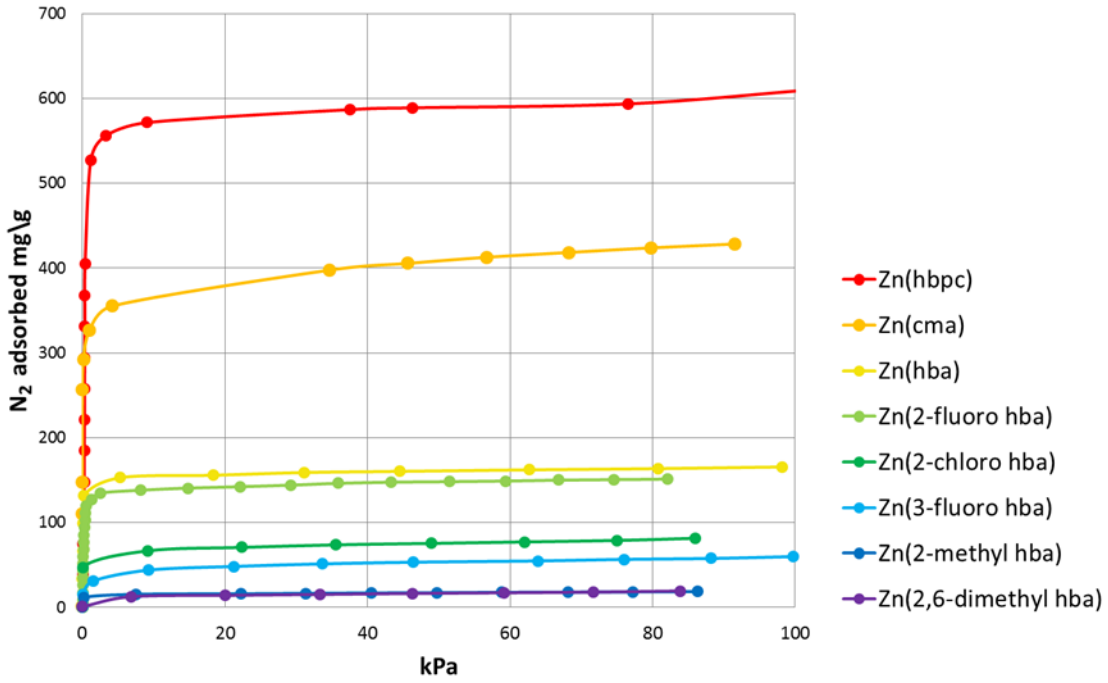

Figure 4.2: 77 K N_2 isotherms displaying the uptake by Zn(hbpc), Zn(cma), Zn(hba) Zn(2-chloro hba), Zn(2-methyl hba), Zn(2,6-dimethyl hba), Zn(2-fluoro hba) and Zn(3-fluoro hba). The horizontal axis indicates the pressure of N_2 gas whilst the uptake is represented on the vertical axis.

The maximum adsorption, BET and Langmuir surface areas are summarised in **Table 4-2** along with surface area (S.A.) for common MOFs/coordination polymers. The larger channels of Zn(cma) and Zn(hbpc), unsurprisingly, result in increased maximum adsorption of N_2 at 77 K and greater BET and Langmuir surface areas when compared to the parent Zn(hba) material. Zn(hbpc) adsorbs close to four times the amount of N_2

than Zn(hba) while Zn(cma) adsorbs close to two times the amount. Substitution of the aromatic ring on the hba^{2-} ligand in Zn(hba) on either the 2 or 3 position, leads to a decrease in maximum adsorption of N_2 at 77 K and BET and Langmuir surface areas, when compared to those for Zn(hba). For substitution on the 2-position, fluoro groups have the least impact, Zn(2 fluoro hba) adsorbing close to the same amount of N_2 as Zn(hba), while methyl groups have the greatest impact on calculated surface area with Zn(2-methyl hba) adsorbing just over 10% the amount of N_2 adsorbed by Zn(hba). Interestingly when the hba^{2-} ligand is substituted on the 2 position with a methyl group, further substitution on the 6 position does not significantly change the calculated BET or Langmuir surface area. As discussed previously in the introduction, the assumptions and limitations of the BET and Langmuir surface area calculations provide only an estimation of the true internal surface area of MOF/PCP materials.

Table 4-2: A summary of 77 K N_2 isotherms for Zn(hba) family of networks along with common MOF materials.

	Max adsorption (mg/g)	**BET S.A. (m^2/g)**	**Langmuir S.A. (m^2/g)**
Zn(hba)	165.5	588	597
Zn(cma)	546.1	1196	1471
Zn(hbpc)	610.6	2014	2190
Zn(2-chloro hba)	85.2	199	275
Zn(2-methyl hba)	19.5	50	63
Zn(2,6-dimethyl hba)	21.4	40	54
Zn(2-fluoro hba)	151.2	377	524
Zn(3-fluoro hba)	59.8	124	193
MOF-5[7]	--	3800	--
MOF-177[8]	--	4750	--
IRMOF-74[9]	--	1350	--
UIO-66[10]	--	--	1187
HKUST-1[11]	--	1615	--
MIL-101[12]	--	4230	--
SIFSIX-3-Ni[13]	--	386	--
TIFSIX-3-Ni[14]	--	200	--

When comparing the estimated surface areas of the Zn(hba) family of frameworks to those of prominent MOFs in the literature, it is clear that they have internal surface areas that are modest compared to leading adsorbers. The substituted derivatives of

Zn(hba) have BET estimated surfaces areas between 40 and 377 m^2/g , Zn(hba) has a BET surface area of 588 m^2/g, while the extended networks Zn(cma) and Zn(hbpc) have BET surface areas of 1196 and 2014 m^2/g respectively. This falls short of the BET surface areas of the materials with larger framework voids, e.g. MIL-101 4230 m^2/g, MOF-177 4750 m^2/g etc. The lower capacity is not necessarily undesirable, as the channels with smaller cross-sectional area of the Zn(hba) family of networks may allow for greater framework-guest interaction. An example of this is provided by SIFSIX-3-Ni and TIFSIX-3-Ni, which both have low BET surface area, but excellent adsorption of CO_2 at room temperature and low pressure. [13,14]

4.4 CH_4 adsorption

CH_4 isotherms were measured for all compounds at 298, 273 and 258 K. Upon inspection of the 298 K CH_4 isotherms for the Zn(hba)-type networks, it is evident that all exhibit typical behaviour of a type I isotherm (**Figure 4.3**). Interestingly Zn(cma) exhibits the highest adsorption capacity at the maximum pressure measured of just under 3000 kPa, although Zn(hbpc) has the highest calculated BET and Langmuir surface areas. It should be recognised that at the maximum pressure measured, isotherms for both Zn(cma) and Zn(hbpc) have not plateaued and thus maximum adsorption for each compound has not been attained.

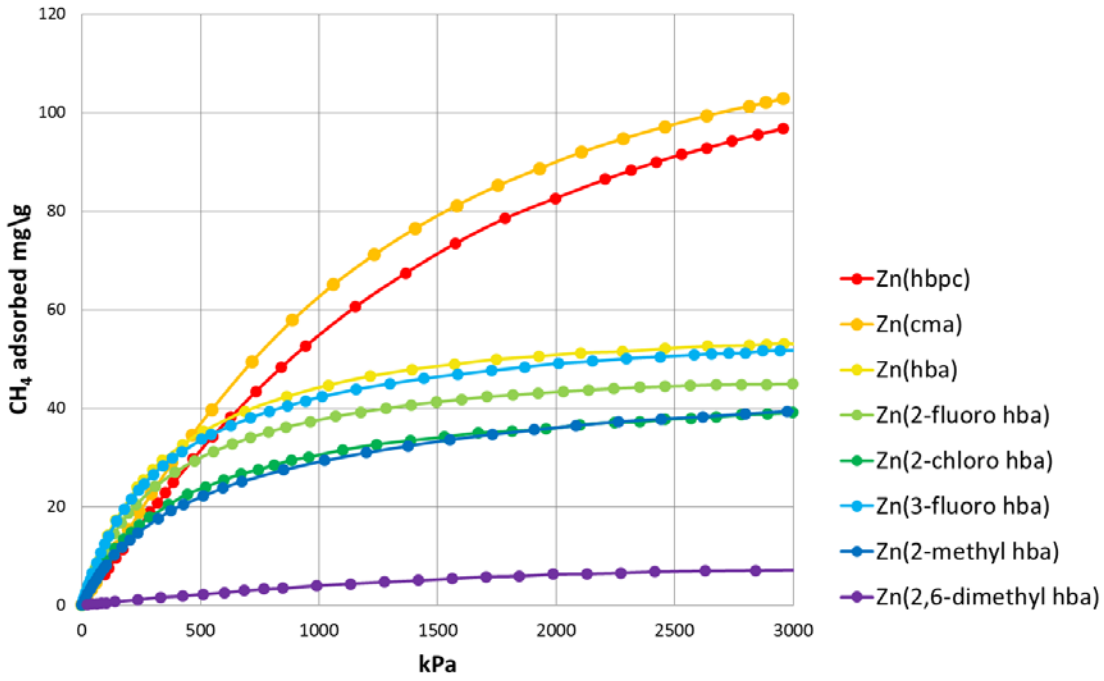

Figure 4.3: CH_4 isotherms of Zn(hbpc), Zn(cma), Zn(hba), Zn(2-chloro hba), Zn(2-methyl hba), Zn(2,6-dimethyl hba), Zn(2-fluoro hba) and Zn(3-fluoro hba) at 298 K

The estimated surface areas of Zn(3-fluoro hba), for both BET and Langmuir, are lower than those of Zn(2-fluoro hba) and Zn(2-chloro hba), yet Zn(3-fluoro hba) displays near equivalent adsorption to Zn(hba). This would imply that while substitution on the 3-position significantly lowers the intra-framework surface area of the network, it has much less of an impact on the overall adsorption capacity. Furthermore, Zn(2-methyl hba) adsorbs a similar amount to Zn(2-chloro hba), which is far more CH_4 than would be predicted from the estimated surface areas.

Zero loading binding enthalpies were calculated using the virial method, tabulated in **Table 4-3** alongside 100 kPa adsorption and maximum measured adsorption. Included in the table are common MOFs from the literature for comparative purposes. In making comparison it is not uncommon for CH_4 adsorption isotherm to be measured up to 10,000 kPa, however instrumentation employed in this investigation has a limit of 3,000 kPa. **Table 4-3** includes the pressure at which the maximum reported adsorption was obtained for each MOF/PCP. (Q_{st} calculation details and CH_4 isotherms measured at 273 and 258 K are available in section A.1.1 of the Appendix)

Table 4-3: Table summarising the 298 K CH_4 adsorption at 100 kPa, maximum adsorption and binding enthalpy for the Zn(hba) family of networks and prominent porous coordination polymers/MOFs in the literature.

	100 kPa adsorption (mg/g)	**Max adsorption**		**Binding enthalpy (kJ/mol)**
		(mg/g)	**(kPa)**	
Zn(hba)	14.1	52.9	3000	-21
Zn(cma)	7.9	103.5	3000	-16
Zn(hbpc)	6.3	96.7	3000	-17
Zn(2-chloro hba)	9.0	39.5	3000	-27
Zn(2-methyl hba)	8.1	39.7	3000	-25
Zn(2,6-dimethyl hba)	0.5	7.2	3000	-10
Zn(2-fluoro hba)	12.0	44.9	3000	-21
Zn(3-fluoro hba)	13.0	51.7	3000	-19
MOF-5[15]	8.5	293	10000	-12.3
MOF-177[16]	--	242	8000	--

Ni-MOF-74[17]	35.6	184	6000	-21.4
Mg-MOF-74[15]	--	200	10000	-18.5
CO-MOF-74[15]	--	158	10000	-19.5
UIO-66[18,19]	7.9	91	10000	-18
UIO-66-NH_2[18,19]	10.6	89	10000	-20
UiO-66-NO_2[19]	10.8	53	2000	-21
HKUST-1[17]	19.4	154	6000	-17
MILL-100[20]	--	166	8000	-19
MILL-101c[20]	--	250	8000	-18
MAF-38[21]	--	257	8000	$-21^{\dagger}/-31^{\ddagger}$

†Binding enthalpy at low loading
‡Binding enthalpy at high loading

In comparison to reported materials that display the highest CH_4 sorption, the Zn(hba) family of networks adsorbs somewhat less in terms of maximum uptake and falls significantly short of DOE targets. At 100 kPa, however, the Zn(hba)-type compounds adsorb 0.5 to 14.0 mg/g of CH_4, which is on par with other MOFs that do not possess open metal sites. The association between host and guest in the case of Zn(2-chloro hba), shows a relatively high binding enthalpy of -27 kJ/mol, which is amongst the highest reported.[15,22]

4.5 CO_2 Adsorption

Gas sorption experiments with CO_2 were performed using Zn(hbpc), Zn(cma), Zn(hba), Zn(2-chloro hba), Zn(2-methyl hba), Zn(2,6-dimethyl hba), Zn(2-fluoro hba) and Zn(3-fluoro hba). Isotherms were measured at 298, 273 and 258 K to determine binding enthalpies. It is clear upon inspection of the 298 K CO_2 isotherms presented in **Figure 4.4**, that Zn(cma), Zn(hba), Zn(2-chloro hba), Zn(2-methyl hba), Zn(2-fluoro hba) and Zn(3-fluoro hba) exhibit type I isotherm behaviour. The Zn(hbpc) and Zn(2,6-dimethyl hba) isotherms, however, exhibit an unexpected "S-shaped" kink, resembling a type IV isotherm. It is of particular interest that the maximum CO_2 uptake of Zn(2,6-dimethyl hba) converges with the maximum uptake of Zn(2-methyl hba) after the kink. This suggests that at a critical pressure of CO_2, the available void volume in Zn(2,6-dimethyl hba) increases to equal that of Zn(2-methyl hba).

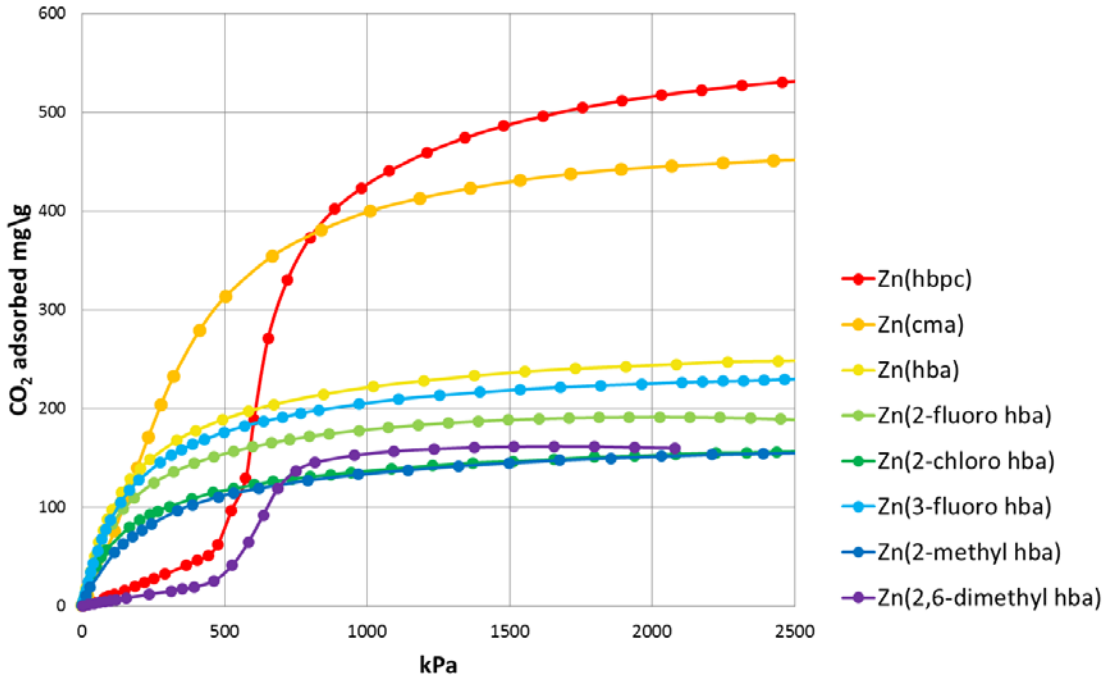

Figure 4.4: 298 K CO_2 isotherms of Zn(hbpc), Zn(cma), Zn(hba), Zn(2-chloro hba), Zn(2-methyl hba), Zn(2,6-dimethyl hba), Zn(2-fluoro hba) and Zn(3-fluoro hba).

In literature examples, the S-shaped isotherm has been observed for 'breathing' network materials.[23–26] These materials undergo a reversible structural change upon the introduction of guest molecules, which is observable in the X-ray powder diffraction patterns. In order to determine if structural change accompanies the gas uptake, powder diffraction experiments were conducted at the Australian Synchrotron. The compounds Zn(hbpc) and Zn(2,6-dimethyl hba) were placed in a "Norby cell", **Figure 4.5**, and their X-ray powder diffraction patterns were measured whilst exposed to CO_2 at various pressures.

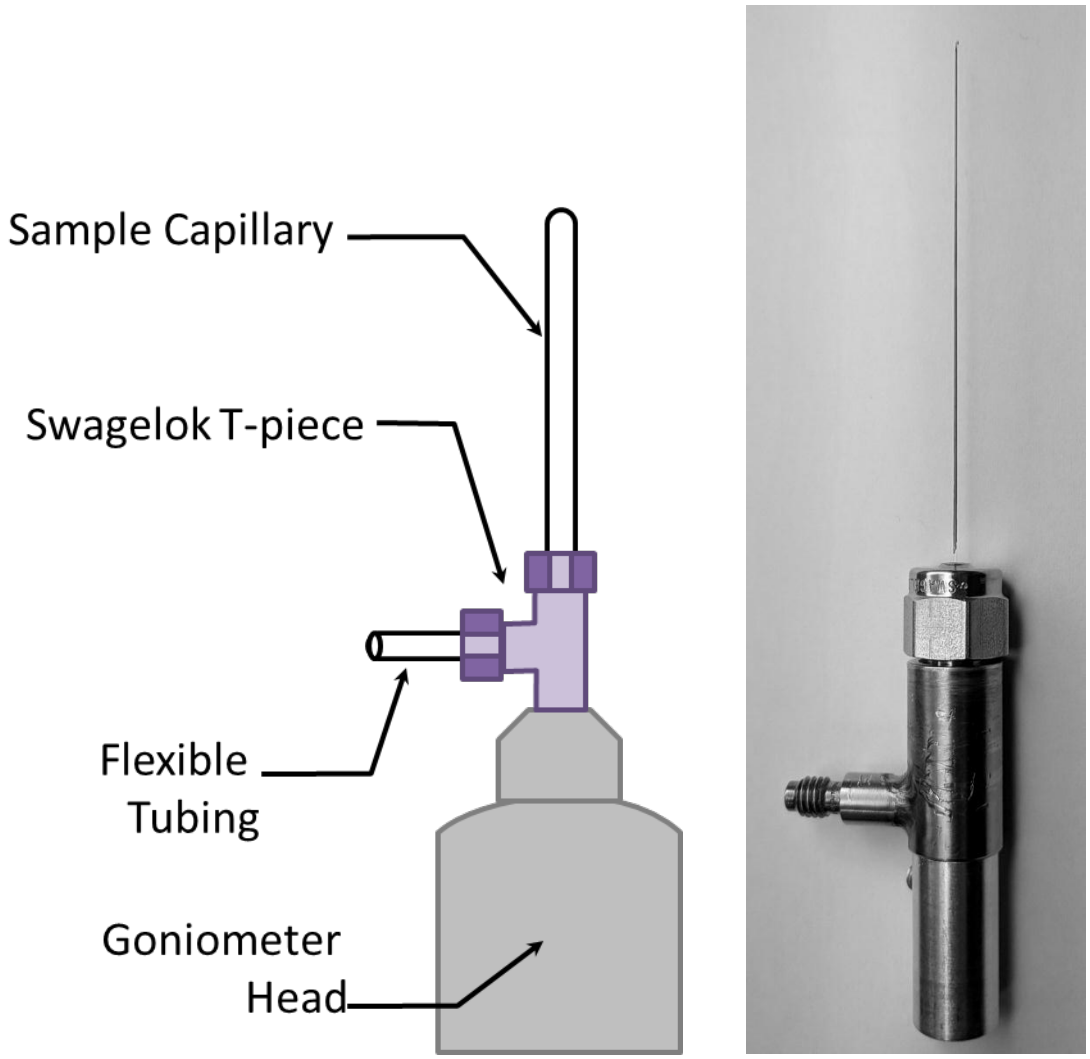

Figure 4.5: Schematic representation of the Norby cell **(left)** and a photograph of the Norby cell **(right)** used to expose Zn(2,6-dimethyl hba) powder to pressures up to 400 kPa of CO_2 during X-ray powder diffraction experiments. The sample could be evacuated by applying a vacuum through the modified Swagelok T-piece and the flexible tubing. The CO_2 was introduced to the sample through the same modified Swagelok T-piece and the flexible tubing.

In order to confirm that potential structural changes had been completed, fast-scan powder patterns were recorded at each set of conditions until no further changes were apparent. The conditions under which the powder patterns are recorded are summarised in **Table 4-4** and the powder patterns are presented in **Figure 4.6**.

Table 4-4: Summary of the experimental conditions for each consecutive powder pattern taken of Zn(2,6-dimethyl hba). The powder patterns indicated are presented in **Figure 4.6**.

Powder pattern	Temperature	Measurement conditions
1	300 K	As synthesised Zn(2,6-dimethyl hba)
		↓ Heated to 470 K under vacuum
2	470 K	Evacuated Zn(2,6-dimethyl hba) at 470 K
		↓ Cooled to 250 K
3	250 K	Evacuated Zn(2,6-dimethyl hba) at 250K
		↓ Exposed to 400 kPa of CO_2
4	250 K	Zn(2,6-dimethyl hba) exposed to CO_2 at 250K
		↓ Heated to 440 K under vacuum
5	440 K	Evacuated Zn(2,6-dimethyl hba) at 440 K

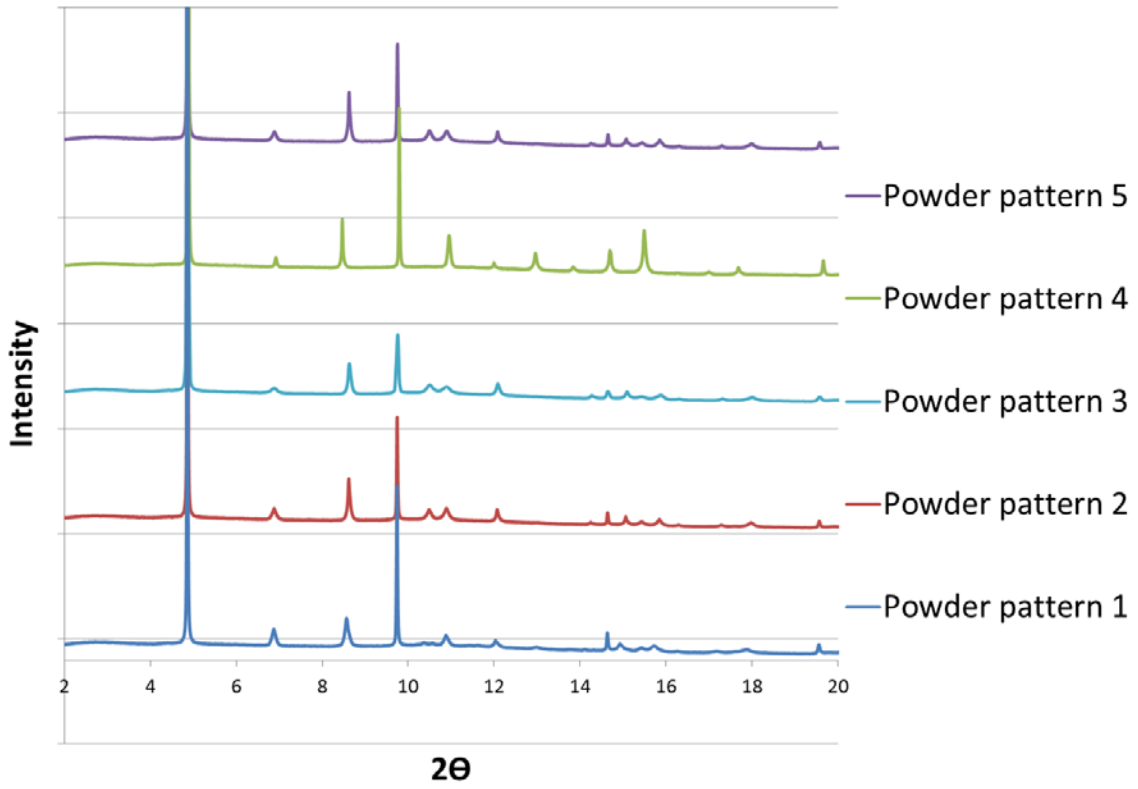

Figure 4.6: X-ray powder diffraction patterns of the same sample of Zn(2,6-dimethyl hba). Blue: The original Zn(2,6-dimethyl hba) X-ray powder diffraction pattern measured at 300 K. Red: X-ray powder diffraction pattern after Zn(2,6-dimethyl hba) was evacuated at 470 K. Turquoise: X-ray powder diffraction pattern of Zn(2,6-dimethyl hba) at 250 K. Green: X-ray powder diffraction pattern of Zn(2,6-dimethyl hba) after exposure to 4 bar of CO_2 at 250 K. Purple: X-ray powder diffraction pattern of Zn(2,6-dimethyl hba) upon re-evacuation at 440 K

Indexing of powder pattern 1 indicate cell dimensions of $a = b = 9.122$ Å $c = 6.305$ Å. This matches the cell that is commonly determined from single crystal data, however as indicated in Chapter 3, the single cell has true dimensions of $a = b = 9.118$ Å $c = 12.496$ Å. The failure to detect weak reflections consistent with the 12.496 Å c axis is the reason that the diffraction data commonly indexes to the smaller $a = b = 9.122$ Å $c = 6.305$ Å unit cell. A change in the pattern is evident when the sample is placed under vacuum at

470 K. In particular, an extra peak appears at 10.48° 2Θ. Indexing of this pattern, (pattern 2), provides a unit cell of $a = b = 9.117$ Å $c = 12.488$ Å. It would thus appear that the process of evacuation improves the long range ordering in the crystal and allows the true unit cell to become apparent. When the sample is cooled to 250 K, still under vacuum, the powder pattern (pattern 3) remains consistent with an $a = b = 9.111$ Å $c = 12.204$ Å unit cell. When the sample is loaded with 4 kPa of CO_2 at 250 K the peak at 10.48° 2Θ is absent and indexing of the pattern (pattern 4) returns to the $a = b = 9.070$ Å $c = 6.426$ Å cell obtained on the un-evacuated sample at 300 K. It would thus appear that when the channels are evacuated, long range ordering occurs to give the true cell of $a = b = 9.115$ Å $c = 12.487$ Å. When guests occupy the channels the smaller cell is obtained. (Indexing details can be found in section 7.2.4 of Chapter 7 and Appendix A.3)

In order to provide a rationalisation for the CO_2 adsorption behaviour, collaborative work with Dr. Ravichandar Babarao from RMIT University produced simulations of the Zn(2,6-dimethyl hba) framework with various loadings of CO_2. These provided an insight into structural changes associated with the loading of the framework with CO_2 molecules at various pressures. Crystallographic coordinates of Zn(2,6-dimethyl hba) with one, two, three and four CO_2 molecules were simulated at 0 K. The positions of the CO_2 molecules in the unit cell of Zn(2,6-dimethyl hba) at the different loadings are represented in **Figure 4.7**.

a)

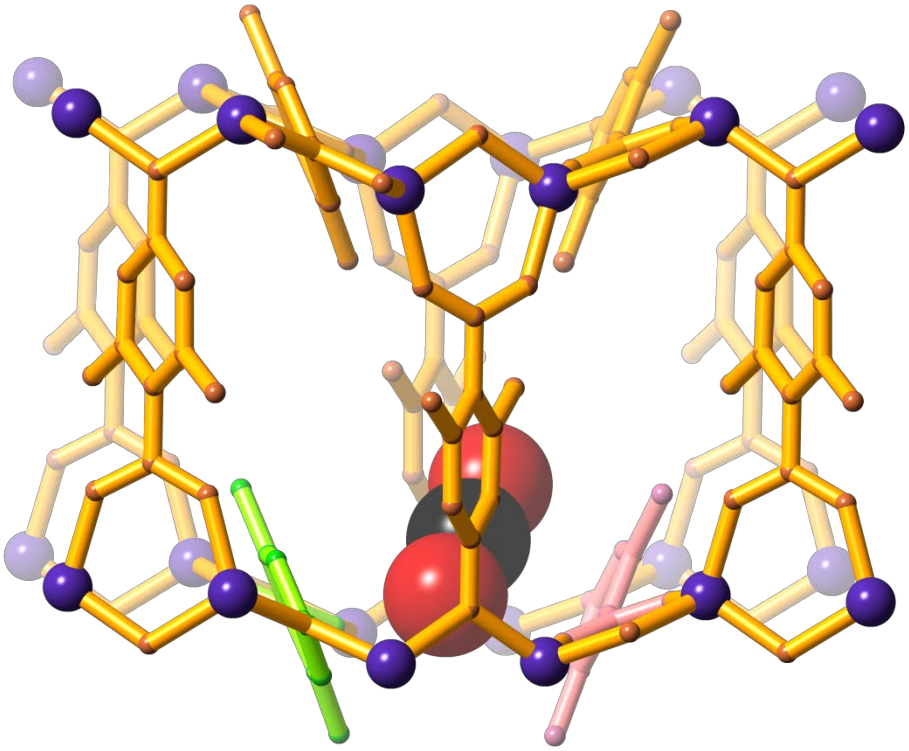

b)

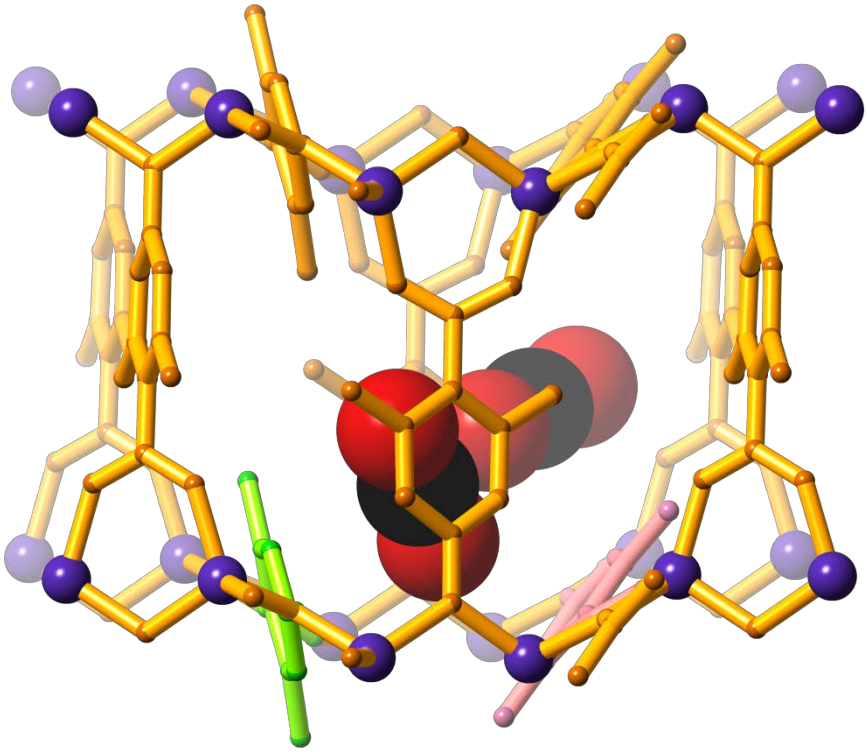

c)

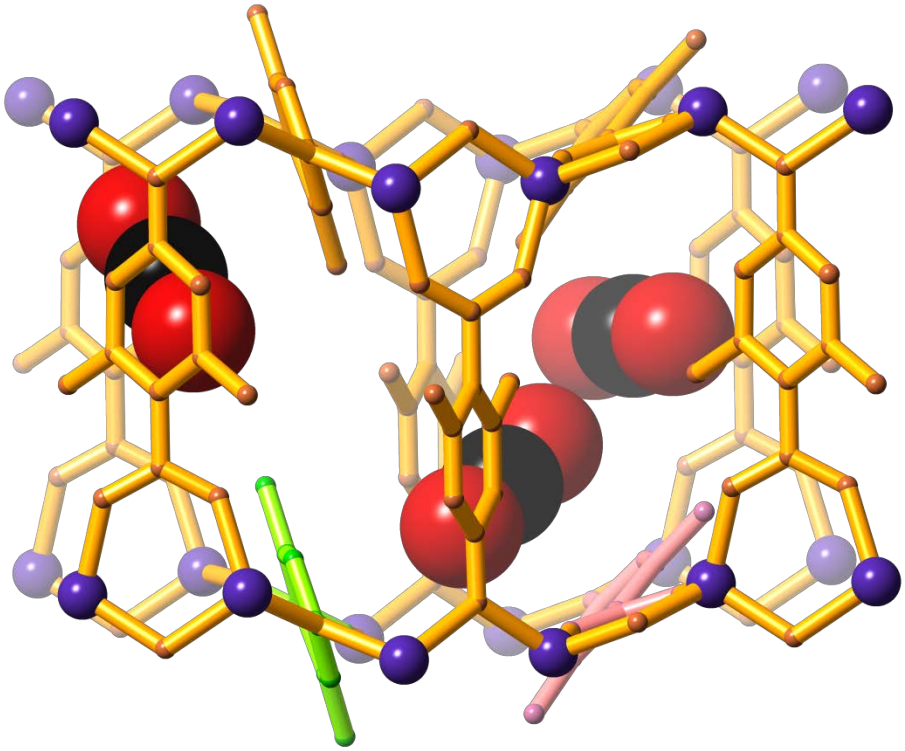

d)

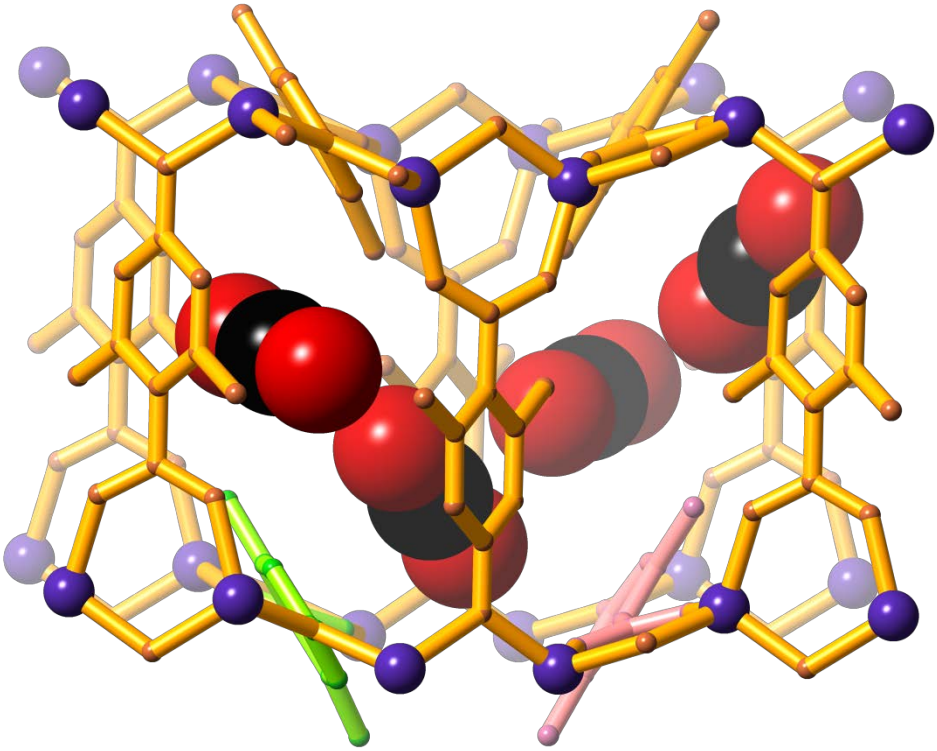

Figure 4.7: The Zn(2,6-dimethyl hba) framework with **a)** with one CO_2 molecule, **b)** with two CO_2 molecules, **c)** with three CO_2 molecules and **d)** with four CO_2 molecules. CO_2 molecules shown using space filling representations. The 2,6-dimethyl hba^{2-} ligands are represented in orange atom and bonds. For clarity H atoms are not shown.

As the number of CO_2 molecules increases in the unit cell of Zn(2,6-dimethyl hba) the degree of rotation of the aromatic ring in relation to the mean plane of the channel wall changes. From zero to one CO_2 molecule the change is negligible. However, once two CO_2 molecules are introduced, the degree of rotation of the aromatic rings of the two ligands that cradle the CO_2 molecule in relation to the channel wall changes from 67° and 67° (**Figure 4.7a** green and pink ligands respectively) to 78° and 51°(**Figure 4.7b** green and pink ligands respectively). Interestingly, as the amount of CO_2 further increases the degree of rotation of the aromatic faces on these ligands begins to decrease, moving the methyl groups on the 2,6-dimethyl hba^{2-} ligand out of the void space of the unit cell. The degree of rotation decreases from 78° and 51° to 65° and 52° (**Figure 4.7c** green and pink ligands respectively) with three CO_2 molecules. When four CO_2 molecules are simulated in the unit cell the degree of rotation changes from 65° and 52° to 58° and 58° (**Figure 4.7d** green and pink ligands respectively). The degree of rotation of the aromatic ring in relation to the channel walls at the different loadings of CO_2 are summarised in **Table 4-5**. This further supports the hypothesis that the Zn(2,6-dimethyl hba) undergoes a structural change upon exposure to CO_2.

Table 4-5: A table summarising the degree of rotation of the aromatic ring compared to the channel direction.

Number of CO_2 atoms	Degree of rotation
0	67°, 67°
1	67°, 67°
2	78°, 51°
3	65°, 52°
4	58°, 58°

The change in accessible void space within the simulated structure of Zn(2,6-dimethyl hba) is apparent upon comparison of the channels with and without CO_2 present, as shown in **Figure 4.8**. The void space is shown to run in a helical fashion along the unique direction. As the degree of rotation of the aromatic ring changes with increased amounts of CO_2, the accessible void space within the Zn(2,6-dimethyl hba) channels increases, as can be seen upon comparison of **Figure 4.8a, b** and **c**. **Figure 4.8c** and **f** shows the accessible voids within Zn(2-methyl hba). The void space within Zn(2,6-dimethyl hba) twists in a helical fashion, whereas in Zn(2-methyl hba) the helical twist is less prominent. Given the apparent difference in the channel volume between Zn(2,6-dimethyl hba) and (Zn(2-methyl hba) in the simulated structures (**Figure 4.8b** and **Figure 4.8c**) it is somewhat surprising on first inspection that the two compounds are able to adsorb similar quantities of CO_2 at the maximum pressure measured. This may reflect the fact that in each case the cross-sectional area of the channel is not large enough to accommodate more than one CO_2 molecule.

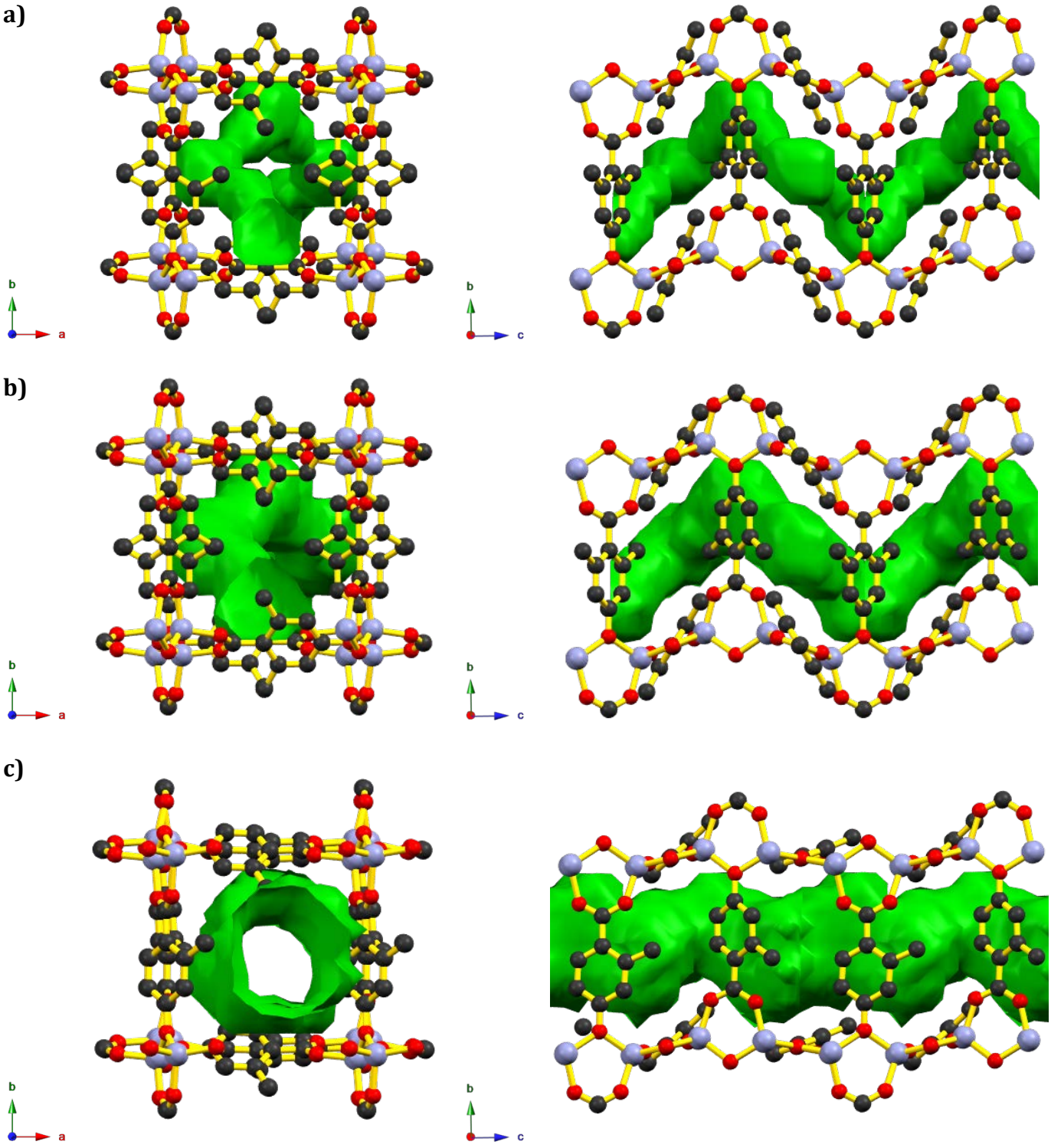

Figure 4.8: A representation of the accessible void space of **a)** Zn(2,6-dimethyl hba) along the direction of the channel **(left)** and perpendicular to the channel direction **(right)**, **b)** Zn(2,6-dimethyl hba) dosed with four CO_2 molecules per unit cell viewed along the direction of the channel **(left)** and perpendicular to the channel direction **(right)**and **c)** Zn(2-methyl hba) viewed along the direction of the channel **(left)** and perpendicular to the channel direction **(right)**.

The framework simulations by Dr Babarao match with the experimental data, as can be seen in **Figure 4.9**. The experimental data has notable inflections in the isotherms occurring at 0.5 and 3 CO_2 molecules per unit cell before reaching a maximum uptake at slightly below 4 CO_2 molecules per unit cell. As the temperature of the isotherm decreases, the maximum uptake of CO_2 increases. The inflections in the isotherm occur at lower pressures of CO_2 but occur at the approximately the same CO_2 loading.

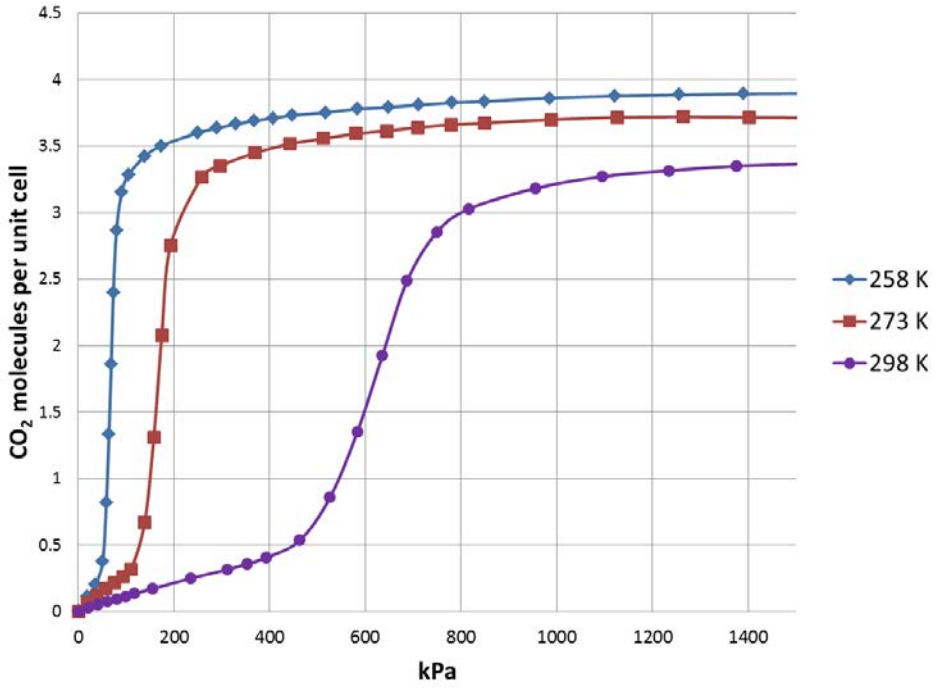

Figure 4.9: Zn(2,6-dimethyl hba) CO_2 isotherms at 258, 273 and 298 K showing the number of CO_2 atoms present in the material per unit cell.

In contrast to Zn(2,6-dimethyl hba), there were no significant changes in the X-ray powder diffraction patterns of Zn(hbpc) when the sample was evacuated or exposed to 400 kPa of CO_2 at 250 K.

In a typical gas adsorption experiment, when a sample is exposed to CO_2, a data point is recorded once the pressure remains within ±1% of the exposed pressure for 300 seconds. If the variation exceeds ±1% the 300 second period commences again. This is done in an attempt to ensure that the sample has reached equilibrium and is no longer adsorbing gas, before the data point in the isotherm is actually measured. When this "equilibrium time" is increased from 300 seconds to 600 seconds in the Zn(hbpc) 298 K CO_2 isotherm, the S-shaped kink is less apparent, with no significant change to the maximum uptake, as shown in **Figure 4.10**. Therefore it is believed that the S-shaped kink in the Zn(hbpc) CO_2 isotherm results purely from the slow kinetics of CO_2 adsorption. In contrast, when the equilibrium time of CO_2 uptake of Zn(2,6-dimethyl hba) is increased from 300 seconds to 600 seconds, there is no significant change in the isotherm.

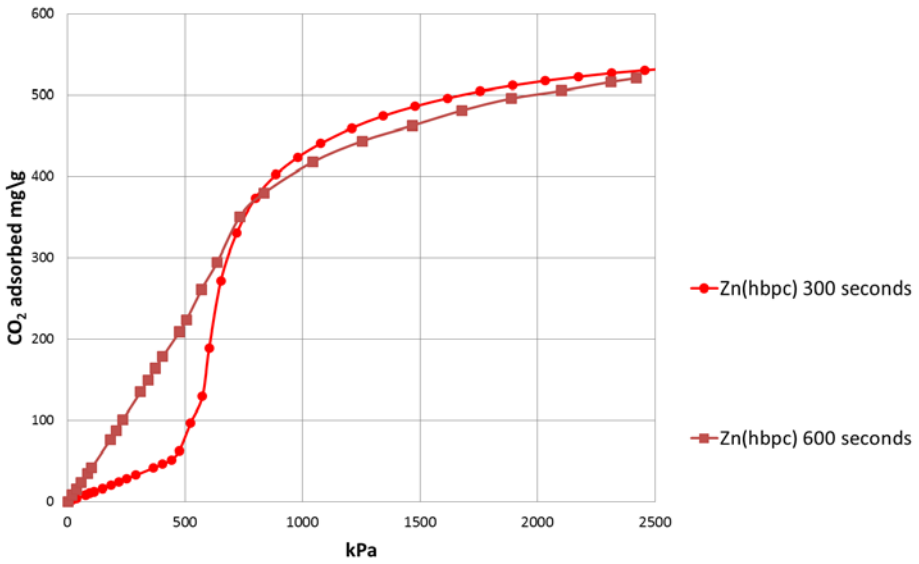

Figure 4.10: Comparison of the Zn(hbpc) 298K isotherm given 300 seconds and 600 seconds equilibrium time respectively. Circles: When the sample is exposed to CO_2 and once the pressure remains within ±1% exposed pressure for 300 seconds the data point is recorded. Squares: When CO_2 is exposed to the sample once the pressure remains within ±1% kPa for 600 seconds, the data point is recorded.

CO_2 adsorption at 100 kPa, the maximum adsorption and the binding enthalpy of the Zn(hba) family of networks, in addition to prominent porous coordination polymers/MOFs in the literature, are presented in **Table 4-6**. Zn(hba) has a binding enthalpy of -29 kJ/mol. Substitution of the aromatic ring in the 2-position increases the binding enthalpy to 30 kJ/mol for a methyl group and to 31 kJ/mol for a chloro or fluoro group. Although, of the substituted networks, Zn(3-fluoro hba) adsorbs closest to that of Zn(hba) at both high and low pressure, it would seem that substitution at the 3-position with a fluoro group decreases the binding enthalpy to -25 kJ/mol. The larger channels of Zn(cma) and Zn(hbpc) result in an increased overall uptake but lower uptake at 100 kPa. Note that it was not possible to conduct a binding enthalpy for Zn(hbpc) given the shape of the isotherm. (Q_{st} calculation details and CO_2 isotherms measured at 273 and 258 K are available in section A.1.2 of the Appendix)

Table 4-6: CO_2 adsorption at 100 kPa, maximum adsorption and binding enthalpy for the Zn(hba) family of networks and prominent porous coordination polymers/MOFs in the literature.

	100 kPa adsorption (mg/g)	**Max adsorption (mg/g)**	**Binding enthalpy (kJ/mol)**
Zn(hba)	87.9	250.5	-29
Zn(cma)	75.9	453.0	-27
Zn(hbpc)	$11.9^{\dagger}/41.2^{\ddagger}$	533.3	N/A
Zn(2-chloro hba)	56.8	156.7	-31
Zn(2-methyl hba)	54.1	157.6	-30
Zn(2,6-dimethyl hba)	5.6	160.0	N/A

Zn(2-fluoro hba)	83.0	188.1	-31
Zn(3-fluoro hba)	86.7	230.0	-25
Mg-MOF-74[27,28]	352◊	625	-47
Ni-MOF-74[27]	256◊	--	-41
Co-MOF-74[27]	306◊	--	-37
HKUST-1[29]	193	573	-29
UiO-66[19]	79	310	-25.6
UiO-66-NH_2[19]	131	369	-27.9
UiO-66-NO_2[19]	114	251	-31.7
MIL-101c[20]	640	1760	-45
MIL-100[20]	88	850	-63
NOTT-116/PCN-68[30]	61	1410	-21.2
PCN-61[30]	53	1100	-21.0
PCN-66[30]	80	1200	-26.2
MOF-200[31]	30	2400	--
MOF-177[28,31]	40	1470	--
MOF-5[31]	80	870	--
SIFSIX-3-Ni[14,32]	120	--	-45
TIFSIX-3-Ni[14]	108	--	-50

† 300 second equilibrium time
‡ 600 second equilibrium time
◊Measured at 296 K

At 100 kPa the Zn(hba) family of networks adsorb CO_2 in similar amounts to leading adsorbents without open metal sites. Adsorbents with open metal sites (e.g. MIL-101,

Mg-MOF-74), however, adsorb more CO_2 and possess binding enthalpies much larger than that of the Zn(hba) family of networks. SIFSIX-3-Ni and TIFSIX-3-Ni are also both materials with small non-intersecting pores and possess binding enthalpies significantly larger than that of the Zn(hba) family of networks. At higher pressure, the Zn(hba) family of networks adsorb less CO_2 than the MOFs with larger void space, but the Zn(hba) family of networks generally have higher binding enthalpy than these compounds.

4.6 H_2 adsorption

H_2 isotherms were measured at 77 K and 87 K for each compound. Upon inspection of the 77 K H_2 isotherms it is apparent that those for Zn(cma), Zn(hba), Zn(2-chloro hba), Zn(2-methyl hba), Zn(2,6-dimethyl hba), Zn(2-fluoro hba) and Zn(3-fluoro hba) exhibit type I isotherm behaviour (**Figure 4.11**) Negligible hysteresis is indicated on the desorption path. The Zn(hbpc) isotherm, however, superficially resembles a type IV isotherm with considerable hysteresis, **Figure 4.12**.

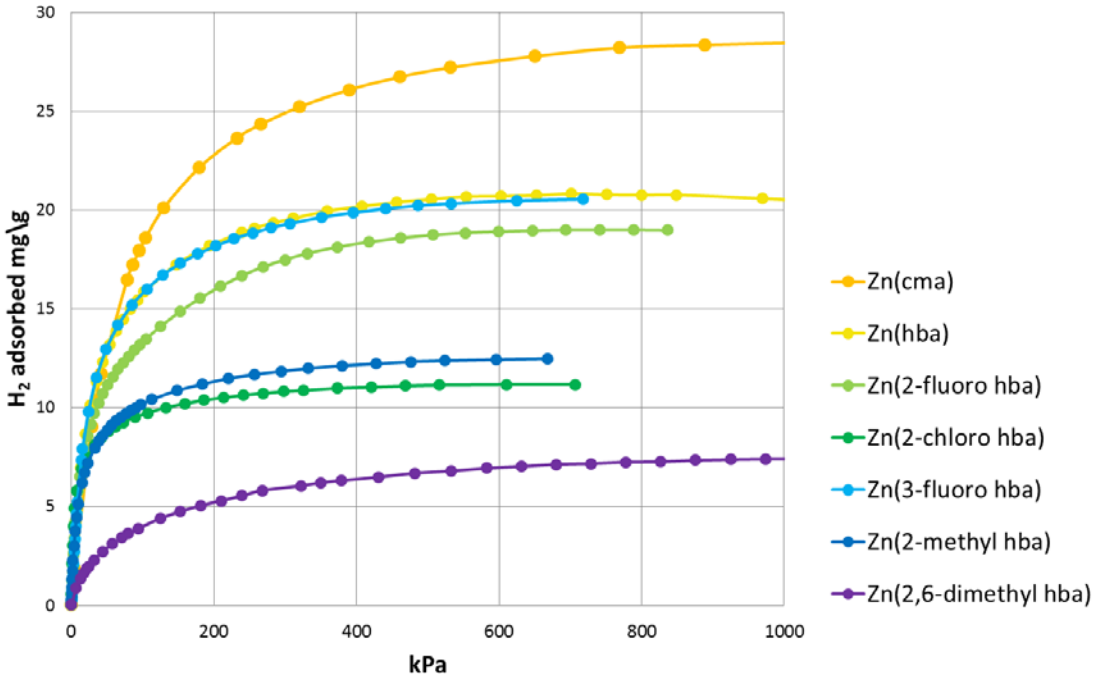

Figure 4.11: 77 K H_2 isotherms of Zn(cma), Zn(hba), Zn(2-chloro hba), Zn(2-methyl hba), Zn(2,6-dimethyl hba), Zn(2-fluoro hba) and Zn(3-fluoro hba)

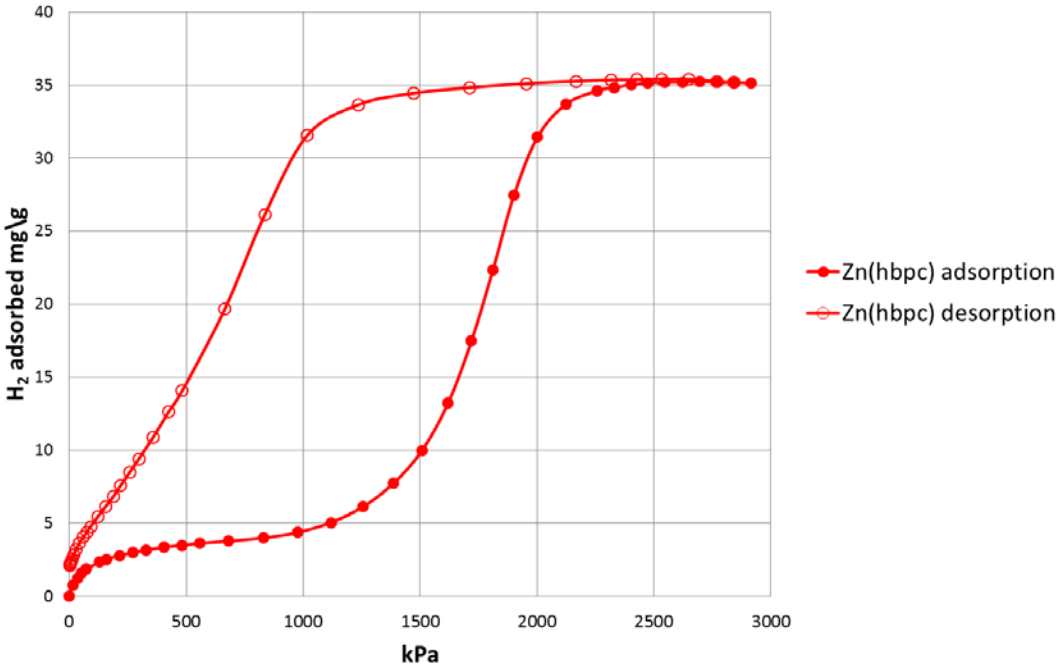

Figure 4.12: 77 K H_2 adsorption and desorption isotherms of Zn(hbpc). Adsorption is represented with filled circles and desorption by empty circles.

At pressures between 0 and 1000 kPa, only a small amount of H_2 was adsorbed by Zn(hbpc). However, as the pressure was raised above 1000 kPa, Zn(hbpc) continued to adsorb H_2. Once the pressure was raised above 1500 kPa, a sharp rise in the H_2 uptake was observed, reaching a maximum of 35.1 mg/g at 2800 kPa. In the desorption process, only when the pressure falls below 1000 kPa does the material begin to lose the adsorbed H_2. In a publication from the Abrahams-Robson group (in which the candidate was a co-author) this behaviour was attributed to network flexibility.[33] In light of the evidence from diffraction studies of Zn(hbpc) with CO_2 adsorption (section 4.5) in which no structural changes are observed, the cause of the "kink" in the isotherm is uncertain. Interestingly, the isotherm does not undergo significant change when the equilibrium time is increased. Reported coordination polymers with channels, including the IRMOF-74 series, in the literature do not exhibit this phenomenon.[15,34–36]

Binding enthalpies for H_2 adsorption were calculated from the 77 K and 87 K isotherms using the virial method and are summarised in **Table 4-7** alongside maximum adsorption. Zn(hba) and Zn(3-fluoro hba) adsorb similar amounts of H_2, again showing that in the Zn(hba) family of frameworks, fluorine substitution at the 3-position on the aromatic ring has a smaller effect than fluorine substitution at the 2-position, in regards to adsorption. Substitution at the 2-position, however, does increase the binding enthalpy of the system. The binding enthalpy of Zn(hba) for H_2 is -6.0 kJ/mol, whereas the binding enthalpies of Zn(2-fluoro hba), Zn(2-methyl hba) and Zn(2-chloro hba) are -

6.8, -7.6 and -8.4 kJ/mol respectively. (Q_{st} calculation details and H_2 isotherms measured at 87 K are available in section A.1.3 of the Appendix)

Table 4-7: Table summarising the 77 K H_2 isotherms.

	100 kPa adsorption (mg/g)	**Max adsorption (mg/g)**	**Binding enthalpy (kJ/mmol)**
Zn(hba)	15.9	20.8	-6.0
Zn(cma)	18.6	28.1	-6.1
Zn(hbpc)	2.3	35.1	N/A
Zn(2-chloro hba)	9.7	11.2	-8.4
Zn(2-methyl hba)	10.2	12.5	-7.6
Zn(2,6-dimethyl hba)	4.0	7.3	-8.1
Zn(2-fluoro hba)	13.4	19.0	-6.8
Zn(3-fluoro hba)	16.0	20.6	-6.0
MOF-5[37]	10.3	48.8	-3.8
MOF-177[38]	10	75	--
IRMOF-74[39]	22	32	-10.3
UIO-66[40]	17	26	--
HKUST-1[37]	16.8	36.4	-4.5
MIL-100[41]	15	38	-6.3
MIL-101b[41]	12	61	-10

In comparison to common MOFs in the literature, the Zn(hba) family of frameworks adsorb similar amounts of H_2 at 100 kPa, but do not have the same overall capacity for H_2 as materials with larger void volumes as indicated by measurements at higher pressures. However, the Zn(hba) family of frameworks do have high binding enthalpies for H_2 adsorption for a material without open metal sites.

4.7 General Trends

The work described in this chapter reveals that Zn(hbpc), Zn(cma), Zn(hba), Zn(2-chloro hba), Zn(2-methyl hba), Zn(2,6-dimethyl hba), Zn(2-fluoro hba) and Zn(3-fluoro hba) are all capable of adsorbing the gases CO_2, H_2, CH_4 and N_2. Unsurprisingly, when compared to Zn(hba), materials with longer ligands, such as Zn(hbpc) and Zn(cma), have a higher calculated surface area as well as a greater maximum uptake. However, when comparing adsorption at lower pressures, in most cases, Zn(hba) is capable of adsorbing more gas than Zn(hbpc) and Zn(cma) at pressures up to 100 kPa. In regards to the substituted Zn(hba) frameworks, a reduced uptake of gases is usually associated with greater crowding in the channels. Nevertheless the presence of substituents generally leads to an enhancement of binding enthalpies.

Although Zn(3-fluoro hba) has lower BET and Langmuir surface areas than both Zn(2-fluoro hba) and Zn(2-chloro hba), it consistently adsorbed more CO_2, H_2 and CH_4. In fact Zn(3-fluoro hba) adsorbs CO_2, H_2 and CH_4 to a level close to that of Zn(hba). This suggest that although substitution at the 3-position of the aromatic ring on the hba^{2-}

ligand leads to a smaller surface area, the guest accessible void space is not significantly reduced.

Most of the isotherms of Zn(hbpc), Zn(cma), Zn(hba), Zn(2-chloro hba), Zn(2-methyl hba), Zn(2,6-dimethyl hba), Zn(2-fluoro hba) and Zn(3-fluoro hba) show typical type I behaviour. Only the CO_2 isotherms of Zn(2,6-dimethyl hba) and Zn(hbpc) and the H_2 isotherms of Zn(hbpc) showed S-shaped kinks in the isotherm. Computational simulations along with powder diffraction experiments suggest that Zn(2,6-dimethyl hba) undergoes a structural change once a critical amount of CO_2 enters the channels, between 1 and 2 CO_2 molecules per unit cell. It is suspected that the aromatic rings that line the channels of Zn(2,6-dimethyl hba) become closer to parallel with the average plane of the channel wall, allowing a similar amount of CO_2 to be adsorbed as that found for Zn(2-methyl hba) at high pressure. The S-shaped kink found in the CO_2 isotherms of Zn(hbpc) becomes less obvious when longer equilibrium times for the gas adsorption experiment are used which suggests that it is due to slow diffusion kinetics of CO_2 into the network. The S-shaped kink present in the Zn(2,6-dimethyl hba) CO_2 isotherms and the Zn(hbpc) H_2 isotherms persists with increased equilibrium time. As Zn(hbpc) does not show structural changes in the powder diffraction patterns the kink in the isotherm is not attributed to framework breathing. The reason for the kink is not clear at present.

Despite the modest overall capacity of the Zn(hba) family of networks compared to leading MOFs described in the literature, they are able to take up similar amounts of gas

at approximately one atmosphere. Where there is substitution on the aromatic rings of the ligands within the networks, the binding enthalpies for H_2, CH_4 and CO_2, are generally high compared to porous framework materials that do not possess open metal sites. The high binding enthalpies have been attributed to the smaller intra-framework channels allowing guest molecules to interact with multiple surfaces at the same time.

4.8 Concluding remarks

The Zn(hba) network has shown to be robust, as all gas sorption experiments are conducted in sequence on the same material. There is considerable scope for functionalisation and further research may include the exploration of longer and/or further substituted ligands and their gas adsorption properties. Although the networks display modest uptake when compared to other prominent MOFs, the optimisation of both ligand length and substitution, may lead to a material possessing both high capacity and binding enthalpy. CO_2, H_2, CH_4 and N_2 are by no means the only guest that the Zn(hba) family of networks are capable of adsorbing. The adsorption properties of the Zn(hba) of networks for anaesthetic gases and vapours are explored in the following chapter.

4.9 References

[1] C. H. Yu, C. H. Huang, C. S. Tan, *Aerosol Air Qual. Res.* **2012**, *12*, 745–769.

[2] Y. He, W. Zhou, G. Qian, B. Chen, *Chem. Soc. Rev.* **2014**, *43*, 5657–78.

[3] H. W. Langmi, J. Ren, B. North, M. Mathe, D. Bessarabov, *Electrochim. Acta* **2014**, *128*, 368–392.

[4] J.-R. Li, R. J. Kuppler, H.-C. Zhou, *Chem. Soc. Rev.* **2009**, *38*, 1477–1504.

[5] A. F. Ismail, K. Chandra Khulbe, T. Matsuura, *Gas Separation Membranes*, Springer International Publishing, Cham, **2015**.

[6] F. Ambroz, T. J. Macdonald, V. Martis, I. P. Parkin, *Small Methods* **2018**, *2*, 1800173.

[7] S. S. Kaye, A. Dailly, O. M. Yaghi, J. R. Long, *J. Am. Chem. Soc.* **2007**, *129*, 14176–14177.

[8] H. Furukawa, M. A. Miller, O. M. Yaghi, *J. Mater. Chem.* **2007**, *17*, 3197.

[9] S. Kim, E. Brostromer, D. Xing, J. Jin, S. Chong, H. Ge, S. Wang, C. Gu, L. Yang, Y. Q. Gao, et al., *Science* **2013**, *339*, 816–819.

[10] J. H. Cavka, S. Jakobsen, U. Olsbye, N. Guillou, C. Lamberti, S. Bordiga, K. P. Lillerud, *J. Am. Chem. Soc.* **2008**, *130*, 13850–13851.

[11] Y. Chen, X. Mu, E. Lester, T. Wu, *Prog. Nat. Sci. Mater. Int.* **2018**, *28*, 584–589.

[12] G. Férey, C. Mellot-Draznieks, C. Serre, F. Millange, J. Dutour, S. Surblé, I. Margiolaki, *Science* **2005**, *309*, 2040–2.

[13] S. K. Elsaidi, M. H. Mohamed, H. T. Schaef, A. Kumar, M. Lusi, T. Pham, K. A. Forrest, B. Space, W. Xu, G. J. Halder, et al., *Chem. Commun.* **2015**, *51*, 15530–15533.

[14] D. G. Madden, D. O'Nolan, K. J. Chen, C. Hua, A. Kumar, T. Pham, K. A. Forrest, B. Space, J. J. Perry, M. Khraisheh, et al., *Chem. Commun.* **2019**, *55*, 3219–3222.

[15] J. A. Mason, M. Veenstra, J. R. Long, *Chem. Sci.* **2014**, *5*, 32–51.

[16] H. Furukawa, N. Ko, Y. B. Go, N. Aratani, S. B. Choi, E. Choi, A. O. Yazaydin, R. Q. Snurr, M. O'Keeffe, J. Kim, et al., *Science* **2010**, *329*, 424–428.

[17] Y. Peng, V. Krungleviciute, I. Eryazici, J. T. Hupp, O. K. Farha, T. Yildirim, *J. Am. Chem. Soc.* **2013**, *135*, 11887–11894.

[18] A. D. Wiersum, J. S. Chang, C. Serre, P. L. Llewellyn, *Langmuir* **2013**, *29*, 3301–3309.

[19] G. E. Cmarik, M. Kim, S. M. Cohen, K. S. Walton, *Langmuir* **2012**, *28*, 15606–15613.

[20] P. L. Llewellyn, S. Bourrelly, C. Serre, A. Vimont, M. Daturi, L. Hamon, G. De Weireld, J.-S. Chang, D.-Y. Hong, Y. Kyu Hwang, et al., *Langmuir* **2008**, *24*, 7245–7250.

[21] J. M. Lin, C. T. He, Y. Liu, P. Q. Liao, D. D. Zhou, J. P. Zhang, X. M. Chen, *Angew. Chemie - Int. Ed.* **2016**, *55*, 4674–4678.

[22] Y. Lin, C. Kong, Q. Zhang, L. Chen, *Adv. Energy Mater.* **2017**, *7*, 1601296.

[23] P. K. Thallapally, M. R. Kishan, C. A. Fernandez, P. B. McGrail, J. Tian, J. L. Atwood, S. J. Dalgarno, J. E. Warren, *J. Am. Chem. Soc.* **2008**, *130*, 16842–16843.

[24] F. Salles, G. Maurin, C. Serre, P. L. Llewellyn, C. Knöfel, H. J. Choi, Y. Filinchuk, L. Oliviero, A. Vimont, J. R. Long, et al., *J. Am. Chem. Soc.* **2010**, *132*, 13782–13788.

[25] Y. Y. Liu, S. Couck, M. Vandichel, M. Grzywa, K. Leus, S. Biswas, D. Volkmer, J. Gascon, F. Kapteijn, J. F. M. Denayer, et al., *Inorg. Chem.* **2013**, *52*, 113–120.

[26] M. Alhamami, H. Doan, C. Cheng, *Materials (Basel).* **2014**, *7*, 3198–3250.

[27] A. J. Matzger, S. R. Caskey, A. G. Wong-Foy, A. J. Matzger, S. R. Caskey, A. G. Wong-Foy, *J. Am. Chem. Soc.* **2008**, *130*, 10870–10871.

[28] Z. R. Herm, J. A. Swisher, B. Smit, R. Krishna, J. R. Long, *J. Am. Chem. Soc.* **2011**, *133*, 5664–5667.

[29] L. Grajciar, A. D. Wiersum, P. L. Llewellyn, J. S. Chang, P. Nachtigall, *J. Phys. Chem. C* **2011**, *115*, 17925–17933.

[30] D. Yuan, D. Zhao, D. Sun, H. C. Zhou, *Angew. Chemie - Int. Ed.* **2010**, *49*, 5357–5361.

[31] H. Furukawa, K. E. Cordova, M. O'Keeffe, O. M. Yaghi, *Science* **2013**, *341*, DOI 10.1126/science.1230444.

[32] K.-J. Chen, Q.-Y. Yang, S. Sen, D. G. Madden, A. Kumar, T. Pham, K. A. Forrest, N. Hosono, B. Space, S. Kitagawa, et al., *Angew. Chemie Int. Ed.* **2018**, *57*, 3332–3336.

[33] K. F. White, B. F. Abrahams, R. Babarao, A. D. Dharma, T. A. Hudson, H. E. Maynard-Casely, R. Robson, *Chem. - A Eur. J.* **2015**, *21*, 18057–18061.

[34] S. M. Humphrey, J. S. Chang, S. H. Jhung, J. W. Yoon, P. T. Wood, *Angew. Chemie - Int. Ed.* **2007**, *46*, 272–275.

[35] X. Sen Wang, L. Meng, Q. Cheng, C. Kim, L. Wojtas, M. Chrzanowski, Y. S. Chen, X. P. Zhang, S. Ma, *J. Am. Chem. Soc.* **2011**, *133*, 16322–16325.

[36] Y. L. Dong, L. Xu, X. Di Yang, Z. Su, H. K. Liu, *Inorg. Chem. Commun.* **2019**, *104*, 14–18.

[37] B. Panella, M. Hirscher, H. Pütter, U. Müller, *Adv. Funct. Mater.* **2006**, *16*, 520–524.

[38] A. G. Wong-Foy, A. J. Matzger, O. M. Yaghi, *J. Am. Chem. Soc.* **2006**, *128*, 3494–3495.

[39] K. Sumida, C. M. Brown, Z. R. Herm, S. Chavan, S. Bordiga, J. R. Long, *Chem. Commun.* **2011**, *47*, 1157–1159.

[40] S. E. Bambalaza, H. W. Langmi, R. Mokaya, N. M. Musyoka, J. Ren, L. E. Khotseng, *J. Mater. Chem. A* **2018**, *6*, 23569–23577.

[41] M. Latroche, S. Surblé, C. Serre, C. Mellot-Draznieks, P. L. Llewellyn, J. H. Lee, J. S. Chang, H. J. Sung, G. Férey, *Angew. Chemie - Int. Ed.* **2006**, *45*, 8227–8231.

Chapter 5 Table of Contents

Chapter 5 – Anaesthetic Capture

5.1 Introduction

The use of anaesthetics in surgery extends back to the 1840s. As early as 1842 Crawford Long utilised "sulfuric ether", better known today as diethyl ether, to anaesthetise patients in his dental surgery.[1] In 1846 William T.G. Morton gave a public demonstration in which he anaesthetised a patient in order to remove a tumour from the patient's neck.[2] Since this time, surgical procedures, that were previously impossible, could now be conducted in a manner that did not cause the patient undue distress because anaesthetics were able to induce unconsciousness.

Around the same time as the discovery of the analgesic and sedative effects of ether, Robert M. Glover and James Y. Simpson showed that chloroform has a similar anaesthetic effect to diethyl ether.[3] At approximately the same time there was interest in the anaesthetic effects of nitrous oxide from Horace Wells, Gardner Q. Colton and John M. Riggs.[4] In 1845 Wells gave an unsuccessful public demonstration of the anaesthetic effects of nitrous oxide but further work succeeded in demonstrating the usefulness of nitrous oxide as an anaesthetic.[5] Although a partial pressure of nitrous oxide in excess of 1 atm (achieved through hyperbaric conditions) is required to induce unconsciousness, nitrous oxide, colloquially known as "laughing gas", has been used as an effective analgesic and sedative around the world for the last 150 years.[6]

Building upon this preliminary work on anaesthetics, chloroform, diethyl ether and nitrous oxide were used widely for general anaesthetics well into the first half of the

20th century. Today anaesthesia has been classified into three groups: general anaesthesia,[7] which causes reversible loss of consciousness; local anaesthesia,[8] which blocks the sensation of pain to the region of the body to which they are administered; and regional anaesthesia,[9] which causes a reversible loss of sensation to a limited region of the body, usually through administration to a nerve or nerve bundles (neuro-axial block, e.g. spinal, epidural). The work described in this chapter will focus on the capture of anaesthetics used for general anaesthesia that are inhaled.

Since the 19th Century many other compounds have been discovered and used for general anaesthesia, such as 1,1,2-trichloroethene (**Figure 5.1a**)[10] and cyclopropane (**Figure 5.1b**)[11]. The discovery of halothane (**Figure 5.1c**, 2-chloro-2-bromo-1,1,1-trifluoroethane) in 1955 as a non-flammable and non-pungent anaesthetic led to a decrease in the popularity of the traditional anaesthetics which were flammable and/or acted as irritants.[12] When administered, halothane maintained unconsciousness in patients at concentrations of less than 1%v; in a 40 year old male, of average weight, 0.75%v halothane is all that is required to keep the patient anaesthetised. The main disadvantage of halothane is that it can cause damage to the liver resulting in a condition known as halothane hepatitis.[13] For this reason halothane has been superseded by modern anaesthetics, namely isoflurane (**Figure 5.1c**, 2-chloro-2-(difluoromethoxy)-1,1,1-trifluoroethane), sevoflurane (**Figure 5.1d**, 1,1,1,3,3,3-hexafluoro-2-(fluoromethoxy)propane) and desflurane (**Figure 5.1e**, 2-(difluoromethoxy)-1,1,1,2-tetrafluoroethane). Of the three, isoflurane is now used less commonly for human patients but is still widely employed by veterinarians.[14]

a) b) c)

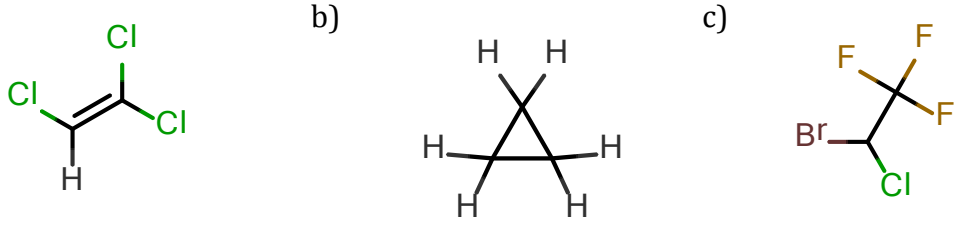

d) e) f)

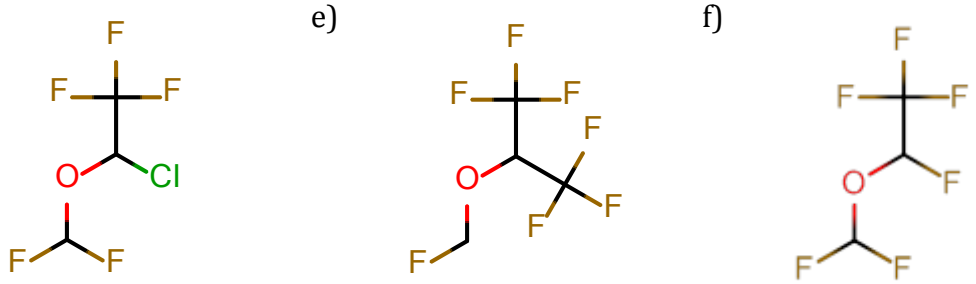

Figure 5.1: The anaesthetics **a)** trichloroethylene **b)** cyclopropane **c)** halothane **d)** isoflurane, **e)** sevoflurane and **f)** desflurane

The procedure commonly employed in modern anaesthesia involves administration of a variety of medications which lead to induction of unconsciousness, act as analgesics and promote muscle relaxation. These three are commonly referred to as the "The Triad of General Anaesthesia", **Figure 5.2**.[15]

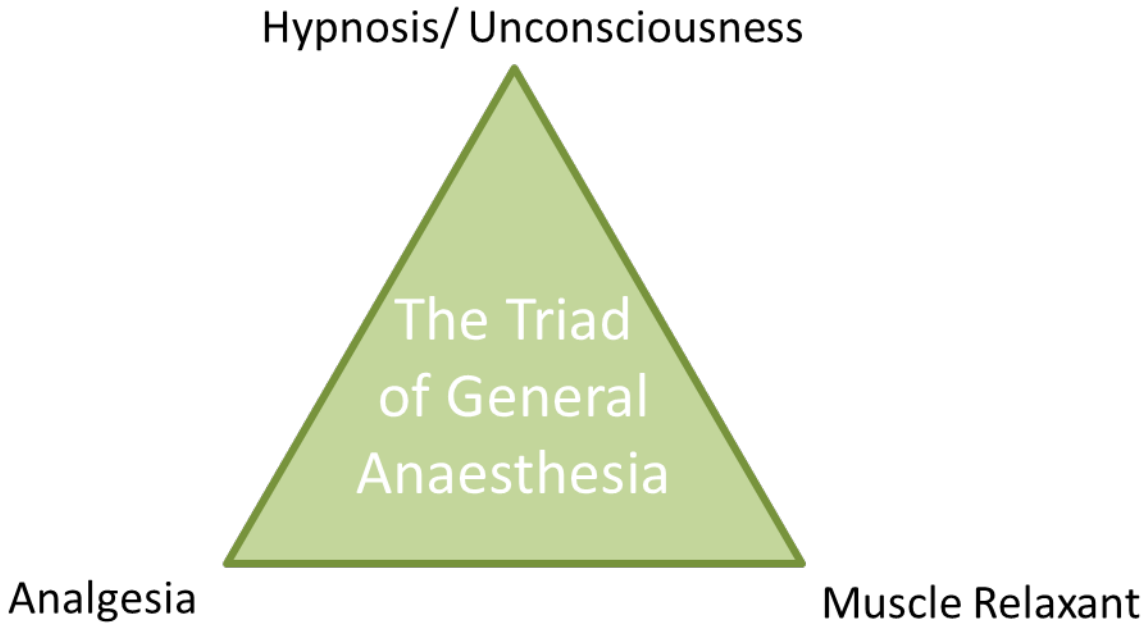

Figure 5.2: A visual representation of "The Triad of General Anaesthesia".

An anaesthetist may administer anywhere between three to fifteen different medications over the course of a procedure. Induction is achieved through drugs such as propofol, ketamine, etomidate and thiopental that are administered by intravenous injection with the purpose of inducing rapid loss of consciousness.[16] Analgesics used include opiates and narcotics, and are used to block pain responses from the patient.[17] Muscle relaxants, such as suxamethonium chloride, rocuronium and atricurium work primarily to relax the skeletal muscles of the body, allowing for lower doses of analgesics to prevent motor response.[18,19] Inhalation anaesthetics are used to maintain patient unconsciousness during the operation. As the name suggests, inhalation anaesthetics are administered continuously over the course of the operation through inhalation, through a face mask or more commonly intubation after unconsciousness. Modern inhalation anaesthetics, such as isoflurane, sevoflurane and desflurane, are very effective, requiring only very low concentrations to maintain unconsciousness. All are

volatile liquids with boiling points of 48.5, 58.6 and 23.5 °C for isoflurane, sevoflurane and desflurane respectively. **Table 5-1** below shows the minimum alveolar concentration (MAC) of some inhalation anaesthetics to maintain effectiveness.[20] Nitrous oxide may be used in conjunction with other anaesthetics, however, there is a growing trend away from this approach. In regards to the use of nitrous oxide, it is seldom used by itself as it would require hyperbaric conditions in order to maintain unconsciousness. It is most commonly used in combination with other anaesthetics.

Table 5-1: MAC (minimum alveolar concentration, %v) of inhalation anaesthetics that is needed to inhibit motor response in 50% of subjects in response to surgical stimulus*

Agent	**Age**		
	1 year	**40 years**	**80 years**
Halothane	0.95	0.75	0.58
Isoflurane	1.49	1.17	0.91
Sevoflurane	2.29	1.80	1.40
Desflurane	8.30	6.60	5.10
Nitrous Oxide	133	104	81

*Data from R. W. D. Nickalls, W. W. Mapleson, *Br. J. Anaesth.* 2003, *91*, 170–174[20]

The mechanism of action for inhalation anaesthetics is not well understood. In general the vast majority of the inhaled anaesthetic molecules (>95%) are exhaled in an unchanged form because the human body does not metabolise many of the commonly used inhalation anaesthetics.[21–25] Given that only a small proportion of inhaled anaesthetic is metabolised by the body, a substantial amount is released, upon

exhalation, into the environment. The exhaust of an anaesthesia machine is collected via vacuum and ultimately is released into the atmosphere. Given that isoflurane, sevoflurane and desflurane are all strong infrared absorbers and have long lifetimes in the environment there has been considerable interest in the effect these compounds have with respect to global warming. A common approach to quantifying the environmental impact of these halogenated ethers is to compare the global warming impact of these molecules with that of carbon dioxide. In this respect the Global Warming Potential index, (GWP_{20}) is commonly employed. The GWP_{20} index provides an indication of the relative contribution of a gas toward global warming over a 20 year timeframe normalised to carbon dioxide. By definition, the GWP of carbon dioxide over any time period is equal to 1. The GWP_{20} of isoflurane, desflurane and sevoflurane are 1800, 5550 and 795 respectively,[26] i.e. several hundred to thousands of times greater than that of carbon dioxide.

Nitrous oxide is not only a known greenhouse gas, but thought to be the dominant ozone depleting substance of the 21st Century.[27] Although medical procedures do contribute to N_2O emissions the main sources of N_2O emissions are from nitric acid and adipic acid production facilities.[28] Thus the release of anaesthetic gases/vapours poses a significant environmental problem as, in general, they are extremely potent greenhouse gases.[29]

Given there was estimated to be well over 300 million major surgical procedures performed throughout the world in 2012,[30] there is both an environmental and economic incentive to capture and recycle anaesthetic vapour.

One device that has been developed to capture inhalation vapours is the Anaesthetic Conservation Device (AnaConDa™)[31] which uses activated carbon as the absorptive material. AnaConDa™ is capable of reintroducing 90% of exhaled anaesthetic back to the patient, but needing replacement every 24 hours.[32] This was developed as a disposable replacement for anaesthesia machines, for use in the Intensive Care Unit (ICU).

Figure5.3: A photograph of the anaesthetic conservation device (AnaConDa™)[33]

A second approach to minimise the environmental impact of inhalation anaesthetics has been developed by the Canadian company, Bluezone. Bluezone produces canisters (marketed under the name, Deltasorb®) which employ a porous zeolite material (Deltazite®) as an adsorbent which is able to scavenge fluorinated ethers from the exhaust line of an anaesthetic machine. Once the canisters are full they are returned to

the manufacturer for recycling. The isoflurane absorption capacity of host material is reported as ~13 g of per 100 g of Deltazite®.[34] The anaesthetic vapour is removed by flushing the Deltazite® with pressurised steam.

In addition to activated carbon and zeolite materials other less conventional porous materials, such as discrete molecular systems have been investigated as host systems for anaesthetic capture.[35] In 2015 Teng-Hao Chen *et al* from the University of Houston synthesised an elegant self-assembled hydrogen bonded network material obtained by the crystallisation of 4-(4-{3,5-bis[2,3,5,6-tetrafluoro-4-(1H-pyrazol-4-yl)phenyl]phenyl}-2,3,5,6-tetrafluorophenyl)-1H-pyrazole. As indicated in **Figure 5.4** the molecule forms hydrogen bonds with identical molecules forming honeycomb-like sheets. The crystalline material is capable of absorbing approximately 60% by mass of sevoflurane and isoflurane. It remains to be seen if this material has a practical application given the anticipated economic challenges associated with generating the fluorinated compound on a commercial scale. Furthermore, it is not clear, given the nature of the hydrogen bonded network, that the material would be robust enough to survive repeated cycles of absorption and desorption.

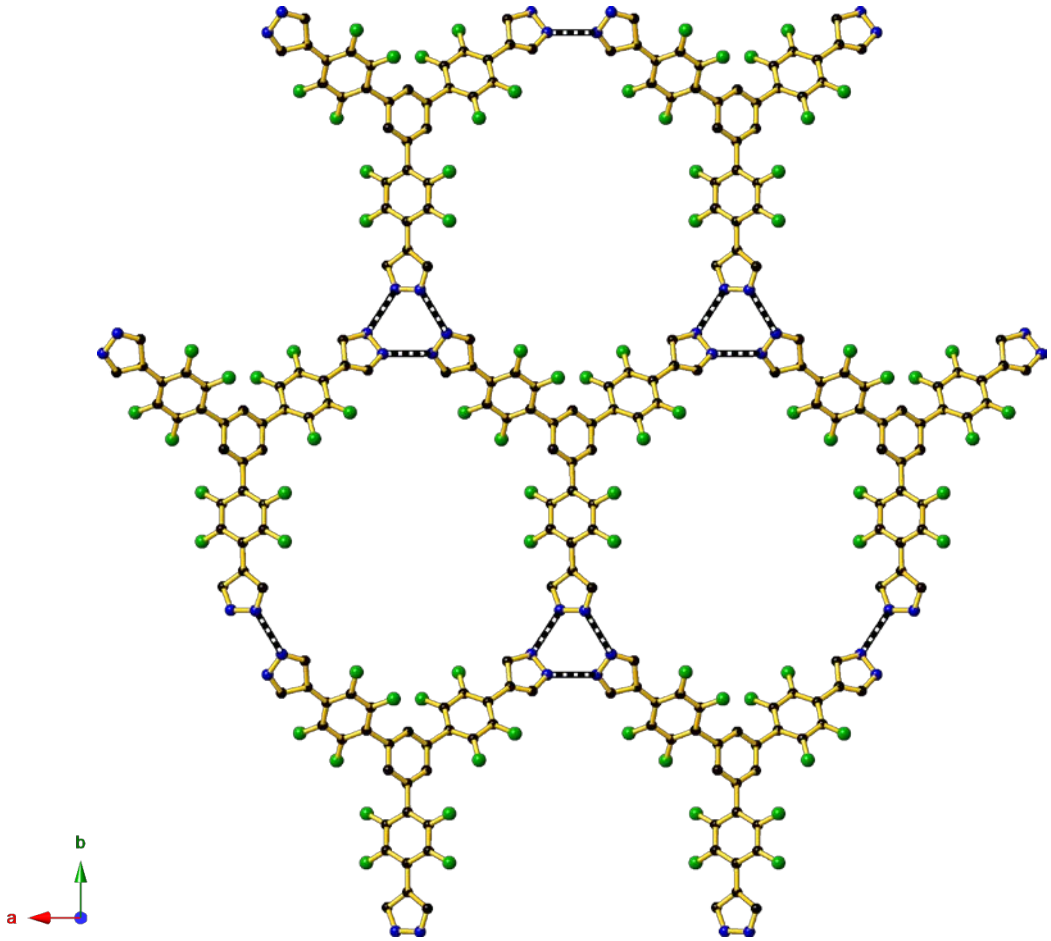

Figure 5.4: The extended structure of 4-(4-{3,5-bis[2,3,5,6-tetrafluoro-4-(1H-pyrazol-4-yl)phenyl]phenyl}-2,3,5,6-tetrafluorophenyl)-1H-pyrazole showing part of the 2D hydrogen bonded network. Hydrogen bonds are indicated with black and white striped connections. Hydrogen atoms have been omitted for clarity.

Materials such as activated carbons and zeolites are certainly capable of capturing inhalation anaesthetics, however, there is little prospect of fine-tuning the pores in these adsorbent materials to optimise capture storing and recycling of anaesthetic. Amongst a range of candidate materials, porous coordination polymers are particularly well-suited for the role of anaesthetic capture, recovery and storage because it is possible to exert control over pore size, shape and surface. Investigations involving the

capture, storage and recycling of N_2O,[36–39] and fluorinated ethers[35,40,41] by porous coordination polymers, have to-date been limited.

As part of investigations into robust porous networks described in the previous chapters, the porous coordination polymers of the Zn(hba) family of networks have been examined as potential test compounds for the capture and recycling of anaesthetic vapours.

The simple modular design of this family of coordination polymers means that the adsorption characteristics of the porous material may be controlled by selection of an appropriate phenolate-carboxylate ligand. Such control may make it possible to deliberately construct a porous network that is optimised for the capture, recovery or storage of a specific inhalation anaesthetic.

5.2 Work reported in this chapter

Presented in this chapter are the results of an investigation of the uptake of isoflurane and sevoflurane by Zn(hba) the family of networks described in the introduction and chapter 3. Although the use of N_2O as an anaesthetic is decreasing, it is still widely used. Thus, the adsorption properties of N_2O on the Zn(hba) family of networks are also described over a range of temperatures. In addition to the capture of isoflurane, sevoflurane and N_2O, this study has been extended to include xenon, which as discussed further in the chapter, exhibits a number of desirable features as an anaesthetic.

5.3 Anaesthetic gas uptake

Similar to the gas sorption experiments described in chapter 4, the gas adsorption isotherms of N_2O were measured at 258, 273 and 298 K on the compounds Zn(hbpc), Zn(hba), Zn(3-fluoro hba), Zn(2-fluoro hba), Zn(2-chloro hba), Zn(2-methyl hba) and Zn(2,6-dimethyl hba).

The most striking feature of **Figure 5.5** is the high adsorption of Zn(hbpc). The isotherm begins to plateau at a pressure of ~1500 kPa with an uptake greater than 500 mg/g, a value more than twice that found for Zn(hba). This result undoubtedly reflects the large cross-sectional area of the channels in Zn(hbpc). Whilst the isotherm shape for Zn(hbpc) appears to closely resemble a type I isotherm, it has a slight "s" shape. The s-shape is more pronounced in the 258 and 273 K isotherms (appendix A.1.4.2). Similar behaviour is found for CO_2 as described in section 4.5 of chapter 4. Unlike CO_2, however, when the equilibrium time for each data point measurement was extended beyond the normal period from 300 to 600 s (see section 4.5 of chapter 4 for further details relating to the equilibrium time) the s-shape remained unchanged. Extending the equilibrium time further from 600 to 1800 still resulted in no change in the isotherm. This is surprising as N_2O and CO_2 have similar, structures and are isoelectronic.

Similar to the isotherms obtained with CO_2 in chapter 4, the N_2O adsorption isotherms of Zn(hba), Zn(3-fluoro hba), Zn(2-fluoro hba), Zn(2-chloro hba) and Zn(2-methyl hba) resemble type 1 isotherms, as shown in **Figure 5.5**. Not surprisingly, given the absence

of halogen atoms or methyl groups on the phenyl ring in these networks, Zn(hba) shows the highest adsorption value although the adsorption of Zn(2-fluoro hba) is only marginally lower. Interestingly Zn(2,6-dimethyl hba) retains its s-shaped kink even after the equilibrium time of the gas adsorption experiment is set to 600 seconds. As indicated in section 4.5 of chapter 4, the corresponding CO_2 adsorption isotherm for Zn(2,6-dimethyl hba) have similar shapes. Additional isotherms measured at 273 and 258 K are presented in the appendix (appendix A.1.4).

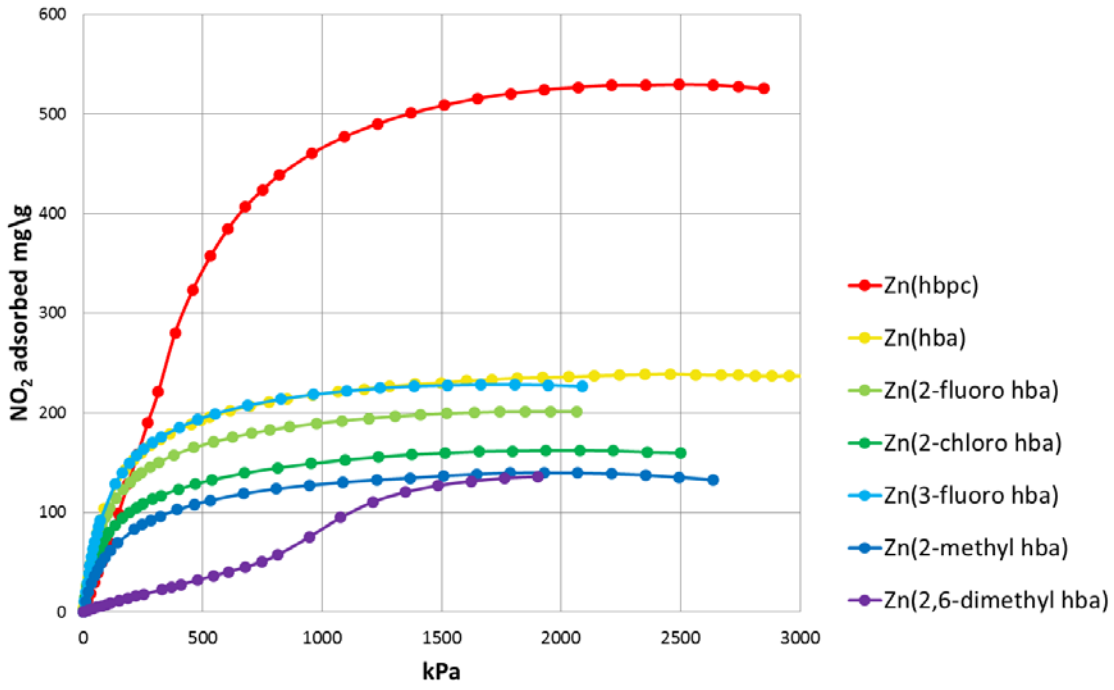

Figure 5.5: N_2O gas sorption isotherms of Zn(hbpc), Zn(hba), Zn(3-fluoro hba), Zn(2-fluoro hba), Zn(2-chloro hba), Zn(2-methyl hba) and Zn(2,6-dimethyl hba) measured at 298 K

With respect to the capture of anaesthetics under conditions that maybe found in a real application, comparisons are probably best made at pressures approaching 100 kPa.

The amount of N_2O adsorbed at 100 kPa is listed in **Table 5-2**. At atmospheric pressure, the absorbed nitrous oxide is significantly higher than that observed for the materials MOF-5 and MOF-177.[36] Zn(hba) and Zn(3-fluoro hba) adsorb similar amounts of N_2O to Ni-MOF and ZIF-7. Comparisons of the N_2O uptake with the materials, zeolites 4A and 5A (both distinct from Deltazite) reveal that Zn(hba) has a slightly lower capacity to zeolite 4A and half that of zeolite 5A under the same conditions.[36,42] (N_2O isotherms measured at 273 and 258 K are available in section A.1.4 of the appendix)

Table 5-2: Summary of uptake of N_2O at 100 kPa by the Zn(hba) family of networks in addition to selected MOF and zeolite-type materials.

	100 kPa adsorption (mg/g)
Zn(hba)	109
Zn(3-fluoro hba)	110
Zn(2-fluoro hba)	99
Zn(2-chloro hba)	78
Zn(2-methyl hba)	68
Zn(hbpc)	65
MOF-5[36]	50
MOF-177[36]	10
Ni-MOF[39]	125
ZIF-7[38]	110
Zeolite 5A[36]	180
Zeolite 4A[42]	150

The calculated N_2O isosteric adsorption enthalpies for Zn(hba) and its substituted derivatives were determined using isotherms collected at 258, 273 and 298 K. The Zn(hba) family of networks has N_2O binding enthalpies ranging from -29 kJ/mol to -32 kJ/mol, see **Table5-3**. The substituted materials, Zn(3-fluoro hba), Zn(2-fluoro hba), Zn(2-chloro hba), Zn(2-methyl hba) and Zn(2,6-dimethyl hba), all have slightly higher binding enthalpies than Zn(hba). This has been attributed to the narrower channels of the substituted networks allowing N_2O to interact with additional surfaces of the channel at once. Interestingly, while most of the compounds have similar binding enthalpies for CO_2, the binding enthalpy of Zn(3-fluoro hba) for CO_2 is calculated to be only -25 kJ/mol. This difference in binding enthalpy may prove advantageous if the separation of N_2O and CO_2 is required. (Q_{st} calculation details are available in section A.1.4 of the appendix)

Table5-3: Calculated binding enthalpies for the adsorption of N_2O by members of the Zn(hba) family of compounds

Compound	**Binding Enthalpy (kJ/mol)**
Zn(hba)	-29
Zn(3-fluoro hba)	-30
Zn (2-fluoro hba)	-32
Zn (2-chloro hba)	-31
Zn (2-methyl hba)	-30

With a MAC of 104% in an average 40 year old male, N_2O by itself would require hyperbaric conditions to achieve anaesthesia alone. During anaesthesia, N_2O is

generally used to reduce the MAC of a second inhalation agent and to increase the rate of induction. Gas combinations of N_2O and O_2, of up to 70% N_2O and 30% O_2, have been used as a carrier gas mixtures for the second inhalation agent.[43,44] The isotherms indicate that the Zn(hba) family of networks are capable of adsorbing N_2O at pressures that would be used with patients. Through the inclusion of appropriate functional groups on the aromatic ring(s) of the ligand, it may be possible to enhance the affinity of N_2O for the framework.

Storage containers filled with an adsorbent material, such as one of the Zn(hba) family of network materials, would allow considerable quantities of gases such as N_2O to be stored under much lower pressures than that commonly employed in metal cylinders. These storage containers, which would not require the strength of the metal cylinder but could hold a comparable quantity of N_2O are likely to be far less cumbersome and easier to transport. Lightweight alternatives may have application in the delivery of N_2O to remote areas for medical purposes, for example, assisting women in labour in isolated towns or villages. Given the high uptake of N_2O by Zn(hbpc) at moderate pressures (~10 atm), as indicated by the isotherm in **Figure 5.5**, Zn(hbpc) might be particularly well-suited to the role of as an adsorbent material on a lightweight storage device.

5.4 Fluorinated ether uptake

The ability of the Zn(hba) family of networks to capture volatile fluorinated ethers, such as isoflurane and sevoflurane was also examined. To determine if the material were

capable of accommodating the guest molecules within the pores of the network, a simple experimental procedure was developed in which the adsorbent material was placed on an analytical balance and exposed to vapour of a volatile anaesthetic. The change in mass of the sample upon adsorption of the fluorinated ether was then monitored.

The experimental setup used to monitor uptake of the volatile guest involved placing a glass bell jar over the powdered adsorbent sample while on the pan of an analytical balance, as indicated schematically in **Figure 5.6**. Using a quick fit connection at the top of the bell jar, a glass vessel containing liquid anaesthetic was suspended in the bell jar. As the vapour fills the chamber, the solid adsorbent material is able to capture the anaesthetic molecules. No attempts were made to control the temperature, with the measurement performed under ambient laboratory conditions, at an approximate temperature of 20 °C. The mass increases of the solid sample were monitored over time and the data was directly recorded onto a computer.

Whilst this experimental setup is somewhat crude in that there was no attempt to measure the vapour pressure within the bell jar, the screening measurements do provide a semi-quantitative indication of the ability of the various porous materials to capture volatile anaesthetics.

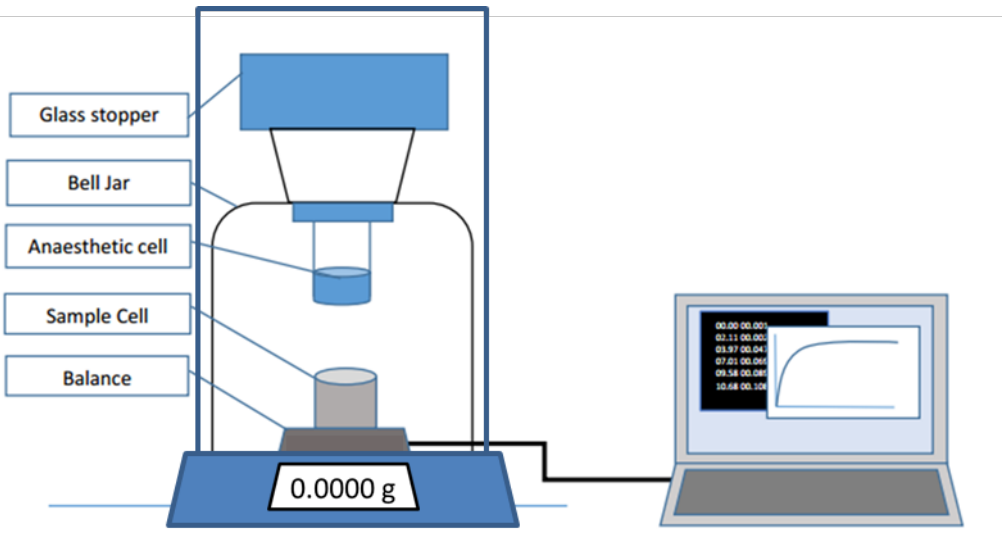

Figure 5.6: Diagram of the anaesthetic uptake measurement procedure

The uptake over time of each of the compounds examined is presented in **Figure 5.7**. Of the compounds investigated it was found that the frameworks with wider channels provide higher uptake of anaesthetic. This matches the general trends observed in the gas sorption results discussed in chapter 4. It is important to note that before the material was exposed to the fluorinated ether vapour that there was no mass increase indicating that the activated Zn(hba) family of networks were not adsorbing other gases or vapours (e.g. water) from the atmosphere to any significant extent.

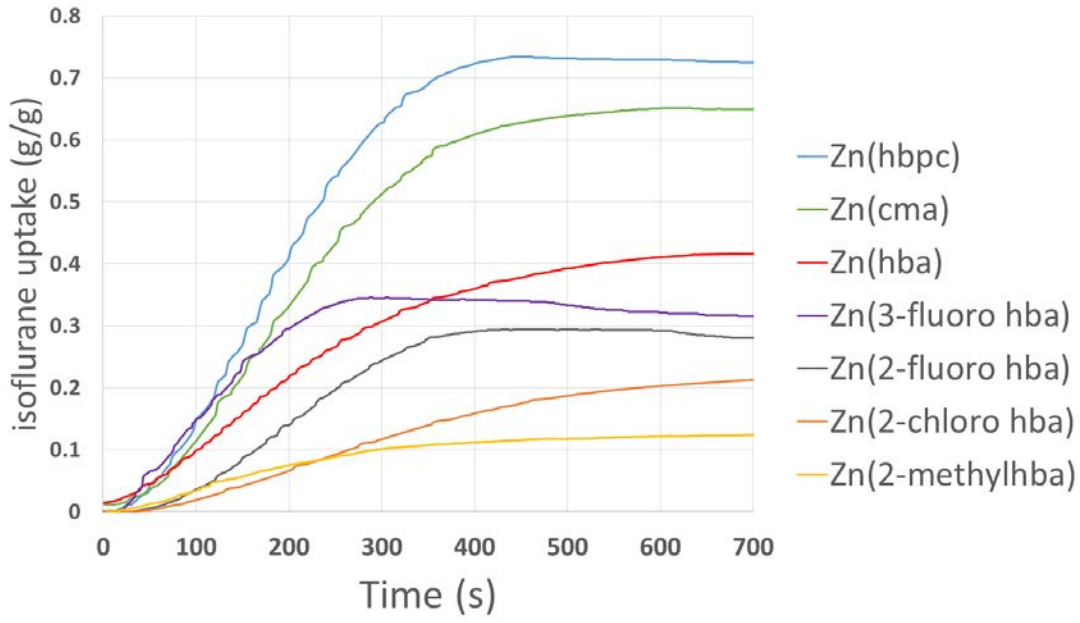

Figure 5.7: Uptake of Isoflurane over time in Zn(hbpc), Zn(cma), Zn(hba), Zn(2-fluoro hba), Zn(3-fluoro hba), Zn(2-methyl hba) and Zn(2-chloro hba)

Zn(hba) was found to adsorb approximately 400 mg/g of isoflurane. As indicated above, the networks with larger channels, Zn(cma) and Zn(hbpc), adsorb larger amounts of isoflurane, 650 and 720 mg/g respectively. Of the substituted networks, Zn(3-fluoro hba), Zn(2-fluoro hba), Zn(2-methyl hba) and Zn(2-chloro hba), adsorb less isoflurane than Zn(hba), 350, 300, 200 and 120 mg/g respectively. A small mass loss is apparent for Zn(3-fluoro hba) and Zn(2-fluoro hba).

TGA was performed on a Zn(hba), that had been exposed to isoflurane, between 25 and 350 °C, (**Figure 5.8**), to assess how well the host material holds onto the isoflurane once removed from exposure to the vapour. The TGA trace shows that Zn(hba) loaded with isoflurane undergoes a mass loss of ~25% when heated to above 60°C. This corresponds to a ~83% retention of the isoflurane that was originally adsorbed by

Zn(hba). Also shown in **Figure 5.8** is the TGA trace for the activated (desolvated) parent network. As expected it shows negligible change in mass over the temperature range 25 to 350 °C.

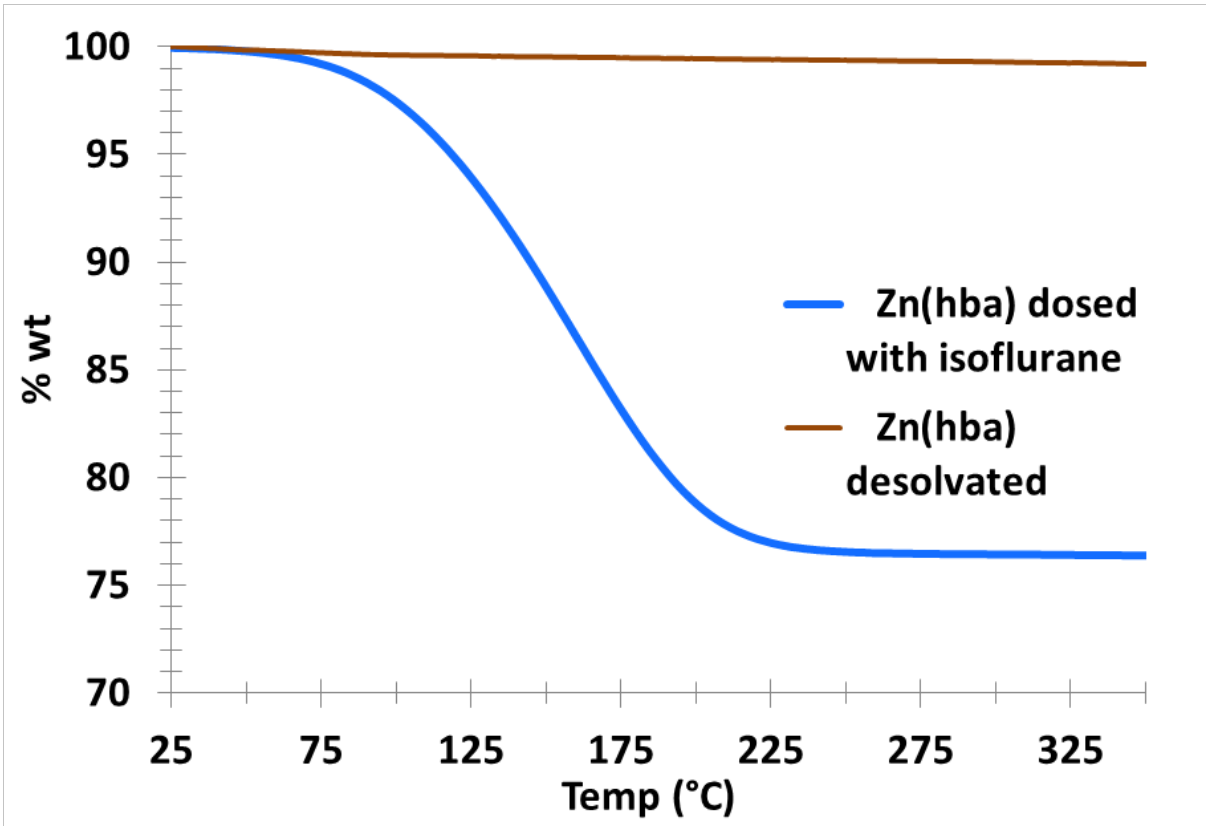

Figure 5.8: TGA of Zn(hba) conducted between 25 to 350°C. Zn(hba) represented by the brown line is the activated Zn(hba) material, while the blue line represents activated Zn(hba) that has been exposed to isoflurane vapour.

Encouraged by this preliminary investigation of isoflurane, a collaboration was established with Dr Peter Southon and Prof Cameron Kepert of the School of Chemistry at the University of Sydney in order to determine the uptake of the anaesthetic over a wide range of partial pressures, employing a more quantitative approach. These measurements were performed using an Intelligent Gravimetric Analysis (IGA)

instrument at the University of Sydney. Under the operation of Dr Peter Southon isotherms measured at 298 K are presented in **Figure 5.9**. Remarkably, the majority of the isoflurane adsorption took place at very low pressures, <0.5 mbar, much lower than the concentration administered to patients, which is approximately 20 mbar during the maintenance phase of the anaesthetic delivery (for an average 40 year old male patient). Higher vapour pressures are commonly employed during the initial stages of anaesthesia.[45]

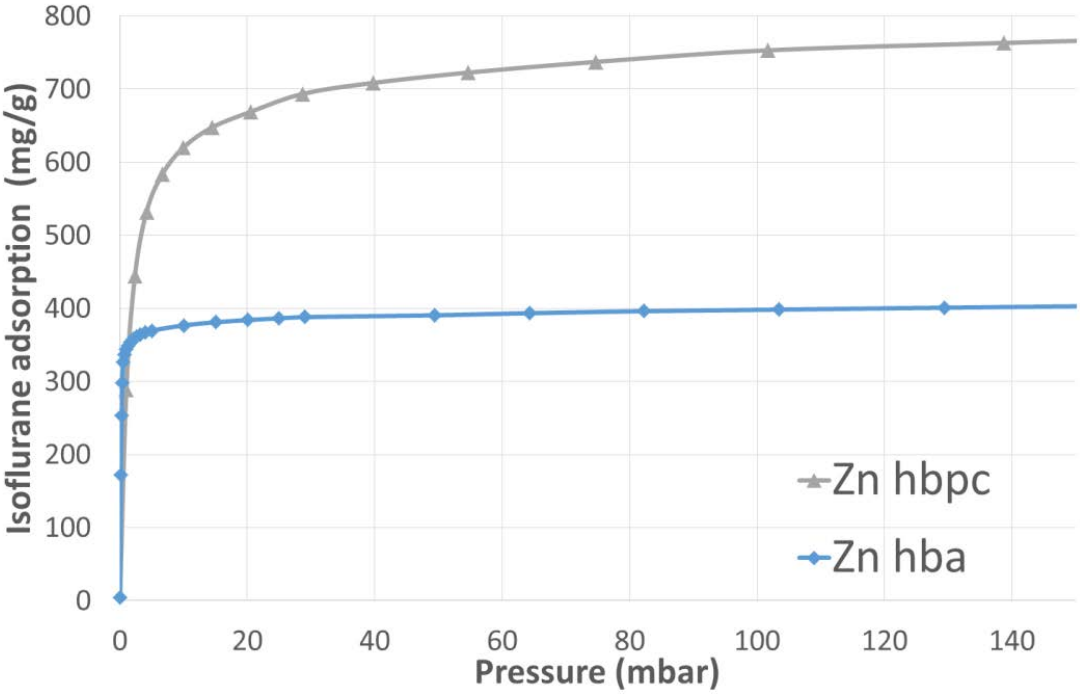

a)

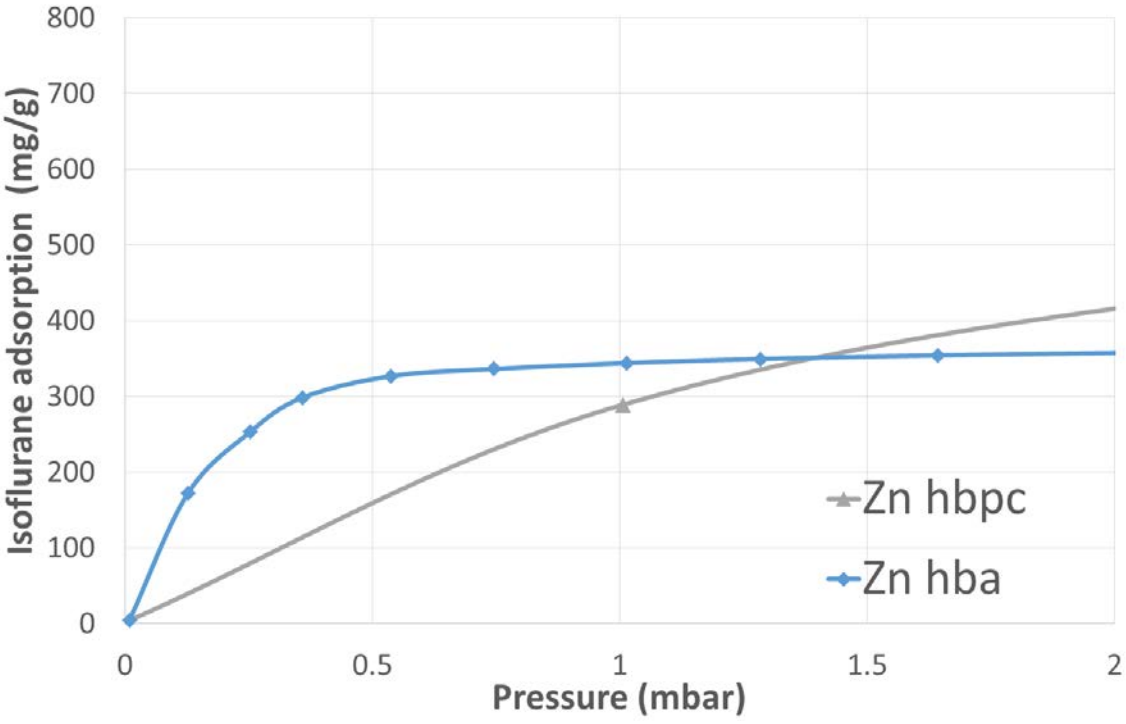

b)

Figure 5.9: Isotherms indicating the uptake of isoflurane by of Zn (hba) and Zn(hbpc) at 298 K **a)** between 0 and 150 mbar **b)** between 0 and 2 mbar.

Encouraged by the results, further anaesthetic uptake measurement using the bell jar method described earlier were conducted with sevoflurane. The resulting mass changes are presented in **Figure 5.10**.

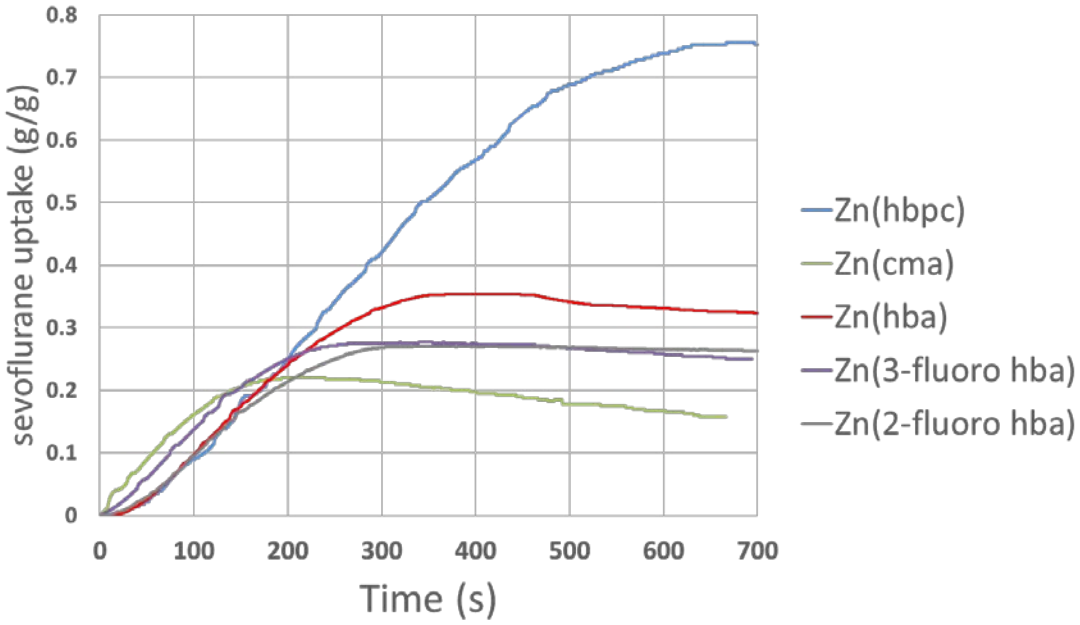

Figure 5.10: Uptake of Sevoflurane over time in Zn(hbpc), Zn(cma), Zn(hba), Zn(2-fluoro hba) and Zn(3-fluoro hba).

Of the seven compounds tested, only Zn(hba), Zn(2-fluoro hba), Zn(3-fluoro hba) and Zn(hbpc) adsorbed sevoflurane in substantial quantities. While Zn(cma) takes up sevoflurane initially, the balance shows a drop in mass consistant with the loss of the sevoflurane. Although Zn(hba), Zn(3-fluoro hba) show a small loss of sevoflurane overtime it is nowhere to the same extent as Zn(cma). Zn(2-methyl hba) and Zn(2-chloro hba) did not take up sevoflurane. This may be due to the methyl\chloro groups present in the frameworks making the channels too small for sevoflurane to enter. It is reasonable to expect that isoflurane has a smaller kinetic diameter than sevoflurane in the vapour phase. It is uncertain why Zn(cma) adsorbs significantly less sevoflurane

than isoflurane, yet Zn(hbpc) adsorbs similar amounts of sevoflurane and isoflurane. One hypothesis is that the larger channels in Zn(cma) do not allow sevoflurane to interact with multiple surfaces at once, decreasing the affinity the sevoflurane has for the network. On the other hand, in Zn(hbpc) a 'cooperative adsorption' effect may take place where the sevoflurane is capable of interacting with the channel walls of Zn(hbpc) as well as a number of adjacent sevoflurane molecules, as indicated in **Figure 5.11**. Of course this is only speculation. Compared to the isoflurane uptake in the Zn(hbpc), the sevoflurane uptake seems to be slower, taking more time to plateau. Isoflurane uptake in Zn(hbpc) reaches maximum adsorption at approximately 400 seconds, in the sevoflurane uptake the maximum is only reached after 650 seconds. This difference may reflect the lower volatility of sevoflurane resulting in a larger time required to reach liquid-vapour equilibrium.

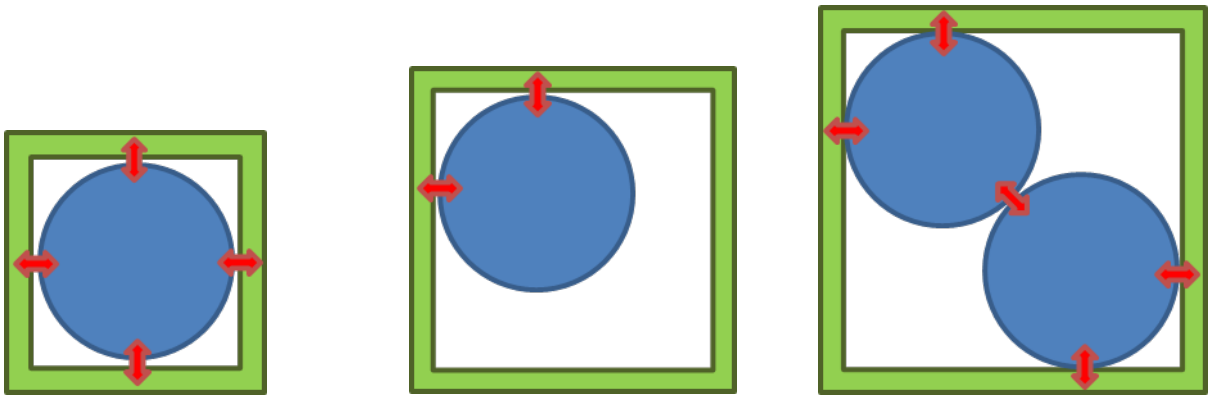

Figure 5.11: A representation of a guest molecule, shown as a blue circle, interacting with the surfaces of a channel, shown in green. **a)** the guest is capable of interacting with four surfaces at once, highlighted with a red double headed arrow. **b)** the guest molecule is only capable of interaction with two surfaces at once. **c)** the guest molecule is capable of interaction with two channel surfaces as well as an adjacent guest molecule.

Further experiments conducted by Dr Southon showed that the uptake behaviour of sevoflurane in the Zn(hba) material was almost identical to that of isoflurane, **Figure 5.12**.

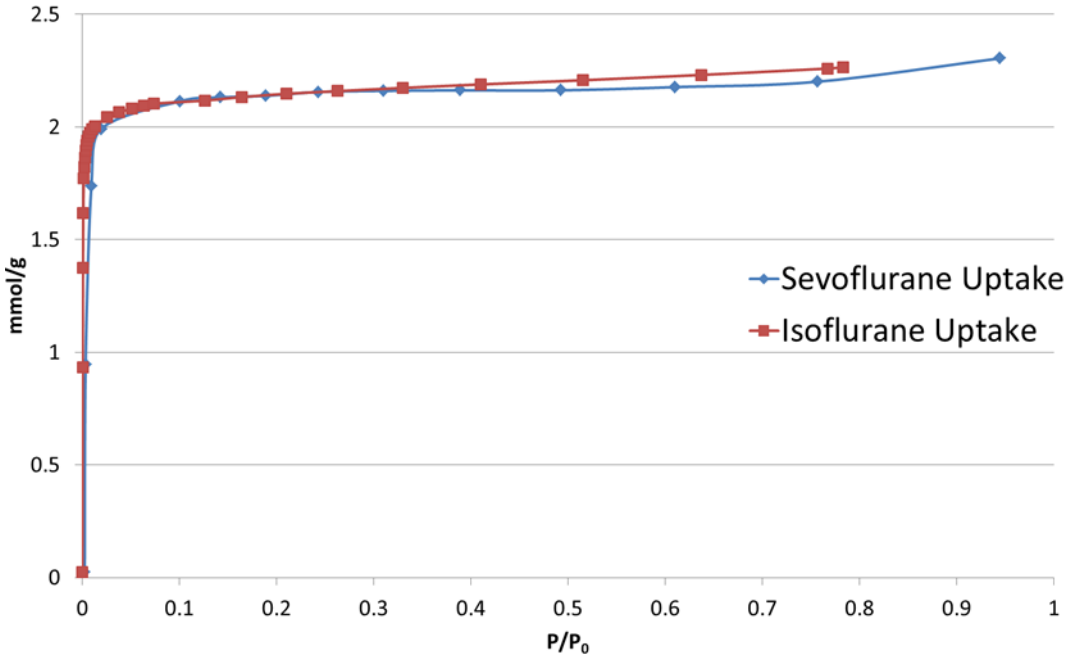

Figure 5.12: Isotherms comparing the uptake of sevoflurane and isoflurane in Zn(hba) at 298 K.

The maximum uptake of isoflurane and\or sevoflurane for Zn(hbpc), Zn(cma), Zn(hba), Zn(2-fluoro hba), Zn(3-fluoro hba), Zn(2-methyl hba) and Zn(2-chloro hba) as well as other MOFs in the literature are presented in **Table 5-4**.

Table 5-4: Zn(hbpc), Zn(cma), Zn(hba), Zn(2-fluoro hba), Zn(3-fluoro hba), Zn(2-methyl hba), Zn(2-chloro hba) and MOF\PCP materials in the literature and their corresponding maximum uptake of isoflurane and\or sevoflurane.

Compound	Anaesthetic	Absorbed amount (mg/g)
Zn(hba)	Isoflurane†	417
	Sevoflurane†	450
Zn(cma)	Isoflurane	650
	Sevoflurane	220
Zn(hbpc)	Isoflurane†	775
	Sevoflurane	750
Zn(3-fluoro hba)	Isoflurane	350
	Sevoflurane	270
Zn(2-fluoro hba)	Isoflurane	300
	Sevoflurane	270
Zn(2-methyl hba)	Isoflurane	120
Zn(2-chloro hba)	Isoflurane	220
Cr-MIL-101 pellet[41]	Sevoflurane	900
Cr-MIL-101 powder[40]	Sevoflurane	1500
Fluorinated trispyrazole-based framework [35]	Isoflurane	598
	Sevoflurane	594

†IGA measurements preformed at the University of Sydney **Figure 5.9** and **Figure 5.12**.

The Zn(hba) family of frameworks have been shown to adsorb between 120 mg/g to 775 mg/g of isoflurane. Whilst there have been only limited studies of uptake of fluorinated ethers by network materials it is interesting to compare the adsorption measured in this current work with literature examples. One of the most porous MOF-type materials, with a reputation for high capacity, is MIL-101. In its powdered form Cr-MIL-101 adsorbs approximately twice as much as Zn(hbpc) but only 20 % more if compared to Cr-MIL-101 in it pelletised form.[40,41] The fluorinated hydrogen bond network described earlier and represented in **Figure 5.4** was shown to adsorb amounts of sevoflurane and isoflurane intermediate between Zn(hba) and Zn(hbpc). It is noted that the presence of halogen and methyl groups on the phenyl lead to a reduction in adsorption capacity. It should be recognised however that high capacity is only one of a number of important considerations in identifying the best adsorbent material. Retention of the guest molecules, recyclability, cost of the material, in addition to environmental considerations will also be factors that need to be taken into account with respect to identifying the best adsorbent material for fluorinated ethers.

In order to firmly establish that Zn(hba) is capable of absorbing fluorinated ethers under "real world" conditions a collaborative effort was established with an anaesthetist (Dr Forbes McGain) at a major hospital, Western General hospital, Sunshine (a suburb in Melbourne, Victoria). A "prototype" anaesthesia uptake device that would be capable of being inserted between the anaesthesia machine and the wall exhaust, ensuring the waste anaesthetic gas would go through the prototype anaesthesia device before being exhausted into the outside atmosphere, **Figure 5.13**, was developed.

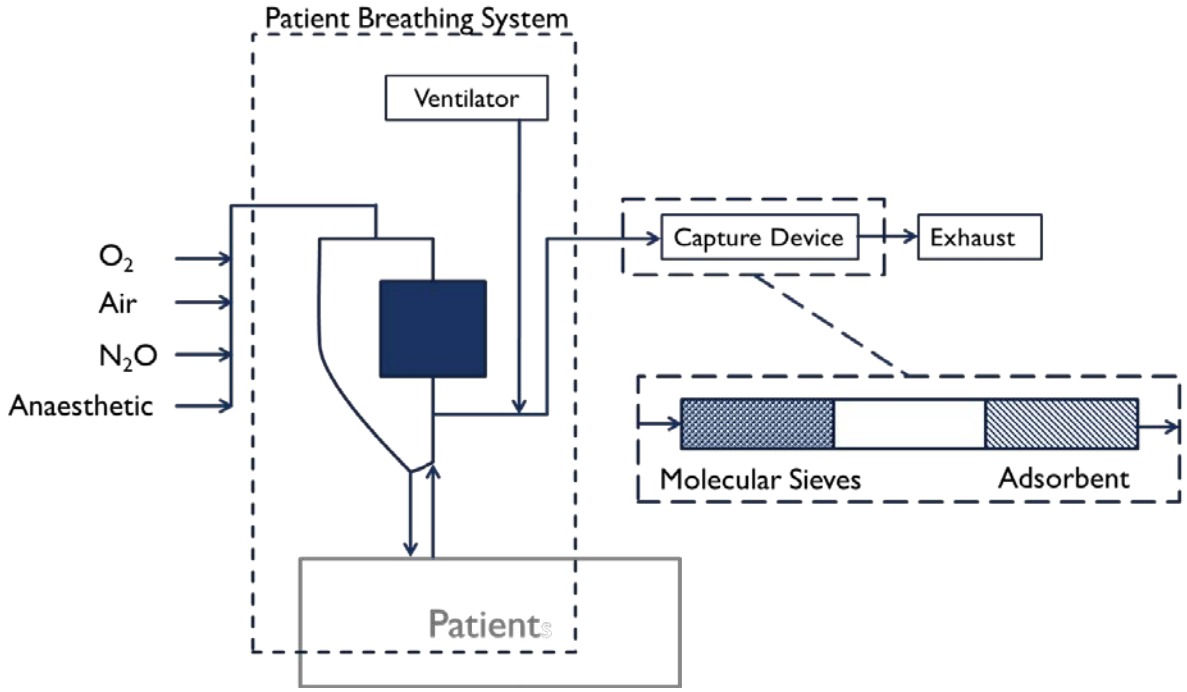

Figure 5.13: Diagram of the an anaesthesia machine with our capture divice spliced in just before the exhaust

The device consisted of two taps to allow easy isolation of the materials from the exhaust and two glass chambers, the first filled with molecular sieves (Zeolite 3A, tested and found to not adsorb anaesthetic) and the latter with our adsorbent material, **Figure 5.14**. The purpose of the molecular sieves was to ensure that all mass gain by the material could be attributed to the anaesthetic vapour, even though preliminary investigations show that the activated material did not readily adsorb moisture from the atmosphere. The secondary glass chamber was designed such that it could be easily detached and independently weighed.

Figure 5.14: A Picture of the prototype anaesthetic capture device

A vacuum cable, **Figure 5.15**, was kindly donated by Dr McGain to facilitate connection to the anaesthesia machine. The purple connection is screwed into the anaesthesia machine, while the yellow connection is screwed into a vacuum line fitted into the wall of operating theatre, **Figure 5.16**. This cable was cut in half and both cut ends connected to the prototype capture device. Once attached to the anaesthesia machine, vacuum would pull waste anaesthetic gas out of the anaesthesia machine and through the prototype capture device.

Figure 5.15: A vacuum cable held by Associate Professor Brendan Abrahams. The purple connection is screwed into the anaesthesia machine while, the yellow connection is screwed into a vacuum line fitted on a wall mount in the operating theatre.

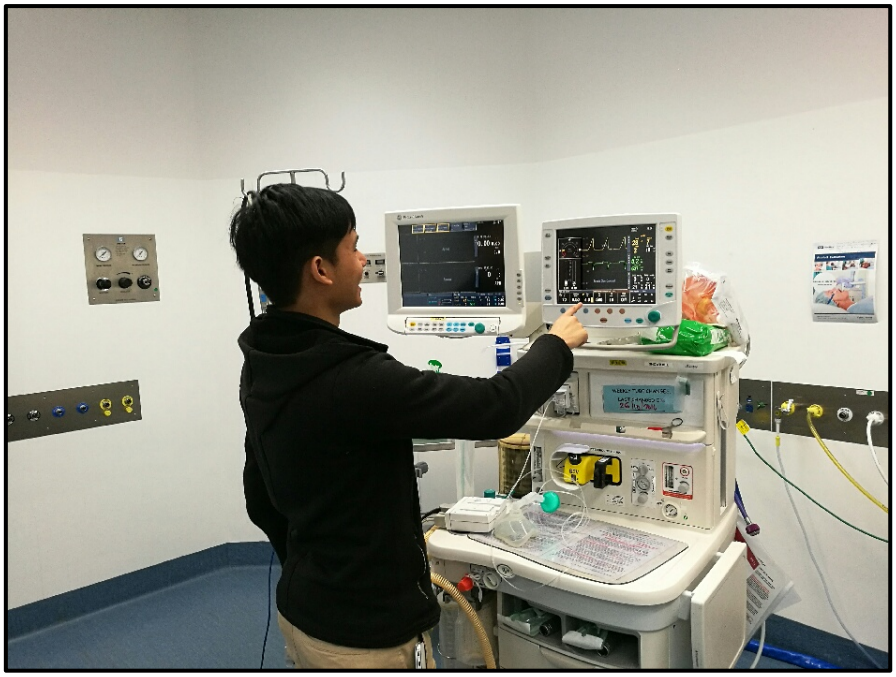

Figure 5.16: The anaesthesia machine used in the initial sevoflurane capture experiments. The wall mounted vacuum lines are visible behind the anaesthesia machine.

Initial experiments have shown that at 1 L/min for 10 minutes of 4% sevoflurane the Zn(hba) material was able to capture ~74 % of the sevoflurane that passed through the machine, showing anaesthetic capture under "real world" conditions. Sevoflurane was able to be isolated from Zn(hba) loaded with sevoflurane at Sunshine Hospital. Zn(hba) loaded with sevoflurane was heated to 60 °C under vacuum. The sevoflurane was able to be condensed by cooling the vapours using either liquid nitrogen or an acetone and dry ice mixture. The purity of the sevoflurane was confirmed with ^{1}H and ^{19}F solution NMR spectra.

Although Zn(hba) was demonstrated to capture sevoflurane, the introduction of the anaesthetic capture device restricted the flow of the anaesthesia to below acceptable

limits. The Zn(hba) powder was too densely compacted to facilitate appropriate exhaust flow. One strategy that is currently being explored is the pelletisation of the Zn(hba) material. Recent results have shown some success with pellets made from 2 wt% polymethyl methacrylate as well as pellets made from 10 wt% polytetrafluoroethene powder.

5.5Xenon

Although not in routine use, xenon is able to act as an anaesthetic.[46–55] Xenon was first discovered by British chemists Sir William Ramsay and Morris W. Trave in 1898, but it was not until the 1940s that the anaesthetic effects of xenon were first demonstrated by J. H. Lawrence.[56] In regards to its medical application, many anaesthetists claim that xenon has the characteristics of an ideal inhalation anaesthetic agent, having many beneficial effects over common modern anaesthetics. It is non-flammable, non-explosive, has low toxicity, is environmentally benign, organ protective[46–48], allows rapid induction/emergence,[49] has more favourable hemodynamic, neurohumoral and anti-nociceptive properties,[50] requires lower propofol dosage to inhibit reaction to surgical stimulus,[51] and is 1.5 time more potent than nitrous oxide.[52] Furthermore, xenon has also displayed seemingly unique neuroprotective properties.[53–55] Unfortunately, however, xenon's widespread use is currently not practical due to the high production cost, which is associated with its isolation from air.[57]

Xenon is produced mainly as a by-product of industrial oxygen production; approximately 10 million m^3 of air is required to obtain 1 m^3 of xenon. A major cost is

associated with the cryogenic distillation of xenon and krypton. Medical grade high purity xenon can cost as much as USD$5000 per kg.[58]

A cost analysis simulation of xenon as an anaesthetic, based on a 40-year-old patient model weighing 70 kg undergoing elective minor surgery with endotracheal intubation and mechanical ventilation was conducted in 1999. The cost of the anaesthetic for the 240 minute surgery was predicted to cost USD$356 for closed-circuit xenon, USD$52 for closed-circuit nitrous oxide-isoflurane, USD$94 for semi-closed nitrous oxide-isoflurane and USD$84 for semi-closed technique with nitrous oxide-sevoflurane.[59]

To alleviate the energy and capital intensive cryogenic purification of xenon, adsorptive separation of xenon from other noble gases, such as krypton, using porous materials has been investigated. Both zeolite[60] and zeolite-like[61] porous materials have been considered. Recently, porous coordination polymer/MOF materials have also been tested for their potential in aiding the gas separation of xenon and krypton. Thallapally *et al* in 2012 demonstrated the greater xenon selectivity of NiDOBDC (also known as Ni-MOF-74 or CPO-27-Ni) compared to MOF-5 and activated carbon.[62] Following the success of the capture of fluorinated anaesthetics in the Zn(hba) family of networks, we reported the potential use of the Zn(hba) family of networks for xenon recovery used in anaesthesia.[63] Further work by Thallapally and co-workers has shown that MOFs PCN-12, HKUST-1 and NiDOBDC can be used for anaesthetic xenon recovery.[64] The efficient capture and reuse of xenon from waste anaesthesia gas may lead to viable widespread use of this ideal anaesthetic.

One such recycling device, developed by Georgieff and co-workers in Ulm, Germany, is able to remove accumulated nitrogen, oxygen, and volatile organics to obtain relatively pure xenon. A cold trap removes the volatile substances and the remaining gas mixture of oxygen nitrogen and xenon is compressed (55 atm) and cooled (< 16 °C) to condense liquid xenon (xenon 89%, oxygen 8.2%, nitrogen 3.8%). [65] Dingley and Mason have also developed a cryogenic scavenging system, achieving up to 98.2% xenon recovery.[66]

It was found that the Zn(hba) family of compounds has a high affinity for the adsorption of xenon, potentially capable of capturing xenon from waste anaesthesia. The xenon gas sorption isotherms at 298, 273 and 258 K were measured on Zn(hba), Zn(hbpc), Zn(2-fluoro hba) and Zn(2-methyl hba). Unfortunately, due the cost of xenon, gas sorption isotherms were only completed on selected members of the Zn(hba) family of compounds. The 298 K xenon uptake isotherms for Zn(hba), Zn(hbpc), Zn(2-fluoro hba) and Zn(2-methyl hba) are displayed in **Figure 5.17**. Similar to the CO_2, H_2 and N_2O uptake isotherms discussed earlier, the Zn(hbpc) xenon isotherm shows a step in the adsorption isotherm at approximately 250 kPa. The material shows steady, almost linear, uptake of xenon up until 250 kPa of xenon, at which point the uptake sharply increases. Only after the pressure rises above 300 kPa does the isotherm begin to plateau, resulting in an overall xenon uptake of 1020 mg/g at close to 1000 kPa.

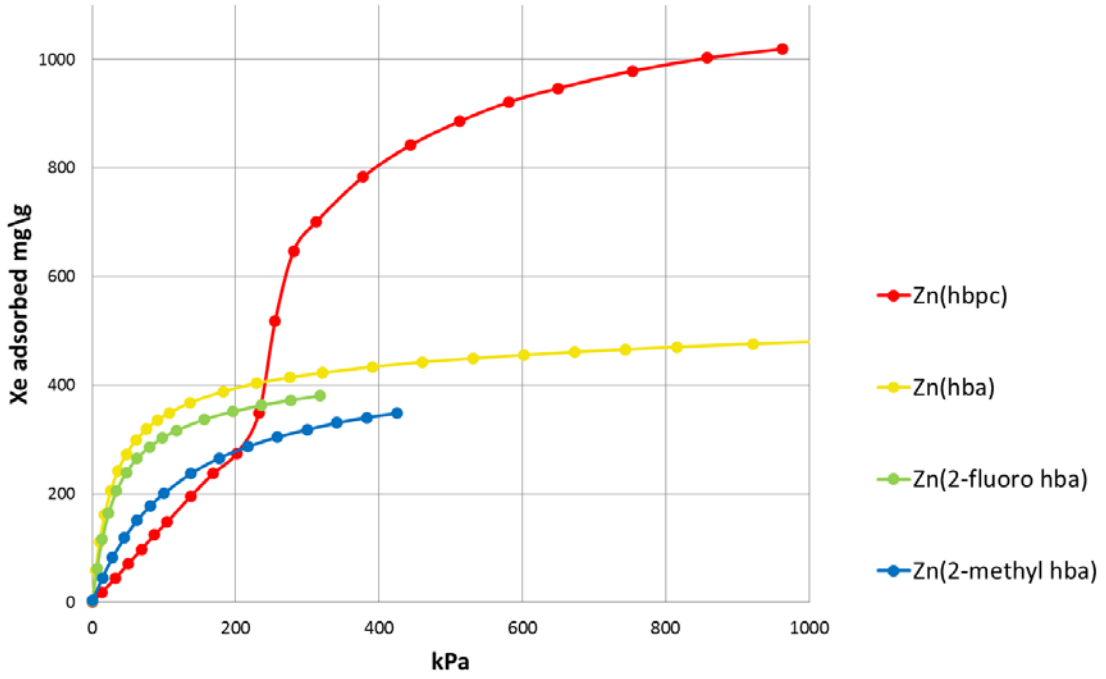

Figure 5.17: The 298 K Xenon uptake isotherms of Zn(hba), Zn(2-fluoro hba) and Zn(2-methyl hba)and Zn(hbpc)

The calculated xenon isosteric adsorption enthalpies for Zn(hba), Zn(2-fluoro hba) and Zn(2-methyl hba) were determined using isotherms collected at 258, 273 and 298 K. The initial adsorption phase isosteric heat of adsorption enthalpy values are presented in **Table 5-5**. (Q_{st} calculation details and Xe isotherms measured at 273 and 258 K are available in section A.1.5 of the appendix)

Xenon has a van der Waals radii of 2.16 Å.[67] Zn(hba) has a channel diameter of ~5.5 Å, van der Waals surface to van der Waals surface, and a xenon binding enthalpy of -27 kJ/mol. Zn(2-fluoro hba) has a binding enthalpy of -29 kJ/mol. The higher binding enthalpy is attributed to the narrower channels of Zn(2-fluoro hba) compared to

Zn(hba). Zn(2-methyl hba) has the highest binding enthalpy at -34 kJ/mol. Simulations provided by Dr Babarao (see section 3.3 of chapter 3) indicate that Zn(2-methyl hba) has similar channel width but with methyl groups protruding into the channel. The Zn(2-methyl hba) coordination polymer has amongst the highest reported binding enthalpy for xenon, **Table 5-5**. Not surprisingly, MOF materials with large intra-framework voids (MOF-5, MOF-74-Ni, Cu(HFIPBB) and MFU-41) have significantly lower binding enthalpies for xenon. Like the Zn(hba) family of networks, SBMOF-1 is also a porous material with non-intersecting channels and possesses a high a xenon binding enthalpy of -35 kJ/mol. It is apparent that frameworks possessing channels with a diameter close to that of the atomic diameter of xenon have superior xenon binding enthalpy.

Table 5-5: Xenon binding enthalpies in the Zn(hba) family of compounds in addition to common network materials

Compound	**Xe Binding Enthalpy (kJ/mol)**
Zn(hba)	-27
Zn(2-fluoro hba)	-29
Zn(2-methyl hba)	-34
MOF-5[62]	-15
MOF-74-Ni[62]	-22
Cu(HFIPBB)[68]	-15
MFU-41[69]	-20
HKUST-1[69]	-27

$Co_3(HCOO)_6$[70]	-28
SBMOF-1[71]	-35
CROFOUR-1-Ni[72]	-37

Given the ability to tailor coordination polymers by adding substituents or functional groups, to the selected framework further optimisation of the binding properties of Zn(hba) family of compounds for xenon adsorption may be possible. For example, additional gas adsorption experiments using different functionalised derivatives of the Zn(hba) family of frame works may give clues toward maximising the binding enthalpy of the material. Furthermore, the framework may be simultaneously designed for unfavourable sorption of krypton to aid xenon purification. Xenon/krypton selectivity has been strongly linked to 1-D channels with a pore diameter only slightly larger than the kinetic diameter of xenon.[73,74] It is foreseeable that if the theoretical sweet spot pore diameter can be achieved with a favourable chemical environment, then an ideal separation agent may be synthesised.

Although Zn(hba), Zn(2-fluoro hba), Zn(2-methyl hba)and Zn(hbpc) have been shown to adsorb xenon, additional work must be completed to ascertain if these compounds are capable of selectively capturing/separating xenon from gas mixtures. Due to financial restraints and the prohibitive cost of xenon, further gas sorption experiments were beyond the scope of this thesis.

5.6 Concluding remarks

The Zn(hba) family of network materials have been shown to adsorb the inhalation anaesthetics N_2O, isoflurane and sevoflurane.

The isotherms indicate that the Zn(hba) family of networks are capable of adsorbing N_2O at pressures that would be exposed to patients. Further modification of the Zn(hba) family of networks with appropriate functional groups may enhance the N_2O binding enthalpy of the framework. The high overall uptake capacity of Zn(hbpc) for N_2O indicates that it may be suited as a medium for long term storage of nitrous oxide under moderate pressure.

Preliminary investigations have shown that Zn(hba) is capable of adsorbing significant quantities of isoflurane and sevoflurane at partial pressures less than that which would be exhaled by a patient. A prototype anaesthetic capture device loaded with Zn(hba) was capable of capturing 74% of the total sevoflurane that passed through an anaesthesia machine. Sevoflurane which was captured on Zn(hba) at Western General Hospital was able to be transported back to the University of Melbourne and isolated. The material was heated at 60 °C under vacuum and the recovered sevoflurane vapour was condensed back into liquid form using either liquid nitrogen or acetone/dry ice. Less energy intensive sevoflurane condensation methods are currently being explored. Work beyond the scope of this thesis, but currently ongoing, relates to the pelletisation of Zn(hba) using the binding agents polymethyl methacrylate and

polytetrafluoroethene. Further refinement in the pelletisation process is required to ensure structural integrity of the pellet without sacrificing overall uptake.

Xenon has the characteristics of an ideal inhalation anaesthetic agent, having many beneficial effects over common modern anaesthetics. The cost associated with the isolation of xenon prohibits its widespread use as an inhalation anaesthetic. Zn(hba), Zn(2-fluoro hba), Zn(2-methyl hba)and Zn(hbpc) have been shown to able to adsorb xenon, with Zn(2-methyl hba) having a particularly high xenon binding enthalpy. Frameworks that have non-intersecting channels, whose dimensions are close to the van der Waals diameter of xenon are shown to have high xenon binding enthalpy. Additionally creating a material that facilitates the separation of xenon and krypton, may reduce an important costly process in the isolation of xenon gas.

Of additional interest is the capture of radon. Like xenon, radon is a naturally occurring odourless and colourless noble gas. Unlike the rest of the noble gases, however, radon is radioactive. Discovered in 1900 by Professor Friedrich Ernst Dorn,[75] radon is produced in nature primarily from the radioactive decay of ^{226}Ra,[76] which itself is found in phosphate rock, shales, granite, gneiss, schist, and limestone.[77–85] Radon gas generated in the soil is thought to migrate into the basement or ground level of houses through cracks and openings.[86–88] Radon gas released by building materials has also become an important pollutant in indoor air. Main sources of radioactive ^{222}Rn include indoor building material such as plaster, granite brick sand and cement.[89] Radon has been found to build up to relatively high concentrations in enclosed spaces with a low

degree of air movement.[90] Inhalation of air with high concentrations of radon over long periods of time has been linked to elevated risk of lung cancer.[91,92] Radon may be responsible for up to 22,000 lung cancer related deaths in the USA each year.[93] ^{222}Rn itself has a half-life of 3.8 days, allowing it to diffuse through soil and into the air before decaying by α particle emission. Radon's decay products, ^{218}Po and ^{214}Po, are both solid α-particle emitters with much shorter half-lives, and tend to deposit on the bronchial epithelium with dust particulates, exposing the cells to α-particles.[89] The radon decay chain is shown in **Figure 5.18**.

Tailoring the pores of Zn(hba) to match the size of radon may lead to a material that can passively capture radon in open air, lowing the risk of lung cancer to occupants or workers who are exposed to radon emitting sources on a daily basis. Perhaps, frameworks with non-intersecting channels, whose dimensions are close to the atomic diameter of radon, may have high affinity for radon.

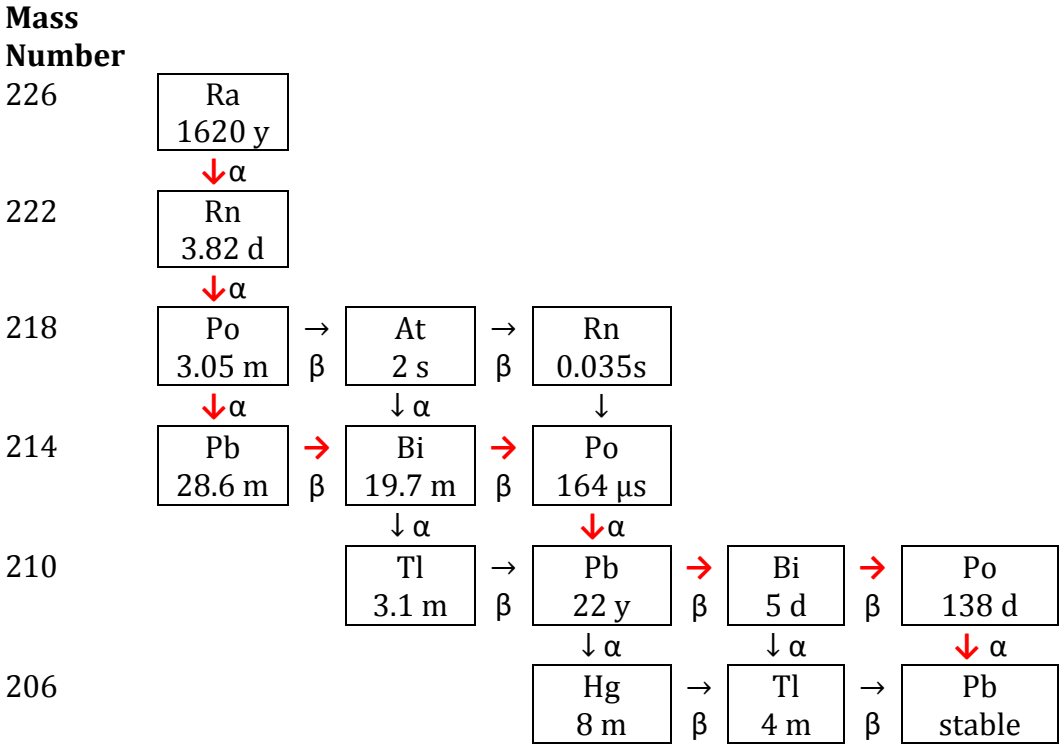

Figure 5.18: A representation of the radon-decay chain. The most probable decay pathway takes place along the chain marked with thick arrows. The half-lives of each isotope are given underneath each elemental symbol in seconds (s), minutes (m), days (d), or years (y).[76]

5.7 References

[1] E. A. Underwood, *Br. J. Anaesth.* **1951**, *2*, 895.

[2] R. HARDY, *Am. J. Psychiatry* **2001**, *158*, 2103–2104.

[3] J. Wawersik, *Anaesthesiol. Reanim.* **1997**, *22*, 144–52.

[4] H. W. Erving, *Yale J. Biol. Med.* **1933**, *5*, 421–30.

[5] R. P. Haridas, *Anesthesiology* **2013**, *119*, 1014–1022.

[6] S. M. Brown, J. R. Sneyd, *BJA Educ.* **2016**, *16*, 87–91.

[7] P. Sykes, *Br. Dent. J.* **1988**, *164*, 134–135.

[8] T. Ryan, A. Hodge, R. Holyoak, R. Vlok, T. Melhuish, M. Binks, G. Hurtado, L. White, *ANZ J. Surg.* **2019**, *89*, 827–832.

[9] C. Wahal, A. Kumar, S. Pyati, *Indian J. Anaesth.* **2018**, *62*, 94.

[10] W. K. NOWILL, C. R. STEPHEN, P. W. SEARLES, *Arch. Surg.* **1953**, *66*, 35.

[11] E. I. Eger, B. Brandstater, L. J. Saidman, M. J. Regan, J. W. Severinghaus, E. S. Munson, *Anesthesiology* **1965**, *26*, 771–777.

[12] B. C. Walker, S. R. Walker, *Trends and Changes in Drug Research and Development : Proceedings of the Society for Drug Research 20th Anniversary Meeting Held at the Pharmaceutical Society of Great Britain, London 26 September 1986*, Springer Netherlands, **1988**.

[13] P. Habibollahi, N. Mahboobi, S. Esmaeili, S. Safari, A. Dabbagh, S. M. Alavian,

Hepat. Mon. **2011**, *11*, 3–6.

[14] J. Loeb, A. Waters, *Vet. Rec.* **2018**, *183*, 704.

[15] The Royal College of Anaesthetists, "RCoA - Guide for novice trainees," can be found under https://www.e-lfh.org.uk/e-learning-sessions/rcoa-novice/content/started/type.html, **2018**.

[16] D. F. Stowe, Z. J. Bosnjak, J. P. Kampine, *Anesth. Analg.* **1992**, *74*, 547–558.

[17] C. Staahl, A. M. Drewes, *Basic Clin. Pharmacol. Toxicol.* **2004**, *95*, 97–111.

[18] J. L. B. Ffarcs, *Ann. R. Coll. Surg. Engl.* **1983**, *65*, 93–96.

[19] J. Demers-Pelletier, P. Drolet, M. Girard, F. Donati, *Can. J. Anaesth.* **1997**, *44*, 1144–1147.

[20] R. W. D. Nickalls, W. W. Mapleson, *Br. J. Anaesth.* **2003**, *91*, 170–174.

[21] E. D. Kharasch, M. D. Karol, C. Lanni, R. Sawchuk, *Anesthesiology* **1995**, *82*, 1369–78.

[22] R. L. Carpenter, E. I. Eger, B. H. Johnson, J. D. Unadkat, L. B. Sheiner, X. Wang, A. Anis, E. Ely, G. Fisher, A. Kirkham, et al., *Anesthesiology* **1986**, *65*, 201–205.

[23] E. D. Kharasch, *Acta Anaesthesiol. Belg.* **1996**, *47*, 7–14.

[24] M. Nuscheler, P. Conzen, K. Peter, *Anaesthesist* **1998**, *47 Suppl 1*, S24–S32.

[25] D. D. Koblin, *Anesth. Analg.* **1992**, *75*, S10-6.

[26] T. Stocker, *Climate Change 2013 Ipcc*, WMO, IPCC Secretariat, Geneva, **2013**.

[27] A. R. Ravishankara, J. S. Daniel, R. W. Portmann, *Science* **2009**, *326*, 123–5.

[28] J. C. Groen, J. Pérez-Ramírez, W. Zhu, *J. Chem. Eng. Data* **2002**, *47*, 587–589.

[29] S. M. Ryan, C. J. Nielsen, *Anesth. Analg.* **2010**, *111*, 92–8.

[30] T. G. Weiser, A. B. Haynes, G. Molina, S. R. Lipsitz, M. M. Esquivel, T. Uribe-Leitz, R. Fu, T. Azad, T. E. Chao, W. R. Berry, et al., *Lancet* **2015**, *385*, S11.

[31] P. V Sackey, C.-R. Martling, F. Granath, P. J. Radell, *Crit. Care Med.* **2004**, *32*, 2241–2246.

[32] Sedana Medical AB, :: "Sedana Medical - The AnaConDa Technology People ::," can be found under http://www.sedanamedical.com/aboutanaconda_po.php, **2014**.

[33] Sedana Medical AB, "AnaConDa," can be found under https://www.sedanamedical.com/?page_id=5032, **n.d.**

[34] D. J. Doyle, R. Byrick, D. Filipovic, F. Cashin, *Can. J. Anaesth.* **2002**, *49*, 799–804.

[35] T.-H. Chen, W. Kaveevivitchai, A. J. Jacobson, O. Š. Miljanić, *Chem. Commun.* **2015**, *51*, 14096–14098.

[36] D. Saha, Z. Bao, *Environ. Sci. Technol.* **2010**, *44*, 1820–1826.

[37] A. J. Fletcher, E. J. Cussen, T. J. Prior, M. J. Rosseinsky, C. J. Kepert, K. M.

Thomas, *J. Am. Chem. Soc.* **2001**, *123*, 10001–10011.

[38] D.-L. Chen, N. Wang, F.-F. Wang, J. Xie, Y. Zhong, W. Zhu, J. K. Johnson, R. Krishna, *J. Phys. Chem. C* **2014**, *118*, 17831–17837.

[39] X. Zhang, W. Chen, W. Shi, P. Cheng, *J. Mater. Chem. A* **2016**, *4*, 16198–16204.

[40] N. Gargiulo, a. Peluso, P. Aprea, Y. Hua, D. Filipović, D. Caputo, M. Eić, *RSC Adv.* **2014**, *4*, 49478–49484.

[41] Y. Hua, N. Gargiulo, A. Peluso, P. Aprea, M. Eić, D. Caputo, *Chemie-Ingenieur-Technik* **2016**, *88*, 1730–1738.

[42] D. Saha, S. Deng, *J. Chem. Eng. Data* **2010**, *55*, 3312–3317.

[43] F. Ally N Alai, MD, "Nitrous Oxide Administration: Overview, Indications, Contraindications," can be found under https://emedicine.medscape.com/article/1413427-overview#showall, **2017**.

[44] D. E. Emmanouil, R. M. Quock, *Anesth. Prog.* **2007**, *54*, 9–18.

[45] A. Aranake, G. A. Mashour, M. S. Avidan, *Anaesthesia* **2013**, *68*, 512–522.

[46] B. Preckel, N. C. Weber, R. D. Sanders, M. Maze, W. Schlack, *Anesthesiology* **2006**, *105*, 187–197.

[47] B. Bein, J. Höcker, J. Scholz, *Anasthesiol. Intensivmed. Notfallmed. Schmerzther.* **2007**, *42*, 784–791.

[48] M. Derwall, M. Coburn, S. Rex, M. Hein, R. Rossaint, M. Fries, *Minerva Anestesiol. 75*, 37–45.

[49] T. Goto, H. Saito, M. Shinkai, Y. Nakata, F. Ichinose, S. Morita, *Anesthesiology* **1997**, *86*, 1273–8.

[50] F. BOOMSMA, J. RUPREHT, A. J. M. I. VELD, F. H. DE JONG, M. DZOLJIC, B. LACHMANN, *Anaesthesia* **1990**, *45*, 273–278.

[51] A. R. Barakat, M. N. Schreiber, J. Flaschar, M. Georgieff, S. Schraag, *Anesth. Analg.* **2008**, *106*, 823–829.

[52] S. Petersen-Felix, M. Luginbuhl, T. W. Schnider, M. Curatolo, L. Arendt-Nielsen, A. M. Zbinden, *Br. J. Anaesth.* **1998**, *81*, 742–747.

[53] D. Ma, H. Yang, J. Lynch, N. P. Franks, M. Maze, H. P. Grocott, *Anesthesiology* **2003**, *98*, 690–8.

[54] D. Ma, S. Wilhelm, M. Maze, N. P. Franks, *Br. J. Anaesth.* **2002**, *89*, 739–746.

[55] A. Nagata, S. Nakao, N. Nishizawa, M. Masuzawa, T. Inada, K. Murao, E. Miyamoto, K. Shingu, *Anesth. Analg.* **2001**, *92*, 362–368.

[56] J. H. Lawrence, W. F. Loomis, C. A. Tobias, F. H. Turpin, *J. Physiol.* **1946**, *105*, 197–204.

[57] F. G. Kerry, CRC Press, Boca Raton, **2007**, pp. 100–104.

[58] L. Chen, P. S. Reiss, S. Y. Chong, D. Holden, K. E. Jelfs, T. Hasell, M. A. Little, A. Kewley, M. E. Briggs, A. Stephenson, et al., *Nat. Mater.* **2014**, *13*, 954–960.

[59] *J. Clin. Anesth.* **1999**, *11*, 477–481.

[60] C. G. Saxton, A. Kruth, M. Castro, P. A. Wright, R. F. Howe, *Microporous Mesoporous Mater.* **2010**, *129*, 68–73.

[61] G. Couderc, T. Hertzsch, N. R. Behrnd, K. Krämer, J. Hulliger, *Microporous Mesoporous Mater.* **2006**, *88*, 170–175.

[62] P. K. Thallapally, J. W. Grate, R. K. Motkuri, *Chem. Commun.* **2012**, *48*, 347–349.

[63] B. F. Abrahams, A. D. Dharma, P. S. Donnelly, T. A. Hudson, C. J. Kepert, R. Robson, P. D. Southon, K. F. White, *Chem. - A Eur. J.* **2017**, *23*, 7871–7875.

[64] S. K. Elsaidi, D. Ongari, W. Xu, M. H. Mohamed, M. Haranczyk, P. K. Thallapally, *Chem. - A Eur. J.* **2017**, *23*, 10758–10762.

[65] T. S. Aziz, *Int. Anesthesiol. Clin.* **2001**, *39*, 1–14.

[66] J. Dingley, R. S. Mason, *Anesth. Analg.* **2007**, *105*, 1312–1318.

[67] A. Bondi, *J. Phys. Chem.* **1964**, *68*, 441–451.

[68] C. A. Fernandez, J. Liu, P. K. Thallapally, D. M. Strachan, *J. Am. Chem. Soc.* **2012**, *134*, 9046–9049.

[69] a. Soleimani Dorcheh, D. Denysenko, D. Volkmer, W. Donner, M. Hirscher, *Microporous Mesoporous Mater.* **2012**, *162*, 64–68.

[70] H. Wang, K. Yao, Z. Zhang, J. Jagiello, Q. Gong, Y. Han, J. Li, *Chem. Sci.* **2014**, *5*,

620.

[71] D. Banerjee, C. M. Simon, S. K. Elsaidi, M. Haranczyk, P. K. Thallapally, *Chem* **2018**, *4*, 466–494.

[72] M. H. Mohamed, S. K. Elsaidi, T. Pham, K. A. Forrest, H. T. Schaef, A. Hogan, L. Wojtas, W. Xu, B. Space, M. J. Zaworotko, et al., *Angew. Chemie Int. Ed.* **2016**, *55*, 8285–8289.

[73] B. J. Sikora, C. E. Wilmer, M. L. Greenfield, R. Q. Snurr, *Chem. Sci.* **2012**, *3*, 2217.

[74] C. M. Simon, R. Mercado, S. K. Schnell, B. Smit, M. Haranczyk, *Chem. Mater.* **2015**, *27*, 4459–4475.

[75] J. R. PARTINGTON, *Nature* **1957**, *179*, 912–912.

[76] *Health Effects of Exposure to Radon*, National Academies Press, Washington, D.C., **1999**.

[77] F. S. Al Saleh, B. Al-berzan, *Education* **2007**, *2*, 25–36.

[78] A. I. Abd El-mageed, A. H. El-Kamel, A. Abbady, S. Harb, A. M. M. Youssef, I. I. Saleh, *Radiat. Phys. Chem.* **2011**, *80*, 710–715.

[79] G. Carrera, M. Garavaglia, S. Magnoni, G. Valli, R. Vecchi, *J. Environ. Radioact.* **1997**, *34*, 149–159.

[80] A. Sakoda, Y. Nishiyama, K. Hanamoto, Y. Ishimori, Y. Yamamoto, T. Kataoka, A. Kawabe, K. Yamaoka, *Appl. Radiat. Isot.* **2010**, *68*, 1180–1184.

[81] E. I. Hamilton, *Sci. Total Environ.* **1990**, *92*, 284–285.

[82] H. F. Lucas Jr, F. H. Ilcewicz, *J. Am. Water Works Assoc.* **1958**, *50*, 1523–1532.

[83] T. K. Ball, D. G. Cameron, T. B. Colman, P. D. Roberts, *Q. J. Eng. Geol.* **1991**, *24*, 169–182.

[84] A. Sakoda, Y. Ishimori, K. Yamaoka, *Appl. Radiat. Isot.* **2011**, *69*, 1422–1435.

[85] A. C. Baker, C. Toque, *J. Radiol. Prot.* **2005**, *25*, 127–140.

[86] W. W. Nazaroff, H. Feustel, A. V. Nero, K. L. Revzan, D. T. Grimsrud, M. A. Essling, R. E. Toohey, *Atmos. Environ.* **1985**, *19*, 31–46.

[87] C. O. Loureiro, L. M. Abriola, J. E. Martin, R. G. Sextro, *Environ. Sci. Technol.* **1990**, *24*, 1338–1348.

[88] K. L. Revzan, W. J. Fisk, A. J. Gadgil, *Indoor Air* **1991**, *1*, 173–189.

[89] S. Darby, D. Hill, A. Auvinen, J. M. Barros-Dios, H. Baysson, F. Bochicchio, H. Deo, R. Falk, F. Forastiere, M. Hakama, et al., *Br. Med. J.* **2005**, *330*, 223–226.

[90] E. P. Radford, *Environ. Health Perspect.* **1985**, *VOL. 62*, 281–287.

[91] A. Martín Sánchez, J. de la Torre Pérez, A. B. Ruano Sánchez, F. L. Naranjo Correa, *J. Environ. Radioact.* **2012**, *107*, 86–91.

[92] A. El-Gamal, G. Hosny, *East. Mediterr. Heal. J.* **2008**, *14*, 1257–1269.

[93] J. Milner, C. Shrubsole, P. Das, B. Jones, I. Ridley, Z. Chalabi, I. Hamilton, B.

Armstrong, M. Davies Prof., P. Wilkinson, *BMJ* **2014**, *348*, 1–12.

Chapter 6 Table of Contents

Chapter 6 – Conclusion

6.1 Thesis summary

The work described in this thesis focused upon the synthesis, structures and host properties of porous networks in which metal centres are linked by bridging organic ligands. In particular the emphasis has been on porous materials that possess parallel non-intersecting channels.

In chapter 2 the synthesis and structures of Li^+ based ionic networks generated by the compounds Hpaa and Hpeb were described. The investigation described the synthesis and structure of lightweight Li^+ based networks with small non intersecting channels. Li(paa)·DMF possesses chains consisting of 6-membered edge sharing Li-O-Li-O-C-O rings that closely resemble those found in the desolvated Li(inic) network. In fact they share the same topology. In contrast to Li(inic)·S, which was able to adsorb a variety of gases upon desolvation the Li(paa)·DMF network material does not appear to be as robust as Li(inic) and redissolves as soon as the mother liquor surrounding the crystals is exposed to the atmosphere. It is proposed that the moisture in the atmosphere is responsible for the dissolution. Shortly after the dissolution of Li(paa)·DMF, crystals of dense Li(paa) separate from solution. The dense Li(paa) structure resembles that of the dense Li(inic) structure.

Perhaps not surprisingly, the use of the longer ligand peb^- gives two materials neither of which have channels, $[Li_2(peb)(H_2O)_7](peb)\cdot H_2O$ and Li(peb)DMSO. It would seem that formation of the porous ionic networks is favoured when relatively short anions are used.

In chapter 3 the family of Zn(hba) structures has been expanded using the ligands 2-chloro hba^{2-}, 2-methyl hba^{2-}, 2,6-dimethyl hba^{2-}, 2-fluoro hba^{2-} and 3-fluoro hba^{2-}. Single crystal analysis did not prove very informative because of the severe twinning and disorder yielding diffraction patterns with broad, streaky reflections. Nevertheless powder diffraction confirmed the formation of the Zn(hba)-type network. Structural analysis using computer simulations was employed to determine the lowest energy conformation of the Zn(2-methyl hba) and Zn(2,6-dimethyl hba) structures. Synthetic and structural results suggest that a wide range of substituents could be introduced on the hba^{2-} ligands and produce a similar porous structure to that of Zn(hba). This provides encouragement that the pores could be further tailored for specific adsorption purposes.

It should be noted that there were three ligands related to hba^{2-} that failed to yield the Zn(hba)-type structure. Perhaps not surprisingly, Zn(hpOa) did not form the desired product because the introduction of the oxygen atom led to the formation of a 5-membered chelate ring. Similarly, in the case of Zn(hpHNa) the formation of chelate groups leads to a different structural outcome. The tetrafluoro hba^{2-} ligand also failed to yield the Zn(hba)-type structure. This was most surprising given that fluorine is only slightly larger that hydrogen. The reason for the formation of the dense structure for Zn(tetrafluoro hba) remains unclear, but would appear to be related to a preference for tetrafluoro hba^{2-} to make face-to-face contacts with adjacent tetrafluoro hba^{2-} ligands.

In chapter 4 the gas sorption properties of the Zn(hba) family of networks were described. For the gases N_2, CH_4, CO_2 and H_2 the compounds incorporating the longer ligands, cma^{2-} and $hbpc^{2-}$, displayed higher adsorption whereas those with substituted ligands adsorbed to a lesser extent, when compared to Zn(hba). The smaller cross-sectional area of the non-intersecting channels in the Zn(hba) family of networks clearly lead to lower overall gas uptake capacity, although the adsorption of gases at 100 kPa was found to be comparable to MOF materials that do not possess open metal sites.

Of particular interest is the anomalous behaviour observed in the isotherms for Zn(hbpc) with H_2 and CO_2 and the isotherms for Zn(2,6-dimethyl hba) with CO_2, each of which possessed "S" shaped kinks which superficially resembled type-IV isotherms. When the equilibrium time of the Zn(hbpc) CO_2 isotherm was extended, the kink in the isotherm noticeably decreased. This behaviour has been tentatively attributed to the slow kinetics of CO_2 adsorption.

In contrast, on increasing the equilibrium time for the adsorption of CO_2 by Zn(2,6-dimethyl hba) resulted in no change to the isotherm. Subsequent experiments at the Powder Diffraction beamline at the Australian Synchrotron revealed that Zn(2,6-dimethyl hba) undergoes a structural change when evacuated and a further change when exposed to CO_2 gas. Simulations performed by Dr Babarao from RMIT revealed that the degree the methyl groups in Zn(2,6-dimethyl hba) protrude into the channels changes when exposed to high pressures of CO_2.

The maximum CO_2 uptake of Zn(2,6-dimethyl hba) approaches the maximum uptake of Zn(2-methyl hba) after the S-shaped kink. This is surprising given that it is anticipated that the additional methyl group in the 2,6-dimethyl hba^{2-} ligand would lead to a significant reduction in the void space. Analysis of the void volume in the computer simulated structure, however, indicates that the intra-framework volume increases as the loading of CO_2 increases.

Zn(3-fluoro hba) adsorbs CO_2, H_2 and CH_4 to a level close to that of Zn(hba) despite having amongst the lowest BET and Langmuir estimated surface area. This suggest that although substitution on the 3-position of the aromatic ring on the hba^{2-} ligand leads to a smaller surface area, the guest accessible void space is not significantly reduced. Substitution on the 2-position, on the other hand, generally results in networks with lower capacity but higher binding enthalpy.

The results obtained suggest that incorporating ligands bearing substituents at the 3-position does not significantly reduce the total amount adsorbed; however, this is based only upon evidence for 3-fluoro hba. Materials substituted on the 2-positions, however, may be better suited to situations where adsorption at low pressures is desirable while total uptake is less important.

Overall a general trend found with this work is that large pore size is clearly linked to increased storage capacity of an adsorbent material but the binding enthalpy is commonly lower in materials with larger voids than that found in materials with

smaller pores. This has been attributed to increased opportunity for a guest molecule to interact with multiple surfaces in materials with small pores. This is desirable when gases are present in only very low concentrations or associate only very weakly with a host material. Although small pore materials generally have superior binding enthalpies, their limited capacity, in terms of mass/mass uptake, is a significant drawback to their use.

In chapter 5 the Zn(hba) family of frameworks were shown to capture the anaesthetics N_2O, Xe, isoflurane and sevoflurane. The N_2O isotherms indicate that the Zn(hba) family of networks are capable of adsorbing N_2O at pressures and concentrations that would allow their use in hospitals. Through the inclusion of appropriate functional groups on the aromatic rings of the ligands, it may also be possible to enhance the affinity of N_2O for the framework. Storage containers filled with one of the Zn(hba) family of networks, would allow considerable quantities of gases, such as N_2O, to be stored under much lower pressures than those employed in metal cylinders. Zn(hbpc) might be well-suited to the role of an adsorbent material in a lightweight storage device.

The Zn(hbpc) N_2O isotherm closely resembles a type I isotherm. Closer inspection however, reveals that much like the Zn(hbpc) CO_2 isotherm, the Zn(hbpc) N_2O isotherm has a slight S-shape, which is more pronounced in the 258 and 273 K isotherms. Extending the equilibrium time resulted in no change in the isotherm, which is somewhat surprising as N_2O and CO_2 have are isoelectronic with similar structures.

Collaboration with Prof Cameron Kepert and Dr Peter Southon from the University of Sydney showed that Zn(hba) is capable of capturing significant quantities of sevoflurane and isoflurane well below the concentration exhaled by patients. TGA revealed that Zn(hba) is capable of retaining ~83% of captured isoflurane below 60 °C.

A prototype anaesthetic capture device, developed by the candidate, was shown to capture 74% of the anaesthetic sevoflurane which was passed through an anaesthesia machine. It was pleasing to find that the sevoflurane which was captured could be recovered by heating and subsequent condensation. This work provides a proof of concept for the effective recycling of inhalation anaesthetics.

6.2 Future work

There are three areas where work described in the thesis could be extended.

1. Synthesis of Li^+ based network materials

The ionic Li^+ based networks have non-intersecting channels that generally provide high guest to host interactions. It may be possible to further increase the strength of this interaction through the use of substituted $inic^-$ related ligands, much like in the Zn(hba) family of networks. The generation of larger Li^+ based networks may be possible by incorporating ligands with an even larger distance between the pyridyl and carboxylate group. It would seem, however, that Li^+ based porous networks with larger channels have lower stability. Synthesis of a porous framework with larger channels than that of the open-type Li(inic) framework for practical application may very well be a futile

endeavour, however the introduction of substituents as was described in chapter 3 may lead to enhanced stability.

2. Synthesis of Zn(hba)-type network materials

Zn(hba)-type networks have shown a high degree of structural diversity, leaving considerable scope for future work. It may be possible for the introduction of greater functionality in to the framework by incorporating ligands with larger substituents. Perhaps ligands longer than that of hba^{2-} would be required as the channels may get too crowded.

3. Uptake of anaesthetics.

Proof of concept has been demonstrated for the effective recycling of inhalation anaesthetics with Zn(hba). Work has gone to the next phase where sorbent materials in terms of cost, recyclability, capacity, binding enthalpy and environmental impact are being considered. Discussions are currently underway with two organisations (at the time of submission of this thesis) regarding the commercialisation of this technology.

Chapter 7 Table of Contents

Chapter 7 – Experimental

7.1 Single crystal x-ray diffraction

7.1.1 Supernova

Single crystals of Li(paa)·DMF, Li(peb)DMSO, Zn_2(tetrafluoro hba)$(OAc)_2$, Zn(tetrafluoro hba)(MeOH)·MeOH, Cu$(HhpOa)_2(H_2O)_2$ and Zn(HhpHNa) were analysed on an Oxford Diffraction Supernova diffractometer with Cu Kα microfocus radiation (λ = 1.54184 Å). Data collection, reduction and adsorption corrections were all performed with CrysAlisPro from Agilent Technologies.[1]

Diffraction frames were fitted with CrysalisPro, with filtering to the identified cell centring, smart background correction, outlier rejection to space group and equivalent Friedel mates. Adsorption corrections used were of the empirical multi-scan type.[2]

7.1.2 Australian Synchrotron MX1 beamline

Single crystals of $[Li_2(peb)(H_2O)_7](peb)\cdot H_2O$ and Li(paa) were analysed on the MX1 beamline at the Australian Synchrotron with synchrotron radiation (λ = 0.7109 Å). Data was collected for a single phi scan, with frames collected every degree (φ = 0 - 360°, κ = 0, ω = 0). An Oxford Diffraction CryoJet 5 system maintained a sample temperature of 100 K. Cell refinement and data reduction was performed with XDS.[3] Multi-scan absorption corrections were performed with XDS or SADABS.[4]

7.2 Powder x-ray diffraction

7.2.1 Australian Synchrotron PD beamline

Powder x-ray diffraction data for Zn(hba), Zn(2-fluoro hba), Zn(3-fluoro hba), Zn(2-chloro hba), Zn(2-methyl hba) and Zn(2,6-dimethyl hba) were collected on the Powder Diffraction beamline at the Australian Synchrotron. The sample was loaded into a 0.3 mm Lindemann tube, sealed with fire and mounted on the Powder Diffraction beamline using either a goniometer head or Norby cell. The beamline was set up with an energy of 16 KeV. To cover the gaps between detector modules, 2 datasets were collected with the detector set 5° apart and then merged to a single dataset. Samples were held to the experimental temperature by the Cryostream device.

7.2.2 Synergy-S

Powder x-ray diffraction data for Li(paa), $[Li_2(peb)(H_2O)_7](peb)\cdot H_2O$, Zn_2(tetrafluoro hba)$(OAc)_2$, $Cu(HhpOa)_2(H_2O)_2$ and Zn(HhpHNa) were conducted on a Rigaku Oxford Diffraction Synergy-S using CuKα (1.54184 Å) monochromated X-ray radiation. The samples were loaded into a 0.3 or 0.5 mm Lindemann tube, sealed with fire and mounted on a goniometer head. 5 minute collections between 0 and 50° 2θ, detector distance 77 mm, were collected. Samples were held at 298 K with an N_2 stream from an Oxford Diffraction Cryostream device.

The theoretical powder patterns were generated in Mercury[5] from refined models obtained from single crystal x-ray data.

7.2.3 GSAS-II

Indexing of Zn(hba), Zn(2-fluoro hba), Zn(3-fluoro hba), Zn(2-chloro hba), Zn(2-methyl hba) and Zn(2,6-dimethyl hba) were completed on GSAS-II.[6] A baseline was generated using the background function "Chebyschev" with the number of coefficients set to three. Debye scattering number of terms was set to zero. Peaks in background were set to zero. The auto search function was used to generate an initial peak list. Peaks were added or removed to better fit the powder diffraction data. Once all peaks were identified their position, intensity, sigma and gamma values where refined. For indexing, the max Nc/Nobs value was set to 2 and the start volume was set to 25. De Wolff figure of merit values (M_{20}) and X_{20} were used as sorting criteria.

7.2.4 Conograph

Indexing for solvated Zn(2,6-dimethyl hba), evacuated Zn(2,6-dimethyl hba), evacuated at 250 K Zn(2,6-dimethyl hba), CO_2 dosed Zn(2,6-dimethyl hba) and re-evacuated Zn(2,6-dimethyl hba) were completed using Conograph GUI ver 0.9.[7] For peak search the number of data points used for smoothing at each point was set to 9. Lower threshold for peak heights was set to c = 5.0. Error values for intensities were used. For indexing, an exhaustive search was used with the number of peaks used for, search set to AUTO. The zero point shift was estimated for each powder experiment. The number of peaks used for computation of FOM was 20. De Wolff figure of merit values (M) were used as sorting criteria. Upper and lower thresholds of computed lines were generated automatically.

7.3 Single crystal structure solution

Structures were solved using SHELXT[8] and refined with SHELXL[9] using a full-matrix least squares refinement based on F^2. Non-hydrogen atoms were refined with anisotropic thermal parameters. Higher symmetry cell checks were conducted by the PLATON program.[10] Hydrogen atoms were generally held to idealised positions using the automatic H-fix routine in Olex2.[11] The generated cifs were all checked using the IUCr tool for structure solution verification, CheckCIF.[12]

7.4 Crystallographic Terminology

All crystallographic output values were calculated using the program SHELXL[9], which are defined by the following equations

$$R_1 = \frac{\sum\left||F_o| - |F_c|\right|}{\sum|F_o|}$$

$$wR_2 = \left(\frac{\sum[w(F_o^2 - F_c^2)^2]}{w(F_o^2)^2}\right)^{\frac{1}{2}}$$

$$GooF = S = \left(\frac{\sum[w(F_o^2 - F_c^2)^2]}{n_{ref} - n_{param}}\right)^{\frac{1}{2}}$$

$$w = \frac{1}{\sigma^2(F_o^2) + (aP)^2 + bP}$$

$$P = \frac{F_c^2 + max(F_o^2, 0)}{3}$$

$$R_{int} = \frac{\sum|F_o^2 - F_c^2(mean)|}{\sum(F_o^2)}$$

where:

F_o =observed structure factors

F_c = calculated structure factor

n_{ref} = number of reflections

n_{param} = number of parameters

a, b = weight parameters

Anisotropic temperature factor is defined by:

$$T = e^{\left[-2\pi^2\left(h^2\dot{a}^2U_{11} + k^2\dot{b}^2U_{22} + l^2\dot{c}^2U_{33} + hk\dot{a}\dot{b}U_{12} + hl\dot{a}\dot{c}U_{13} + kl\dot{b}\dot{c}U_{23}\right)\right]}$$

Isotropic temperature factor is defined by:

$$T = e^{\left[-8\pi^2U_{iso}\left(\frac{sin\theta}{\lambda}\right)^2\right]}$$

7.5 Gas adsorption studies

Gas sorption data were measured using a Sieverts-type BELsorp-HP automatic gas sorption apparatus (Bel Japan Inc.).

The 'ultra-high' purity CO_2, H_2, CH_4, N_2, N_2O, Xe and He used for sorption studies were purchased from BOC, Coregas or Air Liquide. Non-ideal gas behaviour at high pressures of each gas at each measurement and reference temperature was corrected for. Source data were obtained from the NIST fluid properties website.[13]

Sample compartment temperatures, 258, 273 and 298 K, were controlled by a Julabo F25-ME chiller/heater that re-circulated fluid at +/- 0.1 °C through a capped, jacketed stainless steel flask housed within a polystyrene box. A calibrated external Pt 100 temperature probe monitored the flask temperature.

Cryogenic temperatures, 77 and 87 K, were maintained with a BEL liquid N_2 level controller. Liquid N_2 and Ar where used to maintain the temperatures 77 and 87 K respectively. Samples were kept at the measurement temperature for a minimum of 1 hr after the desired temperature had been achieved to allow full thermal equilibrium to be attained before data measurement commenced.

Isosteric heats of adsorption (Q_{st}) were calculated using a least-squares fitting of a virial-type thermal adsorption equation that modelled $\ln(P)$ as a function of the amount

of surface excess of gas sorbed over all measurement temperatures.[14] Only data up to the maximum surface excess were modelled. The modelling was performed by the 'Solver' function on Microsoft Excel, with 0.000001 precision, 5% tolerance, 0.0001 convergence and using the Newton search for algorithms, which fitted the virial-type equation coefficients: a0, through to a5 and the constant.

BET and Langmuir surface areas were estimated from 77 K N_2 isotherms using the BELMaster™ program.

7.6 Elemental analysis

Microanalyses were performed at the Campbell Microanalytical Laboratory at the University of Otago, Dunedin, New Zealand.

7.7 Intelligent gravimetric analysis

Intelligent gravimetric analyses were performed by Dr Peter Southon and Prof. Cameron Kepert at the University of Sydney.

Isoflurane and Sevoflurane vapour adsorption measurements on Zn(hba) up to 300 mbar were performed using an IGA002 Intelligent Gravimetric Analyser supplied by Hiden Analytical Ltd. 65.5 mg of pre-evacuated Zn(hba) were initially heated to 130 °C under vacuum (~10-5 mbar) for five hours and then heated to 250 °C for 23 hours. The sample was then cooled to the analysis temperature of 25 °C under vacuum to the dry

mass of 64.18 mg. The temperature of the sample was maintained at 25 ±0.1 °C and the sample chamber was pressurised to a set pressure of the adsorbate and allowed to equilibrate for a minimum of 30 min before moving to the next pressure point.

7.8 Thermogravimetric analysis

Thermogravimetric analysis measurements were performed by an SDTA851 analyser. Isothermal and dynamic measurements from room temperature to 450 °C were carried out on solid samples (~5 mg) placed in alumina crucibles while under an N_2 atmosphere, (purge gas flow rate 30 ml/min). The sample is initially held at 25 °C then heated at 4 °C/min to 450 °C.

7.9 Infrared spectroscopy

Infrared spectrawere obtained as KBr disks using a Bruker TENSOR-27 FT-IR spectrophotometer between 4000 – 400 cm^{-1} with 4cm^{-1} resolution with 32 scans and normalised as transmittance spectra with background corrections.

7.10 Nuclear Magnetic Resonance

NMR spectra (^{1}H, ^{13}C and ^{19}F) were measured using a Varian MR400 (400 MHz). Chemical shifts were referenced internally to residual solvent (D_6DMSO). Spectra were obtained at 295 K.

7.11 Computational simulations

Computational structure simulations were conducted by Dr Ravi Babarao from RMIT.

7.11.1 Structure models for Zn(2-methyl hba) and Zn(2,6-dimethyl hba)

The models used for Zn(2-methyl hba) and Zn(2,6-dimethyl hba) were constructed by using the Zn(hba) crystal structure as a starting point and using the Materials Studio Visualizer software.[15] Optimizations employing DFT theory methods were preformed using VASP 5.4.4 software.[16] Further details related to modelling are presented in Appendix A.5.1.

7.11.2 Location of CO_2 and Binding Energies

Calculations related to the position of the CO_2 molecules within the channels of Zn(2-methyl hba) and Zn(2,6-dimethyl hba), in addition to the binding energies, were performed by Dr Ravi Babarao. Details of the calculations are presented in appendix A.5.2.

7.12 References

[1] Agilent, *CrysAlisPRO*, Agilent Technologies Ltd, Yarnton, England., **2014**.

[2] R. H. Blessing, *Acta Crystallogr. Sect. A Found. Crystallogr.* **1995**, *51*, 33–38.

[3] W. Kabsch, *Acta Crystallogr. Sect. D Biol. Crystallogr.* **2010**, *66*, 125–132.

[4] G. M. Sheldrick, *SADABS, Program for Empirical Absorption Correction of Area Detector Data; Göttingen, Germany, 1996*, University Of Gottingen, **1996**.

[5] C. F. Macrae, P. R. Edgington, P. McCabe, E. Pidcock, G. P. Shields, R. Taylor, M. Towler, J. van de Streek, *J. Appl. Crystallogr.* **2006**, *39*, 453–457.

[6] B. H. Toby, R. B. Von Dreele, *J. Appl. Crystallogr.* **2013**, *46*, 544–549.

[7] A. Esmaeili, T. Kamiyama, R. Oishi-Tomiyasu, *J. Appl. Crystallogr.* **2017**, *50*, 651–659.

[8] G. M. Sheldrick, *Acta Crystallogr. Sect. A Found. Adv.* **2015**, *71*, 3–8.

[9] G. M. Sheldrick, *Acta Crystallogr. Sect. C Struct. Chem.* **2015**, *71*, 3–8.

[10] A. L. Spek, *Acta Crystallogr. Sect. D Biol. Crystallogr.* **2009**, *65*, 148–155.

[11] O. V. Dolomanov, L. J. Bourhis, R. J. Gildea, J. A. K. Howard, H. Puschmann, *J. Appl. Crystallogr.* **2009**, *42*, 339–341.

[12] IUCr, "checkCIF," can be found under https://checkcif.iucr.org/, **2016**.

[13] NIST, "Thermochemical properties of fluid systems," can be found under https://webbook.nist.gov/chemistry/fluid/, **2011**.

[14] L. Czepirski, J. JagiełŁo, *Chem. Eng. Sci.* **1989**, *44*, 797–801.

[15] Dassault SystèmesBIOVIA, *Discovery Studio Modeling Environment*, San Diego, **2019**.

[16] G. Kresse, J. Hafner, *Phys. Rev. B* **1993**, *48*, 13115–13118.

Appendix Table of Contents

A. Appendix

A.1 Gas adsorption studies

Gas sorption data were measured using a Sieverts-type BELsorp-HP automatic gas sorption apparatus (Bel Japan Inc.).

A.1.1CH_4

A.1.1.1Zn(hba)

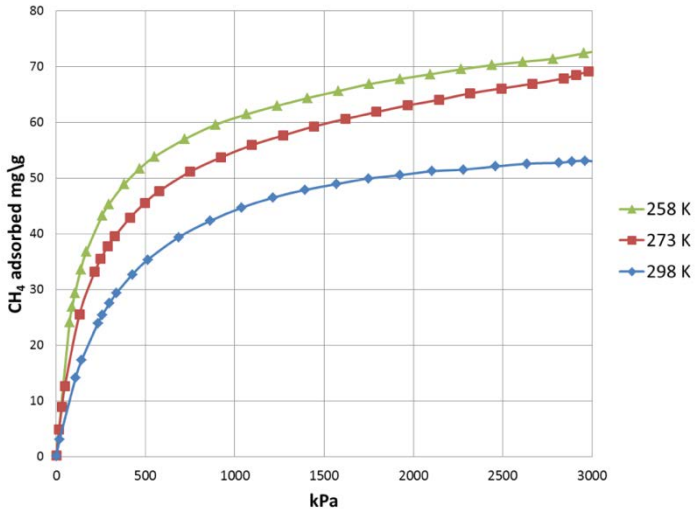

Figure A.1: 258, 273 and 298 K CH_4 isotherms of Zn(hba)

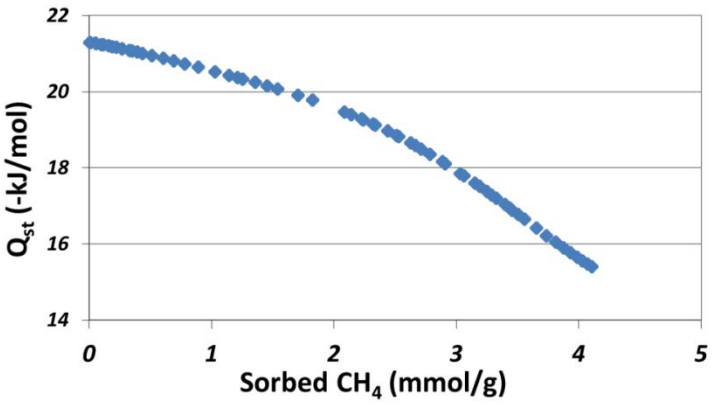

Figure A.2: Calculated Q_{st}(−kJ/mol) vs sorbed CH_4 in Zn(hba)

Table A-1: Optimised virial coefficients for modelling gas sorption calculated from the 258 and 273 K isotherms.

a0	-2561.34
a1	64.64072
a2	51.31321
a3	-39.924
a4	15.58722
a5	-1.78911
b	13.37003
R^2	0.99939465

A.1.1.2Zn(hbpc)

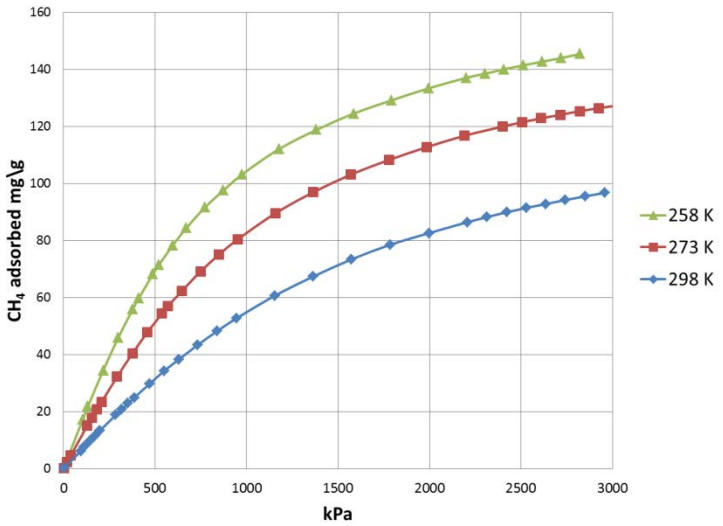

Figure A.3: 258, 273 and 298 K CH_4 isotherms of Zn(hbpc)

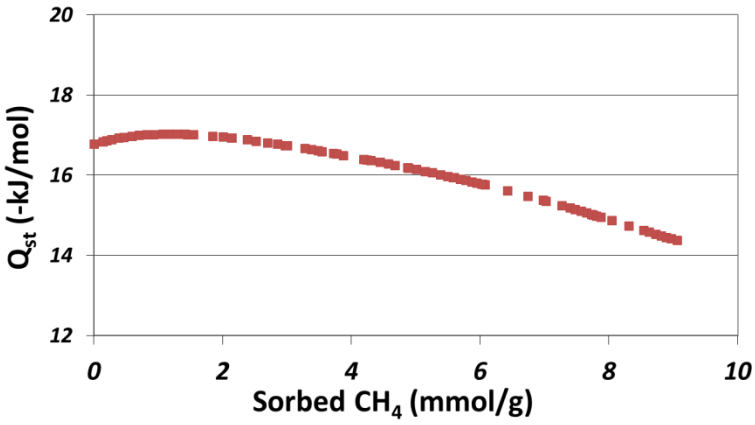

Figure A.4: Calculated Q_{st}(−kJ/mol) vs sorbed CH_4 in Zn(hbpc)

Table A-2: Optimised virial coefficients for modelling gas sorption calculated from the 258, 273 and 298 K isotherms.

a0	-2017.08
a1	-58.3568
a2	34.94897
a3	-6.79884
a4	0.677824
a5	-0.02558
b	12.4043
R2	0.9977149

A.1.1.3Zn(cma)

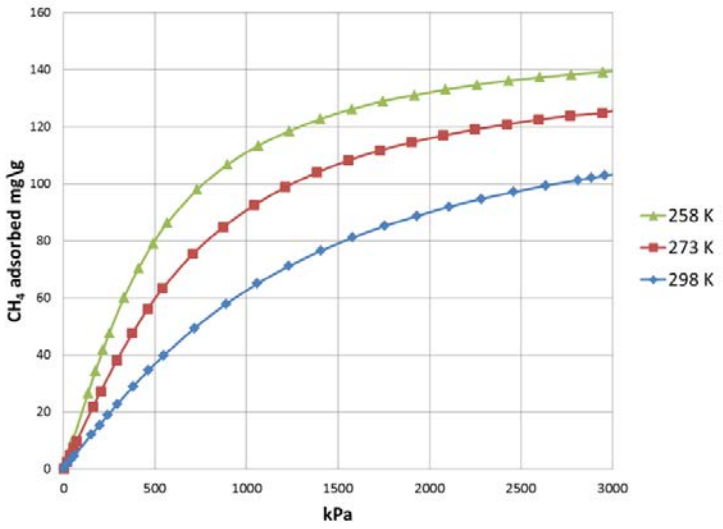

Figure A.5: 258, 273 and 298 K CH_4 isotherms of Zn(cma)

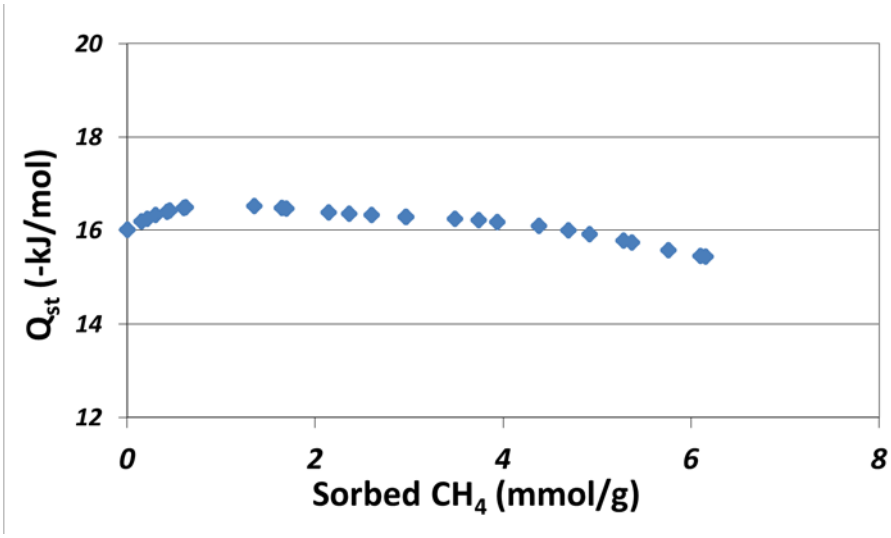

Figure A.6: Calculated Q_{st}(−kJ/mol) vs sorbed CH_4 in Zn(cma)

Table A-3: Optimised virial coefficients for modelling gas sorption calculated from the 258 and 273 K isotherms.

a0	-1924.06
a1	-162.363
a2	138.749
a3	-48.5367
a4	7.686522
a5	-0.44179
b	12.02959
R2	0.999401

A.1.1.4Zn (3-fluoro hba)

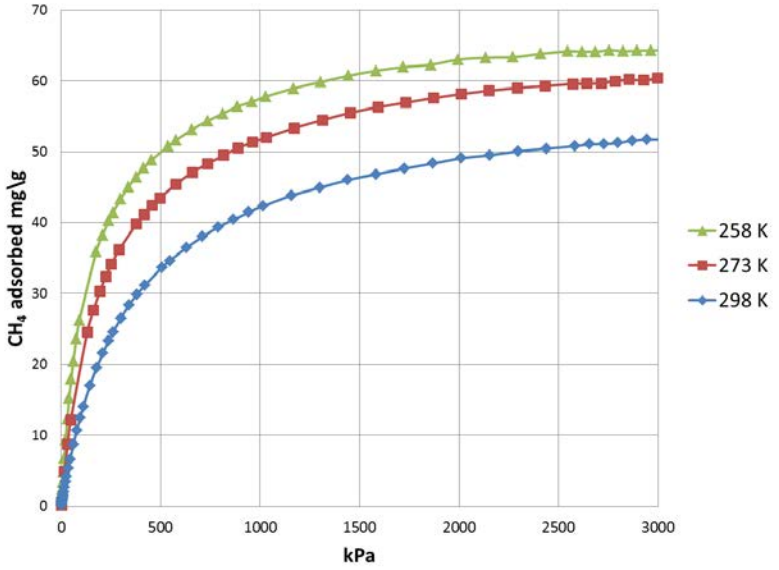

Figure A.7: 258, 273 and 298 K CH_4 isotherms of Zn(3-fluoro hba)

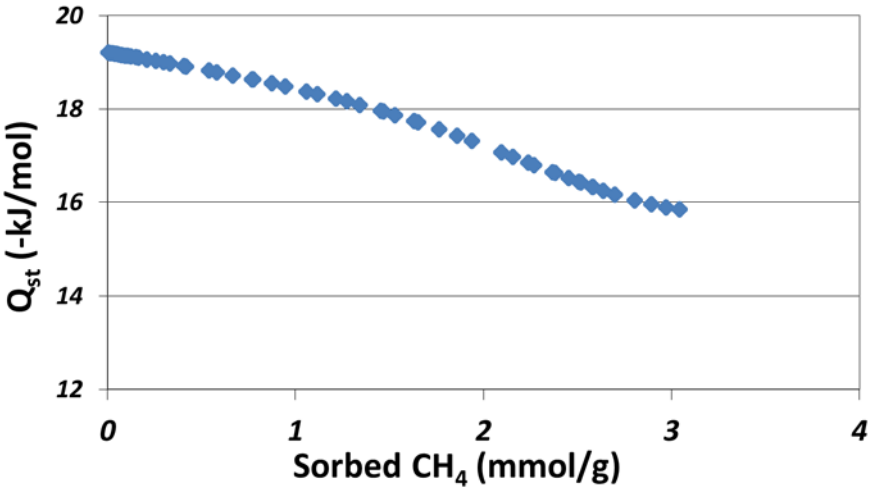

Figure A.8: Calculated Q_{st}(−kJ/mol) vs sorbed CH_4 in Zn(3-fluoro hba)

Table A-4: Optimised virial coefficients for modelling gas sorption calculated from the 258 and 298 K isotherms.

a0	-2309.72
a1	78.61612
a2	23.13695
a3	-22.5671
a4	17.83107
a5	-3.61074
b	12.33861
R^2	0.99871272

A.1.1.5 Zn(2-fluoro hba)

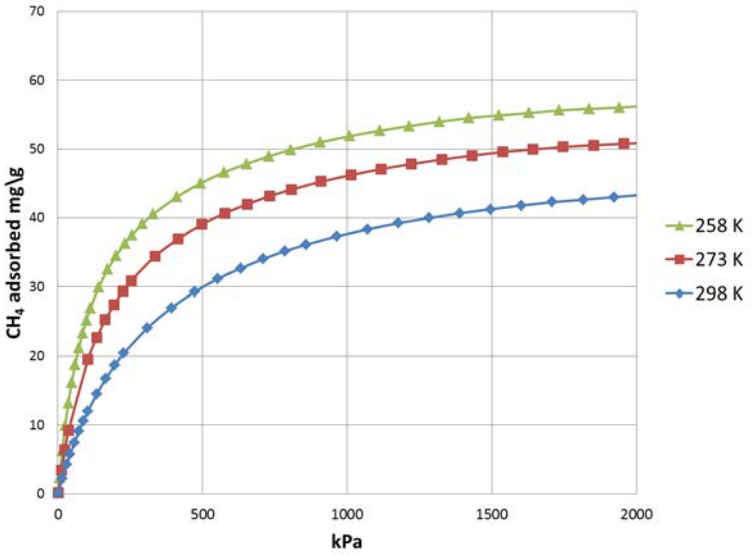

Figure A.9: 258, 273 and 298 K CH_4 isotherms of Zn(2-fluoro hba)

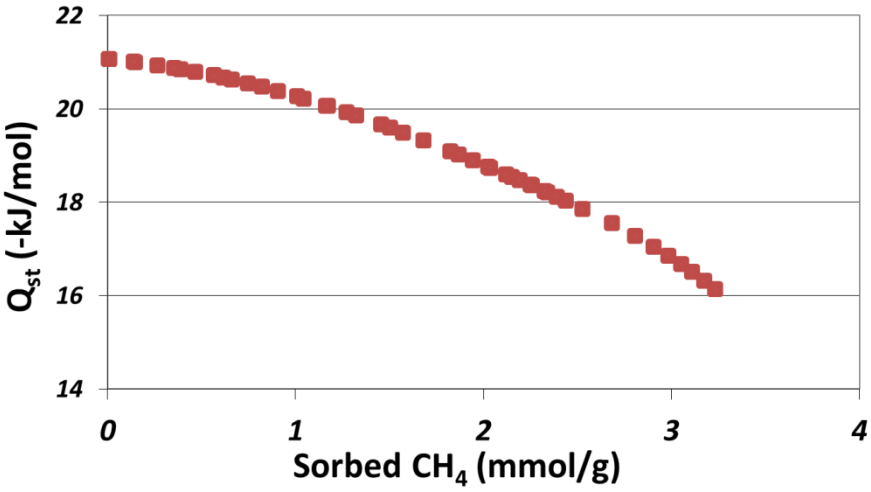

Figure A.10: Calculated Q_{st}(−kJ/mol) vs sorbed CH_4 in Zn(2-fluoro hba)

Table A-5: Optimised virial coefficients for modelling gas sorption calculated from the 258 and 298 K isotherms.

a0	-2534.73
a1	56.61742
a2	19.11693
a3	36.97645
a4	-19.3216
a5	3.036048
b	13.25193
R^2	0.99870159

A.1.1.6 Zn(2-chloro hba)

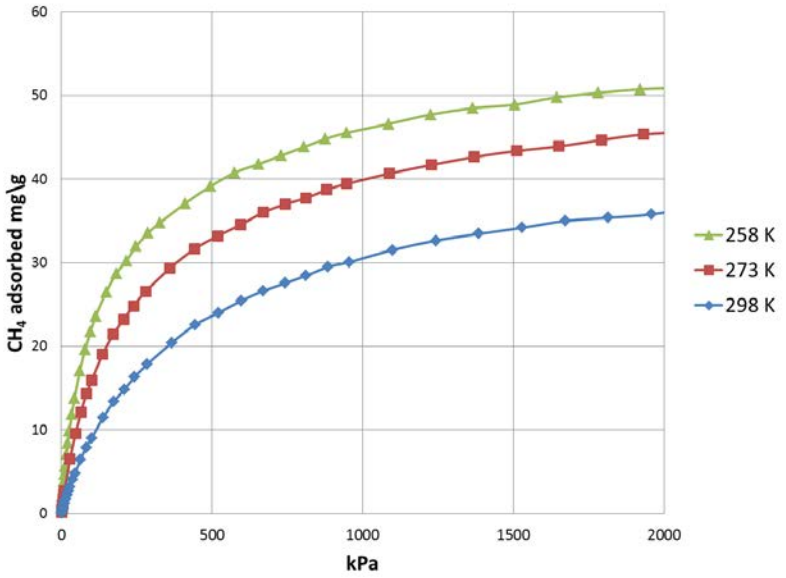

Figure A.11: 258, 273 and 298 K CH_4 isotherms of Zn(2-chloro hba)

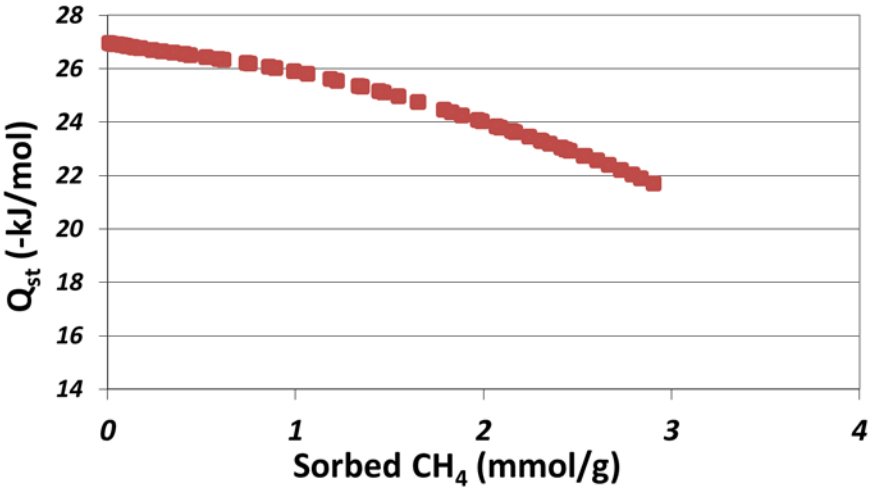

Figure A.12: Calculated Q_{st}(−kJ/mol) vs sorbed CH_4 in Zn(2-chloro hba)

Table A-6: Optimised virial coefficients for modelling gas sorption calculated from the 258 and 273 K isotherms.

a0	-3245.09
a1	167.4446
a2	-160.461
a3	180.906
a4	-66.1028
a5	8.586183
b	16.03831
R^2	0.999584

A.1.1.7 Zn(2-methyl hba)

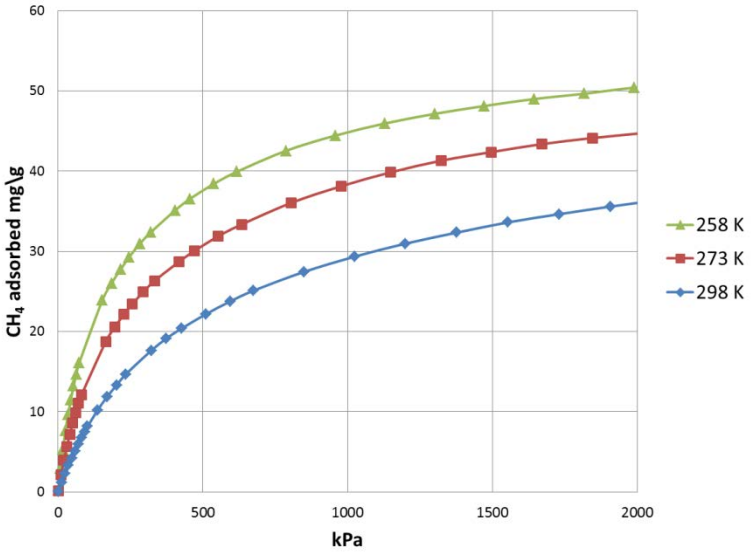

Figure A.13: 258, 273 and 298 K CH_4 isotherms of Zn(2-methyl hba)

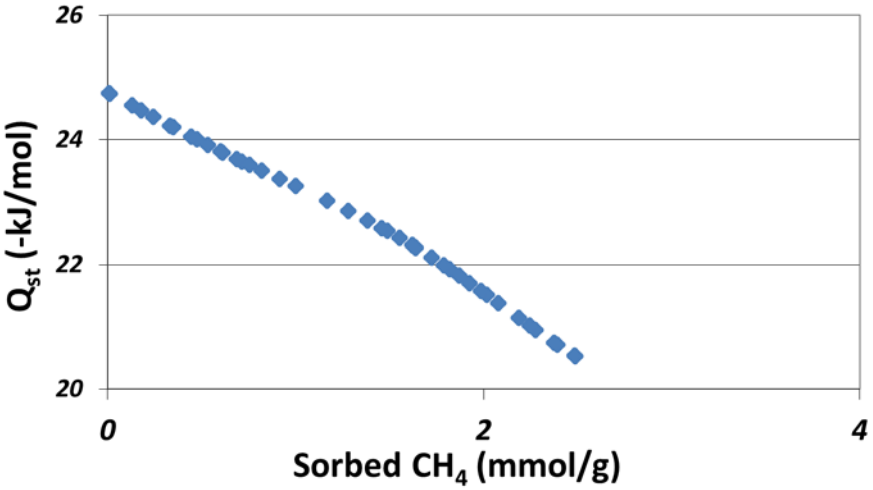

Figure A.14: Calculated Q_{st}(−kJ/mol) vs sorbed CH_4 in Zn(2-methyl hba)

Table A-7: Optimised virial coefficients for modelling gas sorption calculated from the 258 and 273 K isotherms.

a0	-3011.05
a1	373.4273
a2	-459.074
a3	379.5675
a4	-124.083
a5	14.58518
b	15.13914
R^2	0.997971

A.1.1.8 Zn(2,6-dimethyl hba)

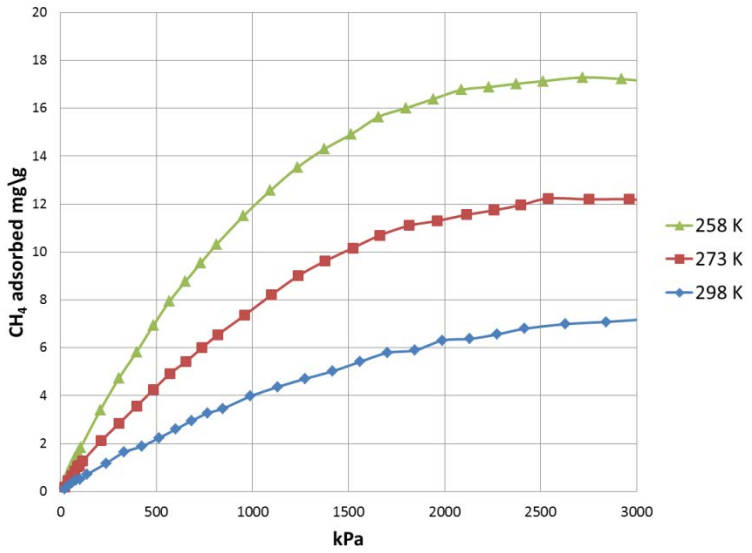

Figure A.15: 258, 273 and 298 K CH_4 isotherms of Zn(2,6-dimethyl hba)

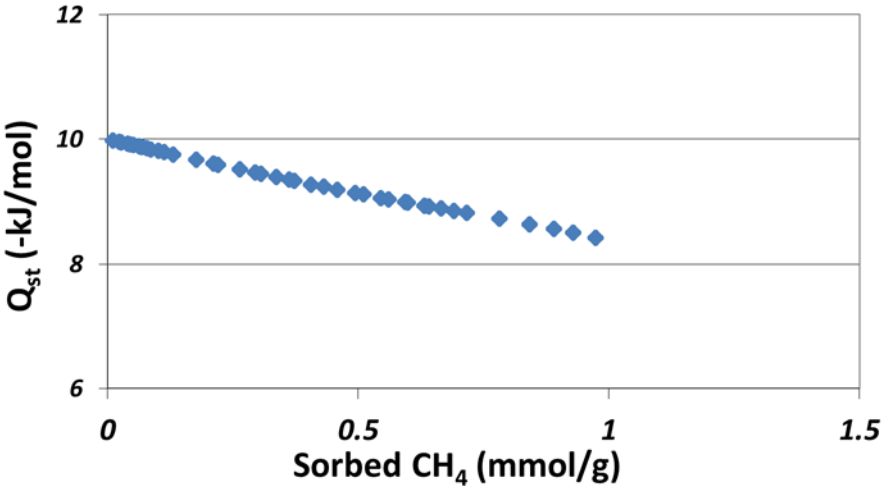

Figure A.16: Calculated Q_{st}(−kJ/mol) vs sorbed CH_4 in Zn(2,6-dimethyl hba)

Table A-8: Optimised virial coefficients for modelling gas sorption calculated from the 258 and 273 K isotherms.

a0	-1201.94
a1	223.9594
a2	8.495368
a3	-73.5335
a4	-31.292
a5	69.67204
b	11.3383
R^2	0.998364

A.1.2 CO_2

A.1.2.1 Zn(hba)

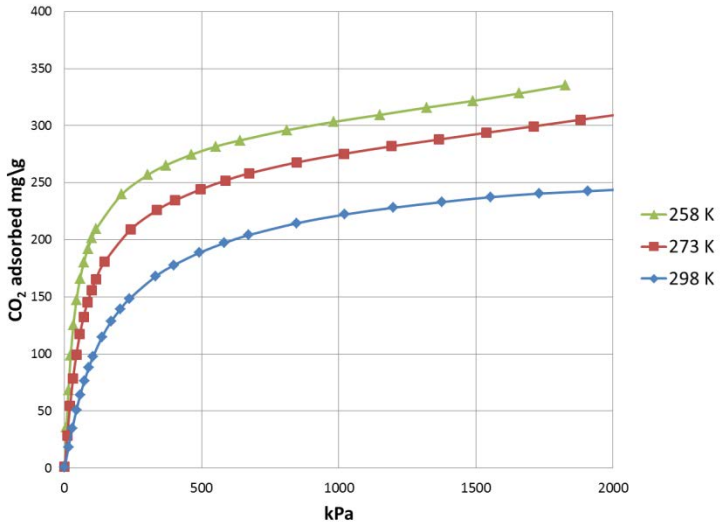

Figure A.17: 258, 273 and 298 K CO_2 isotherms of Zn(hba)

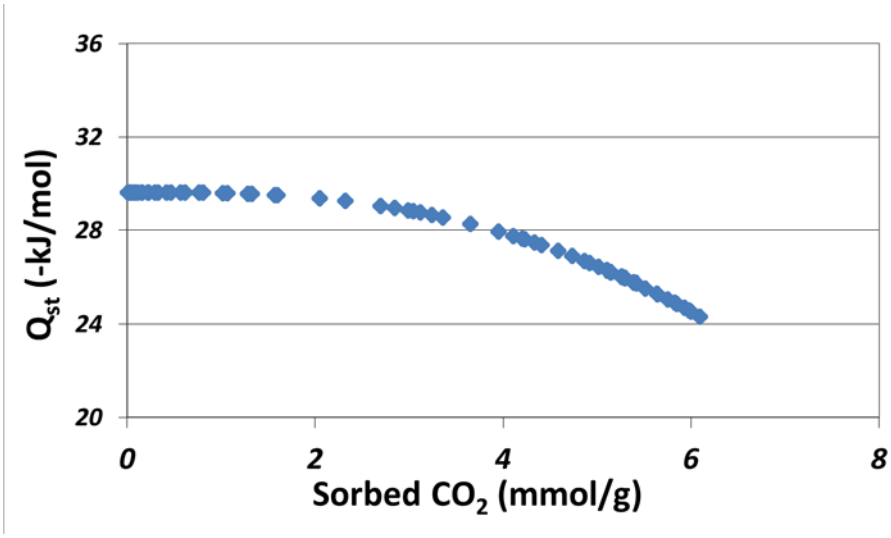

Figure A.18: Calculated Q_{st}(−kJ/mol) vs sorbed CO_2 in Zn(hba)

Table A-9: Optimised virial coefficients for modelling gas sorption calculated from the 258 and 273 K isotherms.

a0	-3558.83
a1	-5.3505
a2	1.376583
a3	4.689539
a4	-0.461
a5	0.022592
b	15.90364
R^2	0.998713

A.1.2.2 Zn(hbpc)

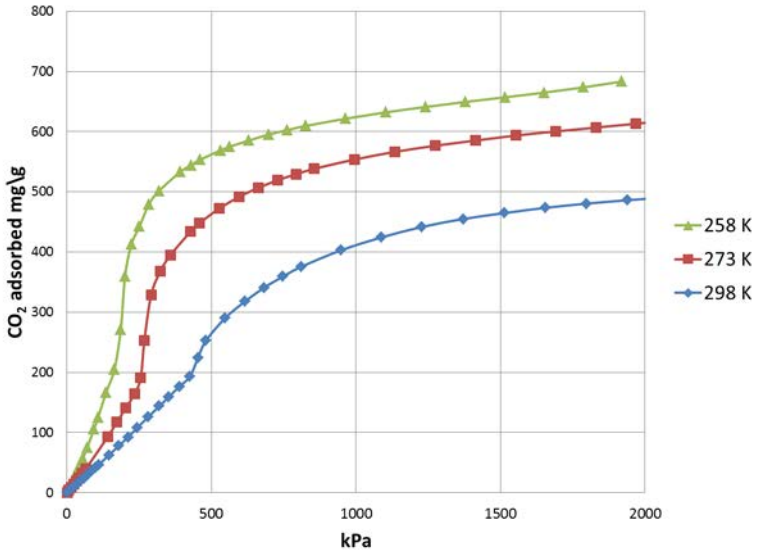

Figure A.19: 258, 273 and 298 K CO_2 isotherms of Zn(hbpc) equilibrium times set to 300 s

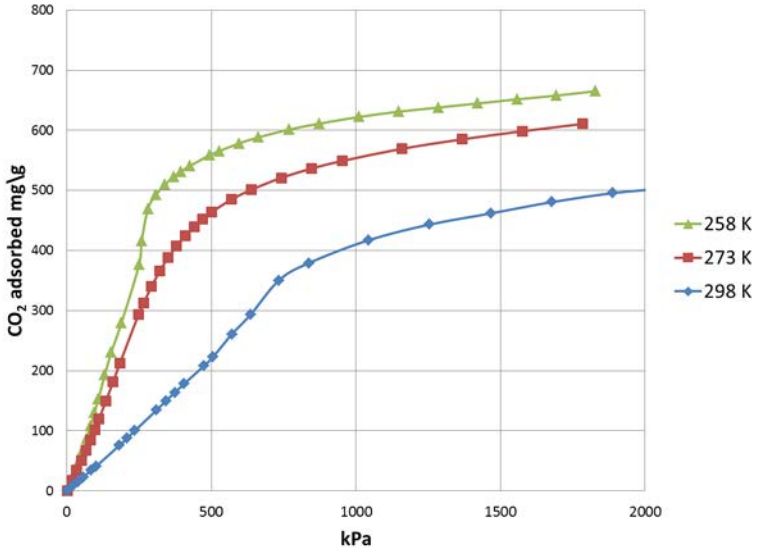

Figure A.20: 258, 273 and 298 K CO_2 isotherms of Zn(hbpc) equilibrium times set to 600 s

A.1.2.3 Zn(cma)

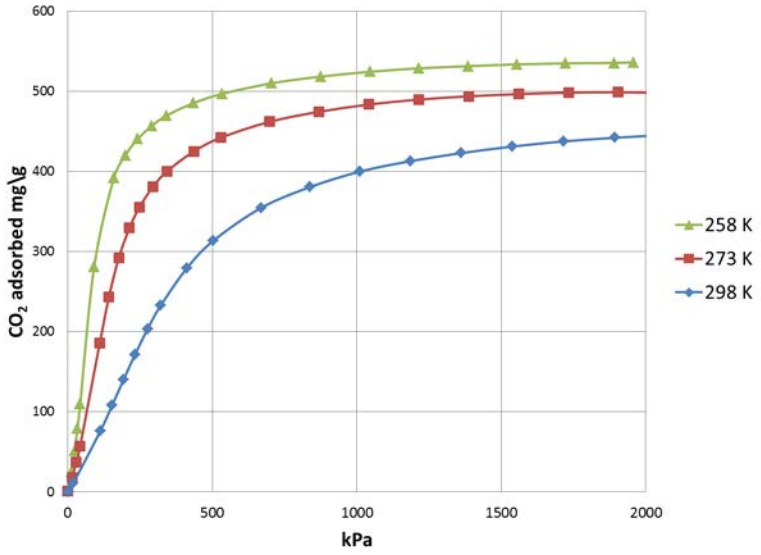

Figure A.21: 258, 273 and 298 K CO_2 isotherms of Zn(cma)

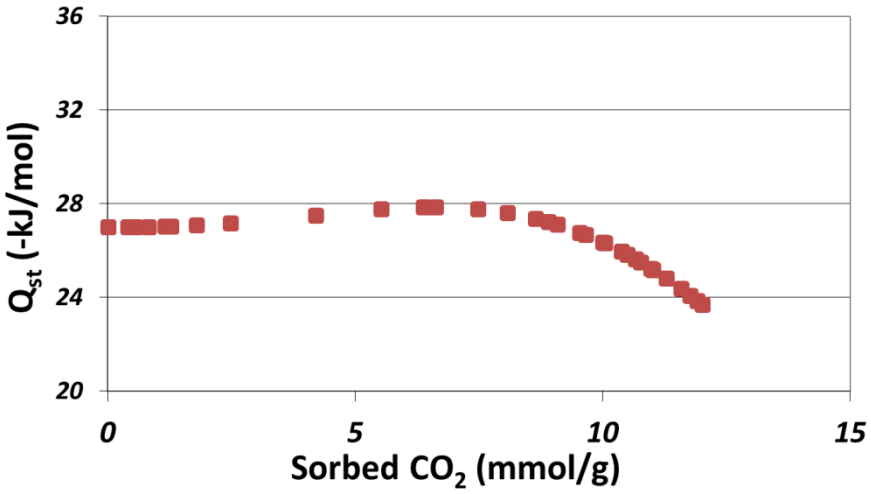

Figure A.22: Calculated Q_{st}(−kJ/mol) vs sorbed CO_2 in Zn(hba)

Table A-10: Optimised virial coefficients for modelling gas sorption calculated from the 258 and 273 K isotherms.

a0	-3245.55
a1	-0.11204
a2	-0.52409
a3	-1.66307
a4	0.269254
a5	-0.00899
b	15.52847
R^2	0.998078

A.1.2.4Zn(3-fluoro hba)

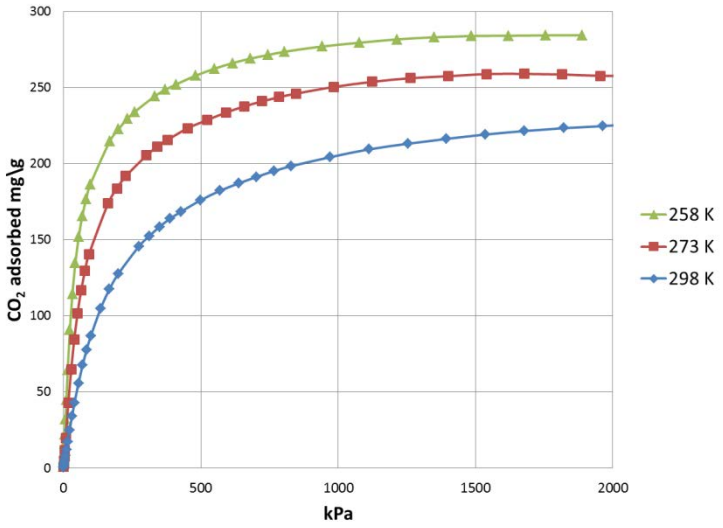

Figure A.23: 258, 273 and 298 K CO_2 isotherms of Zn(3-fluoro hba)

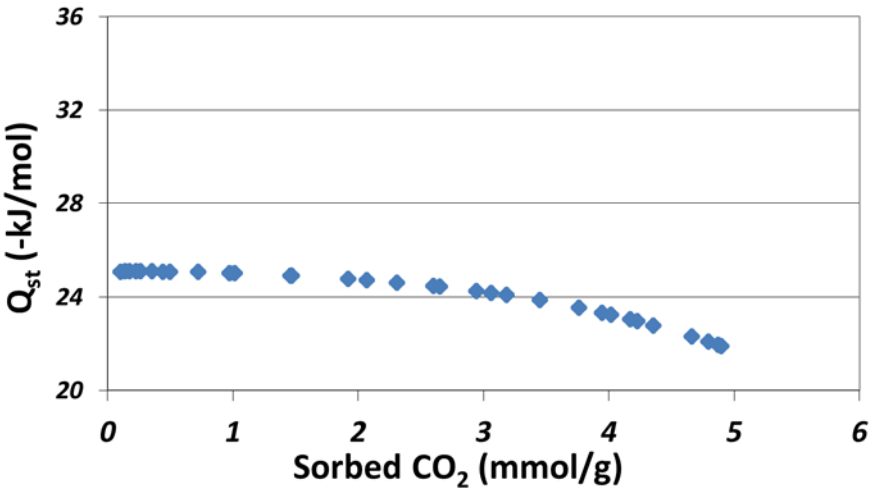

Figure A.24: Calculated Q_{st}(−kJ/mol) vs sorbed CO_2 in Zn(hba)

Table A-11: Optimised virial coefficients for modelling gas sorption calculated from the 258 and 273 K isotherms.

a0	-3015.88
a1	-14.7995
a2	31.38811
a3	-12.3917
a4	3.152983
a5	-0.23273
b	13.92086
R^2	0.998678

A.1.2.5 Zn(2-fluoro hba)

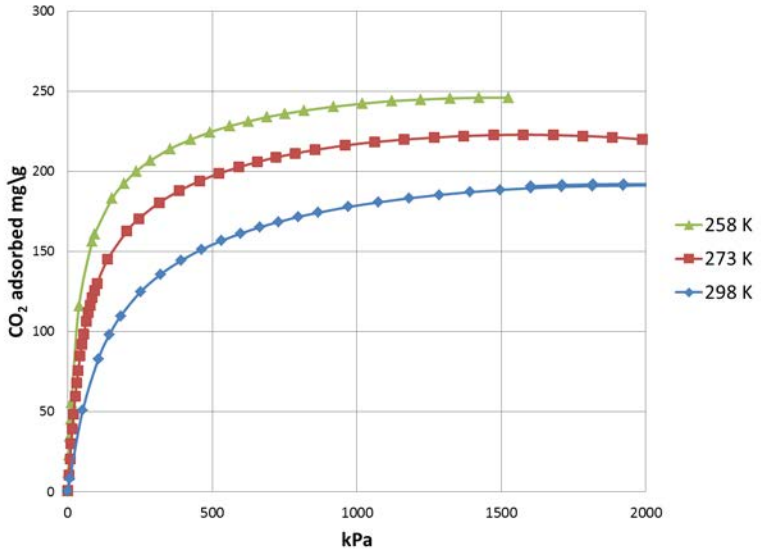

Figure A.25: 258, 273 and 298 K CO_2 isotherms of Zn(2-fluoro hba)

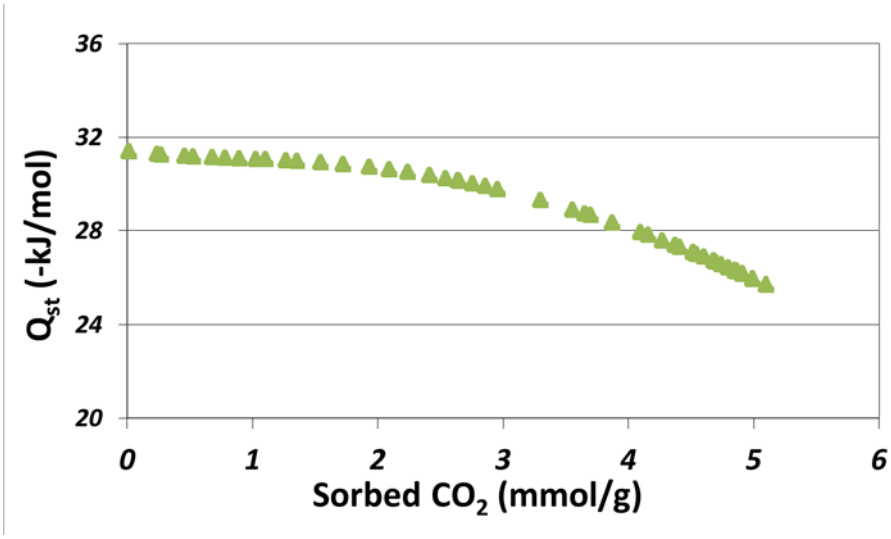

Figure A.26: Calculated Q_{st}(−kJ/mol) vs sorbed CO_2 in Zn(2-fluoro hba)

Table A-12: Optimised virial coefficients for modelling gas sorption calculated from the 258 and 273 K isotherms.

a0	-3777.52
a1	83.04573
a2	-76.6081
a3	39.63893
a4	-6.44994
a5	0.394637
b	16.63627
R^2	0.997645

A.1.2.6 Zn(2-chloro hba)

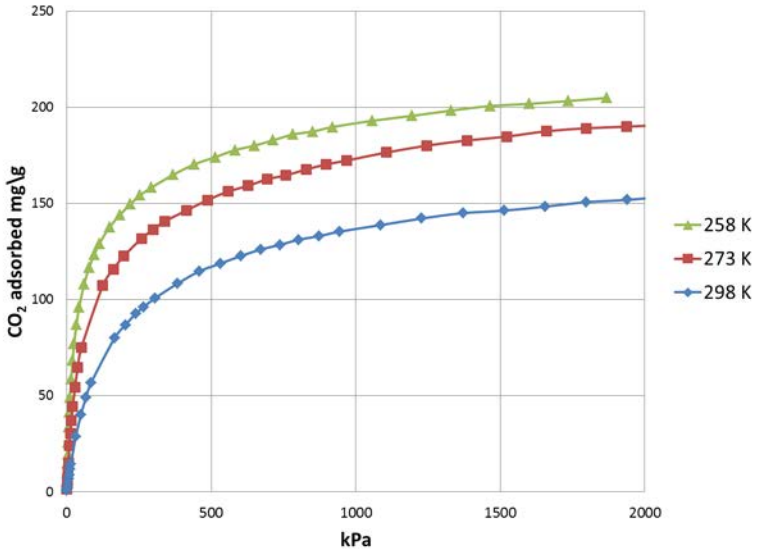

Figure A.27: 258, 273 and 298 K CO_2 isotherms of Zn(2-chloro hba)

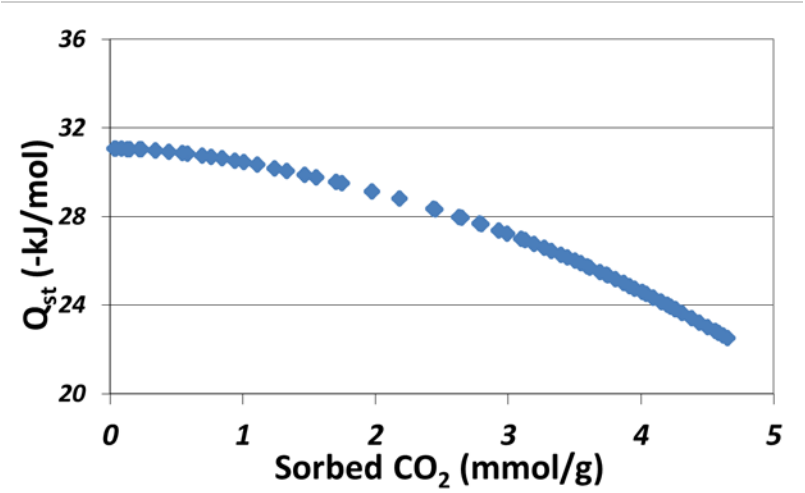

Figure A.28: Calculated Q_{st}(−kJ/mol) vs sorbed CO_2 in Zn(2-chloro hba)

Table A-13: Optimised virial coefficients for modelling gas sorption calculated from the 258 and 273 K isotherms.

a0	-3734.56
a1	-12.4223
a2	116.5652
a3	-40.5016
a4	8.688625
a5	-0.65491
b	16.42145
R^2	0.999784

A.1.2.7 Zn(2-methyl hba)

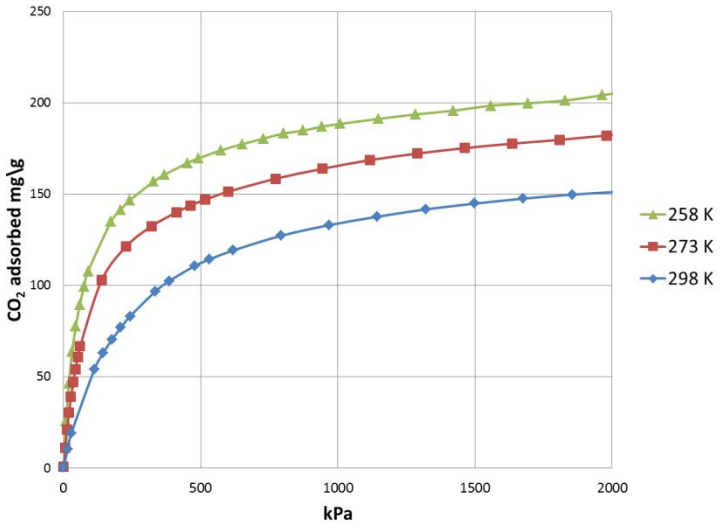

Figure A.29: 258, 273 and 298 K CO_2 isotherms of Zn(2-methyl hba)

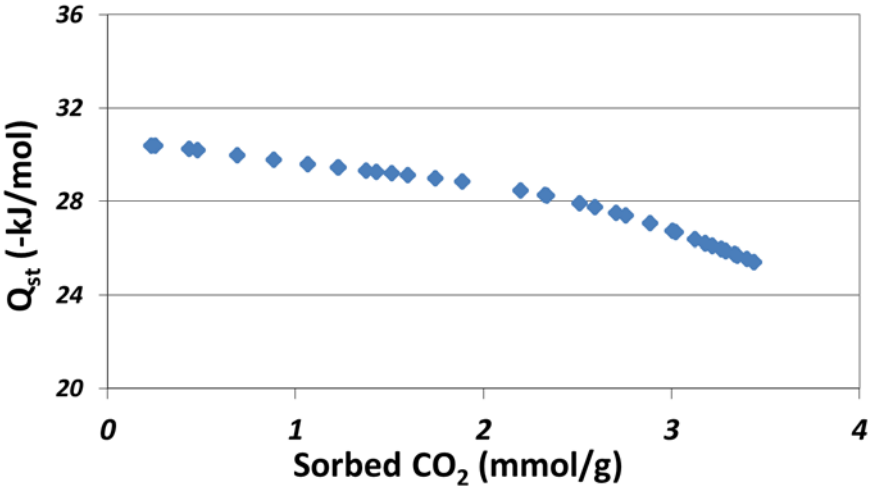

Figure A.30: Calculated Q_{st}(−kJ/mol) vs sorbed CO_2 in Zn(2-methyl hba)

Table A-14: Optimised virial coefficients for modelling gas sorption calculated from the 258 and 273 K isotherms.

a0	-3660.4
a1	-24.2706
a2	265.6497
a3	-208.753
a4	69.0836
a5	-7.54072
b	16.4979
R^2	0.997163

A.1.2.8 Zn(2,6-dimethyl hba)

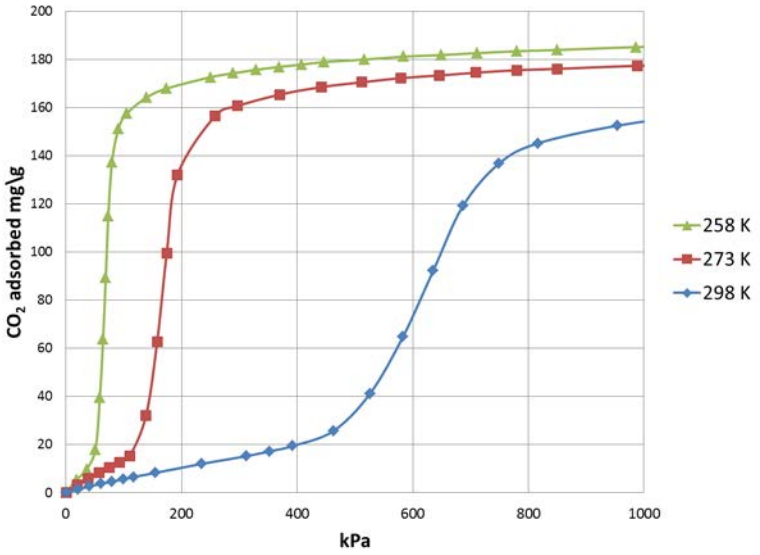

Figure A.31: 258, 273 and 298 K CO_2 isotherms of Zn(2,6-dimethyl hba)

A.1.3 H_2

A.1.3.1 Zn(hba)

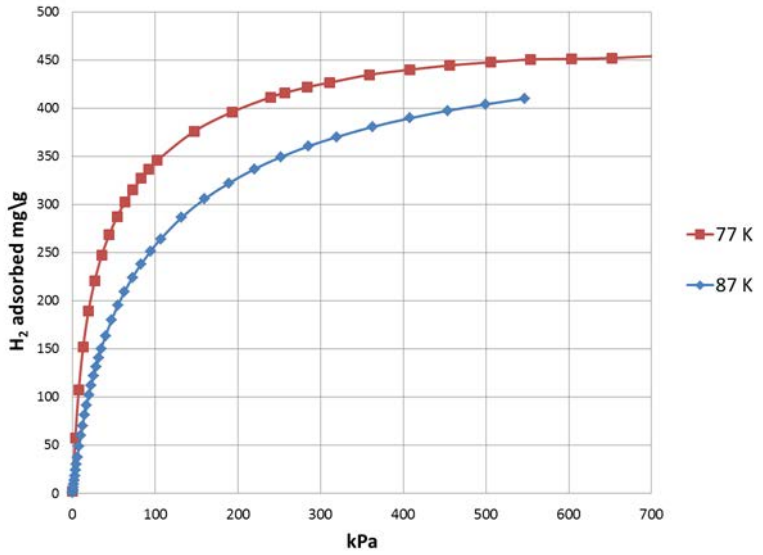

Figure A.32: 77 and 87 K H_2 isotherms of Zn(hba)

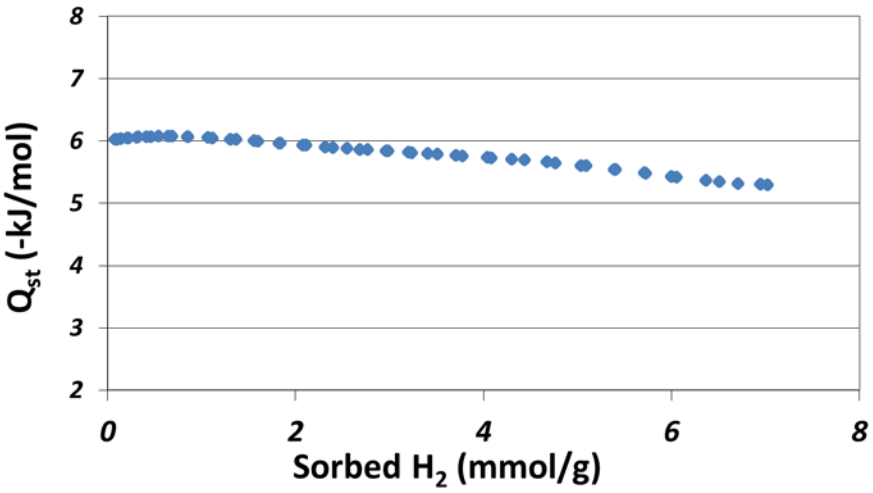

Figure A.33: Calculated Q_{st}(−kJ/mol) vs sorbed H_2 in Zn(hba)

Table A-15: Optimised virial coefficients for modelling gas sorption calculated from the 77 and 87 K isotherms.

a0	-722.1
a1	-30.1838
a2	33.67958
a3	-11.4509
a4	1.730542
a5	-0.09409
b	10.32131
R^2	0.99884

A.1.3.2 Zn(cma)

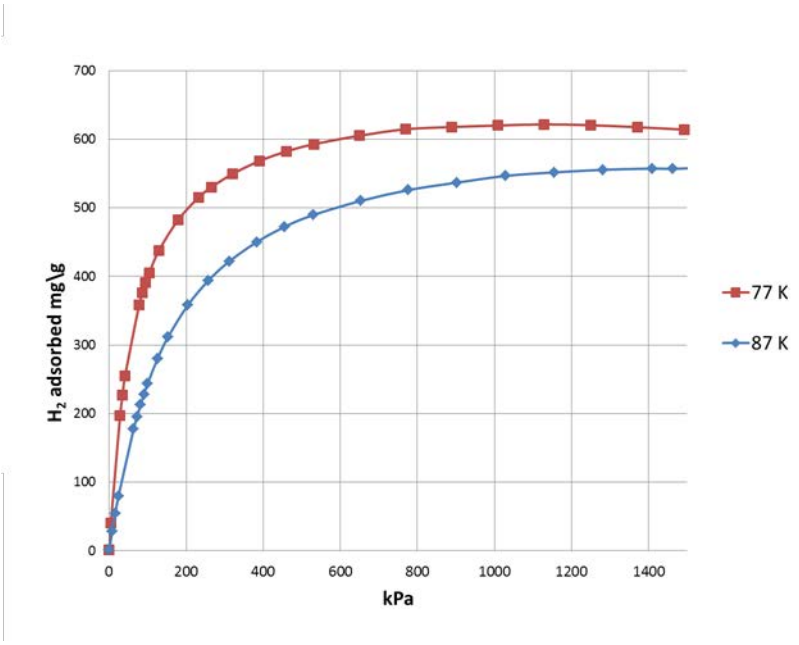

Figure A.34: 77 and 87 K H_2 isotherms of Zn(cma)

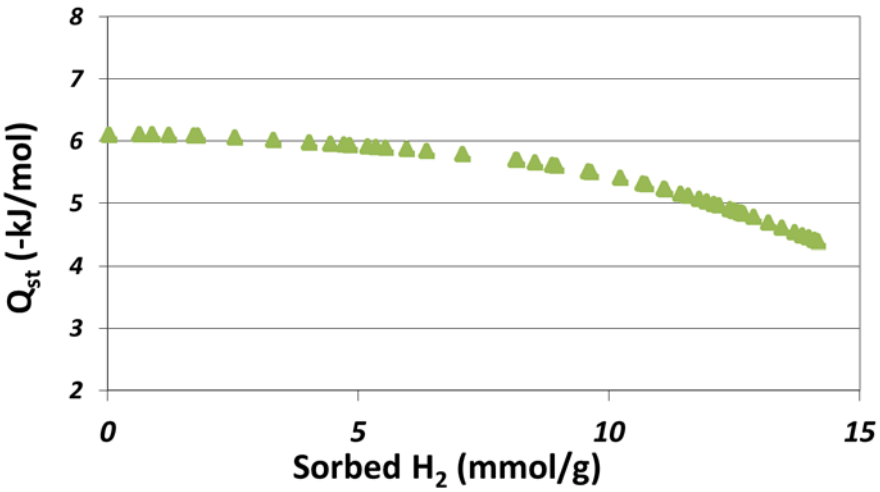

Figure A.35: Calculated Q_{st}(−kJ/mol) vs sorbed H_2 in Zn(cma)

Table A-16: Optimised virial coefficients for modelling gas sorption calculated from the 77 and 87 K isotherms.

a0	-733.14
a1	-3.74149
a2	3.71217
a3	-0.67614
a4	0.057617
a5	-0.00155
b	11.12856
R^2	0.99594

A.1.3.3Zn(3-fluoro hba)

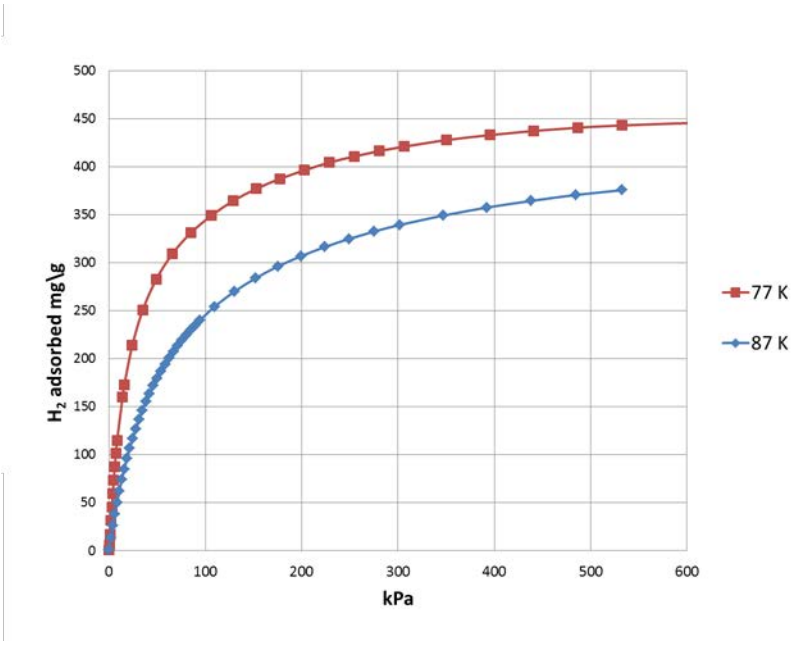

Figure A.36: 77 and 87 K H_2 isotherms of Zn(3-fluoro hba)

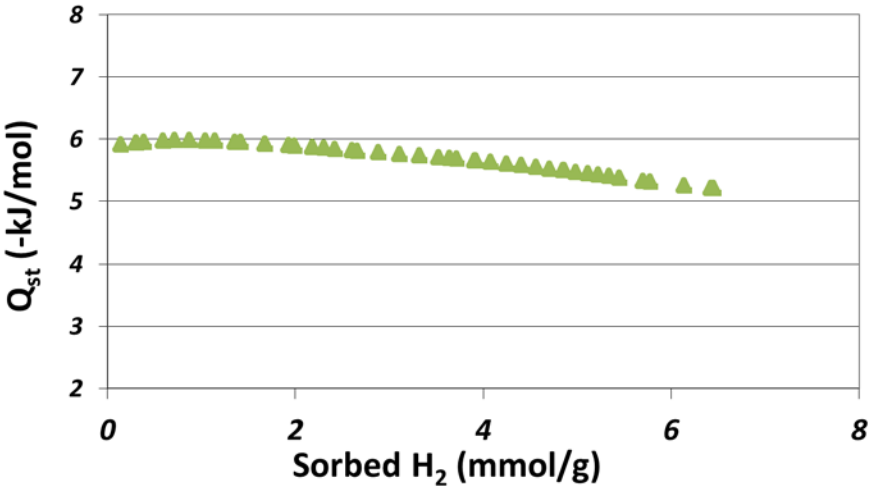

Figure A.37: Calculated Q_{st}(−kJ/mol) vs sorbed H_2 in Zn(3-fluoro hba)

Table A-17: Optimised virial coefficients for modelling gas sorption calculated from the 77 and 87 K isotherms.

a0	-707.063
a1	-34.9479
a2	32.2026
a3	-10.3201
a4	1.589141
a5	-0.09093
b	10.26527
R^2	0.997911

A.1.3.4 Zn(2-fluoro hba)

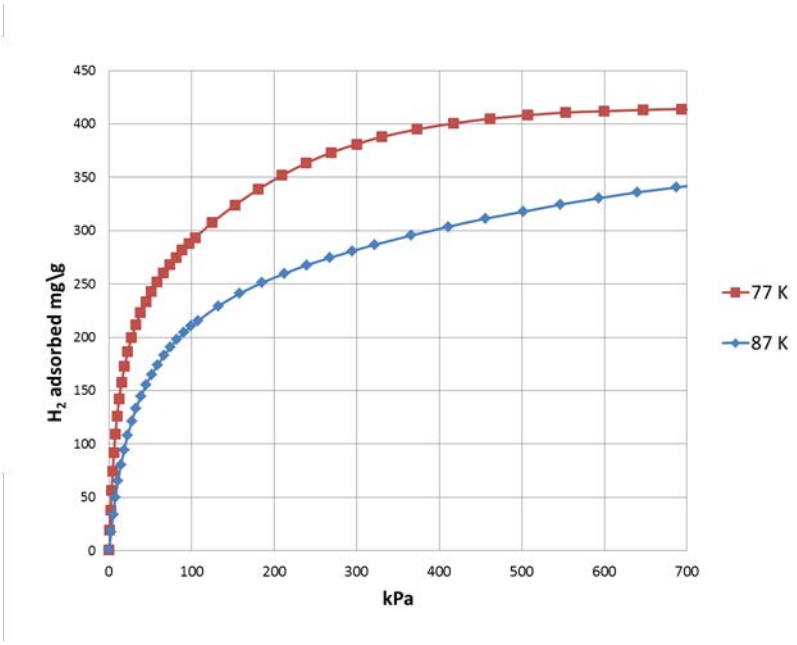

Figure A.38: 77 and 87 K H_2 isotherms of Zn(2-fluoro hba)

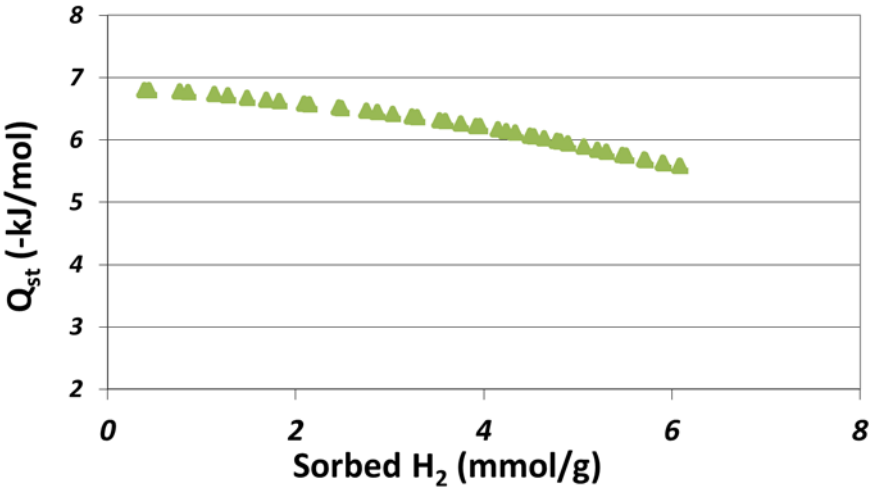

Figure A.39: Calculated Q_{st}(−kJ/mol) vs sorbed H_2 in Zn(2-fluoro hba)

Table A-18: Optimised virial coefficients for modelling gas sorption calculated from the 77 and 87 K isotherms.

a0	-815.489
a1	-14.1323
a2	26.43542
a3	-9.98759
a4	1.798542
a5	-0.11559
b	11.26992
R^2	0.99802

A.1.3.5 Zn(2-chloro hba)

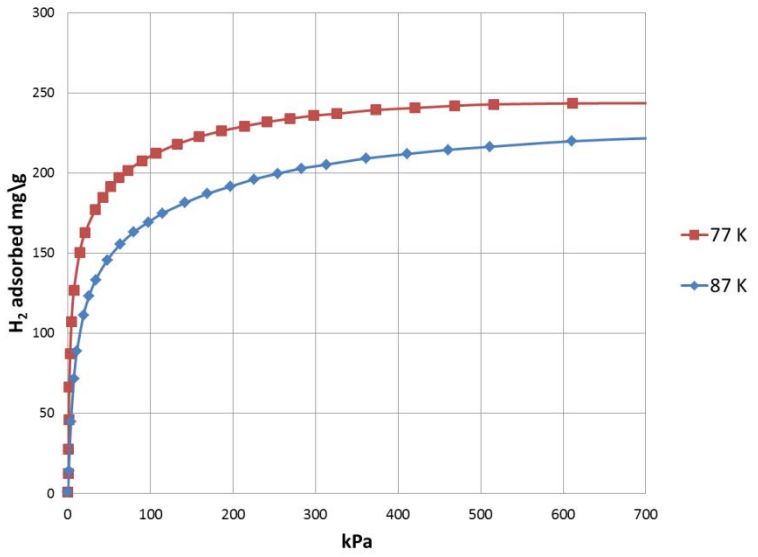

Figure A.40: 77 and 87 K H_2 isotherms of Zn(2-chloro hba)

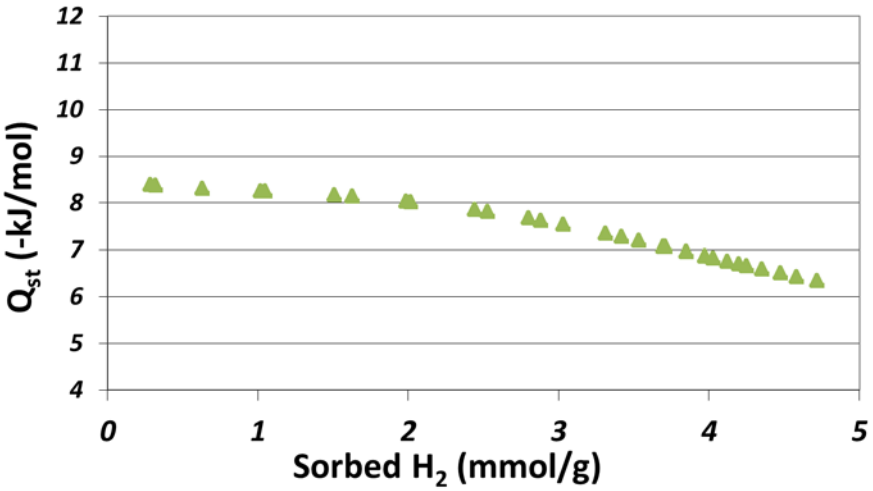

Figure A.41: Calculated Q_{st}(−kJ/mol) vs sorbed H_2 in Zn(2-chloro hba)

Table A-19: Optimised virial coefficients for modelling gas sorption calculated from the 77 and 87 K isotherms.

a0	-1019.66
a1	48.56331
a2	-36.256
a3	16.95246
a4	-2.28728
a5	0.080236
b	12.82302
R^2	0.999124

A.1.3.6 Zn(2-methyl hba)

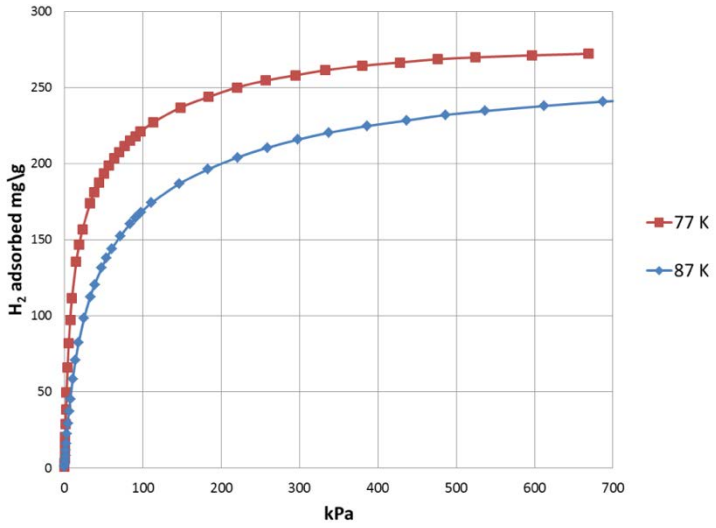

Figure A.42: 77 and 87 K H_2 isotherms of Zn(2-methyl hba)

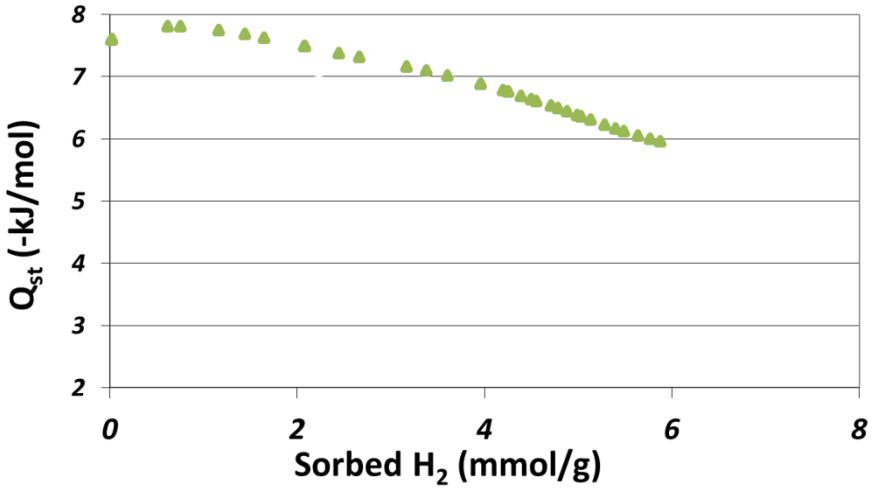

Figure A.43: Calculated Q_{st}(−kJ/mol) vs sorbed H_2 in Zn(2-methyl hba)

Table A-20: Optimised virial coefficients for modelling gas sorption calculated from the 77 and 87 K isotherms.

a0	-910.966
a1	-91.9797
a2	96.37739
a3	-34.4228
a4	5.781891
a5	-0.35711
b	12.73772
R^2	0.999352

A.1.3.7 Zn(2,6-dimethyl hba)

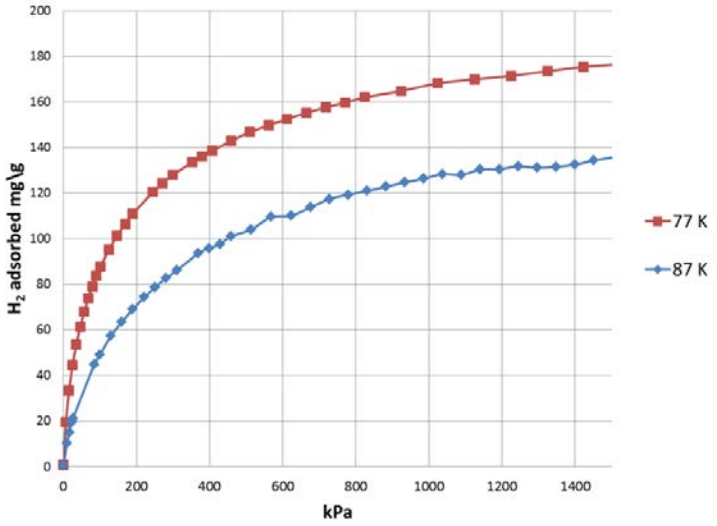

Figure A.44: 77 and 87 K H_2 isotherms of Zn(2,6-dimethyl hba)

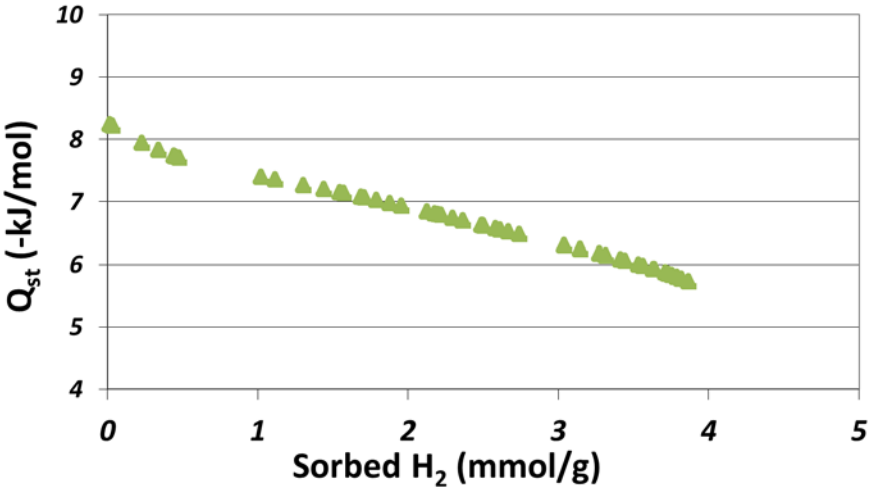

Figure A.45: Calculated Q_{st}(−kJ/mol) vs sorbed H_2 in Zn(2,6-dimethyl hba)

Table A-21: Optimised virial coefficients for modelling gas sorption calculated from the 77 and 87 K isotherms.

a0	-994.267
a1	207.224
a2	-177.599
a3	95.39516
a4	-23.2618
a5	2.134033
b	14.66832
R^2	0.998787

A.1.4 N_2O

A.1.4.1Zn(hba)

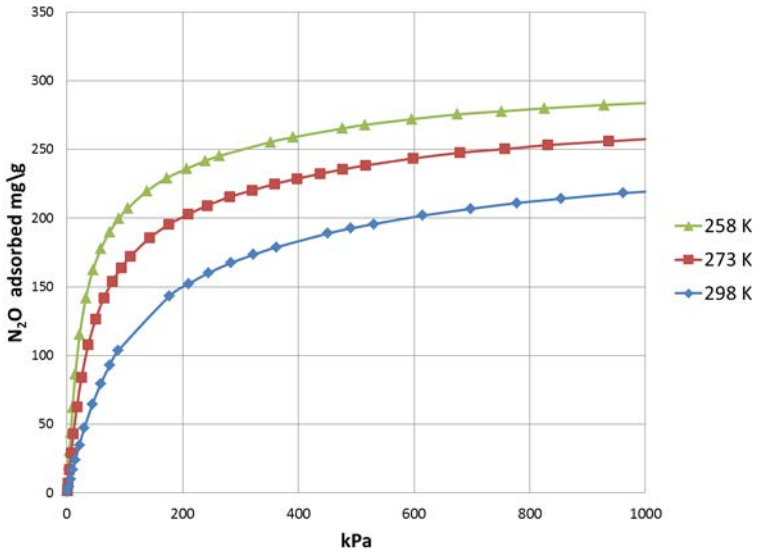

Figure A.46: 258, 273 and 298 K N_2O isotherms of Zn(hba)

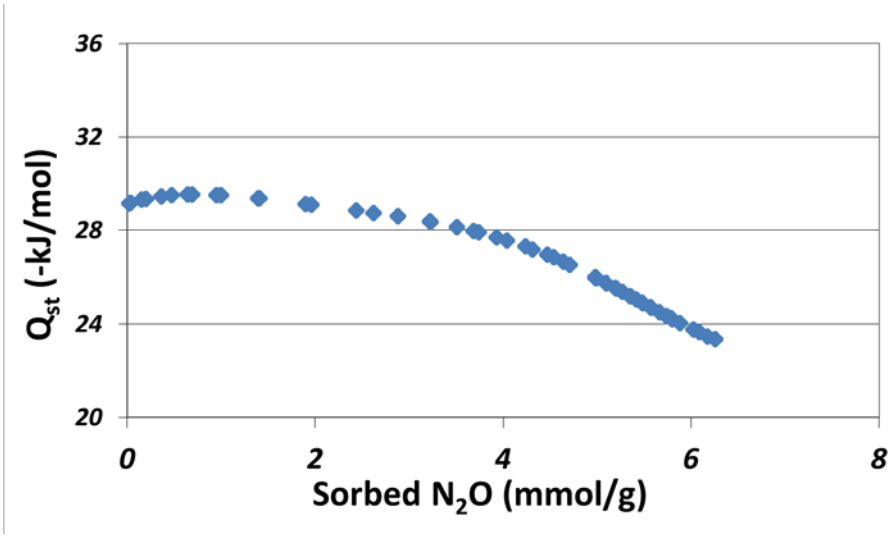

Figure A.47: Calculated Q_{st}(−kJ/mol) vs sorbed N_2O in Zn(hba)

Table A-22: Optimised virial coefficients for modelling gas sorption calculated from the 258 and 273 K isotherms.

a0	-3499.75
a1	-174.651
a2	187.483
a3	-72.3661
a4	13.0994
a5	-0.82435
b	15.49845
R^2	0.998176

A.1.4.2 Zn(hbpc)

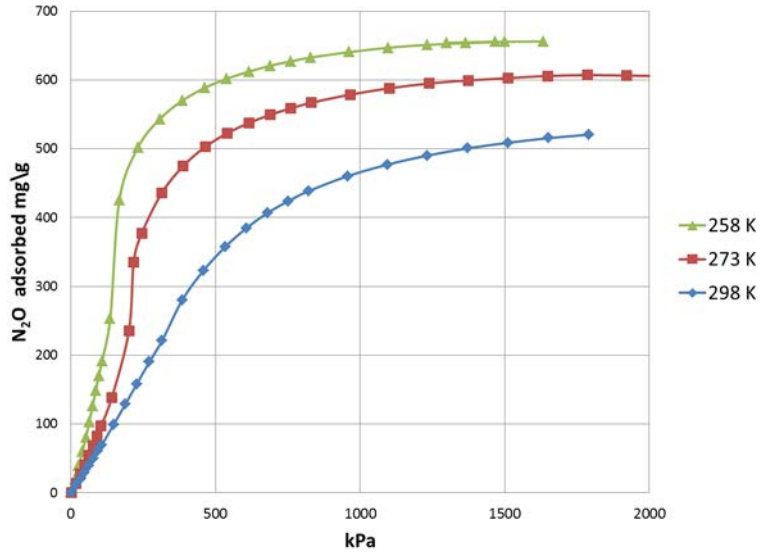

Figure A.48: 258, 273 and 298 K N_2O isotherms of Zn(hbpc)

A.1.4.3Zn(3-fluoro hba)

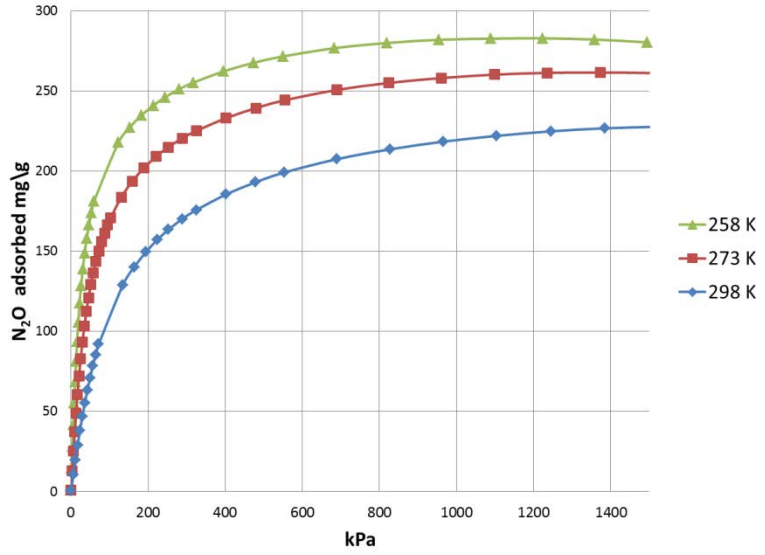

Figure A.49: 258, 273 and 298 K N_2O isotherms of Zn(3-fluoro hba)

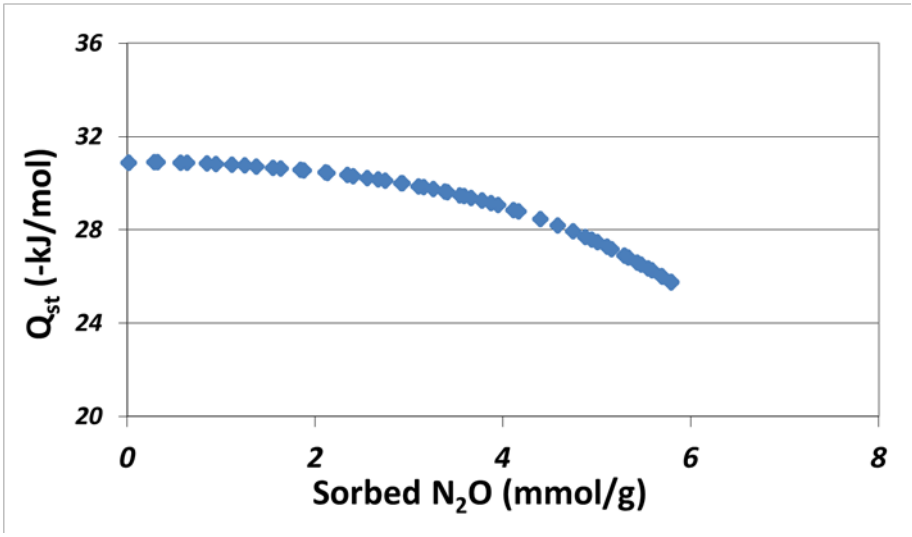

Figure A.50: Calculated Q_{st}(−kJ/mol) vs sorbed N_2O in Zn(3-fluoro hba)

Table A-23: Optimised virial coefficients for modelling gas sorption calculated from the 258 and 273 K isotherms.

a0	-3712.16
a1	-14.2919
a2	26.87571
a3	-6.75831
a4	1.400731
a5	-0.0717
b	16.11328
R^2	0.997142

A.1.4.4 Zn(2-fluoro hba)

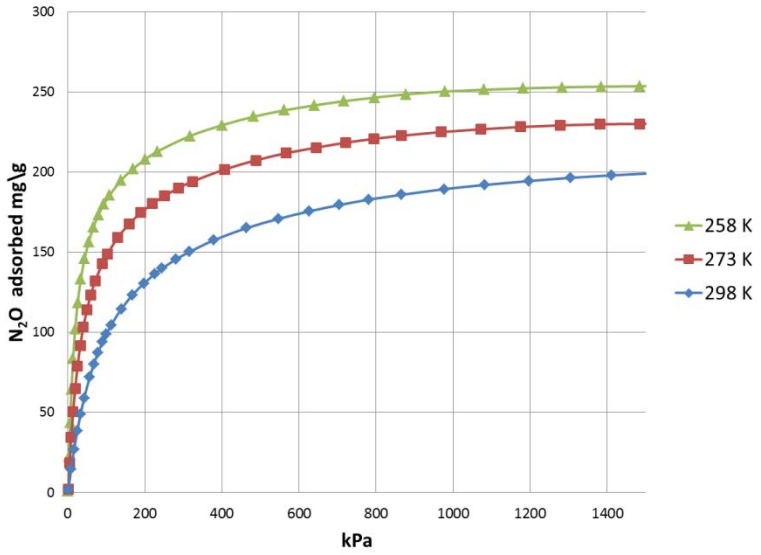

Figure A.51: 258, 273 and 298 K N_2O isotherms of Zn(2-fluoro hba)

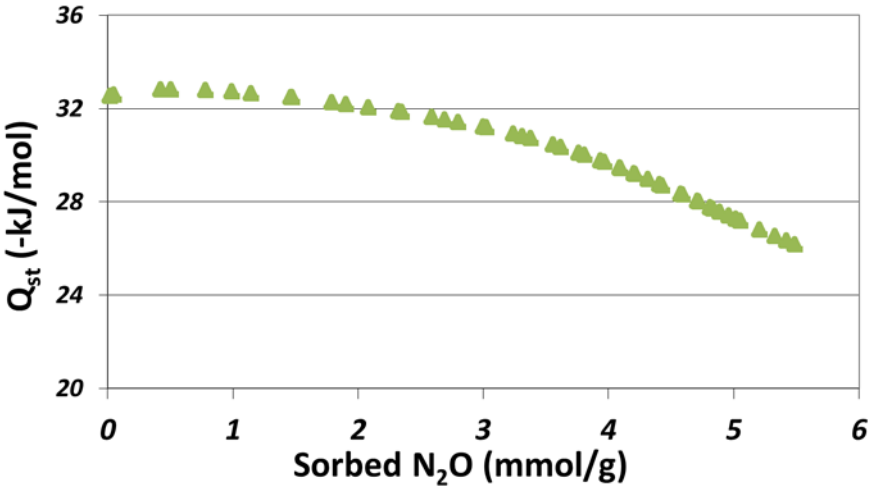

Figure A.52: Calculated Q_{st}(−kJ/mol) vs sorbed N_2O in Zn(2-fluoro hba)

Table A-24: Optimised virial coefficients for modelling gas sorption calculated from the 258 and 273 K isotherms.

a0	-3912.37
a1	-143.657
a2	180.1244
a3	-74.1313
a4	15.27088
a5	-1.09926
b	16.91983
R^2	0.998077

A.1.4.5 Zn(2-chloro hba)

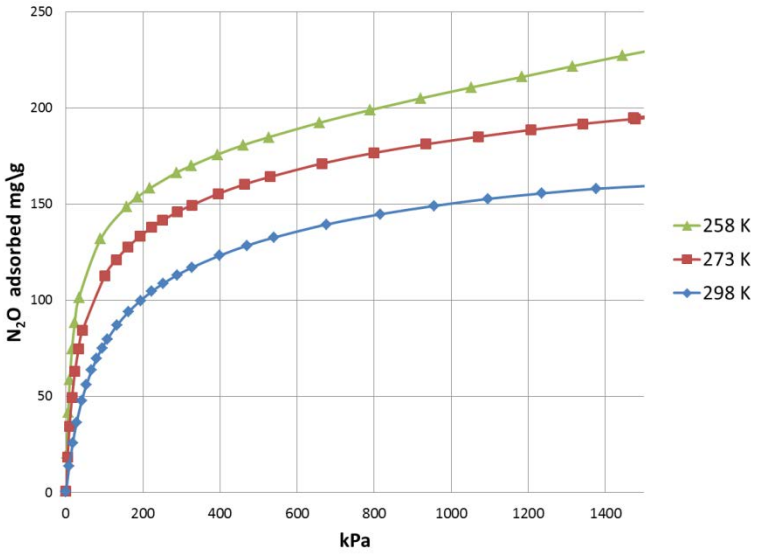

Figure A.53: 258, 273 and 298 K N_2O isotherms of Zn(2-chloro hba)

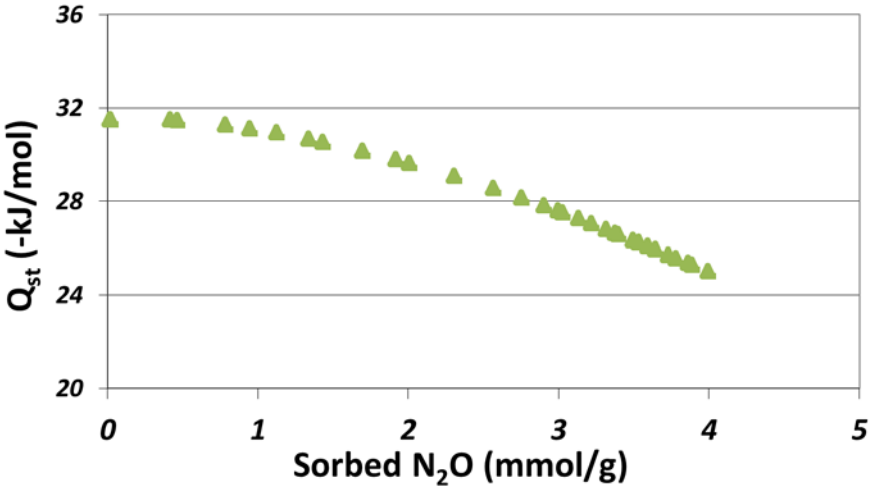

Figure A.54: Calculated Q_{st}(−kJ/mol) vs sorbed N_2O in Zn(2-chloro hba)

Table A-25: Optimised virial coefficients for modelling gas sorption calculated from the 258 and 273 K isotherms.

a0	-3787.64
a1	-52.8993
a2	142.8124
a3	-49.5199
a4	11.60441
a5	-1.06816
b	16.26402
R^2	0.999777

A.1.4.6 Zn(2-methyl hba)

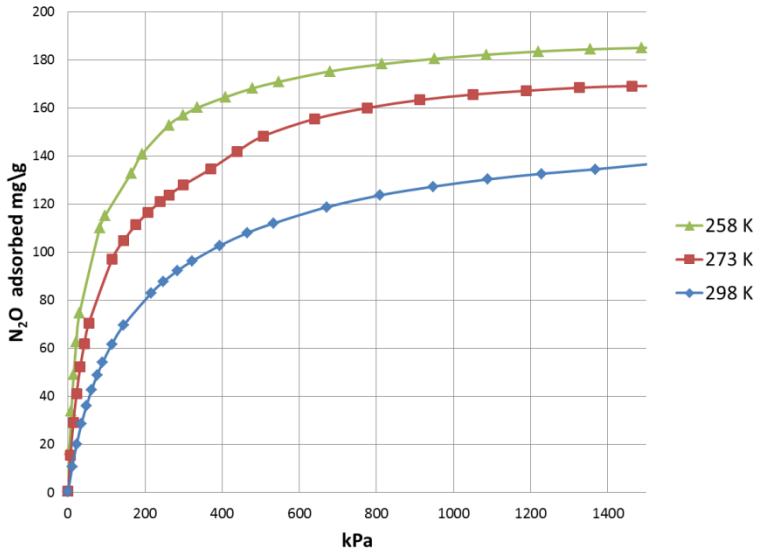

Figure A.55: 258, 273 and 298 K N_2O isotherms of Zn(2-methyl hba)

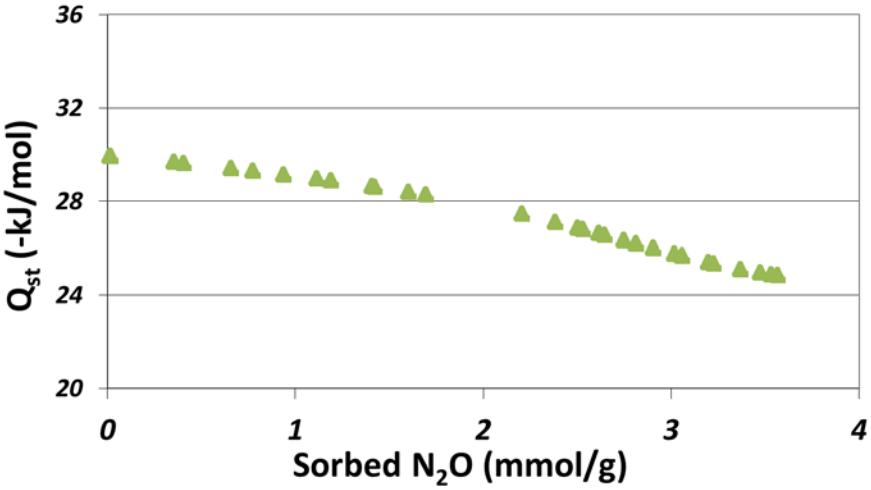

Figure A.56: Calculated Q_{st}(−kJ/mol) vs sorbed N_2O in Zn(2-methyl hba)

Table A-26: Optimised virial coefficients for modelling gas sorption calculated from the 258 and 273 K isotherms.

a0	-3600.83
a1	68.00219
a2	73.39636
a3	-62.2341
a4	28.23488
a5	-4.00339
b	16.04144
R^2	0.999382

A.1.4.7 Zn(2,6-dimethyl hba)

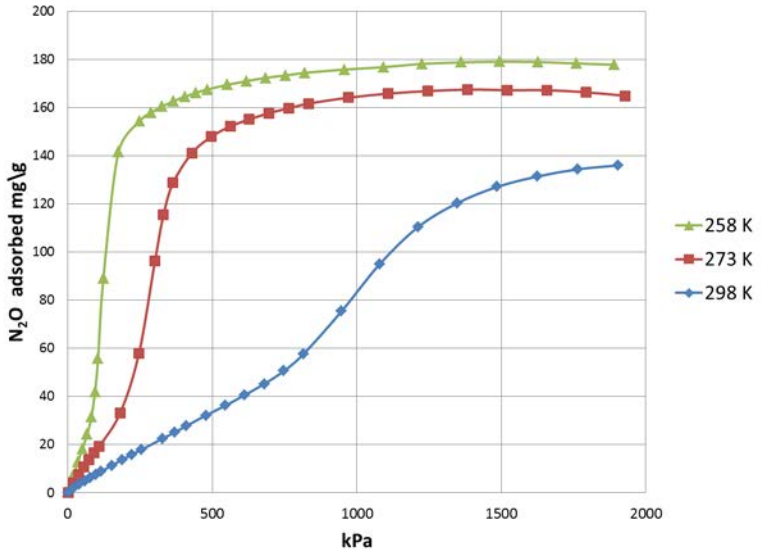

Figure A.57: 258, 273 and 298 K N_2O isotherms of Zn(2,6-dimethyl hba)

A.1.5 Xe

A.1.5.1Zn(hba)

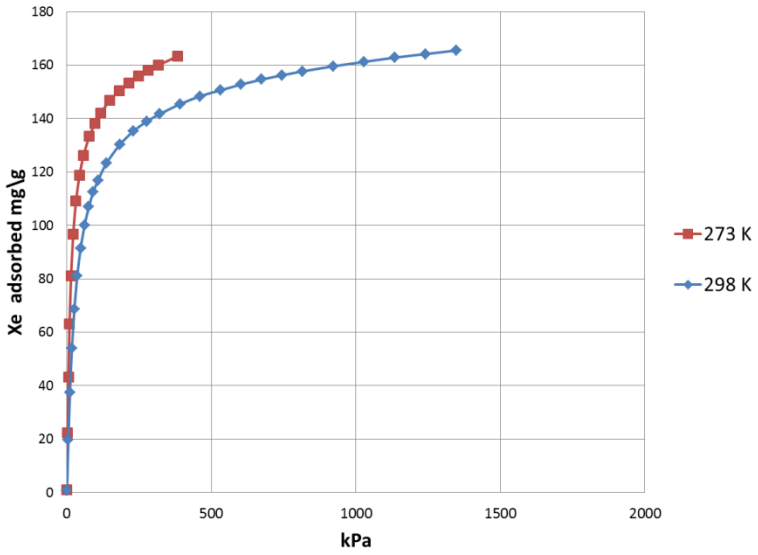

Figure A.58: 273 and 298 K Xe isotherms of Zn(hba)

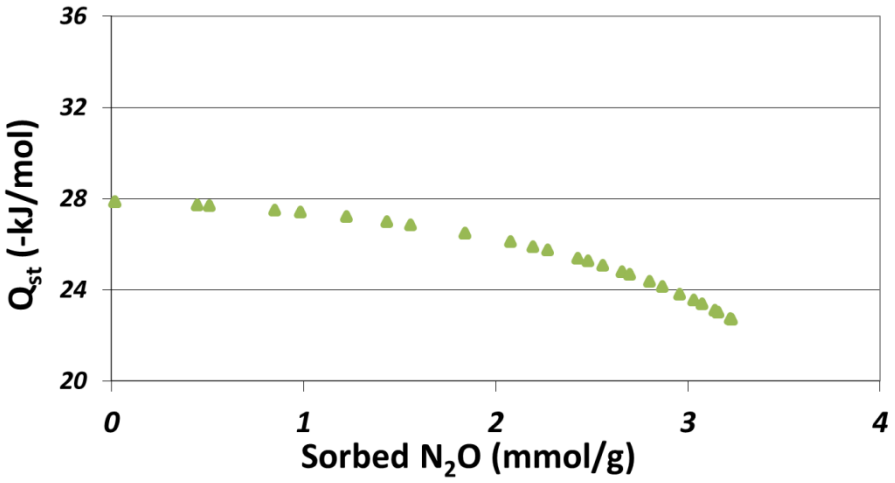

Figure A.59: Calculated Q_{st}(−kJ/mol) vs sorbed Xe in Zn(hba)

Table A-27: Optimised virial coefficients for modelling gas sorption calculated from the 273 and 298 K isotherms.

a0	-3349.36
a1	11.77945
a2	55.84153
a3	-15.8295
a4	4.314835
a5	0.18297
b	13.68079
R^2	0.999074

A.1.5.2 Zn(hbpc)

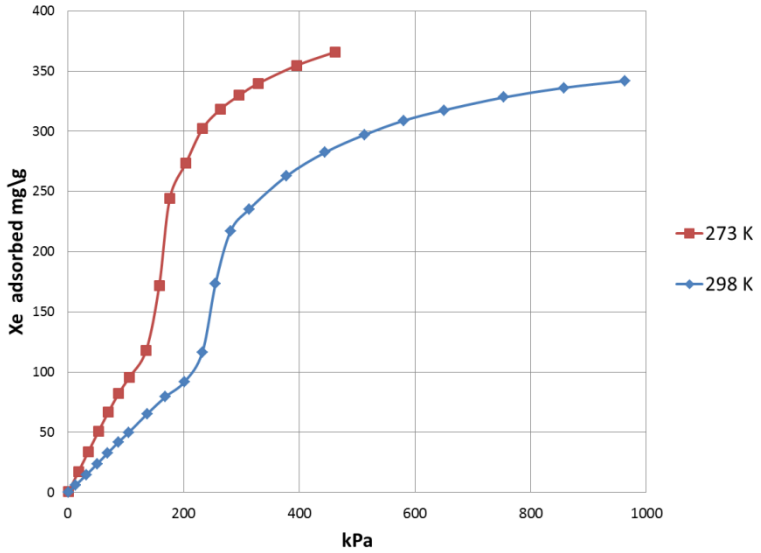

Figure A.60: 273 and 298 K Xe isotherms of Zn(hbpc)

A.1.5.3 Zn(2-fluoro hba)

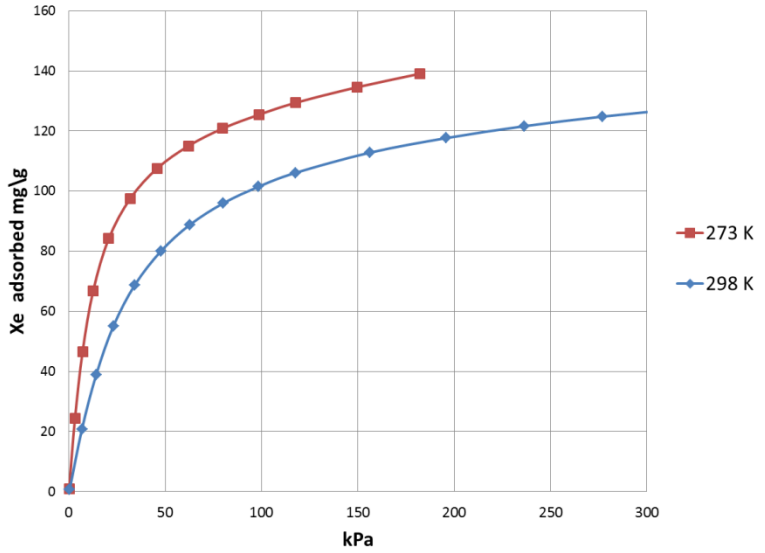

Figure A.61: 273 and 298 K Xe isotherms of Zn(2-fluoro hba)

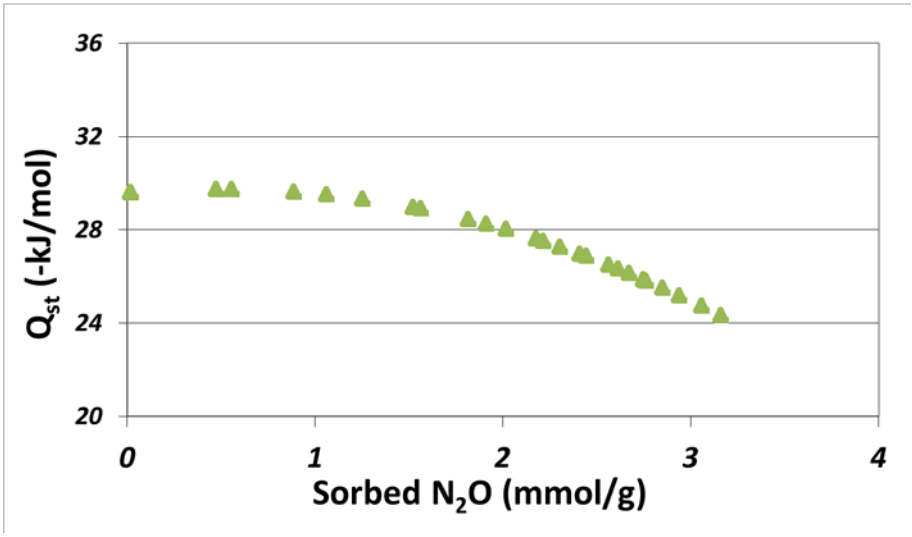

Figure A.62: Calculated Q_{st}(−kJ/mol) vs sorbed Xe in Zn(2-fluoro hba)

Table A-28: Optimised virial coefficients for modelling gas sorption calculated from the 273 and 298 K isotherms.

a0	-3557.72
a1	-75.6498
a2	79.12486
a3	-4.78264
a4	5.397916
a5	-0.97458
b	14.78957
R^2	0.997902

A.1.5.4 Zn(2-methyl hba)

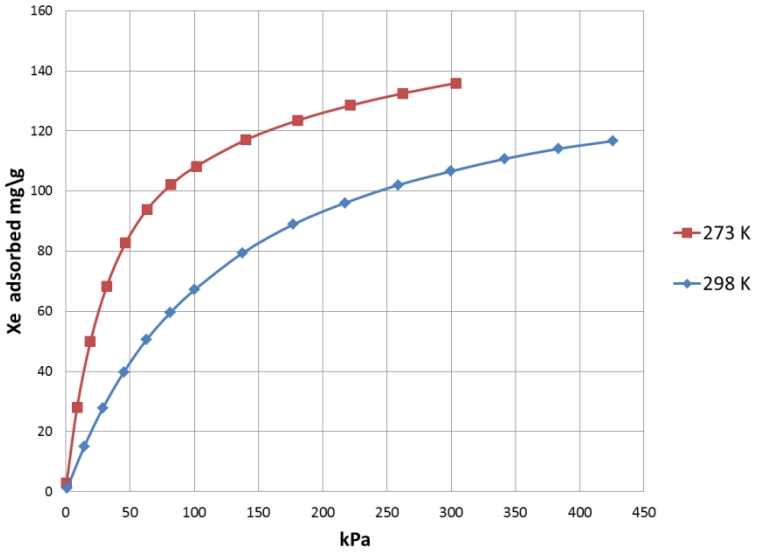

Figure A.63: 273 and 298 K Xe isotherms of Zn(2-methyl hba)

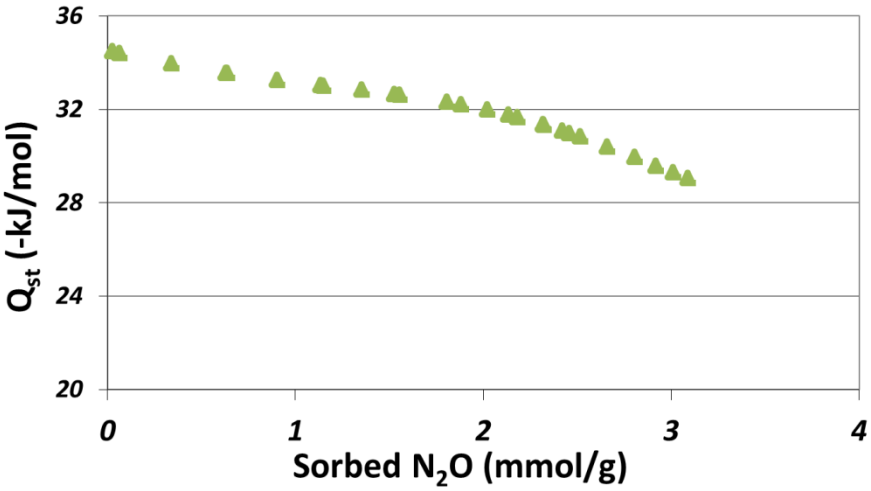

Figure A.64: Calculated Q_{st}(−kJ/mol) vs sorbed Xe in Zn(2-methyl hba)

Table A-29: Optimised virial coefficients for modelling gas sorption calculated from the 273 and 298 K isotherms.

a0	-4152.6
a1	205.9965
a2	13.24105
a3	-103.48
a4	58.45328
a5	-8.44772
b	17.37015
R^2	0.999243

A.2 Thermogravimetric analysis

Thermogravimetric analysis measurements were performed by an SDTA851 analyser.

Experimental details are available in section 7.6 of chapter 7.

A.2.1 Zn(hba)

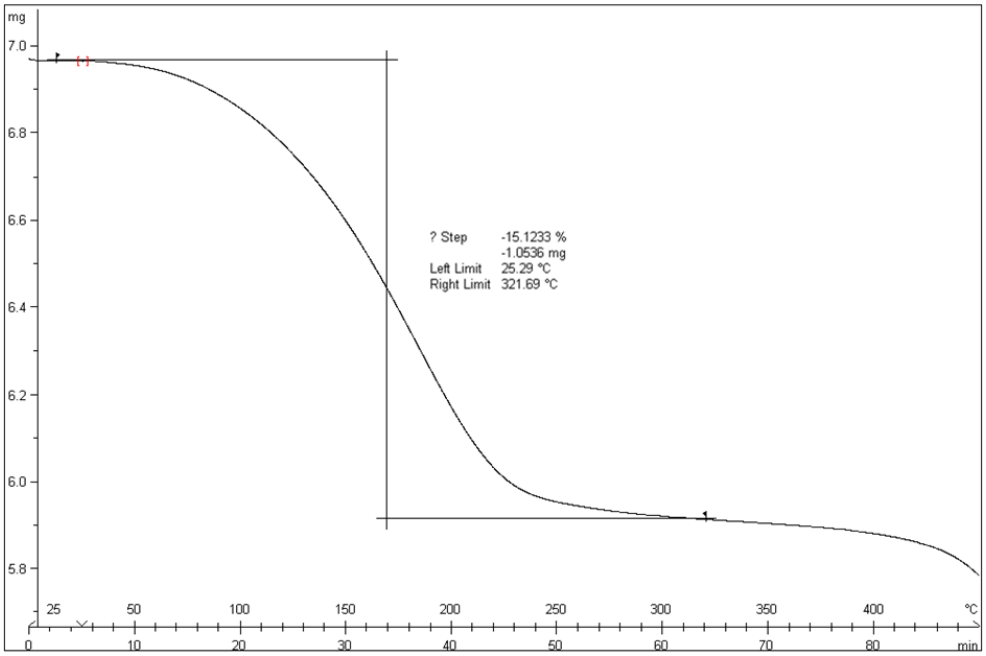

Figure A.65: TGA trace of Zn(hba). The y-axis shows the weight of the sample while the x-axis displays the temperature at with the sample is exposed and the elapsed time.

A.2.2Zn(hbpc)

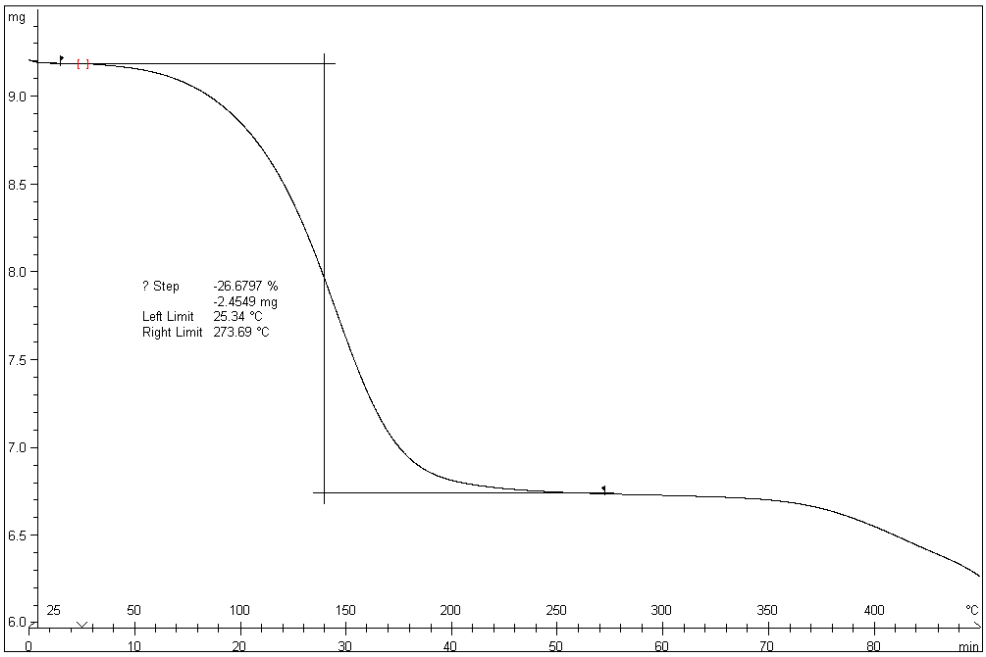

Figure A.66: TGA trace of Zn(hbpc). The y-axis shows the weight of the sample while the x-axis displays the temperature at with the sample is exposed and the elapsed time.

A.2.3 Zn(cma)

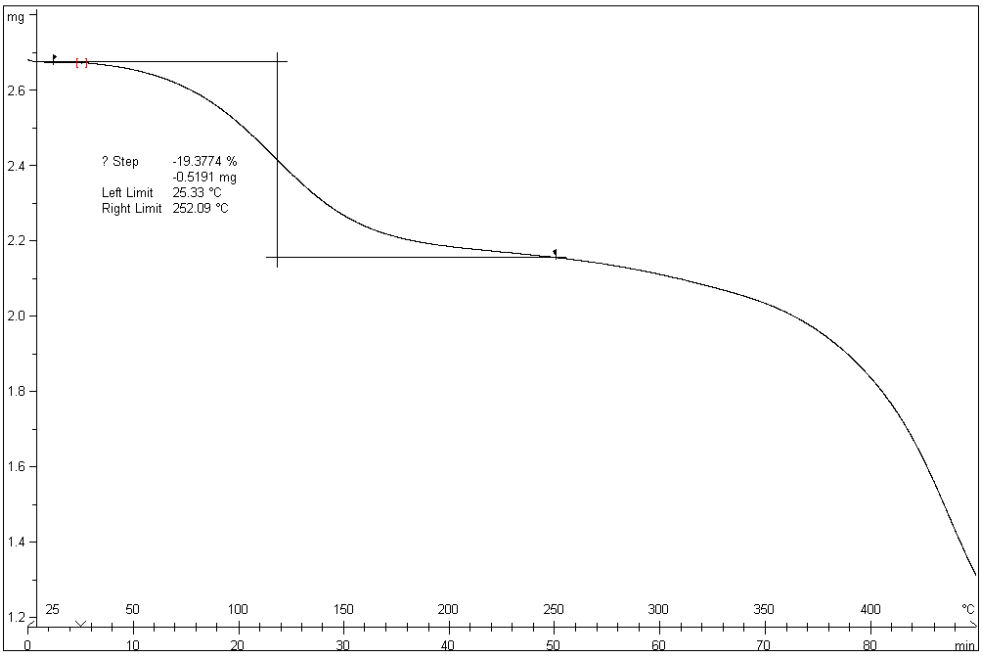

Figure A.67: TGA trace of Zn(cma). The y-axis shows the weight of the sample while the x-axis displays the temperature at with the sample is exposed and the elapsed time.

A.2.4Zn(3-fluoro hba)

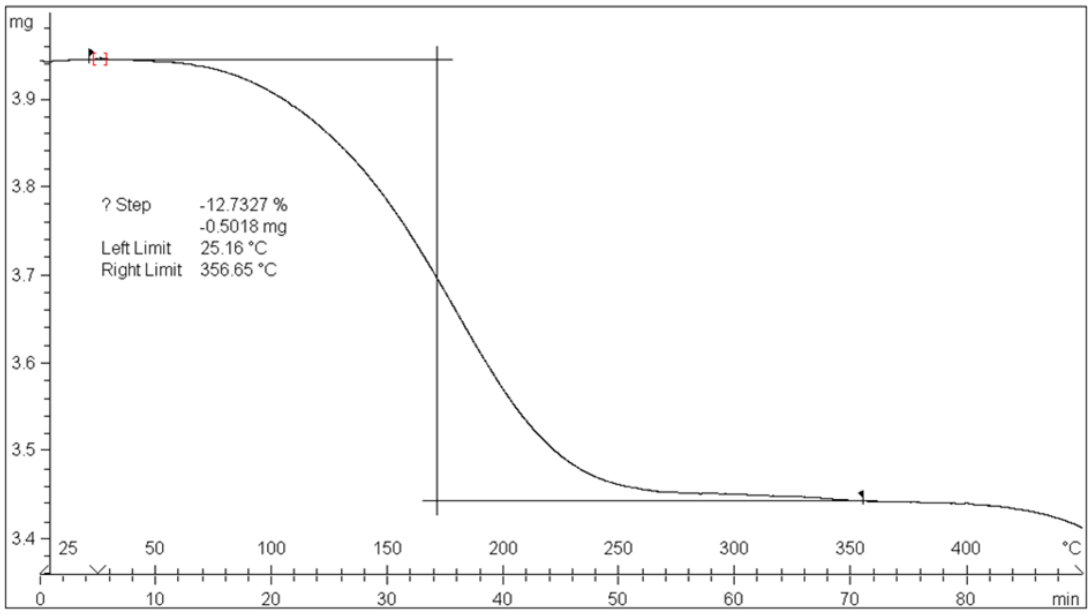

Figure A.68: TGA trace of Zn(3-fluoro hba). The y-axis shows the weight of the sample while the x-axis displays the temperature at with the sample is exposed and the elapsed time.

A.2.5 Zn(2-fluoro hba)

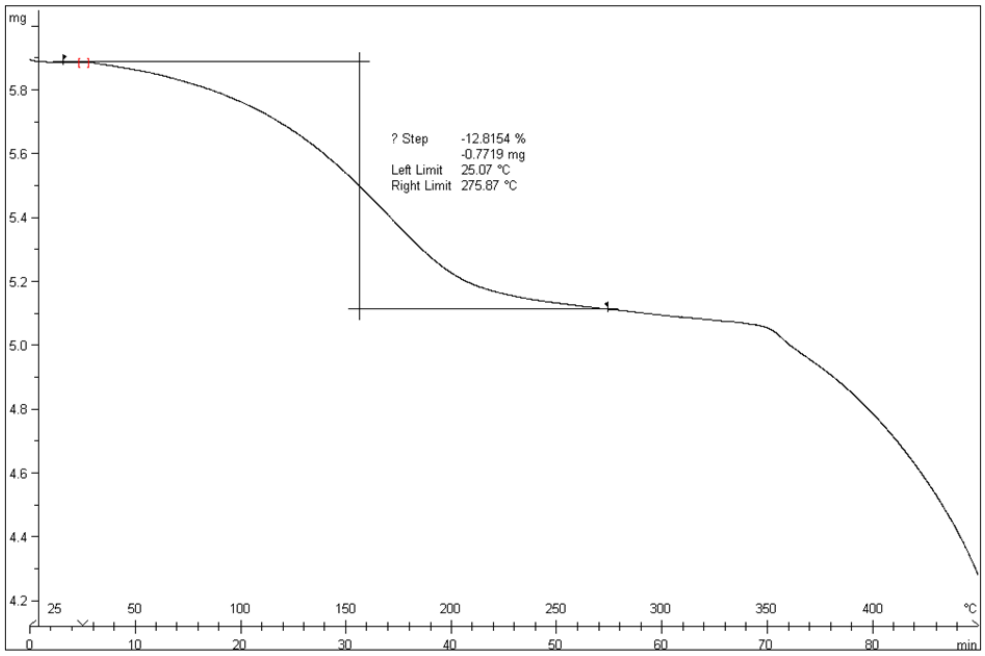

Figure A.69: TGA trace of Zn(2-fluoro hba). The y-axis shows the weight of the sample while the x-axis displays the temperature at with the sample is exposed and the elapsed time.

A.2.6 Zn(2-chloro hba)

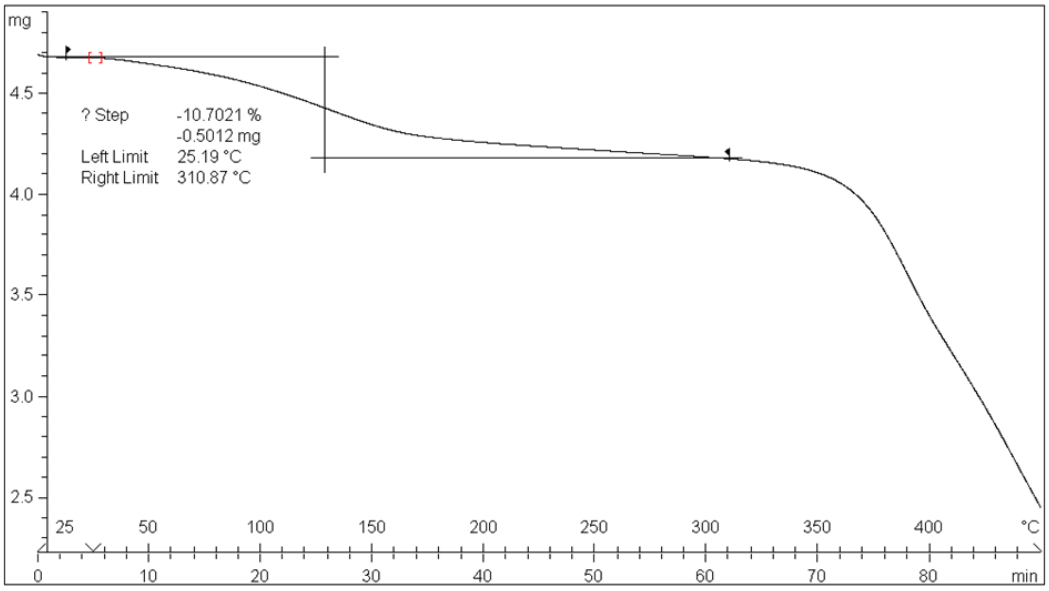

Figure A.70: TGA trace of Zn(2-chloro hba). The y-axis shows the weight of the sample while the x-axis displays the temperature at with the sample is exposed and the elapsed time.

A.2.7 Zn(2-methyl hba)

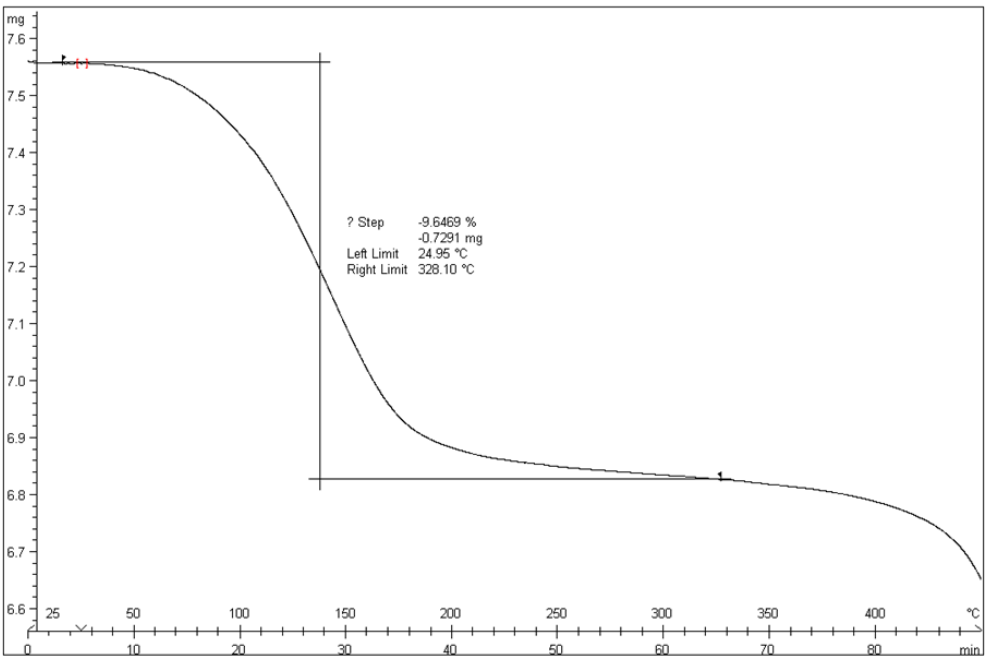

Figure A.71: TGA trace of Zn(2-methyl hba). The y-axis shows the weight of the sample while the x-axis displays the temperature at with the sample is exposed and the elapsed time.

A.2.8 Zn(2,6-dimethyl hba)

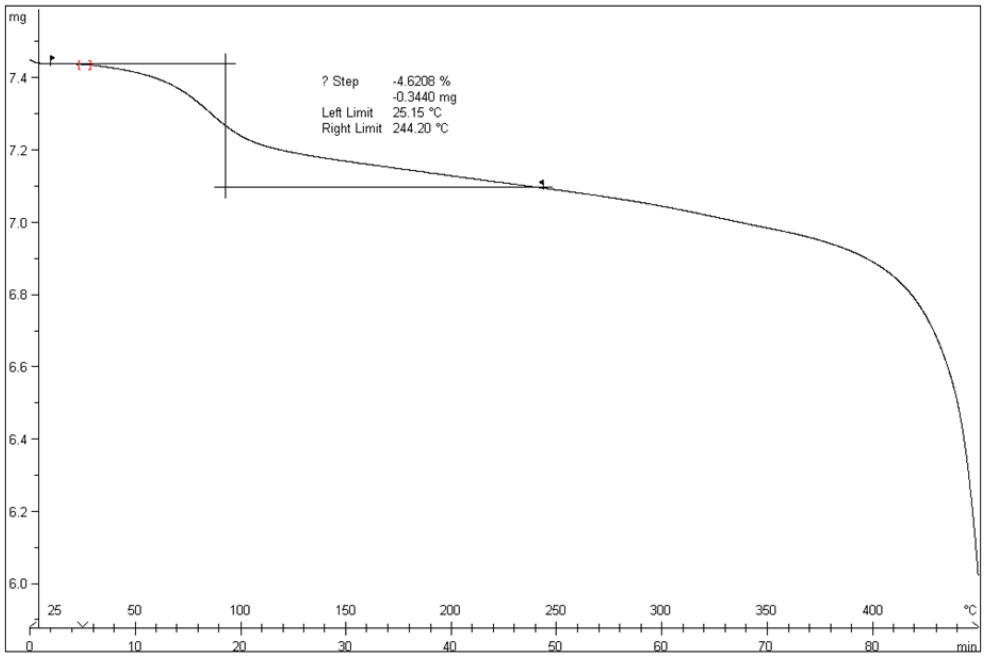

Figure A.72: TGA trace of Zn(2-methyl hba). The y-axis shows the weight of the sample while the x-axis displays the temperature at with the sample is exposed and the elapsed time.

A.3 X-ray powder diffraction peak indexing of Zn(2,6-dimethyl hba)

Indexing for powder patterns 1 through 5 were completed using Conograph GUI ver 0.9.

The details of which can be found in section 7.2.4 of chapter 7.

Powder pattern	Bravais lattice	*a*	*c*	M	Mwu	Mrev	Msym
1	Tetragonal (P)	9.122	6.3050	23.978	15.878	3.530	84.642
2	Tetragonal (P)	9.117	12.488	15.967	11.424	1.768	28.225
3	Tetragonal (P)	9.111	12.455	12.204	8.6540	1.101	13.433
4	Tetragonal (P)	9.070	6.4260	74.218	64.836	5.982	443.959
5	Tetragonal (P)	9.115	12.487	14.448	12.226	0.329	4.752

A.4 Crystallographic information files

Crystallographic information files are available at https://figshare.com/s/27b046b12a29dd997057 or upon request, from the candidate.

A.5 Computational structure simulations

Computational structure simulations were conducted by Dr Ravi Babarao from RMIT.

A.5.1 Structure models for Zn(2-methyl hba) and Zn(2,6-dimethyl hba)

This description of the modelling has been provided by Dr Ravi Barbarao of RMIT University.

The structure models for Zn(2-methyl hba) and Zn(2,6-dimethyl hba) were built up starting with the crystal structure of Zn(hba) previously reported in the literature using the Materials Studio Visualizer software[1]. Each structure was further geometry optimized using Density Functional Theory (DFT) methods including dispersion corrections (DFT-D3)[2] as implemented in the software package VASP 5.4.4[3]. Electron exchange and correlation were described using the generalized gradient approximation Perdew, Burke, and Ernzerhof (PBE)[4] form and the projector-augmented wave potentials were used to treat core and valence electrons.[5] In all cases, a plane-wave kinetic energy cut off of 650 eV and a Gamma-point mesh for sampling the Brillouin zone was used. Both the cell parameters and the ionic coordinates were fully relaxed until the Hellman-Feynman ionic forces were less than 0.01 eV/Å.

A.5.2 Location of CO_2 and Binding Energies

This description of the CO_2 modelling has been provided by Dr Ravi Barbarao of RMIT University.

DFT optimised structures were used in the simulations and the atomic partial charges for the framework atoms were assigned using the Qeq method as implemented in Materials Studio software. The adsorbate CO_2 was mimicked as a three-site model to account for the quadrupole moment. The C–O bond length in CO_2 was 1.18 Å and the bond angle ∠OCO was 180°. The charges on C and O atoms were +0.576e and –0.288e (e = 1.6022 10^{-19} C, the elementary charge), resulting in a quadrupole moment of -1.29 10^{-39} C·m^2. The LJ parameters for CO_2 were σC = 2.789 Å, εC = 29.66 K, σO = 3.011 Å, εO = 82.96 K.[6] The interactions of gas-adsorbent and gas-gas were modelled as a combination of pairwise site-site Lennard-Jones (LJ) and Coulombic potentials. The LJ potential parameters of the framework atoms were adopted from Universal force field.[7]

The initial location of the CO_2 in the periodic cell was obtained from the classical NVT simulated annealing technique. In the simulated annealing method, the temperature is lowered in succession allowing the gas molecule to reach a desirable configuration based on different moves such as rotate, translate and re-position with pre-set probabilities of occurrence. This process of heating and cooling the system was repeated in several heating cycles to find the local minima. Forty heating cycles were

performed where the maximum temperature and the final temperature were 10^5 K and 100 K, respectively.

The static binding energy for CO_2 at zero Kelvin was calculated using the dispersion–corrected semi-empirical DFT-D3 method. It is well-known that standard DFT methods based on generalized gradient approximation do not fully account for the long-range dispersion interactions between the framework and the bound gaseous adsorbates.

Static binding energies (ΔE) at 0 K were calculated using the following expression;

$$\Delta E = E_{MOF+GAS} - E_{MOF} - E_{GAS}$$

where E_x (where x = MOF + GAS, MOF or GAS) refers, respectively, to the total energies of the MOF + gas complex, the isolated MOF, and gas molecule.

A.6 Infra-red spectra

A.6.1 Li(paa)

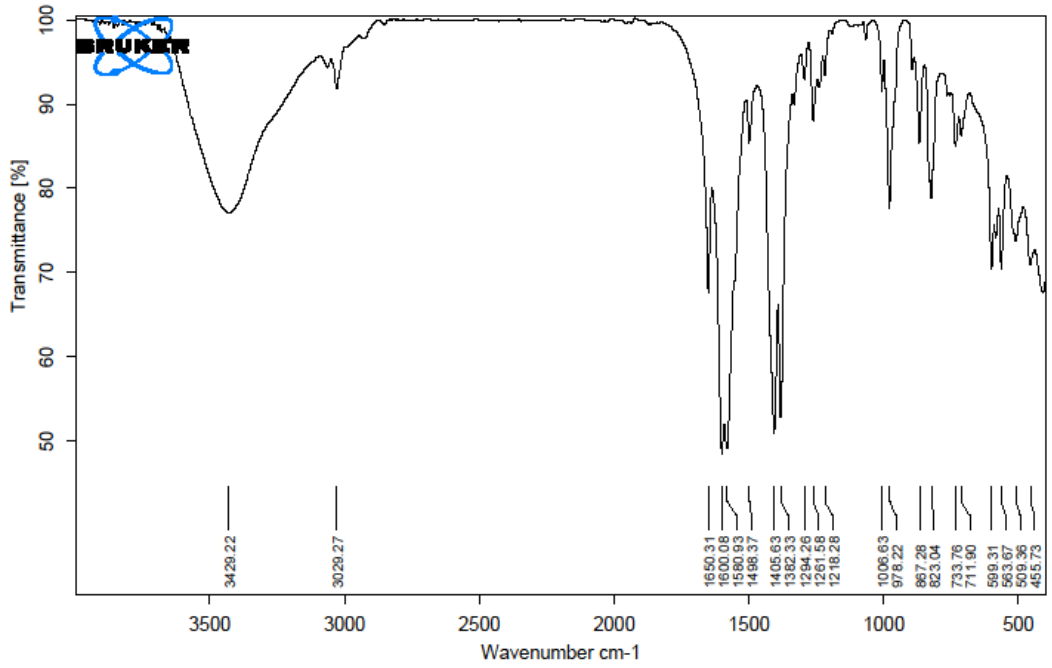

Figure A.73: Infra-red spectra of Li(paa)

A.6.2 $[Li_2(peb)(H_2O)_7](peb)\cdot H_2O$

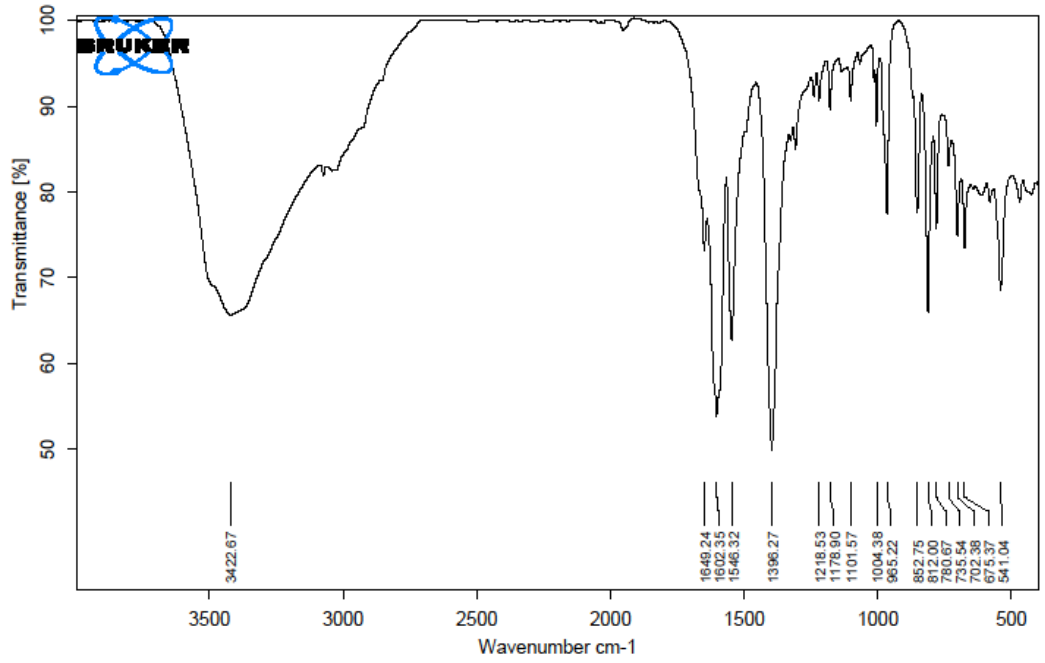

Figure A.74: Infra-red spectra of $[Li_2(peb)(H_2O)_7](peb)\cdot H_2O$)

A.6.3 Zn(2-fluoro hba)

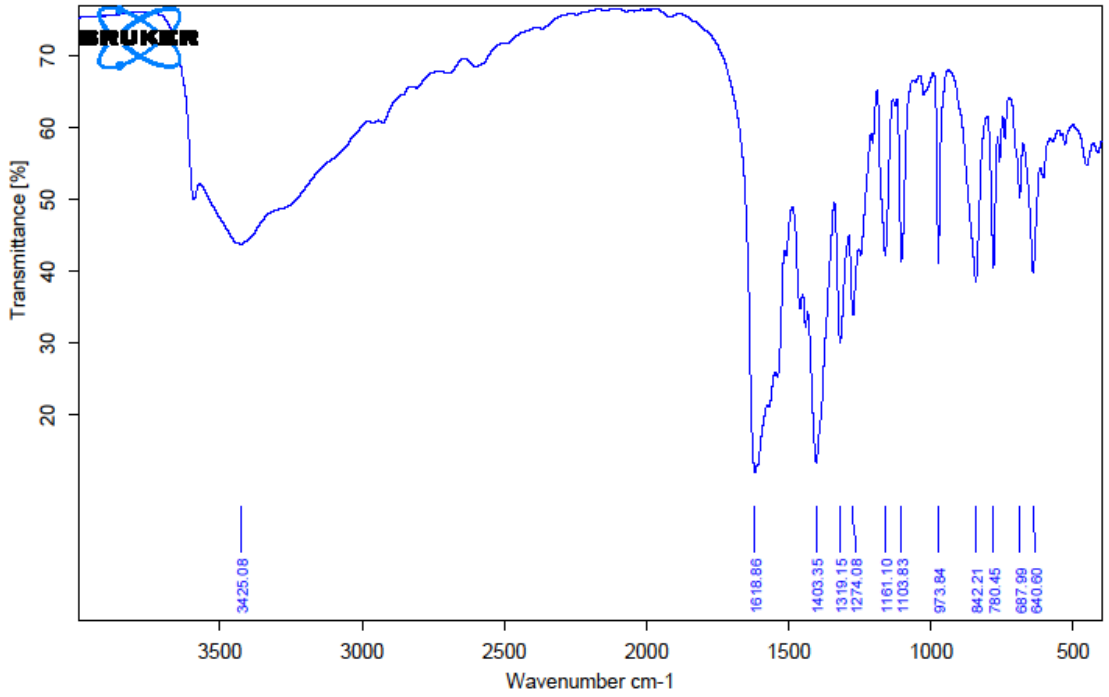

Figure A.75: Infra-red spectra of Zn(2-fluoro hba)

A.6.4 Zn(3-fluoro hba)

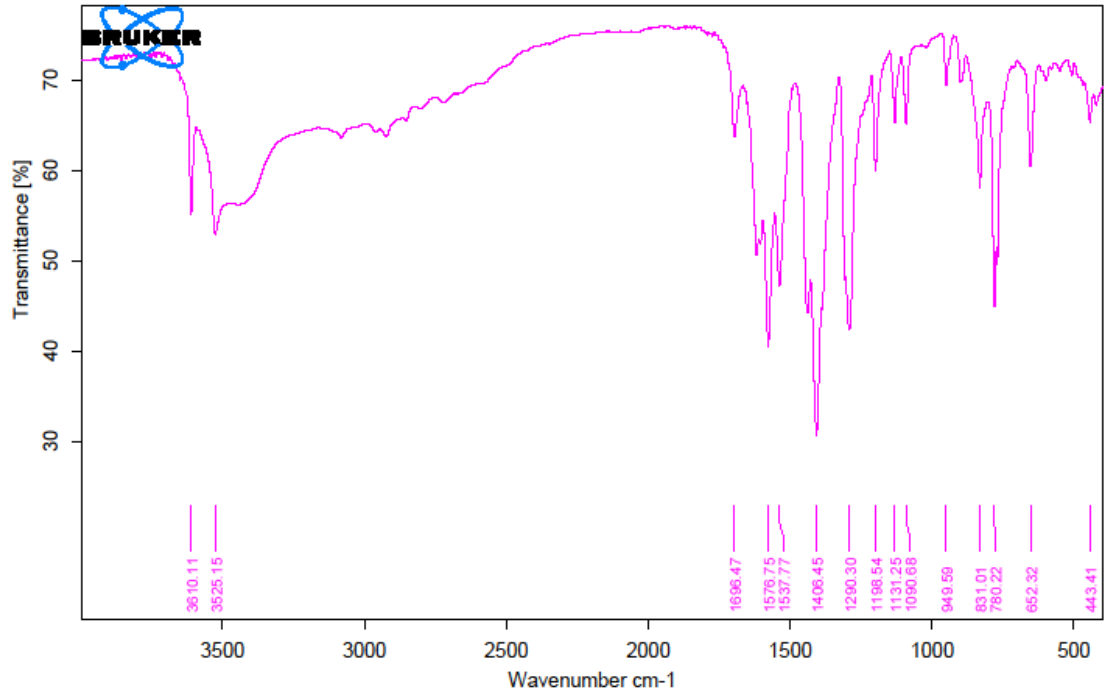

Figure A.76: Infra-red spectra of Zn(3-fluoro hba)

A.6.5 Zn(2-chloro hba)

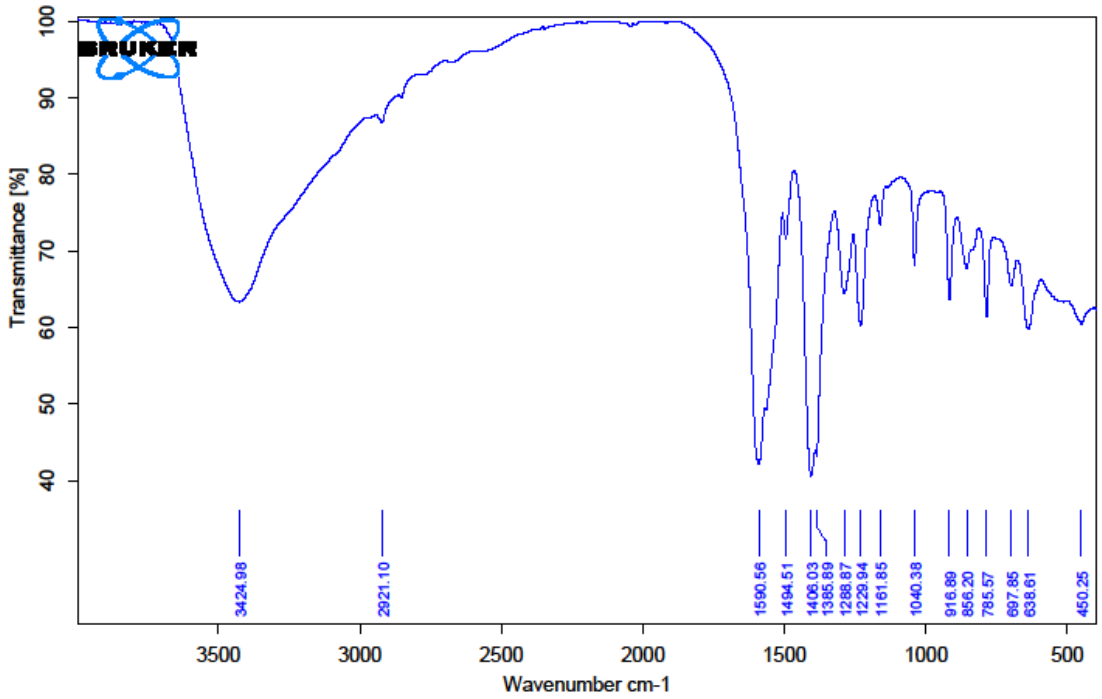

Figure A.77: Infra-red spectra of Zn(2-chloro hba)

A.6.6 Zn(2-methyl hba)

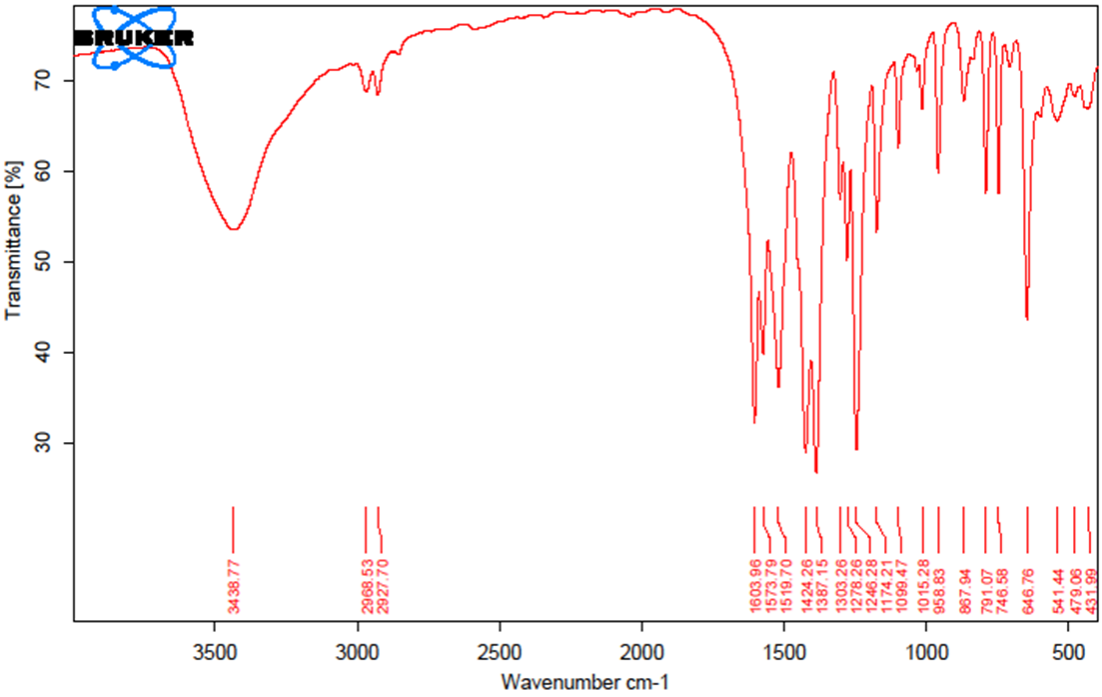

Figure A.78: Infra-red spectra of Zn(2-methyl hba)

A.6.7 Zn(2,6-dimethyl hba)

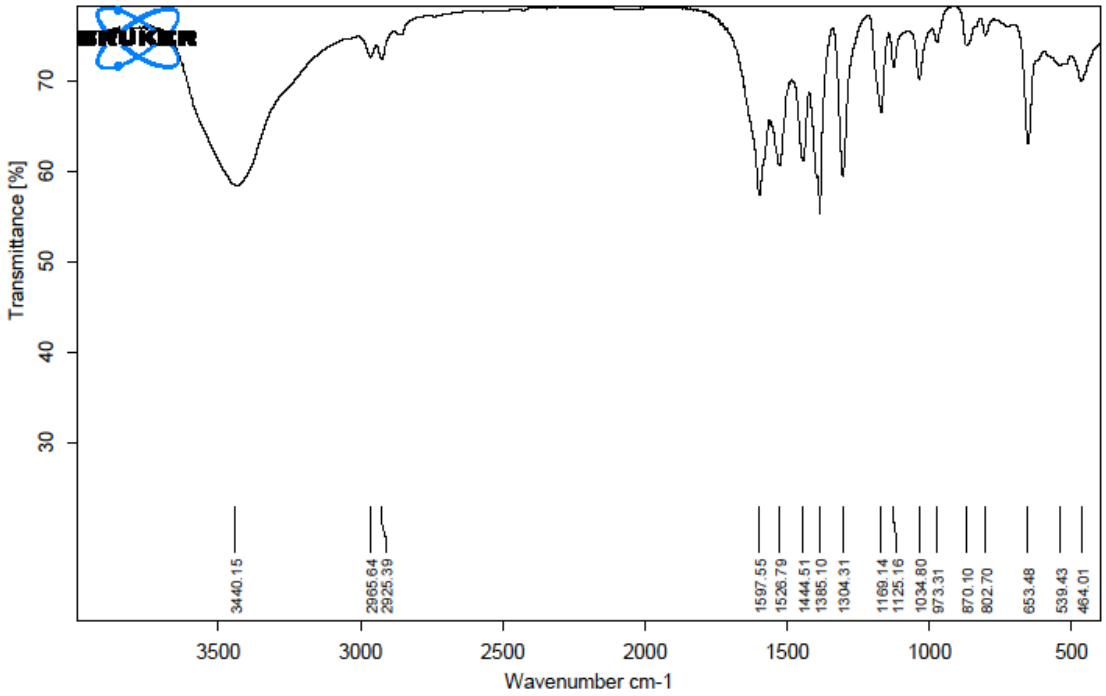

Figure A.79: Infra-red spectra of Zn(2,6-dimethyl hba)

A.6.8 Zn_2(tetrafluoro hba)$(OAc)_2$

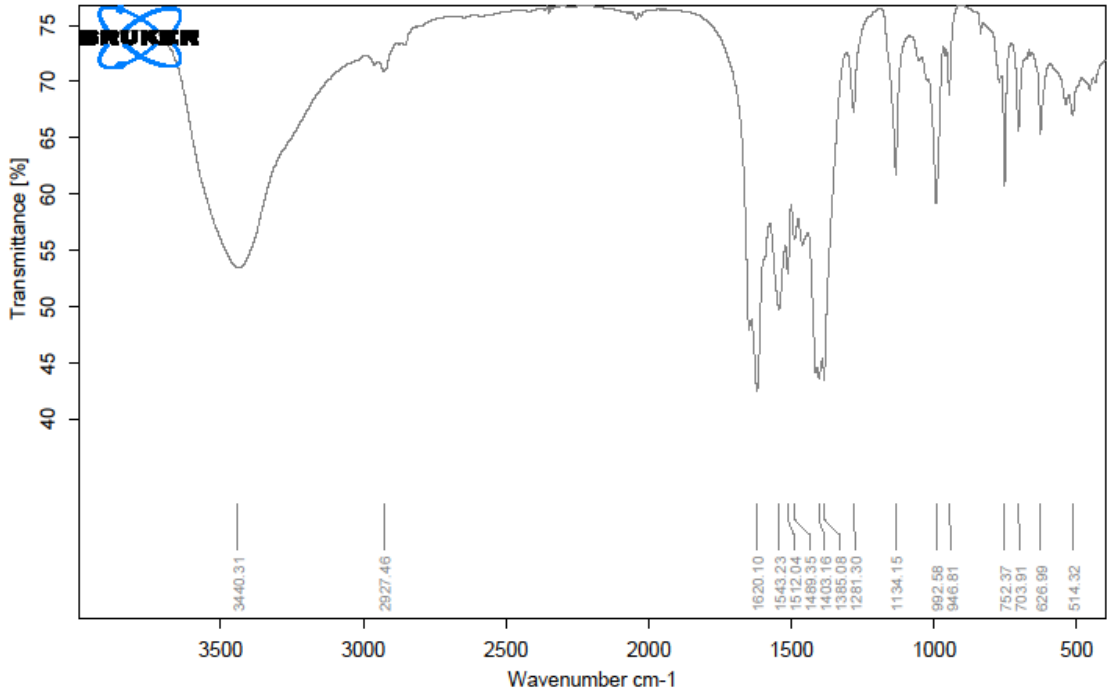

Figure A.80: Infra-red spectra of Zn_2(tetrafluoro hba)$(OAc)_2$

A.6.9 $Cu(HhpOa)_2(H_2O)_2$

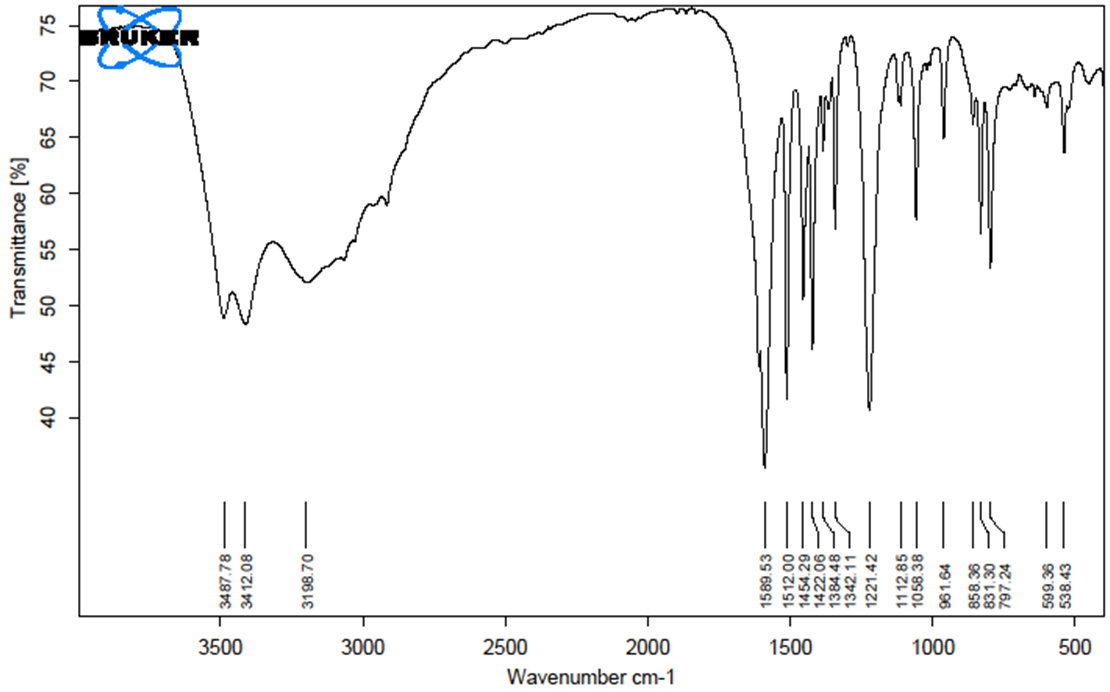

Figure A.81: Infra-red spectra of $Cu(HhpOa)_2(H_2O)_2$

A.6.10Zn(HhpHNa)

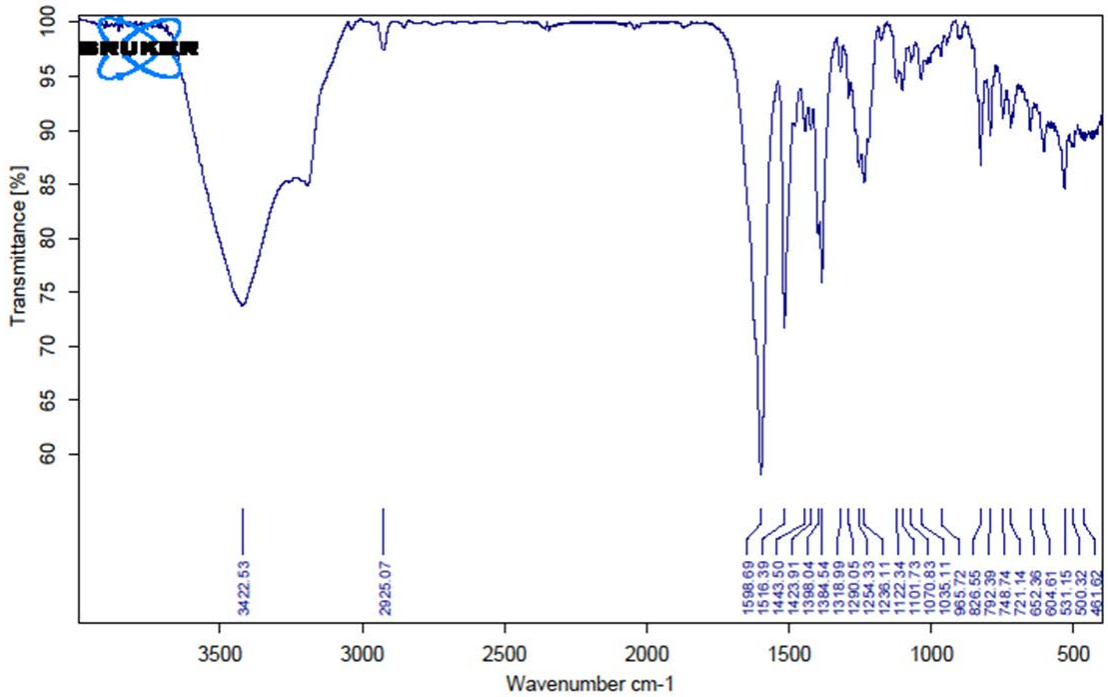

Figure A.82: Infra-red spectra of Zn(HhpHNa)

A.7References

[1] Dassault SystèmesBIOVIA, *Discovery Studio Modeling Environment*, San Diego, **2019**.

[2] S. Grimme, S. Ehrlich, L. Goerigk, *J. Comput. Chem.* **2011**, *32*, 1456–1465.

[3] G. Kresse, J. Hafner, *Phys. Rev. B* **1993**, *48*, 13115–13118.

[4] J. P. Perdew, K. Burke, M. Ernzerhof, *Phys. Rev. Lett.* **1996**, *77*, 3865–3868.

[5] G. Kresse, D. Joubert, *Phys. Rev. B* **1999**, *59*, 1758–1775.

[6] A. Hirotani, K. Mizukami, R. Miura, H. Takaba, T. Miya, A. Fahmi, A. Stirling, M. Kubo, A. Miyamoto, *Appl. Surf. Sci.* **1997**, *120*, 81–84.

[7] A. K. Rappe, C. J. Casewit, K. S. Colwell, W. A. Goddard, W. M. Skiff, *J. Am. Chem. Soc.* **1992**, *114*, 10024–10035.